VNIVERSITAT DE VALÈNCIA

Departament d'Astronomía i Astrofísica
Programa de Doctorat en Física

Numerical treatment of radiation processes in the internal shocks of magnetized relativistic outflows

TESI DOCTORAL

feta per

Jesús Misráyim Rueda Becerril

dirigida per

Dr. Miguel Ángel Aloy Torás
Dr. Petar Mimica

Juliol de 2017

Miguel Ángel Aloy Torás, Profesor Titular del Departamento de Astronomía y Astrofísica de la Universitat de València y Petar Mimica, Investigador Asociado al

Departamento de Astronomía y Astrofísica de la Universitat de València

CERTIFICAN:

Que la presente memoria, titulada: **Numerical treatment of radiation processes in the internal shocks of magnetized relativistic outflows**, ha sido realizada bajo su dirección en el Departamento de Astronomía y Astrofísica de la Universitat de València por Jesús Misráyim Rueda Becerril, y constituye su Tesis Doctoral para optar al grado de Doctor en Física.

Y para que conste firman el presente certificado en Burjassot, a 29 de mayo de 2017

Fdo: Miguel Ángel Aloy Torás

Fdo: Petar Mimica

Abstract

Blazars are a type of active galactic nuclei (AGNs) which are among the most energetic and violent astrophysical objects, alongside γ-ray bursts (GRBs). The physical processes, and, in particular, the relativistic jet itself in which the high energy radiation detected by the terrestrial and space observatories is generated, has been attracting the attention and interest of astronomers and astrophysicists since their discovery. In the present thesis, we investigate the internal shock (IS) model in which two magnetized shells of plasma, with cylindrical geometry, collide forming shock waves, which propagate throughout the plasma accelerating electrons (thermal and nonthermal) in their wake. Those electrons interact with the magnetic field of the jet producing magnetobremsstrahlung emission, which is detected by observations. In this model we also consider that the surroundings of the jet in which this collision takes place are filled with a monochromatic photon field, which emulates the more complex broad line region (BLR) of the AGN. Both photons from the external field and those produced in situ are Compton upscattered by the accelerated electrons.

The main work of the present thesis has been the search of signatures imprinted on the double bump spectral energy distribution (SED) of blazars that may uncover the degree of the shell magnetization and the profile of the electrons energy distribution (EED) injected at the shock front. We have approached the problem numerically, so that a fair fraction of the work has consisted on improving already existing sophisticated numerical tools or developing new ones from scratch. We have used these numerical tools to simulate the IS model and reproduce broadband SEDs of blazars.

To validate our methodology and put bounds on the parameters of our model, observational data has been analyzed so that the generated SEDs are able to reproduce generic observational data and inferred physical trends.

From the Compton dominance and the spectral index of γ-ray photons obtained in our models, we infer that a fair fraction of the blazar sequence could be explained by the shells magnetization; the negligibly magnetized models describing the Flat Spectrum Radio Quasars (FSRQs) region, whereas moderately magnetized shells fall into the BL Lacertae object (BL Lac) region. On the other hand, by including thermal electrons into the population of injected particles and using a numerical tool which reproduces the low energy region of the magnetobremsstrahlung (MBS) emission, we have found that the valley which separates the synchrotron and inverse-Compton (IC) components grows deeper when thermal dominated distributions are injected at the shock front. A slightly varying synchrotron peak between 10^{11}–10^{13} Hz, in contrast with a parameters dependent IC component. These effects induce a scattering in the vertical direction of the Compton dominance-synchrotron peak plane. From this clear fact, we cautiously suggest that the proportions of the thermal/nonthermal electrons have a prominent role explaining the location of blazars in that plane.

Preface

This thesis aims to reveal the physics underlying the phenomenology observed in blazars. The reasons why blazars find themselves among the most appealing Astrophysical objects known and why they are fascinating objects that have stimulated the creativity of several generations of astronomers and astrophysicists will be addressed in Chapter 1.

In Chapter 2 we will elaborate on the physical background on which the MBS and the blazars IS model resides. We will start with the dynamics and electrodynamics of a charged particle immersed in a homogeneous magnetic field. We will continue with the description of the dynamics of colliding shells in the IS model, based on Mimica & Aloy (2012). The last part of this chapter gives an overview of the different types of distributions of particles, the model employed for the injection of particles at a shock front and the evolution of particles in a shocked region in two regimes: with and without including a radiative cooling term active over a finite period of time.

In Chapter 3 we will enclose a detailed description of the numerical techniques and methods developed and used during my stay in the *Computer Aided Modeling of Astrophysical Plasma* (CAMAP) research group with Prof. Miguel Ángel Aloy and Dr. Petar Mimica. The first part of that chapter is focused on the Internal Shocks code developed by Mimica & Aloy (2012), which is the cornerstone of the present work. In the second part we present a detailed description of the code `CHAMBA`: a new computational tool which intends to reproduce the emissivity out of single charged particles moving with arbitrary speed, and also of distributions of particles of arbi-

trary profile in a magnetic field. Our published works (Rueda-Becerril et al. 2014b, 2017) are results out of a systematic and consistent use of these tools.

Chapter 4 is based on research performed in the CAMAP research group with Prof. Miguel A. Aloy and Dr. Petar Mimica, as a continuation of the previously published work (Mimica & Aloy 2012). The work was published in 2014: J. M. Rueda-Becerril, P. Mimica, & M. A. Aloy. The influence of the magnetic field on the spectral properties of blazars. *Monthly Notices of the Royal Astronomical Society*, **438**:1856–1869, Feb. 2014b. doi: 10.1093/mnras/stt2335. RMA14. The work consisted in expanding the parameter space for the internal shocks model of blazars previously scanned with the code developed by Dr. Petar Mimica and Prof. Miguel A. Aloy. The aforementioned code was supplemented with the possibility of computing the photons spectral index of the synthetic models (described in §4.5.1). The observational data was obtained from the *Fermi* LAT Second AGN Catalog (2LAC) database[1]. We performed all the simulations in this chapter in the supercomputer `Tirant`.

Chapter 5 is based on research performed in the CAMAP research group with Prof. Miguel A. Aloy and Dr. Petar Mimica. The work was published in 2017: J. M. Rueda-Becerril, P. Mimica, & M. A. Aloy. On the influence of a hybrid thermal–non-thermal distribution in the internal shocks model for blazars. *Monthly Notices of the Royal Astronomical Society*, **468**:1169–1182, June 2017. doi: 10.1093/mnras/stx476. RMA17. The results described correspond to simulations made by using the internal shocks code (Mimica & Aloy 2012) with a hybrid thermal-nonthermal particles distribution injected (§2.4.2.2), the finite-time particles evolution scheme (§2.4.3.2) and the new numerical tool `CHAMBA` (§3.2). All the simulations where performed using the servers of the Department of Astronomy of Astrophysics of the University of Valencia: `Fujiserver1` and `ARC1`.

Astrophysics has meant to me like walking into the wild. I never knew what I was going to find but every step has brought joy and enlightenment. Knowing a bit of the phenomena which take place out there has been like breathing fresh air in the woods, which enriches your lungs and brings you peace, or like a heavy rain, which soaks you with the vital liquid but it is too much that you have to run for shelter. The process of proposing the development of new numerical tools like `CHAMBA`, has

[1] `https://heasarc.gsfc.nasa.gov/W3Browse/all/fermilac.html`

helped me to get a feeling of what is out there. The process of writing it, on the other hand, has been like climbing a mountain: you never know if you are going to get there or if nature is going to send a storm and make you draw back. We started to climb from high-energy-electrons base camp. We planned the route there, keeping an eye on the weather at all moment for any storm forecast. During the days in base camp we had to deal with fundamental questions like whether it is worth it to go beyond the transrelativistic heights, which so many explorers have gone up and down with great skill over and over for decades, or stay at the foothills of magnetobremsstrahlung mountain. With a *blazarian* impulse we decided to leave the tranquility of base camp and hit the crag. We came across unstable (numerical) gravel ravines, climb and rappel steep cliffs and monumental crags. Ergs and ergs of vertical walls. There were moments where no grip was on sight, praying for the rope to hold. Fortunately for our expedition it did, and we made it to the cyclotron peak.

JMRB

Contents

List of Figures

List of Tables

Acknowledgements

If I were to thank every single person that made this thesis and my graduate studies possible I would need more than a couple of pages. Nevertheless, I want to thank you all.

I would like to thank my supervisors: Prof. Miguel Ángel Aloy and Dr. Petar Mimica. To Miguel Ángel for teaching me that one should never spare in rigor at writing a numerical code so that it may bring reliable results. For his support in harsh situations and always critical and realistic opinions of any situation. For impregnating the philosophy of the scientific method in my every day life and for his patience.

I would like to thank Pere for showing me so many creative and ingenuous ways to develop numerical algorithms. I will always be thankful for so much physics that appeared in the blackboard at relativistic speed. And above all I want to thank you for sharing not only the office but also all those interesting talks about whatever topic and specially so much laughter. Fala i vidimo se!

To all the graduate students at the department. In particular to our dearest friend Juan Antonio Chistoso. For those entertaining hours full of laughter at lunch time. For the 1-euro beers, for the Game of Thrones nights, for those cellphone games. I dare to say that, thanks to you, lunch time was the best hour of the day. I am going to miss you guys! To Sergio (parce) for those mini-breaks talking about latinos stuff, and for those long, long talks with wine and good company.

I want to thank Carmen for all her patience and for taking care of all those com-

puter issues that appeared out of the blue. And also I want to thank gratefully to all the members of the Department of Astronomy and Astrophysics (scholar and staff) for fostering me in the group all these years and letting me get involved in a group where so beautiful science is being held. I am honored. Moltes gracies a tots!

Special thanks go to my parents. For their unconditional support. Without them this manuscript would have never got to an end, nor a beginning. For encouraging me to never give up no matter how hard the wind blows. For being always the polar star and help me always find my way no matter how lost I was. And these lines fall short compared to all that I owe you. Y no, mi chava, no te olvido. I want to thank hugely to my sister. That wonderful, brave, just and admirable woman who has been my friend and mischief partner all my life. For always having a critical and fair point of view. Te admiro, mi chava. Thank you not only for all your lessons on social justice, but also for your trust and your time. It means a lot to me ¡Los quiero harto a los tres!

I want to thank a Wild Woman, a Wolf Woman: Ana. There are no words that can express my gratitude for healing the heart and soul of a crumbling city full of prejudices. My spirit flies to you as the wolf howls to the moon, and back.

I want to thank everybody in Mexico. Family and friends. For all your support and cheers from all across the big pond. In particular I want to thank Prof. Francisco S. Guzmán for his enthusiasm and for encouraging me to dive into the exiting world of Numerical Relativity ten years ago. I am forever grateful for that, Paco.

I want to thank the mountains, crags and all those climbing rascals who, literally, were at the feet of the crag keeping an eye on my life. For showing me the meaning of partnership, to never be afraid and to accept things as they come. ¡Fuerza y honor! And last but not least, I want to thank all the people that happend to be in my life (long or short, for good or bad) during these years of the valencian adventure.

The present thesis was partially financed by the fellowship *Santiago Grisolia* awarded by the Council of Education, Research, Culture and Sports of the Valencian Comunity, and by the fellowship from the Mexican Federal Government for graduate studies abroad awarded by the National Council of Science and Technology (CONACyT).

El camino subía y bajaba: “Sube o baja según se va o se viene. Para el que va, sube; para él que viene, baja.”

Pedro Páramo — Juan Rulfo

A mi tía Mago, quien siempre deseaba que volaramos. Chale…

Esto no se acaba hasta que se acaba.

Margarita Becerril Camacho
(1983–2016)

Chapter 1

Introduction

In the present chapter a brief history and state-of-the-art observations and theoretical models of blazars are described.

1.1 Active Galactic Nuclei

An active galactic nucleus (AGN) is a region of a galaxy that is brighter than normal, typically associated with the presence of a super massive black hole (SMBH) in the galactic center. Its luminosity can reach values $\sim 10^{45}\,\mathrm{erg\,s^{-1}}$. The observations of these objects start in the early XX century when astronomers began to realize that the nuclei of some galaxies had optical emission lines. The first systematic study of the optical emission from these objects was performed by Seyfert (1943). A few years earlier Jansky (1932) discovered a strong radio signal, which he thought to be associated with the Sun, albeit later he concluded that the emission came from the center of the Milky Way (Jansky 1935). These studies are considered a breakthrough for the development of radio astronomy, which saw great progress in the following years. During these years the identification and measurement of the structure of radio sources also made large advances not only in radio but also in optical, e.g.: *Vir A* (*M87*), and *Cyg A* (Shields 1999). Jennison & Das Gupta (1953) discovered that the structure of Cyg A was best modeled as a two-component source, both components having approximately the same intensity (see Figure 1.1). A short time later a jet structure emanating from the nucleus of *M87* was observed by Baade & Minkowski

(1954). A decade later Schmidt (1963) discovered the first quasi-stellar object (QSO): *3C 273*.

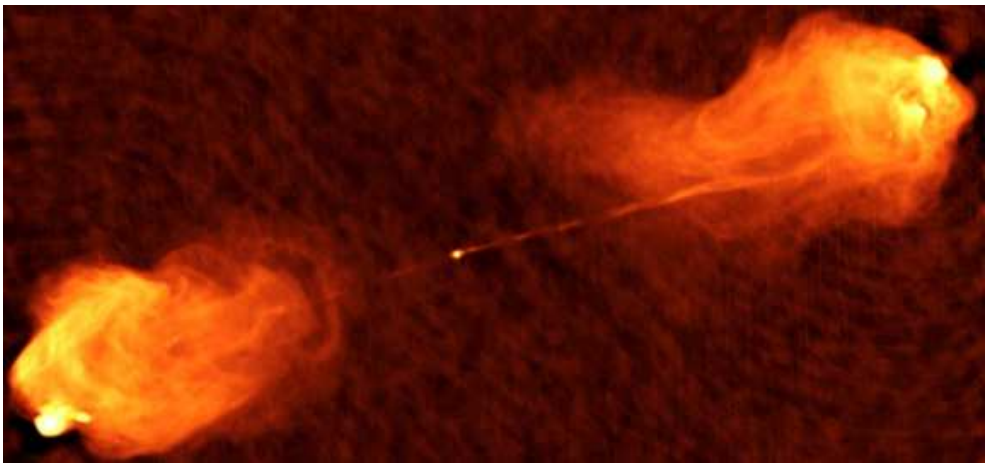

Figure 1.1: Cygnus A *observed by the VLA at* 5 GHz *(Image courtesy of NRAO/AUI).*

A high variability of these objects and their large redshifts have been measured (Matthews & Sandage 1963; Greenstein & Schmidt 1964; Schmidt & Matthews 1964), proving them to be active, extragalactic and being hosted by a galaxy. However, the theoretical foundation of the physics responsible for this emission was not clear. Alfvén & Herlofson (1950) proposed the synchrotron process as responsible for the radio emission coming from the Sun and *radio stars*. With this idea Kiepenheuer (1950) tried to explain the Galactic radio background as synchrotron radiation coming from ultrarelativistic electrons accelerated by the interstellar magnetic fields, taking into account relativistic corrections to the emitted frequency, and later supported by the corrections[1] by Ginzburg (1982). Moreover, Burbidge (1956) estimated that in order to explain the high luminosities in the optical and radio coming from *M87*, the energy supplied to the electrons in the jet, assuming that they are moving in a magnetic field $\lesssim 10^{-2}$ G, had to be $\gtrsim 10^{49}$ erg. Furthermore, De Young & Axford (1967) pointed out that the estimated strength of the intergalactic magnetic field would not be enough to collimate the material ejected from the nucleus of, e.g., *Cyg A*. Disregarding other possible relativistic effects, they proposed that the jet structure is more likely dynamic rather than in hydrostatic equilibrium with the intergalactic

[1]The calculations by Kiepenheuer (1950) carried an error by using the synchrotron approximation for frequencies $\nu \ll \nu_c$ (see §2.2.4) for the case of $\nu > \nu_c$

medium and bering its own magnetic field. This was done by balancing the internal pressure of the jet material with the ram pressure of the intergalactic medium and estimating that the mass of the jet is $\sim 2 \times 10^6 M_\odot$, the density of the jet material $\gtrsim 10^{-30}\,\mathrm{g\,cm^{-3}}$ and the time required to stop it $\lesssim 2 \times 10^5$ yr, this being comparable to the actual age of *Cyg A*.

Until that point there was no preferred candidate to explain the nature of the central object of these kind of radio sources. Reasoning from first principles Lynden-Bell (1969) proposed that the objects in the nuclei of, e.g., *M87*, *Cyg A* or *Sgr A*, result from the collapse of old quasars with a mass $\sim 10^9 M_\odot$, and that a flat disk of gas encompasses these objects. He was the first to propose a model containing both a SMBH and an accretion disc (AD). After several decades and many observations in the whole electromagnetic spectrum, astrophysicists proposed the following scenario for AGNs, which has been so far the most accepted one (Urry & Padovani 1995): A SMBH is surrounded by a luminous AD. Close to the AD the clouds producing broad emission lines (broad line region (BLR)) orbit, and further out there is a thick dusty torus (TD) (or possibly a warped disk). Above the AD there is a hot corona. Finally, the radio jets are launched from a region close to the black hole (BH), and farther above, surrounding the jet, there are clouds which produce the narrow emission lines, called the narrow line region (NLR) (see Figure 1.2).

1.1.1 AGNs zoo

The AGN classification is a challenging topic. The classes of AGNs are multivariate, i.e. they depend not only on the observed morphology but also on spectral characteristics and detection criteria (e.g., Urry & Padovani 1995; Tadhunter 2008; Dermer & Giebels 2016). The first division is made according to their radio loudness; i.e., their radio to optical flux ratio

$$\frac{F_5}{F_B} \gtrsim 10, \tag{1.1}$$

where F_5 and F_B are the radiation flux at 5 GHz and at the B-band (445 nm). In the optical, AGNs can be classified by the brightness and width of their emission lines: broad and bright or narrow and weak.

Along the history of the understanding of AGNs, their taxonomy, divisions and unification have undergone several changes depending on the observational technique used, orientation or morphology of the objects (see Urry & Padovani 1995; Tadhunter

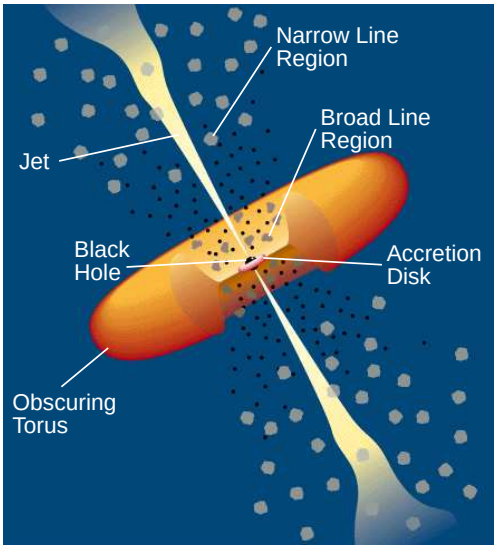

Figure 1.2: *AGNs outline (not in scale). Credit: P. Padovani*

.

2008, for a deep review on the consensus of AGNs classification). However, state of the art observations (e.g. Husemann et al. 2016) have shown that AGNs may change of type in time and therefore their spectral features are not necessarily orientation or morphology-wise dependent but maybe other kind of phenomena (e.g., tidal disruption events (TDEs)), have to be considered. Here we will mention the families the author found exemplary for the context of the present work:

Seyfert 1 Spiral galaxies with broad permitted and forbidden[2] emission lines

Seyfert 2 Spiral galaxies with narrow forbidden lines.

NLRG Narrow line radio galaxies (NLRGs) are radio loud galaxies with narrow emission lines. This kind of galaxies includes the Fanaroff-Riley radio galaxies (Fanaroff & Riley 1974):

FR I The hotspots (brightest regions) are closer to the nucleus of the galaxy and the source becomes fainter as one approaches the outer region. The jets of these galaxies often appear symmetric in radio.

[2]The *forbidden lines* are the spectral lines corresponding to the absorption or emission associated to the less likely transitions of the electrons in an atom.

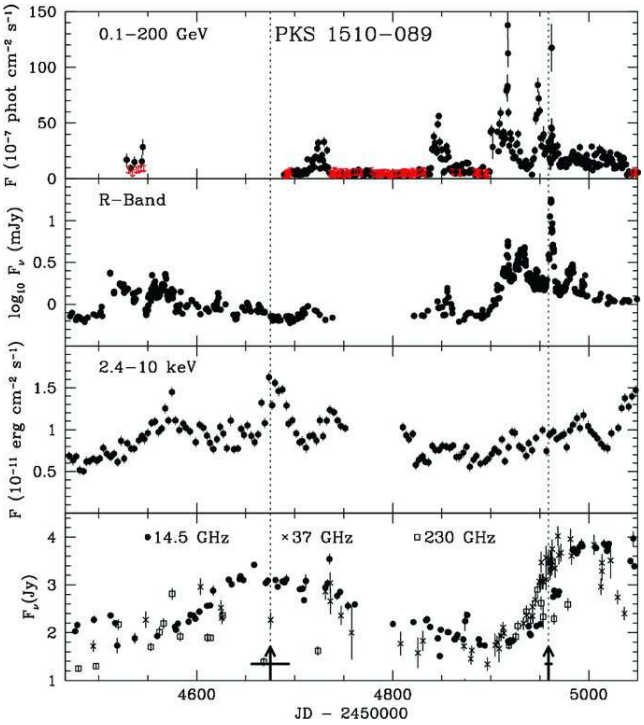

Figure 1.3: *Multiwavelength light curves in γ-rays, optical R band, X-rays and radio. Credits Marscher et al. (2010).*

FR II The hotspots are farther from the nucleus of the galaxy. Their morphology consists in more collimated jets and well recognizable radio lobes.

FSRQ Flat Spectrum Radio Quasars (FSRQs) are radio loud galaxies with broad emission lines.

There is a third species of AGNs, which shows extremely variable spectrum (see Figure 1.3). What characterizes these objects is their small angle to the line of sight of the observer. If the object is radio quiet the object is called a broad absorption line quasar (BAL QSO). Otherwise we are facing a *blazar*[3].

[3]The name *blazar* was coined by the astronomer Edward Spiegel in 1978 to designate those objects with strong nonthermal broadband continuum and narrow emission lines.

1.2 Blazars

Blazars are a kind of highly variable and radio loud AGNs whose features are best explained by nonthermal radiation from a relativistic jet closely aligned to the line of sight of the observer (e.g. Blandford & Rees 1974). The relativistic plasma moves along the jet, which is the channel along which the central engine supplies momentum and energy to the extended radio structures, reaching distances of 0.1–1 Mpc from the nucleus (Urry & Padovani 1995). The broadband continuum of blazars goes from radio frequencies to γ-rays, developing a double bump in their spectral energy distribution (SED) (see below). Blazars typically represent less than 5% of all AGNs (Ajello et al. 2009, 2012)

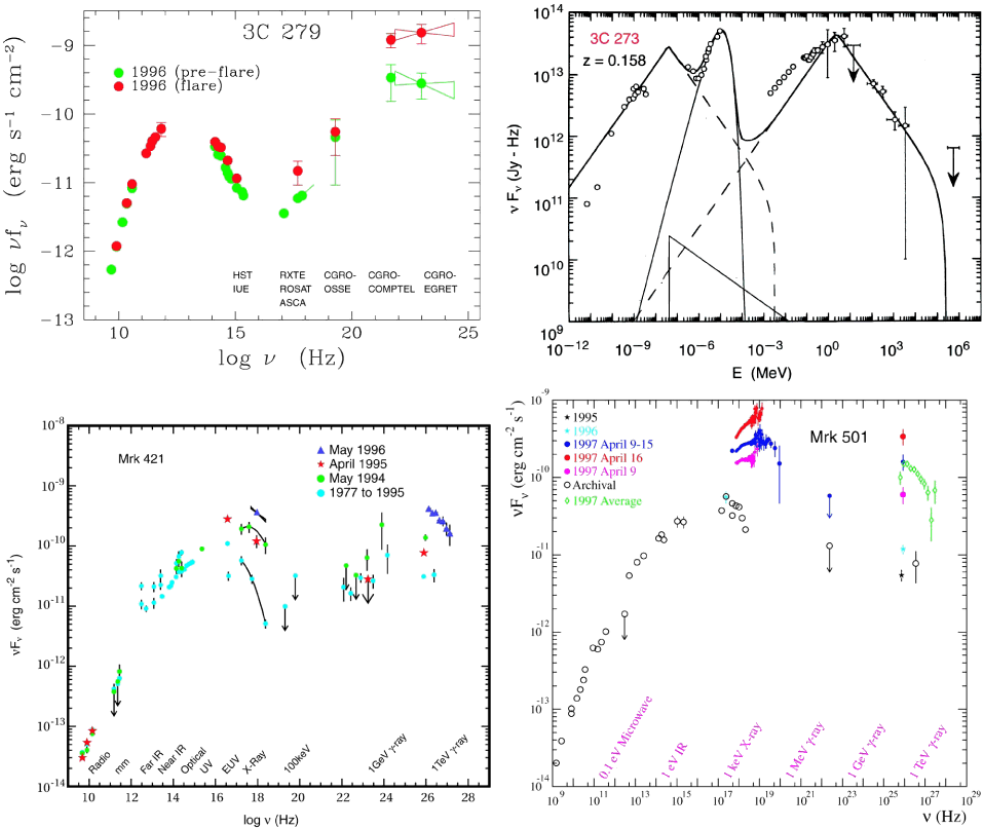

Figure 1.4: *Broadband emission of blazars. Credit: A.E. Wehrle/M.A. Catanese/J.H. Buckley/Whipple Collaboration.*

These objects are named after *BL Lacertae* (see Figure 1.5), first observed by

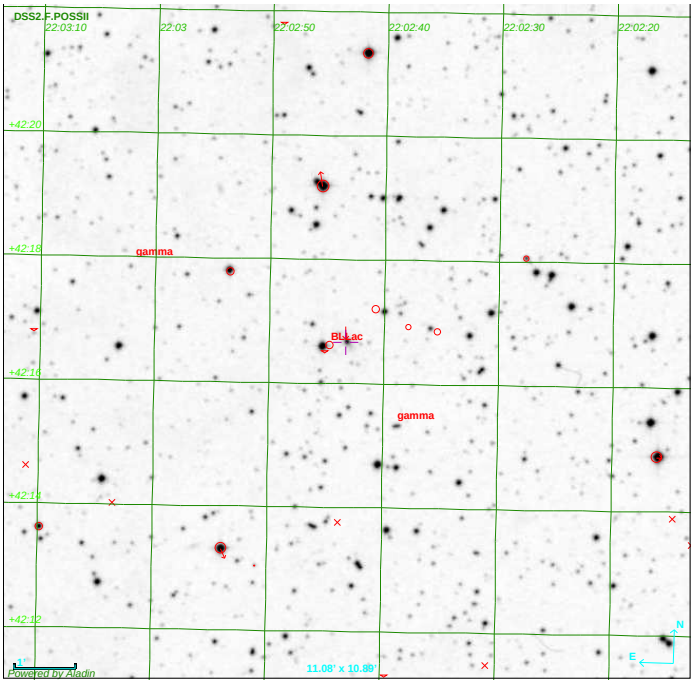

Figure 1.5: BL Lacertae *in the optical band (red). This figure was made using the* Aladin sky atlas *web applet (Bonnarel et al. 2000; Boch & Fernique 2014), using the second Digitized Sky Survey (DSS2).*

Hoffmeister (1929) showing high variability emission lines, but at that time it was categorized as an *irregular variable star* in the *Milky Way*. Later Schmitt (1968) identified *BL Lac* with the radio source *VRO* 42.22.01, finding its radio spectrum to be polarized. A decade later Oke & Gunn (1974) observed that the spectra coming from it showed absorption lines typical of an ordinary giant galaxy with redshift $z = 0.07$.

Blazars are commonly classified according to the relative strength of their observed spectral components. Each component is associated to the contribution of a relativistic jet (nonthermal emission), to the AD and to the BLR (thermal radiation), and to the light from the host, usually a giant elliptical galaxy (Urry et al. 2000). The broadest component of the spectrum is the nonthermal one, and it spans the whole electromagnetic frequency range, usually displaying two broad peaks or "humps" (see Figure 1.4). The lower-frequency peak ranges between 10^{12}–10^{17} Hz (radio and X-rays), while the high-frequency spans from X-rays to γ-rays, and is believed that is caused by the inverse-Compton (IC) scattering (Jones et al. 1974; Hoyle et al. 1966; Fossati et al. 1998).

Depending on the features displayed by their emission lines, blazars can be fur-

ther subdivided into (Sambruna et al. 1996):

BL Lac BL Lacertae objects (BL Lacs) have featureless emission lines or show only weak absorption lines. Their synchrotron peak frequency ranges between radio and X-rays.

FSRQ FSRQs are characterized by broad emission lines. Their synchrotron peak is found between radio an near infrared.

Moreover, depending on the peak frequency of their SEDs synchrotron component ($\nu_{\rm syn}^{\rm obs}$), blazars have been recently further subclassified into low-synchrotron peaked (LSP), intermediate-synchrotron peaked (ISP) and high-synchrotron peaked (HSP) (e.g. Finke 2013). In the former group we can find low-frequency-peaked BL Lac objects (LBLs) and most FSRQs with $\nu_{\rm syn}^{\rm obs}$ $<10^{14}$ Hz, in the intermediate group we find intermediate-frequency-peaked BL Lac objects (IBLs) few FSRQs with $\nu_{\rm syn}^{\rm obs}$ $\approx 10^{14}$–10^{15} Hz, and in the latter group we find high-frequency-peaked BL Lac objects (HBLs) with $\nu_{\rm syn}^{\rm obs}$ $>10^{15}$ Hz (Sambruna et al. 1996; Abdo et al. 2010a; Giommi et al. 2012a).

1.2.1 Blazar models

As we have mentioned above, there is a broad consensus that the low frequency peak is due to the synchrotron emission from relativistic electrons gyrating in a magnetic field. As for the high frequency peak, as mentioned before, it may be the result of IC scattering. To account for observations, different ideas have been put forward about where the seed photons for IC scattering come from. For instance: IC synchrotron photons intrinsic to the jet result in synchrotron self-Compton (SSC) emission (Bloom & Marscher 1996), upscattering of soft photons from a blackbody AD (Dermer & Schlickeiser 1993), upscattering of photons initially from an AD and then scattered by the BLR (Sikora et al. 1994), upscattering of photons coming from the TD (Kataoka et al. 1999) are all examples of external inverse-Compton (EIC) emission.

So far it is unknown where in the jet all the aforementioned emission processes take place. There are several points of view on this regard. For instance, there was a proposal by Blandford & Königl (1979) saying that the radiation comes from inhomogeneities in the jet such as accelerated blobs of plasma or shock waves that travel

along the jet. This model belongs to the so called *multi-zone* models. There are others in this group like the *conical standing shock* (Jorstad & Marscher 2004; Marscher et al. 2008), which proposes that the bright, compact, quasi-stationary features in the innermost regions of the jet revealed by *VLBA*[4] and *VLBI*[5] observations (Jorstad et al. 2005; Fromm et al. 2013) is accounted for by conical standing shocks; these shocks recollimate the ejected material at ultrarelativistic speeds, producing the γ-ray flares. Also the *turbulent extreme multi-zone* model, introduced by Marscher (2014), considers not only ultrarelativistic material crossing the a recollimation shock but also turbulent plasma, accounting for the polarization features in the radio "cores". Another model is the *spine-layer* which proposes a jet with subrelativistic external flow surrounding a much faster inner flow (Henri & Pelletier 1991; Ghisellini et al. 2005).

On the other hand, the observation of "knots" or blobs in jets of AGNs has led to propose *one-zone* models for blazars, which attempt to account for flare emission in the observed spectra (Rees 1978). The most popular, and yet most successful up to date, is the *shock-in-jet* model in which it is assumed that instabilities in the jet, or the intermittent ejection of plasma by the central engine, produce internal shocks (ISs) at some point along the jet (Marscher & Gear 1985; Spada et al. 2001).

1.2.2 The blazar zone

The *blazar zone* is where most of the kinetic energy of the jet is transformed into radiation and where it is assumed that particles are being accelerated (e.g. Bykov et al. 2012). The size of the *blazar zone* has been estimated to be of 10^{15}–10^{17} cm (Georganopoulos et al. 2001). Some models suggested that γ-rays are produced within the BLR and that the γ-ray emitting radius ranges roughly between 0.03–0.3 pc (Ghisellini & Madau 1996, see Figure 1.6). It has also been argued that in relativistic jets of powerful blazars the γ-rays emission regions are within cavities formed by the BLR. However, it has also been observed that the emission region is outside the BLR (e.g. Agudo et al. 2011).

Regarding the particle population of the radiating material in jet there are two main contending models: leptonic and hadronic. In the leptonic model the high-energy emission is produced by relativistic electrons which are accelerated through

[4] Very Long Baseline Array is a system of radio antennas located in New Mexico, USA.

[5] *Very-long-baseline interferometry* is a technique used in astronomy for imaging radio sources.

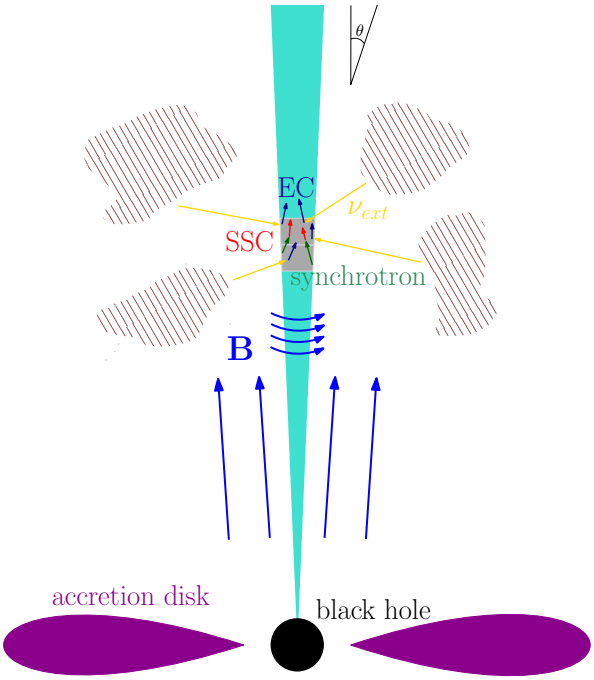

Figure 1.6: *Schematic view of the blazar zone for the model where high energy emission occurs in the BLR.*

shocks or magnetic reconnection that IC upscatter both low frequency photons from the external medium (EIC) and synchrotron photons produced in the jet (SSC). The hadronic model assumes that the relativistic protons (that may be present in the jet besides electrons) are able to produce the high energy emission via proton-synchrotron radiation (for which strong magnetic fields are required) and energy losses due to photomeson production and pair production (Begelman et al. 1990; Mannheim 1993; Mücke et al. 2003)

So far we have not discussed the fact that the magnetic fields are ubiquitous in AGNs. In fact, little is known about the true role that the magnetic field play in the emission of blazars since, depending on the model and the distance from the central engine, the magnetic field has a different influence on the phenomena in the jet; for instance, the magnetic field strength determines the efficiency of electron acceleration at shocks. Nevertheless, detailed studies of the magnetic field strength and geometry have proved useful for approaching to resolve this issue (e.g. Porth et al. 2011; Mimica & Aloy 2012; Janiak et al. 2015).

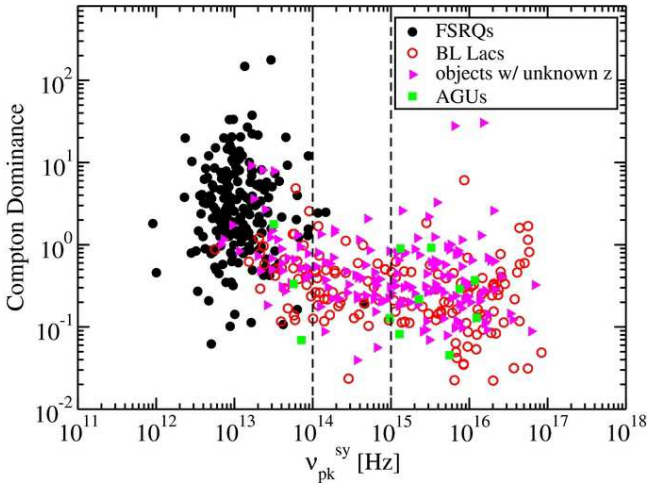

Figure 1.7: Compton dominance *versus synchrotron peak frequency. Credit: Finke (2013).*

1.2.3 The blazar sequence

In an attempt to unify blazars there are hints suggesting that there is an evolutionary trend among these sources. The SED peaks of high luminosity sources shift to higher frequencies in low luminosity sources; i.e., there seems to be an evolutionary trend from FSRQs then to LBLs and finally towards HBLs (Fossati et al. 1998; Böttcher & Dermer 2002). With the aim of clarifying this trend a new parameter was introduced by Finke (2013) which is the *Compton dominance*:

$$A_C := \frac{\mathcal{L}_{\rm IC}}{\mathcal{L}_{\rm syn}}, \tag{1.2}$$

where $\mathcal{L}_{\rm IC}$ and $\mathcal{L}_{\rm syn}$ are the luminosities of the IC and synchrotron components of the SED. It has been observed that in the A_C-$\nu_{\rm syn}^{\rm obs}$ plane there is an "L"-shaped transition from FSRQs to BL Lacs showing the luminosity decrease of the IC component (see Figure 1.7).

By modelling blazar SEDs Ghisellini et al. (1998) found that this sequence can be accounted for by the increasing role of the external photon field in the cooling factor of relativistic electrons in the jet, since the time evolution of the electrons Lorentz factor, γ, is governed by (see §2.4.3):

$$\dot{\gamma} = -\frac{4}{3} c \sigma_{\rm T} \frac{u_{\rm B} + u_{\rm ext}}{m_{\rm e} c^2} \gamma^2 \tag{1.3}$$

where $u_{\rm B}$ and $u_{\rm ext}$ are the magnetic and external photon field energy densities. Based on this, models have been proposed where $u_{\rm ext}$ takes a range of values, or is given as

a function of the distance to the central engine, rather than having a constant value (Ghisellini & Tavecchio 2009; Sikora et al. 2009; Saito et al. 2015).

1.3 The internal shocks model

Shock waves are ubiquitous in nature. In astrophysics they are typically regarded as regions where particles are accelerated and important radiation processes take place. In AGNs, particularly in blazars, there has been some evidence that shock waves appear in the jet. Their origin may be due to either instabilities in the jet flow, arising from the jet/ambient interaction or from the magnetic field topology, or to the non-linear evolution of an inhomogeneous or time-variable jet generation (e.g. Begelman & Kirk 1990; Baring 2012). As mentioned above, the IS (or shock-in-jet) model had an important role in the understanding of the blazar spectra and has been successful in explaining many of the features of the blazar variability and flares.

The internal shocks model for blazars considered in this work rests on the idea that that a central engine ejects shells of plasma with different mass, energy and velocity. This translates into the presence of relative motions in the relativistic jet. Early blobs will decelerate (cool down, with bulk Lorentz factor $\Gamma_{\rm R}$) as they move further away from the central engine (e.g. Rees & Mészáros 1994). Faster shells (with bulk Lorentz factor $\Gamma_{\rm L}$) will catch-up with the slow ones at a time $t_{collision}$ producing "collisions" (see Figure 1.8). During the collision process the plasma is shocked, dissipating energy in the form of acceleration of particles, and in turn as radiation. If magnetic fields are dynamically negligible, two shocks form separated by a contact discontinuity (CD): one propagating into the slower shell (forward shock; FS) and another one slowing down the faster shell (reverse shock; RS).

This model was first proposed almost thirty years ago by Rees (1978) accounting for the optical knots in the *M 87* jet, and later by Marscher & Gear (1985). It was not until the beginning of the past decade that the IS model was revived (e.g. Spada et al. 2001; Bicknell & Wagner 2002; Mimica et al. 2004), and since then this scenario has been thoroughly explored using analytic and (simplified) numerical modelling (Kobayashi et al. 1997; Daigne & Mochkovitch 1998; Spada et al. 2001; Bošnjak et al. 2009; Daigne et al. 2011) and by means of numerical hydrodynamics simulations (Kino et al. 2004; Mimica et al. 2004, 2005, 2007).

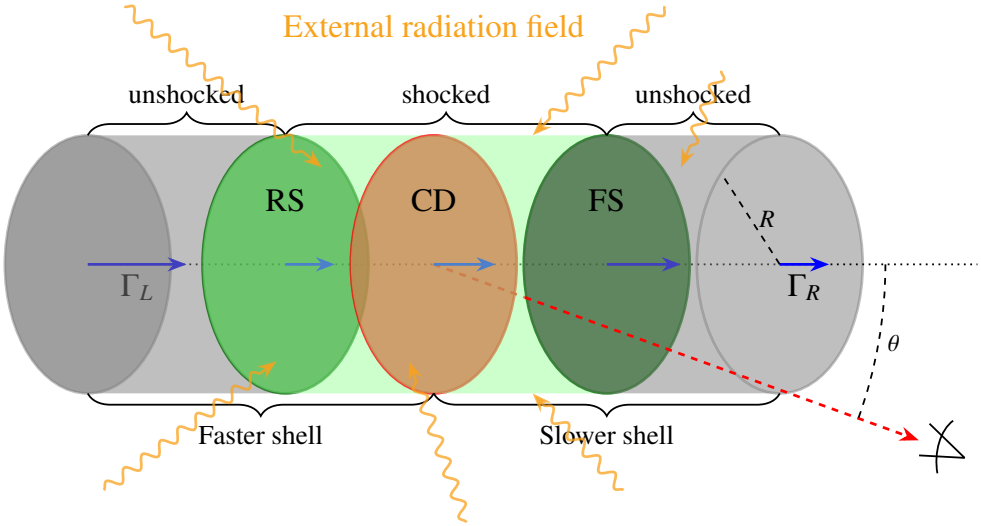

Figure 1.8: *Representation of the internal shocks scenario at $t > t_{collision}$. Here the shells are modeled as cylinders with no sideways expansion and immersed in a external radiation field. The grey regions correspond to the unshocked material. The green regions correspond to the shocked material. Photons illuminating the shocked and produced by external sources are represented with orange zig-zagging arrows. The direction towards the observer is denoted by the red dashe line. This line forms an (small) angle θ with respect to the direction of propagation of the colliding shells.*

More recently, the effects of strong magnetic fields on the shell collisions have been taken into account. Given the fact that synchrotron emission from the accelerated particles in the shocked plasma fits considerably well the observations, the emitting plasma must be magnetized, to some extent. However, the degree of magnetization of the jet flow has not yet been determined, and whether the radiation we observe results from the dissipation of its magnetic energy in addition to its kinetic energy is not known, either. In the case of moderate or strong magnetic fields the IS scenario has to be modified to account for the differences in the dynamics (e.g., the suppression of one of the two shocks resulting in a binary collision Fan et al. 2004; Mimica & Aloy 2010) and the emission properties of the flares (Mimica et al. 2007; Mimica & Aloy 2012; Rueda-Becerril et al. 2014b, 2017).

1.3.1 Acceleration efficiency

The IS model assumes that a fraction ϵ_e of the shock power is transferred to the charged particles and, by means of some acceleration process (e.g. first-order Fermi process; Fermi 1954), these particles are injected into the unshocked material at the shock front. Even in the case in which a plasma is very weakly magnetized (i.e., microscopic magnetic fields tight the particles constituting the plasma, which is assumed to be collisionless), stochastic magnetic fields will be produced *in situ* by shocks through, e.g., the Weibel instability (Weibel 1959; Medvedev & Loeb 1999; Gruzinov & Waxman 1999), converting the free energy of counter-streaming flows into small-scale (skin-depth) magnetic fields. For practical purposes, it is commonly assumed that another fraction ϵ_B of the internal energy density of the plasma is transformed into a magnetic field, whose orientation in space is expected to be random (e.g. Joshi & Böttcher 2011; Mimica & Aloy 2012).

The values of ϵ_e and ϵ_B are up to date unknown. Although, advances have been made on the expected values, both from the observational data (see Santana et al. 2014; Kumar & Zhang 2015), as well as from particle-in-cell (PIC) simulations (e.g. Nishikawa et al. 2003; Hededal et al. 2004; Nishikawa et al. 2005; Sironi & Spitkovsky 2009; Sironi et al. 2013). Moreover, lower boundaries to the fraction of dissipated power have been estimated by Mimica & Aloy (2010) through numerical magnetohydrodynamics (MHD) modeling.

1.3.2 Distribution of particles

From the observed synchrotron spectra of blazars it has been shown that they fit a power-law at its highest frequencies (between optical and X-rays, e.g. Ginzburg & Syrovatskii 1965; Fossati et al. 1998). This evidence tells us that somewhere in a blazar particles are being accelerated in such a way that they follow a power-law in energies (Rybicki & Lightman 1979), or equivalently in Lorentz factors γ, with a cutoff at a maximum value γ_{max}. Ever since this idea was proposed by Ginzburg & Syrovatskii (1963), a pure power-law distribution has been considered for the theoretical modeling of blazars. In order to comply with the relativistic regime in which the synchrotron radiation is emitted, the Lorentz factor distribution of the emitting electrons is customary lower-bounded at a suitably prescribed minimum Lorentz factor γ_{min} (see §2.4.1.2).

In other astrophysical scenarios this spectrum profile (power-law) has been observed as an extension or "tail" of a thermal distribution, e.g. : neutron stars, accretion disks, supenovae, γ-ray bursts (GRBs) (e.g. Ghisellini et al. 1988; Li et al. 1996; Özel et al. 2000; Pe'er & Casella 2009). Moreover, PIC simulations have shown that in relativistic shocks a "hybrid" thermal-nonthermal distribution is naturally produced in shocked plasma models. These kind of distributions range velocities from subrelativistic to ultrarelativistic (see Spitkovsky 2008; Sironi & Spitkovsky 2009; Sironi et al. 2013).

Despite the fact that there is evidence of hybrid distributions (HDs) in relativistic astrophysical scenarios, this kind of distributions have not been deeply studied in the IS model of blazars.

1.4 Numerical treatment of the MBS emission

It has been observed in the spectra of GRBs and AGNs that magnetic fields in their jets play a very important role by their radiative signature. It has been typically assumed that electrons in collisionless shocks are efficiently accelerated until they reach ultrarelativistic energies. Hence, their emission is properly computed as a result of the synchrotron process. However, as we have pointed out in §1.3.2, it is not unlikely that the distribution of shock-accelerated electrons extends towards the moderately relativistic and even sub-relativistic regime. In this case the nice analytical properties of the synchrotron emission mechanism must be replaced by the more accurate magnetobremsstrahlung (MBS) emission. As we shall see in §2.2, a detailed treatment of the spectral evolution of electrons emitting MBS radiation requires involved numerical calculations of integrals performed over sums of infinite series (each of the series terms corresponding to a different harmonic of the gyrofrequency). In this section we review some previous efforts to compute the MBS in astrophysical plasma. The numerical details of such efforts are discussed more throughly in §2.2.

Analytic expressions for the transrelativistic regime were found by Wild & Hill (1971) using accurate approximations of the Bessel functions. Their approximations have been useful for later works building more accurate expressions for the MBS emission and absorption (e.g. Robinson & Melrose 1984; Klein 1987; Wardziński & Zdziarski 2000; Fleishman & Kuznetsov 2010). Later Petrosian (1981) approximated the power radiated (Eq. (2.15)) for a single electron replacing sums of har-

monic contributions by integrals over a continuous distribution of such harmonics. Such approximation is valid in the regime where the harmonics are so close to each other that they are indistinguishable; i.e., for the cases where the frequency is much larger than the gyrofrequency (see §2.2.5). This approach produces a typical relative numerical error between 20 and 30%. Nevertheless, it has been used in different works afterwards (e.g. Ghisellini et al. 1988; Wardziński & Zdziarski 2000; Fleishman & Kuznetsov 2010). Unfortunately, it does not deal with the harmonics in the MBS emission which appear at low frequencies; i.e, near the gyrofrequency, and it is precisely that spectral range that is of interest for this thesis.

On the other hand, over the years numerical methods and techniques that deal with the full cyclosynchrotron emission have been improving. An extensive and concise numerical approach was first performed by Brainerd & Lamb (1987). This method was implemented to calculate the emissivity from a thermal, nonthermal and hybrid distributions in GRBs and applied to fit the photon flux obtained from observations, achieving accurate results. Mahadevan et al. (1996) and later in Wolfe & Melia (2006) artificially *broadened* the harmonics by a small amount in order to facilitate the numerics.

Pe'er & Waxman (2005) developed a code with split regimes in which for frequencies 200 times the gyrofrequency and Lorentz factors lower than 10, the full expression for MBS (see §2.2.2) was computed, and above that threshold the classical synchrotron expression (e.g. Rybicki & Lightman 1979; Jackson 1999) was employed. A similar approached was made by Fleishman & Kuznetsov (2010) by placing a frequency boundary below which the harmonic structure is recovered, and above which the analytic expressions found by Petrosian (1981) and Wild & Hill (1971) are used.

One of the main difficulties in the computation of the MBS emission stems from the interplay between integrals containing Dirac δ-functions with non-trivial arguments and the presence of sums over series of harmonics. Solving this difficulty numerically may be done by either performing analytically those integrals containing the Dirac δ-functions or employing the Dirac δ-functions and using that to compute the limits for the sums over harmonics. The latter option has the advantage that it limits analytically the number of terms to be added up in a sum, which may have an infinite number of contributing terms (a priori), and for which there are no mathe-

matical criteria to ensure numerical convergence. This methodology has been used recently, and proved to be an accurate approach for calculating the harmonics (e.g. Marcowith & Malzac 2003; Leung et al. 2011; Pandya et al. 2016; Rueda-Becerril et al. 2017)

1.5 Motivation

In an attempt to understand blazar observations, many models and hypothesis have been proposed over the years, giving us different ideas about the physics involved in high energy processes. Still, there is not enough observational evidence that can tell us the precise level of importance that each physical processes has in the production of the observed high energy emission (e.g., it is well known that magnetic fields may play an important role in relativistic outflows, but we do not know the jet magnetization nor do we know with certainty whether the magnetic fields play any role at all role in the dissipation processes in the jet). There are models that have been proposed to classify and unify AGNs (and blazars in particular). However, we do not know with certainty that these models describe the true nature of AGNs.

We live in an era when the existing and the upcoming observatories all around the world (including those in space) observe the universe in many spectral bands so that we expect that in the next years much more information about all kinds of objects (blazars among them) will be obtained. However, the impossibility of replicating in the laboratory the necessary conditions to observe and measure the process that produces e.g., blazars flares has favoured the continuous development of sophisticated numerical codes that perform simulations of these processes. These simulation help us obtain a physical insight into the astrophysical phenomena (either by comparison with the existing observational data or by predicting the properties of future events). The state of the art codes for blazars incorporate as much macro- and microphysics as the computational capabilities allow. Typically, a trade-off between the two exists; i.e., one needs to decide how much effort to devote to the large scales (e.g., MHD processes), and how much to the small scales (e.g., shock acceleration). In our work we constantly try to improve our modeling on both sides of the dynamic range of scales present in blazars.

The IS model for blazars has succeeded in modeling observational data (e.g. Böttcher & Dermer 2010). In the present thesis we attempt, based on previous works

(Böttcher & Dermer 2010; Mimica 2004; Mimica & Aloy 2012; Mahadevan et al. 1996; Leung et al. 2011), to go further in exploring the IS scenario in order to find the fingerprint in the SEDs and light-curves of the shell magnetization (macro-scales), and of the properties of the particles injected at the shock front (micro-scales). We take into account the existence of sub- and transrelativistic particles in the injection, and therefore a full cyclotron, synchrotron and cyclo-synchrotron emission processes are considered.

Chapter 2

Theoretical background

2.1 Reference frames

In order to evaluate the radiation seen by a distant observer, we need to compute quantities and transform them among five different reference frames:

Comoving frame of the fluid: the frame moving with the fluid in which the electrons energy distribution (EED) is at rest. This frame coincides with the reference frame of the contact discontinuity (CD) in the collision of two shells. Thus, we will refer to them indistinguishably and use primed symbols to refer to quantities computed in this frame. In order to avoid cluttering the formulae with indices, the exception to this rule are the values of the Lorentz factor (γ) and the velocity (β) of the electrons measured in this frame, as well as the thermodynamic variables (e.g., the number density, n, the temperature, T, the pressure, P, or the specific internal energy, ϵ), which will always refer to the comoving frame and, therefore will be unprimed. We explicitly point out that we assume that the EED is isotropic in the comoving frame of the fluid.

Electron rest frame: this is the reference frame where the electrons are at rest, and is denoted by double primed quantities.

Laboratory frame: the frame in which we set up the hydrodynamic simulations and that remains at rest with respect to the AGN. In that frame the colliding shells are seen to move at relativistic speeds. We will employ unprimed symbols to

express physical quantities in this frame of reference. Lorentz factors will be denoted with Γ in this frame, to not confuse them with the electrons Lorentz factor measured in the comoving frame.

Distant observer frame: the frame of an observer who is close enough to be unaffected by cosmological effects. Variables in this frame will be denoted with the subscript or superscript "obs".

Earth observer frame: this frame is akin to that of the distant observer, but it is located at cosmological distances. The only difference with respect to the distant observer is the cosmological transformations induced by the finite redshift at which the source is located.

2.2 Magnetobremsshtrahlung

The radiation from charged particles traversing a magnetic field is known as MBS (e.g. Ginzburg et al. 1954; Ginzburg & Syrovatskii 1965)[1]. Depending on the speed v of the particles, this radiation is categorized into cyclotron radiation ($v \ll c$) and synchrotron radiation ($v \sim c$). Both regimes have been studied broadly and accurate analytic expressions for each have been developed (e.g. Schwinger 1949; Crusius & Schlickeiser 1986; Blumenthal & Gould 1970). However, the cyclosynchrotron radiation, i.e., the transrelativistic regime of MBS, has no analytic description yet which does not involve infinite sums over harmonics. In this chapter we will describe the equations governing this phenomenon.

2.2.1 Motion of a point charge in a uniform, static magnetic field

Let us consider a charged particle with rest mass m_q and charge q_e following a trajectory $\boldsymbol{r}'(t')$ with velocity $\boldsymbol{\beta}(t')c$, where c is the speed of light, $t' \geq 0$ is the time variable

[1]The term *magnetobremsstrahlung* was being used in the mid fifties and sixties mainly by Vitaly Lazarevich Ginzburg (see Ginzburg, Getmantsev, & Fradkin 1954; Ginzburg & Syrovatskii 1965). However, at those times the term *synchrotron radiation* was widely spread in the scientific community so the standardization of *magnetobremsstrahlung* as the kind of radiation produced by charged particles in a magnetic field could not happen. Besides, at the same time Burbidge (1959) suggested that *synchrotron radiation* should be avoided, suggesting instead the term *acceleration radiation* to describe cosmic radio emission.

measured in the comoving fluid frame[2], in a uniform magnetic field $\boldsymbol{B}' = B'\hat{\boldsymbol{z}}$, where $B' \equiv ||\boldsymbol{B}'||$ is the magnitude of the magnetic field and $\hat{\boldsymbol{z}}$ the unit vector in the z direction. As long as the particle does not move parallel to the magnetic field (i.e., $\boldsymbol{\beta} \nparallel \boldsymbol{B}'$), it will experience a force due to the magnetic field. Such force is known as *Lorentz Force*. The equations which describe its trajectory are (Jackson 1999; Rybicki & Lightman 1979; Longair 2011):

$$\frac{\mathrm{d}(\gamma\boldsymbol{\beta})}{\mathrm{d}t'} = \frac{q_e}{m_q c}\left(\boldsymbol{\beta} \wedge \boldsymbol{B}'\right), \tag{2.1}$$

$$\frac{\mathrm{d}E'}{\mathrm{d}t'} = 0, \tag{2.2}$$

where

$$\gamma = \frac{1}{\sqrt{1-\beta^2}}, \tag{2.3}$$

is the Lorentz factor and $\beta \equiv ||\boldsymbol{\beta}||$. Since the particle possesses no potential energy the total energy E' is purely kinetic. From Eq. (2.2) we can infer that the speed of the particle is constant since the total energy is constant, and so is the Lorentz factor. With this in mind, Eq. (2.1) can be rewritten as follows:

$$\frac{\mathrm{d}(\gamma\boldsymbol{\beta})}{\mathrm{d}t'} = \boldsymbol{\beta} \wedge \boldsymbol{\omega}_{\mathrm{B}}, \tag{2.4}$$

where

$$\boldsymbol{\omega}_{\mathrm{B}} = \frac{q_e \boldsymbol{B}'}{\gamma m_q c} = \frac{\boldsymbol{\omega}_{\mathrm{g}}}{\gamma} \tag{2.5}$$

whose magnitude $\omega_{\mathrm{B}} \equiv ||\boldsymbol{\omega}_{\mathrm{B}}||$ is the gyration angular frequency, or *angular gyrofrequency*, and $\omega_{\mathrm{g}} \equiv ||\boldsymbol{\omega}_{\mathrm{g}}||$ is called the *cyclotron angular frequency*. Let us choose as initial conditions

$$\boldsymbol{r}'(0) = \begin{pmatrix} r'_0 \\ 0 \\ 0 \end{pmatrix}, \qquad \boldsymbol{\beta}(0) = \beta \begin{pmatrix} \sin(\alpha')\cos(\phi'_\alpha) \\ \sin(\alpha')\sin(\phi'_\alpha) \\ \cos(\alpha') \end{pmatrix}, \tag{2.6}$$

where $\beta \equiv ||\boldsymbol{\beta}||$, ϕ'_α is the azimuth angle of the velocity (*phase angle*) and α' the polar angle. Since in our coordinate system the magnetic field is aligned with z-axis, the

[2]The motion of charged particles may be worked out in vacuum, but since we aim to apply the equations here derived to distributions of charged particles immersed in a fluid, we refer the equations of motion to the fluid comoving frame.

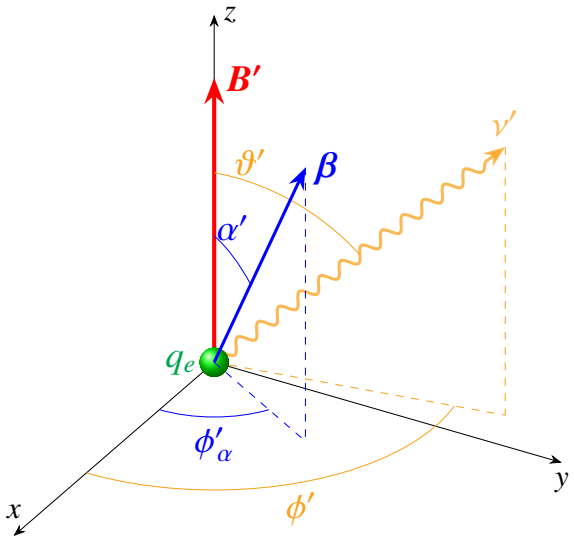

Figure 2.1: *Emission and pitch angles. In the present figure we depict the polar and azimuthal components of the pitch and emission angles by shifting the velocity and Poynting vectors to the magnetic field origin or coordinates.*

polar angle is in fact the angle formed between the magnetic field and the velocity vector (*pitch angle*, see Figure 2.1). We know that in a regular circular motion the phase angle is related to the time variable as $\phi'_\alpha(t') = \omega_B t'$. Taking this into account and with the initial conditions (2.6), the solution of (2.4) is:

$$\boldsymbol{r}'(t') = \boldsymbol{r}'(0) + \begin{pmatrix} r_g \sin(\omega_B t') \\ r_g \cos(\omega_B t') \\ \beta c t' \cos(\alpha') \end{pmatrix}, \qquad \boldsymbol{\beta}(t') = \frac{1}{c}\begin{pmatrix} r_g \omega_B \cos(\omega_B t') \\ -r_g \omega_B \sin(\omega_B t') \\ \beta c \cos(\alpha') \end{pmatrix} \tag{2.7}$$

which describes a helix with *gyration radius* (see Figure 2.2):

$$r_g = \frac{\gamma m_q c^2 \beta \sin(\alpha')}{q_e B'} = \frac{c\beta \sin(\alpha')}{\omega_B}. \tag{2.8}$$

The quantity r_g is also known as the *Larmor radius*. For the case of an electron and of a proton

$$r_g\Big|_{m_q=m_e} \approx 1.704 \times 10^5 \left(\frac{\gamma}{100}\right)\left(\frac{1\,\mathrm{G}}{B'}\right)\mathrm{cm}, \tag{2.9a}$$

$$r_g\Big|_{m_q=m_p} \approx 3.13 \times 10^8 \left(\frac{\gamma}{100}\right)\left(\frac{1\,\mathrm{G}}{B'}\right)\mathrm{cm}, \tag{2.9b}$$

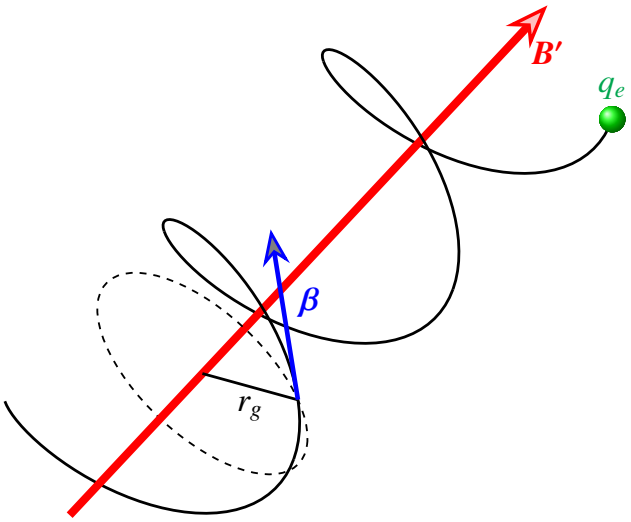

Figure 2.2: *Trajectory of a charged particle in a uniform magnetic field.*

2.2.2 Power spectrum by a point charge in a uniform magnetic field

Accelerated charged particles emit electromagnetic waves. The process of radiation studied in the present thesis is known as *cyclotron* if $\gamma \sim 1$ and *synchrotron* if $\gamma \gg 1$. As mentioned before, the generic name for the radiation from a particle with an arbitrary value of γ is MBS (Ginzburg et al. 1954; Ginzburg & Syrovatskii 1965). In order to know the energy radiated by a particle under the influence of a magnetic field it is necessary to know the electromagnetic fields beforehand.

From classical electromagnetic theory, the values of the fields due to the acceleration of a point charge at any point in space and at any moment in time can be derived from the *Lienard-Wierchert potentials* (see Jackson 1999, §14.1), which are the electromagnetic potentials evaluated at the retarded time. Without lose of generality, let us now chose our coordinate system oriented such that we can define

$$\boldsymbol{\varrho} := \boldsymbol{x'} - \boldsymbol{r'} = \|\boldsymbol{x'} - \boldsymbol{r'}\|(\sin(\vartheta'), 0, \cos(\vartheta'))^T, \tag{2.10}$$

$$\boldsymbol{\varrho}^* := \hat{\boldsymbol{\varrho}} - \boldsymbol{\beta}, \tag{2.11}$$

where $\boldsymbol{x'}$ is a point in space and ϑ' denotes the angle between the emitted radiation and the magnetic field (see Figure 2.1), so that $\varrho \equiv \|\boldsymbol{\varrho}\|, \hat{\boldsymbol{\varrho}} \equiv \boldsymbol{\varrho}/\varrho, \varrho^* \equiv \|\boldsymbol{\varrho}^*\|$ and $\hat{\boldsymbol{\varrho}}^* \equiv \boldsymbol{\varrho}^*/\varrho^*$. The electric and magnetic fields due to a moving charge derived from

the Lienard-Wierchert potentials then read (Jackson 1999):

$$\boldsymbol{E}'(\boldsymbol{x}', t') = q_e \left[\frac{\boldsymbol{\varrho}^*}{\gamma^2 (1 - \hat{\boldsymbol{\varrho}} \cdot \boldsymbol{\beta})^3 \varrho^2} + \frac{\hat{\boldsymbol{\varrho}} \wedge \left(\boldsymbol{\varrho}^* \wedge \dot{\boldsymbol{\beta}} \right)}{c\,(1 - \hat{\boldsymbol{\varrho}} \cdot \boldsymbol{\beta})^3 \varrho} \right]_{t' = \tilde{t}}, \tag{2.12}$$

$$\boldsymbol{B}'(\boldsymbol{x}', t') = \hat{\boldsymbol{\varrho}} \wedge \boldsymbol{E}(\boldsymbol{x}', t')\big|_{t' = \tilde{t}}. \tag{2.13}$$

where $\boldsymbol{E}'$ is the electric field and $\tilde{t} \equiv t' - \varrho(\tilde{t})/c$ is the retarded time. The first term in Eq. (2.12) is known as the *velocity field* and it decays as ϱ^{-2}, whereas the *acceleration field* (the second term), decays as ϱ^{-1}. The acceleration field of both the electric and magnetic fields are transversal to $\hat{\boldsymbol{\varrho}}$. These constitute the *radiation field*. One can obtain the radiated power spectrum per steradian, $\eta_{\omega'}$ (in units of erg s^{-1} Hz^{-1} sr^{-1}), by performing the Fourier transform of the radiation field (see Jackson 1999, §14.5):

$$\eta_{\omega'} = \frac{q_e^2 \omega'^2}{4\pi^2 c} \left\| \int_{-\infty}^{\infty} \mathrm{d}\tilde{t}\, \hat{\boldsymbol{\varrho}} \wedge (\hat{\boldsymbol{\varrho}} \wedge \boldsymbol{\beta}) \exp\left\{ i\omega' \left(\tilde{t} - \frac{\hat{\boldsymbol{\varrho}} \cdot \boldsymbol{r}}{c} \right) \right\} \right\|^2. \tag{2.14}$$

Substituting (2.7) in (2.14) we get (see Melrose & McPhedran 1991; Oster 1961, for the detailed derivation):

$$\eta_{\nu'}(\gamma, \mu', \mu'_\alpha) = \frac{2\pi q_e^2 \nu'^2}{c} \sum_{m=1}^{\infty} \left[\frac{(\mu' - \beta\mu'_\alpha)^2}{1 - \mu'^2} J_m^2(z) + \beta^2 \left(1 - \mu_\alpha'^2\right) \left(\frac{\mathrm{d}J_m(z)}{\mathrm{d}z} \right)^2 \right] \delta(y_m), \tag{2.15}$$

where $\mu' := \cos(\vartheta')$ and $\mu'_\alpha := \cos(\alpha')$ (see Figure 2.1) and we have used the fact that $\omega' = 2\pi\nu'$. In the above equation m annotates the number of the contributing harmonic,

$$y_m \equiv \frac{m\nu_\mathrm{g}}{\gamma} - \nu'(1 - \beta\mu'_\alpha\mu'), \tag{2.16}$$

$$z \equiv \frac{\nu'\gamma\beta \sqrt{1 - \mu'^2}\, \sqrt{1 - \mu_\alpha'^2}}{\nu_\mathrm{g}}, \tag{2.17}$$

$J_m(x)$ is a Bessel function of order m and $\delta(x)$ the Dirac δ-function. Hereafter we will be using the quantity ν_g as well as ν_B (defined below), which correspond to the *cyclotron frequency* and *gyrofrequency*. From Eq. (2.5) we get

$$\nu_\mathrm{B} = \frac{\omega_\mathrm{B}}{2\pi} = \frac{q_e B'}{2\pi\gamma m_q c}, \tag{2.18}$$

$$\nu_\mathrm{g} = \frac{\omega_\mathrm{g}}{2\pi} = \frac{q_e B'}{2\pi m_q c}. \tag{2.19}$$

Using Eqs. (2.18) and (2.19) for the case of an electron; i.e., $q_e = e$, the charge of the electron, and $m_q = m_\mathrm{e}$, the mass of the electron,

$$\nu_\mathrm{g} \approx 2.799 \left(\frac{B'}{1\,\mathrm{G}}\right) \mathrm{MHz}, \tag{2.20a}$$

$$\nu_\mathrm{B} \approx 2.799 \times 10^4 \left(\frac{100}{\gamma}\right)\left(\frac{B}{1\,\mathrm{G}}\right) \mathrm{Hz}, \tag{2.20b}$$

2.2.2.1 The resonance condition

The *resonance condition* (also known as the *Doppler condition*, e.g. Melrose & McPhedran 1991; Oster 1961) arises when the argument y_m of the δ-function is zero; i.e.,

$$\frac{m\nu_\mathrm{g}}{\gamma} - \nu'(1 - \beta\mu'_\alpha\mu') = 0. \tag{2.21}$$

Whenever this conditions is fulfilled, the contribution to the emitted power is non-zero for this harmonic. For slow electrons ($\gamma \sim 1$), first harmonics (small values of m) will dominate appearing as emission lines, while for ultrarelativistic ones ($\gamma \gg 1$) the peak of the power radiated shifts to larger values and the spectrum turns into a continuum (see Figure 3.11).

2.2.2.2 The radiated power

The final step to obtain the power spectrum (erg s^{-1} Hz^{-1}) of a single particle is integrating Eq. (2.15) over emission angles, i.e., computing the integral:

$$P'_{\nu'}(\gamma, \alpha') = \int_0^\pi \int_0^{2\pi} \mathrm{d}\phi'\, \mathrm{d}\vartheta'\, \eta_{\nu'}(\gamma, \vartheta', \alpha'), \tag{2.22}$$

For the purposes of the present work, we do not perform this integral here, but defer that to the following sections, since its value critically depends on the approximations used.

2.2.3 Cyclotron power

The electromagnetic waves from nonrelativistic particles gyrating in a magnetic field are known as *cyclotron radiation*. In the limit where the particle moves with small β, and $m\beta \ll 1$, the first few harmonics in (2.15) are dominating the emission. The Bessel functions can be reduced to simpler expressions and the integrals in Eq. (2.22)

can be performed, arriving to the expression for the power radiated, which is given by (Bekefi 1966; Schwinger 1949; Hirshfield et al. 1961)

$$P'_m(\beta) = \frac{q_e^2 \nu_g^2}{2\pi^2 c} \frac{(m+1)m^{2m+1}}{(2m+1)!} \beta^{2m}. \tag{2.23}$$

In Figure 2.3 we plot the above expression for an electron with $\beta = 0.2$ and 0.1 (cf. Figure 1a of Mahadevan et al. 1996). The m-th harmonic of the power radiated is normalized to the total power P'_T, defined as the sum over all the harmonics[3]. We note that for both cases the first harmonic is $\sim 10^2$ larger than the second harmonic. The slower the particle the smaller is the relative contribution by the subsequent harmonics.

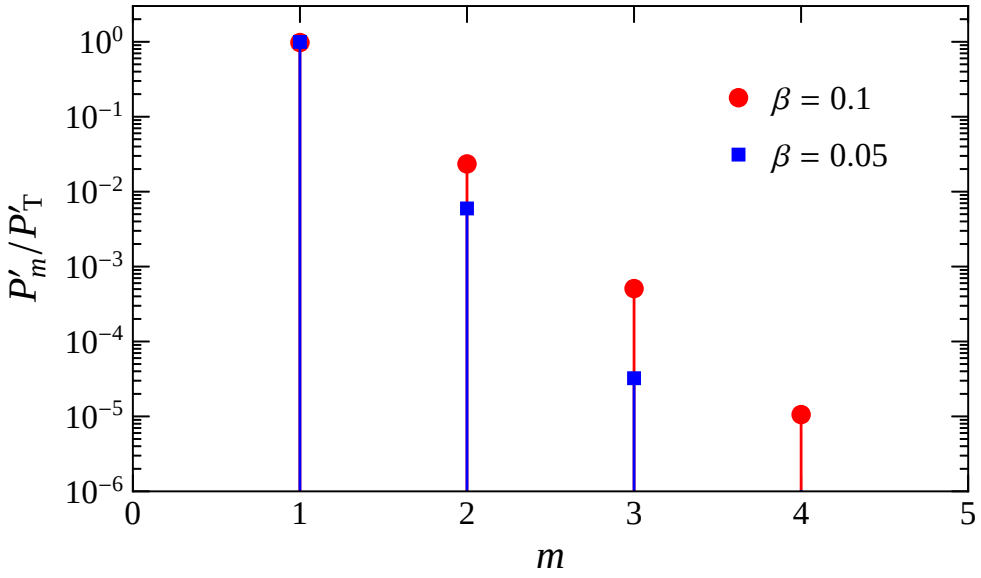

Figure 2.3: *Power radiated in the cyclotron regime. The blue and red lines represent the radiated power normalized to the total emitted power in all the harmonics, P'_T, for an electron with $\beta = 0.1$ and 0.2, respectively.*

2.2.4 Synchrotron power

When an extremely relativistic particle spirals around a magnetic field, it emits electromagnetic waves known as *synchrotron radiation*. This kind of radiation was first

[3]For simplicity and without loss of accuracy in the results, the total power radiated was calculated as $P'_T = \sum_{m=1}^{10} P'_m$, i.e., limiting the infinite sum to the first 11 terms.

reported to have been observed in the laboratory by Elder, Gurewitsch, Langmuir, & Pollock (1947) in a 70 MeV synchrotron at the General Electric Research Laboratory. Ever since, this radiation mechanism has been studied thoroughly both theoretical and experimentally.

The total unpolarized power per unit frequency of the synchrotron radiation is given by (Schwinger 1949; Pacholczyk 1970; Ginzburg & Syrovatskii 1965; Blumenthal & Gould 1970; Rybicki & Lightman 1979)

$$P'_{\nu'}(\alpha', \gamma) = \frac{\sqrt{3} q_e^3 B' \sin\alpha'}{m_q c^2} F\left(\frac{\nu'}{\bar{\nu}_c}\right) \tag{2.24}$$

where

$$\bar{\nu}_c := \frac{3}{2}\gamma^3 \nu_B \sin\alpha' = \frac{3}{2}\gamma^2 \nu_g \sin\alpha' \tag{2.25}$$

is the *critical frequency* of a charged particle with certain pitch angle α' and

$$F(\bar{X}_c) = \bar{X}_c \int_{\bar{X}_c}^{\infty} \mathrm{d}x\, K_{\frac{5}{3}}(x) \approx \begin{cases} \dfrac{4\pi}{\sqrt{3}\Gamma\left(\frac{1}{3}\right)}\left(\dfrac{\bar{X}_c}{2}\right)^{\frac{1}{3}}, & \bar{X}_c \ll 1 \\ \left(\dfrac{\pi \bar{X}_c}{2}\right)^{\frac{1}{2}} \exp\left\{-\bar{X}_c\right\}, & \bar{X}_c \gg 1 \end{cases} . \tag{2.26}$$

where $K_n(x)$ is a modified Bessel function of second kind (Abramowitz & Stegun 1972, §9.6) and $\bar{X}_c \equiv \nu'/\bar{\nu}_c$. The last part of the equation gives the asymptotic expressions for small and large $\bar{X}_c$ (Rybicki & Lightman 1979; Dermer & Menon 2009). The shape of function F is shown in Figure 2.4, as well as its asymptotic approximations. We can gauge that the maximum emission occurs at $\nu_{\mathrm{syn}}^{\mathrm{max}} \sim 0.29\bar{\nu}_c$ (red vertical line in Figure 2.4).

In a randomly oriented magnetic field on small scales compared to the size of the system but large compared to the Larmor radii of the gyrating particles Eq. (2.24) can still be applied. The average over pitch angles in this scenario can be performed resulting in the following expression for the emitted power per unit frequency:

$$P'_{\nu'}(\gamma) = \frac{\sqrt{3} q_e^3 B'}{m_q c^2} \int_{-1}^{1} \mathrm{d}\mu'_\alpha P'_{\nu'}(\alpha', \gamma) = \frac{\sqrt{3} q_e^3 B'}{m_q c^2} CS(X_c). \tag{2.27}$$

Note that in the previous expression the variable

$$X_c \equiv \bar{X}_c \sin\alpha' = \frac{2\nu'}{3\gamma^3 \nu_B}, \tag{2.28}$$

has been introduced to account for the average over pitch angles. We also note that $X_c \equiv \nu'/\nu_c$, where

$$\nu_c := \frac{3}{2}\gamma^3 \nu_B = \frac{3}{2}\gamma^2 \nu_g \tag{2.29}$$

is the synchrotron *critical frequency*. For the case of an electron

$$\nu_c \approx 41.989 \left(\frac{\gamma}{100}\right)^2 \left(\frac{B'}{1\,\mathrm{G}}\right) \mathrm{GHz}. \tag{2.30}$$

The exact analytical expression of $CS(X_c)$ was derived by Crusius & Schlickeiser (1986, hereafter CS86), which reads:

$$\begin{aligned} CS(X_c) =& \frac{\pi}{2} X_c \left(W_{0,\frac{4}{3}}(X_c) W_{0,\frac{1}{3}}(X_c) - W_{\frac{1}{2},\frac{5}{6}}(X_c) W_{-\frac{1}{2},\frac{5}{6}}(X_c) \right) \\ \approx& \begin{cases} 1.80842 X_c^{\frac{1}{3}}, & X_c \ll 1 \\ \dfrac{\pi}{2}\left(1 - \dfrac{11}{18 X_c}\right) \exp\{-X_c\}, & X_c \gg 1 \end{cases} . \end{aligned} \tag{2.31}$$

where $W_{k,m}(X_c)$ are the Whittaker functions (Abramowitz & Stegun 1972, Chapter 13) and the rightmost member contains the asymptotic expansions for high and low values of X_c. This means that the synchrotron radiation peak frequency, $\nu_{\mathrm{syn}}^{\mathrm{max}}$ will be in radio at the extremely high frequency band (EHF) for an ultrarelativistic electron radiating in a magnetic field with strength of $B' = 1\,\mathrm{G}$. In contrast to the cyclotron regime where $\gamma \sim 1$ and for $B' = 1\,\mathrm{G}$, $\nu_c \approx 4.2\,\mathrm{MHz} \sim \nu_g$.

In Figure 2.4 we depict the function $CS(X_c)$ and its asymptotic approximations for $X_c \ll 1$ and $X_c \gg 1$ in dashed and dotted lines, respectively.

2.2.5 Transrelativistic MBS (cyclo-synchrotron) power

As we have seen before, the power radiated from slow and ultra-fast charges can be well approximated. However, the intermediate regime has been a challenge. Petrosian (1981) found an analytic expression for mildly relativistic moving charges. More specifically, an approximation was found, but only valid for $\gamma^2 \ll \nu'/\nu_g$. According to Eq. (8) of Petrosian (1981), the power radiated by a single electron particle, for the specific case of slowly varying pitch angle, reads:

$$P_{\nu'}^{\mathrm{P81}}(\vartheta', \gamma) = \frac{e^2 \nu_g}{c} \left(\frac{\pi \nu'}{\nu_g}\right)^{1/2} \gamma^{-1} \left[\left(1 + \frac{2\cot^2(\vartheta')}{\gamma^2}\right) \left(1 - \beta^2 \cos^2(\vartheta')\right)^{1/4} \right] \mathcal{Z}_{\mathrm{max}}^{2m} \tag{2.32}$$

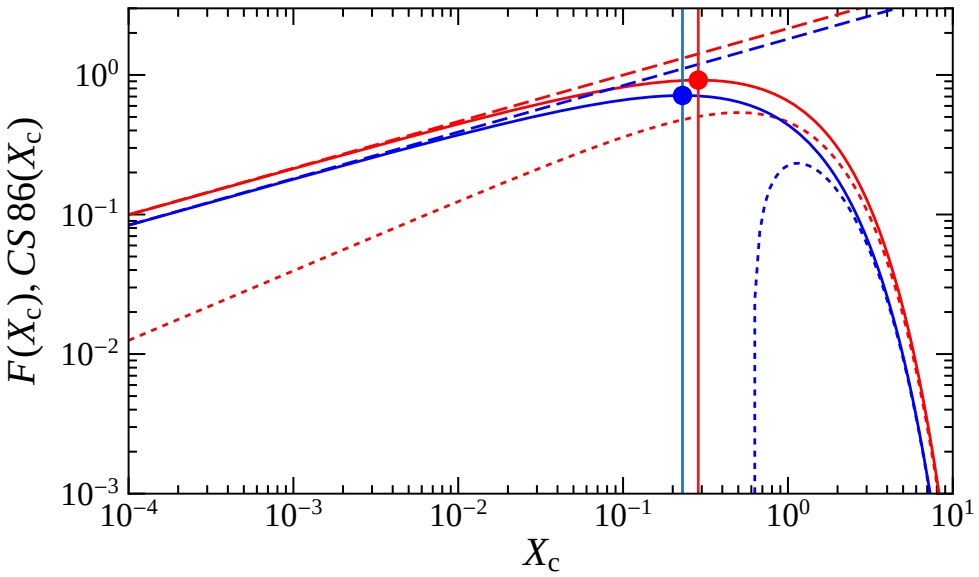

Figure 2.4: *Functions $F(x)$ and $CS(x)$ of the synchrotron radiation in red and blue, respectively, given by* (2.26) *and* (2.31) *as a function of X_c (Eq.* (2.28)*). In dashed lines we show the asymptotic approximations for $X_c \ll 1$ while the dotted lines display the approximations for $X_c \gg 1$. The circles and vertical lines shows the position of the maximum value of each function.*

where,

$$\mathcal{Z}_{\max} = \frac{\tau_p \exp\left[\left(1+\tau_p^2\right)^{-1/2}\right]}{1+\left(1+\tau_p^2\right)^{1/2}}, \quad m = \frac{\nu'}{\gamma\nu_b}\left(1+\tau_p^2\right), \quad \tau_p \equiv \beta\gamma\sin(\vartheta'). \tag{2.33}$$

On the left panel of Figure 2.5 we have plotted Eq. (2.32) for charged particles with Lorentz factors $\gamma = 1.05$, 1.25, 1.5 and 2.0 in black, red, blue and green lines, respectively. The integral over emission angles of (2.32) was calculated by Ghisellini et al. (1988), and reads:

$$P'^{\mathrm{GGS88}}_{\nu'}(\gamma) = \frac{\pi^2 e^2 \nu_g}{3c}\left[1+2\left(\gamma^2-1\right)\left\{1+\gamma\log\left(\frac{\gamma-1}{(\gamma^2-1)^{-1/2}}\right)\right\}\right]^{-1/2} \times \exp\left\{\frac{2\nu'}{\nu_g}\left[1+\gamma\log\left(\frac{\gamma-1}{(\gamma^2-1)^{-1/2}}\right)\right]\right\} \tag{2.34}$$

On the right panel of Figure 2.5 we have plotted Eq. (2.34) for charged particles with Lorentz factors $\gamma = 1.05$, 1.25, 1.5 and 2.0 in black, red, blue and green lines, respectively.

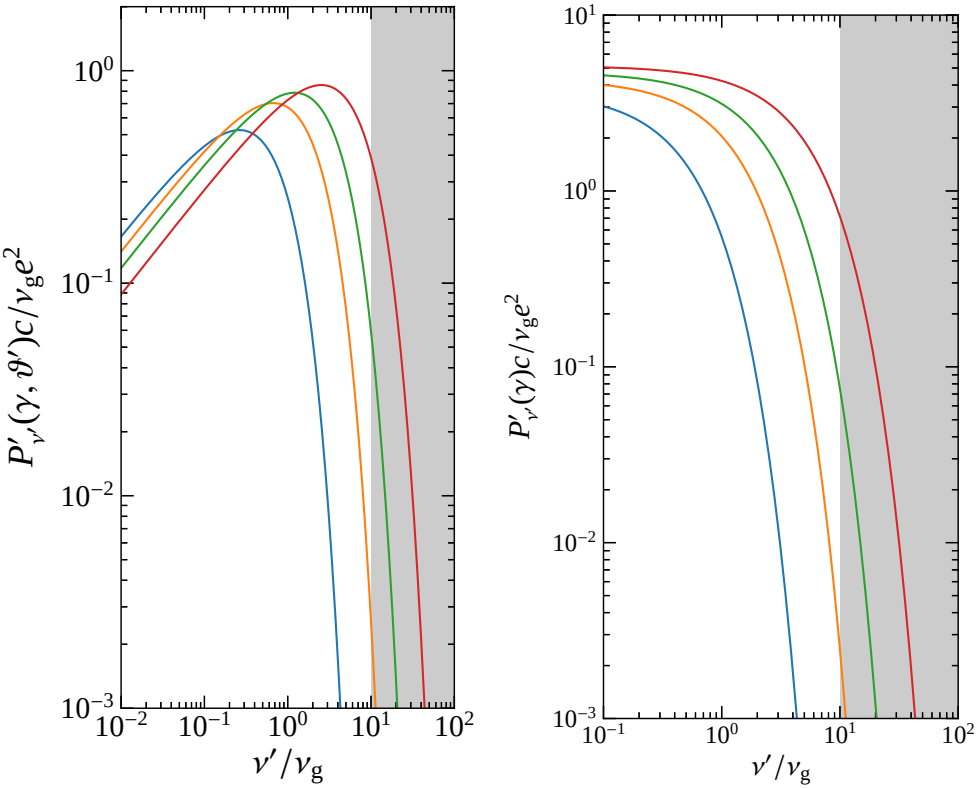

Figure 2.5: *Transrelativistic approximations of MBS power radiated. On the left panel we show the approximation by Petrosian (1981, eq. (8)); Eq.* (2.32) *for* $\vartheta' = \pi/2$. *On the right panel we show the approximation by Ghisellini et al. (1988, eq. (8)); Eq.* (2.34). *The Lorentz factor of the charged particles described here are* $\gamma = 1.05$, 1.25, 1.5 *and* 2.0 *in blue, orange, green and red lines, respectively. The gray region covers the range of frequencies for which the approximation is mostly valid; i.e.,* $\gamma^2 \ll \nu'/\nu_g$.

2.2.6 Emissivity from a distribution of charged particles

In this section we will describe the emissivity due to a distribution of charged particles in a uniform magnetic field using the results obtained in the previous section. Let us consider a distribution of particles immersed in a uniform magnetic field, as

described above. In this scenario each particle will move with its own pitch-angle. The general formulas for the MBS emissivity will be described here.

2.2.6.1 The emission coefficient

The emission coefficient is defined as the energy emitted per unit time, per unit volume, per unit solid angle and per frequency (see Rybicki & Lightman 1979, Chapter 1),

$$j'_{\nu'} = \frac{\mathrm{d}^4 E'}{\mathrm{d}t' \mathrm{d}V' \mathrm{d}\Omega \mathrm{d}\nu'}, \tag{2.35}$$

where $j'_{\nu'}$ has units of erg s^{-1} cm^{-3} Hz^{-1} sr^{-1}. Assuming that our system of particles emits isotropically, the emission coefficient takes the form (Rybicki & Lightman 1979)

$$j'_{\nu'} = \frac{1}{(4\pi)^2} \int_1^\infty \mathrm{d}\gamma \, n(\gamma) P'_{\nu'}(\gamma) \tag{2.36}$$

where $n(\gamma)$ is the particle density at a certain Lorentz factor γ (in units of cm^{-3})

$$P'_{\nu'}(\gamma) = \int_0^{2\pi} \int_{-1}^1 \mathrm{d}\phi'_\alpha \mathrm{d}\mu'_\alpha \int_0^{2\pi} \int_{-1}^1 \mathrm{d}\phi' \mathrm{d}\mu' \, \eta_{\nu'}(\gamma, \vartheta', \alpha'). \tag{2.37}$$

The extra $1/4\pi$ factor in front of the integral in (2.36) comes from the angular normalization of the isotropic particle distribution function. Let us assume that we have a uniform magnetic field $\boldsymbol{B'} = B'\hat{\boldsymbol{z}}$ (as at the beginning of this chapter) and that the distribution of charged particles $n(\gamma)$ is immersed in it. Each charge will spiral following a trajectory described by Eq. (2.7).

Since $\eta_{\nu'}(\gamma, \vartheta', \alpha')$ is independent of ϕ'_α and ϕ', the corresponding integrals over these variables are straightforward. The final expression for $P'_{\nu'}(\gamma)$ is then,

$$P'_{\nu'}(\gamma) = (4\pi)^2 \frac{2\pi q_e^2 \nu'^2}{c} \int_{-1}^1 \int_{-1}^1 \mathrm{d}\mu'_\alpha \mathrm{d}\mu' \, \eta_{\nu'}(\gamma, \mu', \mu'_\alpha). \tag{2.38}$$

Inserting the last result into Eq. (2.36) we get

$$j'_{\nu'} = \frac{2\pi q_e^2 \nu'^2}{c} \int_1^\infty \int_{-1}^1 \int_{-1}^1 \mathrm{d}\gamma \mathrm{d}\mu'_\alpha \mathrm{d}\mu' \, n(\gamma) \eta_{\nu'}(\gamma, \mu', \mu'_\alpha). \tag{2.39}$$

This equation will be implemented numerically in Chapter 3.

2.3 Internal shock dynamics, particles acceleration and how an external observer sees it

As it was mentioned in §1.3, in the IS model it is supposed that there is an intermittency in the material ejection process by a central engine of the AGN. This intermittency means that the engine may launch shells of plasma with varying properties into the outflow. The faster shells can catch up with slower shells in front, causing shell collisions and the formation of shocks in the outflow. Acceleration of particles takes place in the shocked region, and the emission from these particles produces the observed broadband spectrum. In this section we will describe the dynamics of these shocks and the main radiation processes involved. In addition, the analysis here described will be focused on the leptonic model (see §1.2.1), i.e. it is assumed that the population of particles responsible for the observed radiation is composed by leptons, more specifically electrons.

2.3.1 Shock dynamics

Since the jet is highly collimated we assume that the geometry of the emission region to be cylindrical (e.g. Böttcher & Dermer 2010; Joshi & Böttcher 2011; Mimica & Aloy 2012, see Figure 1.8). Assuming that the shock accelerated particles dissipate most of their internal energy through radiation, we can neglect any adiabatic losses (Dermer & Menon 2009, § 11.1). This means that the system will suffer neither lateral nor longitudinal expansion. Indeed, numerical simulations have shown that during the time that the shocks propagate through the shells, the jet suffers negligible sideways expansion (Mimica et al. 2004; Mimica 2004).

2.3.1.1 Riemann solver

With the above considerations we approximate the shells as two cylinders of cold plasma[4], which at the moment of contact, both have a width Δr and cross-sectional radius R, measured in the AGN reference frame (see Figure 1.8). The total jet lumi-

[4] A plasma is said to be cold when its thermal energy is negligible compared to the bulk kinetic (or the sum of the magnetic and kinetic) energy. We assume that by the time they start colliding the shells have stopped accelerating and have converted most of their thermal energy into kinetic.

nosity (power) of the jet is defined as (see Mimica & Aloy 2010, 2012):

$$\mathcal{L} := \pi R^2 \rho c^3 \beta_{\rm l} \Gamma \left[\Gamma(1 + \epsilon + \chi + \sigma) - 1\right]. \tag{2.40}$$

The number of electrons in each (unshocked) shell can be computed using the following expression (see Eq. (3) of MA12):

$$n = \frac{\mathcal{L}}{\pi R^2 m_{\rm p} c^3 \beta_{\rm l} \Gamma \left[\Gamma(1 + \epsilon + \chi + \sigma) - 1\right]}, \tag{2.41}$$

where $m_{\rm p}$ is the proton mass, $\beta_{\rm l}$ the bulk speed the shell in units of c, $\Gamma = (1 - \beta_{\rm l}^2)^{-1/2}$ the bulk Lorentz factor of the shell, ϵ is the specific internal energy, $\chi := P/\rho c^2 \ll 1$ is the ratio between the thermal pressure P and the rest-mass energy density, with ρ as the fluid rest-mass density, and σ the jet magnetization (Eq. (2.44) below).

With this configuration and, once the number density, the thermal pressure, the magnetization, and the Lorentz factor of the faster and of the slower shell have been determined, the collision of magnetized shells can be simplified to a one-dimensional Riemann problem[5]. Hence, we can make use the exact Riemann solver of Romero et al. (2005) to compute the evolution of the shell collision. In particular, we compute the properties of the shocked shell fluid (shock velocity, compression factor, magnetic field) which we then use to obtain the synthetic radiative outcome.

The innermost shell: is the faster shell ejected at a later time. In the Riemann problem this shell corresponds to the left state.

The outermost shell: is the slower shell, ejected at an earlier time. In the Riemann problem this shell is the right state.

The equation of state (EoS) employed for the Riemann problem was the TM EoS (de Berredo-Peixoto et al. 2005; Mignone et al. 2005), which is an approximation to the relativistic ideal gas EoS, more commonly known as the Synge EoS, and reads:

$$\epsilon = \frac{3}{2}\chi + \left[\frac{9}{4}\chi^2 + 1\right]^{1/2} - 1 \tag{2.42}$$

[5] A Riemann problem is an initial value problem consisting of two uniform states located to the left and to the right of a "virtual" membrane. After the membrane is released, the breakup of the initial discontinuity displays a self-similar evolution in many hyperbolic systems of conservation laws as, e.g., the one formed by the relativistic MHD governing equations.

By means of numerical relativistic magnetohydrodynamics (RMHD) parametric study based on the Riemann problem described above, Mimica & Aloy (2010) obtained the region in the σ_R-σ_L plane where either two shocks form as a result of the collision (the forward shock (FS) and the reverse shock (RS) shocks), or a shock and a rarefaction form, or two rarefactions (a forward and a reverse rarefaction) are generated. In the present thesis we will not consider those cases where rarefactions appear. Rather, we will focus on the shell magnetizations for which both shocks exists.

2.3.1.2 Magnetization

Theoretical models propose that poloidal fields (i.e., parallel to the shell propagation direction) decay with distance to the AGN central engine faster than that of toroidal fields (perpendicular to the shell propagation direction, see e.g. Blandford & Rees 1974). At parsec scales the poloidal magnetic field will be negligible (e.g. Komissarov 2012). Accordingly, the large-scale magnetic field $B'_{\rm mac}$ is assumed to be perpendicular to the direction of propagation of the shells.

With this magnetic field setup, in a one-dimensional Riemann problem in RMHD the quantity

$$\mathcal{B} := \frac{B'}{\rho} \tag{2.43}$$

is constant across shocks and rarefactions (but jumps accross the CD, see Romero et al. 2005), where B' and ρ are the comoving magnetic field and the fluid density, respectively. The magnetization is defined as

$$\sigma := \frac{B'^2}{4\pi\rho c^2} = \frac{\mathcal{B}^2\rho}{4\pi c^2} \,. \tag{2.44}$$

Unless said otherwise, hereafter we will denote with subscript i the quantities in the unshocked regions (downstream); i may be R or L, which correspond to the slower and faster shells, respectively. With subscript S we will denote quantities at a shocked region (upstream); S may refer to either the FS or the RS. For instance, σ_L and Γ_L correspond to the magnetization and bulk Lorentz factor, respectively, of the faster shell while σ_R and Γ_R to the same quantities but of the slower shell. Likewise β_{FS} denotes the speed of the FS and β_{RS} the speed of the RS.

Once the shock starts to move away from the CD, the shocked plasma suffers a compression. The density in the shocked region can be written as

$$\rho_{\rm S} = r_{\rm S}\rho_i \tag{2.45}$$

where $r_{\rm S}$ is the compression factor (see Eq. (2.52)), and ρ_i is the density in the unshocked region. In the unshocked region the magnetization is σ_i and, using the fact that $\mathcal{B}$ is a constant across the shock, we have that in the shocked region:

$$\sigma_{\rm S} = \frac{\mathcal{B}^2\rho_{\rm S}}{4\pi c^2} = \frac{\mathcal{B}^2 r_{\rm S}\rho_i}{4\pi c^2} = r_{\rm S}\sigma_i\,. \tag{2.46}$$

As can be seen from Eq. (2.46), the magnetization increases linearly with the shock compression factor. It follows from Eq. (2.46) that the magnetic field strength in the shocked region is

$$B'_{\rm S,mac} = \sqrt{4\pi c^2\rho_{\rm S} r_{\rm S}\sigma_i}. \tag{2.47}$$

As in MA12 and RMA14, we assume that there exists a stochastic magnetic field, $B'_{\rm S,st}$, which is produced *in situ* due to the collision of the shells. By definition its strength is a fraction $\epsilon_{\rm B}$ of the internal energy density of the shocked shell $u'_{\rm S}$, obtained, in our case, by the exact Riemann solver:

$$B'_{\rm S,st} = \sqrt{8\pi\epsilon_{\rm B}u'_{\rm S}}. \tag{2.48}$$

Using relations (2.47) and (2.48), the total strength of an isotropic and stochastic magnetic field in the shocked region is

$$B'_{\rm S} = \sqrt{B'^2_{\rm S,st} + B'^2_{\rm S,mac}}. \tag{2.49}$$

2.3.1.3 Shocks kinematics

As was mentioned before, the scenario we want to study is that in which both shocks appear (see Mimica & Aloy 2012, for details about the conditions when this happens). Assuming this is the case, from the moment the shells establish contact, three waves appear: the FS, the RS and the CD. The CD moves with the shocked fluid; i.e., its speed is the bulk speed of the shocked plasma, $\beta_{\rm l}$. In the reference frame of the CD, which is the same as the comoving fluid frame (§2.1), the FS moves in the positive direction and the RS in the negative direction (see Figure 2.6). The laboratory frame

velocities of these shocks are $\beta_{\rm FS}c$ and $\beta_{\rm RS}c$, respectively. When refering to only a single shock, we will denote its velocity in the laboratory frame as $\beta_{\rm S}c$. Knowing the velocity of the CD and the unshocked shell velocity in the laboratory frame allows us to compute the velocity of any of the shells in the comoving fluid frame,

$$\beta_i' = \frac{\beta_i - \beta_{\rm l}}{1 - \beta_{\rm l}\beta_i}, \tag{2.50}$$

while the velocity of any of the shocks in the CD frame is

$$\beta_{\rm S}' = \frac{\beta_{\rm S} - \beta_{\rm l}}{1 - \beta_{\rm l}\beta_{\rm S}}. \tag{2.51}$$

As stated in Eq. (2.45), the shocked shell suffers a compression as the shock wave crosses. The compression factor is given by (Mimica & Aloy 2010)

$$r_{\rm S} = \frac{\beta_{\rm l} - \beta_{\rm S}}{\beta_i - \beta_{\rm S}} \tag{2.52}$$

Consequently, the width of the compressed shell in the CD frame is

$$\Delta r_{\rm S}' = \Gamma r_{\rm S} \Delta r_i, \tag{2.53}$$

and the time it takes the shock to cross the shell is (see Figure 2.6)

$$t_{cr,{\rm S}}' := \frac{\Delta r_{\rm S}'}{c|\beta_{\rm S}'|} \tag{2.54}$$

2.3.1.4 Kinematics in the Earth observer frame

Let us consider an Earth observer whose line of sight makes an angle θ with the jet axis (assumed to be along the x axis, see Figure 1.8). In the laboratory frame the shock happens at position x and at a certain time $t = t_{\rm collision}$, whereas in the CD reference frame the collision happens at $x' = 0$ and $t' = 0$ (see Figure 2.6). Assuming that the emitting source is located at a luminosity distance d_L, (at a corresponding redshift z), we define the time at which the observer sees the radiation emitted from x at time t (both measured in the lab frame) as

$$t_{\rm obs} := (1+z)\left(t - \frac{x\mu_{\rm obs}}{c}\right) \tag{2.55}$$

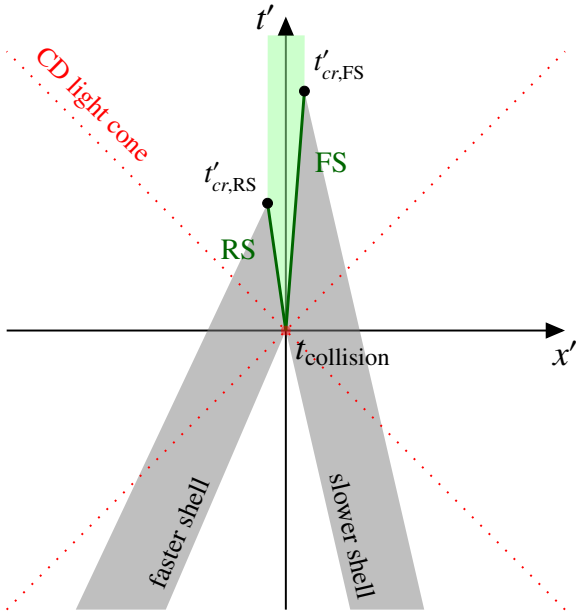

Figure 2.6: *Space-time diagram of the internal shocks model as seen in the CD reference frame (primed coordinates). The red dot corresponds to the time, $t_{collision}$, and place where the shells make contact, which in the primed frame is the origin. The green lines that arise at this point correspond to the FS and RS. The gray regions trace world volumes of the shells. The light green region corresponds to the world volume of the shocked region. The black dots correspond to the moment at which the shocks have crossed the faster shell, in the case of the RS, and the slower shell in the case of the FS. In red dotted lines we depict the light cone of the contact discontinuity.*

where $\mu_{\mathrm{obs}} := \cos\theta$. From relativistic kinematics we know that

$$t = \Gamma\left(t' + \frac{x'\beta_1\mu_{\mathrm{obs}}}{c}\right), \tag{2.56a}$$

$$x = \Gamma\left(x' + \beta_1\mu_{\mathrm{obs}}t'c\right). \tag{2.56b}$$

Substituting (2.56) in (2.55) we get that

$$\frac{t_{\mathrm{obs}}}{1+z} = \Gamma t'(1-\beta_1\mu_{\mathrm{obs}}) + \frac{\Gamma x'}{c}(\beta_1 - \mu_{\mathrm{obs}}), \tag{2.57}$$

which, solving (2.57) for t', leads us to an expression for the time in the CD reference frame, as a function of the observer time t_{obs} and the distance from the CD x':

$$t' = \mathcal{D}\left[\frac{t_{\mathrm{obs}}}{1+z} + \frac{\Gamma x'}{c}(\mu_{\mathrm{obs}} - \beta_1)\right], \tag{2.58}$$

where

$$\mathcal{D} := \frac{1}{\Gamma(1 - \beta_{\rm l}\mu_{\rm obs})} \tag{2.59}$$

is the *Doppler factor*.

Since we are interested in tracking down the evolution of the particles injected behind each shock during the collision it is convenient to introduce the *age* of the particle distribution (in the CD frame). We define it as a time since the shock passes a given point x', i.e. as the difference between the measured time t' and the time at which the shock was at x':

$$t'_{a,\rm S} := t' - \frac{x'}{\beta'_{\rm S} c}. \tag{2.60}$$

Finally, substituting (2.58) and (2.51) into (2.60), the age of particles located at x' that are observed at a time $t_{\rm obs}$ reads (e.g. Böttcher & Dermer 2010; Mimica & Aloy 2012)

$$t'_{a,\rm S} = \mathcal{D}\left[\frac{t_{\rm obs}}{1+z} - \frac{x'}{c}\frac{1 - \beta_{\rm S}\mu_{\rm obs}}{\beta_{\rm S} - \beta_{\rm l}}\right]. \tag{2.61}$$

2.3.2 Particle injection behind shock fronts

Let us assume that the injection of particles occurs during a period $\Delta t'_{\rm acc}$ and a region $\pi R^2 \Delta r'_{\rm acc}$ downstream the shock (e.g., Böttcher & Dermer 2010). $\Delta t'_{\rm acc}$ and $\Delta r'_{\rm acc}$ are related by (Böttcher & Dermer 2010)

$$\Delta t'_{\rm acc} = \frac{\Delta r'_{\rm acc}}{\beta_{\rm S} c}, \tag{2.62}$$

and $\Delta r'_{\rm acc}$ is parameterized as proportional to the proton Larmor radius (2.9b); i.e.,

$$\Delta r'_{\rm acc} = \Delta_{\rm acc} \frac{\Gamma'_i m_{\rm p} c^2}{e B'_{\rm S}}, \tag{2.63}$$

where Γ'_i is the bulk Lorentz factor of each of the shells measured in the CD frame.

The proportionality constant $\Delta_{\rm acc}$ tells how large is the injection region in terms of the proton Larmor radius (e.g., Böttcher & Dermer 2010). As mentioned before, we are going to take a fraction $\epsilon_{\rm e}$ of the internal energy of the shock as the energy injection rate into the acceleration region, whose size and characteristic time scale are described by the previous two equations, thus:

$$\frac{{\rm d}E'_{\rm inj}}{{\rm d}t'} = \pi R^2 \epsilon_{\rm e} u'_{\rm S} \frac{\Delta r'_{\rm acc}}{\Delta t'_{\rm acc}} \tag{2.64}$$

2.3.2.1 Maximum Lorentz factor of accelerated particles

The cooling time-scale of particles with Lorentz factor γ in the comoving frame is (Bednarz & Ostrowski 1996)

$$T_{\rm cool} = \frac{\gamma}{\dot{\gamma}}. \tag{2.65}$$

The maximum Lorentz factor (injection cut-off) is obtained by balancing the cooling time scale with the acceleration time scale. In the special case of the synchrotron and inverse-Compton cooling we have $\dot{\gamma} \propto \gamma^2$ and (e.g., MA12)

$$\gamma_{\rm max} = \left(\frac{3 m_{\rm e}^2 c^4}{4\pi a_{\rm acc} e^3 B'_{\rm S}} \right)^{1/2} \tag{2.66}$$

Among others, the parameter $a_{\rm acc}$ tells us how many cycles crossing the shock front the electron needs before it reaches the maximum energy.

2.3.3 Nonthermal radiation from the shocked region

After the electrons are accelerated the amplified magnetic fields in the shocked region $B'_{\rm S}$ will cause them to gyrate triggering the MBS process (see §2.2.1). We assume that the emission is isotropic. In the shocked region the MBS photons may interact with the ultrarelativistic electrons in what is known as the SSC scattering, which is an special case of the IC process whose seed photons are emitted by MBS (see §3.1.1). Moreover, the jet is assumed to be immersed in a cold monochromatic photon field with energy density $u_{\rm ext}$ and frequency $\nu_{\rm ext}$ as seen in the AGN frame (see Figure 1.8). Interactions of this photon field with the high energy electrons are also considered to take place via inverse-Compton scattering.

2.3.3.1 Radiative transfer

In order to calculate the energy flux $\nu_{\rm obs} F_{\nu_{\rm obs}}$ in the observer rest frame, first we have to solve the radiative transfer equation in the optically thin regime in the CD rest frame (Rybicki & Lightman 1979)

$$\frac{{\rm d}I'_{\nu'}}{{\rm d}s'} = j'_{\nu'}, \tag{2.67}$$

where $I'_{\nu'}$ is the *specific intensity* of a beam, in units of erg s^{-1} cm^{-2} sr^{-1} Hz^{-1}, which has traveled a distance ds'. The most important radiation processes considered con-

tributing to $I'_{\nu'}$: MBS, SSC and EIC. The MBS emissivity is described in §2.2 and is computed as described in §3.2.5.2.

Following the treatment of Mimica (2004), to compute the IC emissivity we assume that the spectrum of the incoming radiation is a power-law. We assume that both the incoming and the outgoing emission are isotropic in the CD frame. The numerical calculation of SSC and EIC emissivities are described in §3.1.1.

2.3.3.2 Flux detected by a distant observer

Making use of Eqs. (2.58), (2.59) and (2.51), we get that, for each shock, the time since the shock acceleration took place is related to the time of observation and x' by

$$t'_{a,\mathrm{FS}} = \mathcal{D}\left[\frac{t_{\mathrm{obs}}}{1+z} - \frac{x'}{c}\frac{1-\beta_{\mathrm{FS}}\mu_{\mathrm{obs}}}{\beta_{\mathrm{FS}}-\beta_{\mathrm{l}}}\right], \tag{2.68a}$$

$$t'_{a,\mathrm{RS}} = \mathcal{D}\left[\frac{t_{\mathrm{obs}}}{1+z} - \frac{x'}{c}\frac{1-\beta_{\mathrm{RS}}\mu_{\mathrm{obs}}}{\beta_{\mathrm{RS}}-\beta_{\mathrm{l}}}\right]. \tag{2.68b}$$

Noting that Eq. (2.68a) is to be used for $x' \geq 0$, and (2.68b) for $x' < 0$. $t'_{a,\mathrm{S}} \leq 0$ means that the shock has not crossed that position yet and therefore particles have still not been accelerated and, consequently, no contribution to the emission has to be taken into account from there.

The observed luminosiy in the CD reference frame is (e.g. MA12)

$$\nu' L'_{\nu'}(t_{\mathrm{obs}}) = \pi R^2 \int_{x'_{\mathrm{min}}(t_{\mathrm{obs}})}^{x'_{\mathrm{max}}(t_{\mathrm{obs}})} \mathrm{d}x' \nu' j'_{\nu'}\left[t'_{a,\mathrm{S}}(t_{\mathrm{obs}}, x')\right], \tag{2.69}$$

where $j'_{\nu'}$ is the emissivity (2.36). The limits of the integral in Eq. (2.69) depend on two factors. The radiation activity happens since the onset of the shock; i.e., starting at $t'_{a,\mathrm{S}} = 0$, and it lasts until the respective shock meets the edge of the shell. Given that we are assuming that both shocks exist, from (2.68) we get that the limits of the integral (2.69) are

$$x'_{\mathrm{min}}(t_{\mathrm{obs}}) = \max\left(\frac{\Gamma c t_{\mathrm{obs}}(\beta_{\mathrm{RS}}-\beta_{\mathrm{l}})}{(1+z)(1-\beta_{\mathrm{RS}}\mu_{\mathrm{obs}})}, -\Delta r'_{\mathrm{L}}\right), \tag{2.70a}$$

$$x'_{\mathrm{max}}(t_{\mathrm{obs}}) = \min\left(\frac{\Gamma c t_{\mathrm{obs}}(\beta_{\mathrm{FS}}-\beta_{\mathrm{l}})}{(1+z)(1-\beta_{\mathrm{FS}}\mu_{\mathrm{obs}})}, \Delta r'_{\mathrm{R}}\right), \tag{2.70b}$$

where $\Delta r'_{\rm L}$ and $\Delta r'_{\rm R}$ are the widths of the left and of the right shells measured in the CD frame, related to their respective width in the laboratory frame by

$$\Delta r'_i = \Gamma_i \Delta r_i \tag{2.71}$$

Finally, knowing that in the observer rest frame (e.g. Dermer 2004)

$$\nu_{\rm obs} = \frac{\mathcal{D}}{1+z}\nu', \tag{2.72}$$

$$F_{\nu_{\rm obs}} = \frac{1+z}{d_{\rm L}^2}\mathcal{D}^3 L'_{\nu'}, \tag{2.73}$$

we get that the energy flux $\nu_{\rm obs} F_{\nu_{\rm obs}}$ received by the observer is

$$\nu_{\rm obs} F_{\nu_{\rm obs}}(t_{\rm obs}) = \frac{\pi R^2 \mathcal{D}^4}{d_{\rm L}^2} \int_{x'_{\rm min}(t_{\rm obs})}^{x'_{\rm max}(t_{\rm obs})} {\rm d}x' \nu' j'_{\nu'}[t'_a(t_{\rm obs}, x')]. \tag{2.74}$$

2.4 Particle distribution

A population of particles at certain moment t is described by an energy distribution function which depends on the nature of the particles, the interactions among them and the medium in which they are immersed. In this section we will describe the main distribution functions of a plasma (charged particles) and how to deal with their evolution.

2.4.1 Kinds of particles distribution

There are two main kinds of particle velocity distribution functions: thermal and nonthermal. More precisely, if the distribution of velocities is Maxwellian (Maxwell-Boltzmann if the speed of the particles is non-relativistic, or Maxwell-Jüttner (Jüttner 1911) if the particles are relativistic, we are talking about a thermal distribution, otherwise the distribution is nonthermal. In the present thesis the particles of interest are electrons and we will describe the distributions composed mainly of them (although they may be part of a plasma composed of other particles as well). Nevertheless, the formalism here presented can be extended to other kinds of charged particles, e.g. protons or ions.

2.4.1.1 Thermal particles

The most general thermal distribution function, expressing the probability distribution per unit Lorentz factor of relativistic thermal particles is the normalized Maxwell-Jüttner distribution (Chandrasekhar 1939; Jüttner 1911). This distribution is temperature, T, dependent and reads:

$$n_{\rm th}(\gamma) = \frac{\gamma^2\beta}{\Theta K_2(1/\Theta)} \exp\left(-\frac{\gamma}{\Theta}\right). \tag{2.75}$$

where $\Theta := k_{\rm B}T/m_q c^2$ is the dimensionless temperature of the charged particles, $k_{\rm B}$ is the Boltzmann constant and $K_2(x)$ is the modified Bessel function of the second kind. In Figure 2.7 we show the shape of (2.75) for electrons (i.e., $m_q = m_{\rm e}$) with different temperatures.

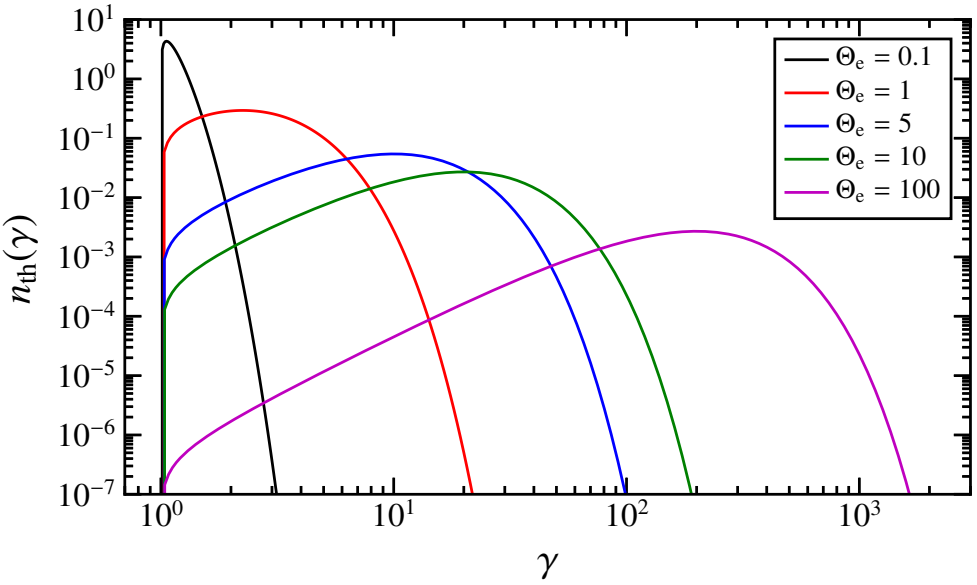

Figure 2.7: *Maxwell-Jüttner distribution function of electrons with different dimensionless temperatures $\Theta_{\rm e}$. In black, red, blue, green and purple we show the distribution function for temperatures $\Theta_{\rm e} = 0.1, 1, 5, 10, 100$, respectively.*

Calculating the first moment of the distribution (2.75) we obtain the average Lorentz factor of the thermal distribution

$$\langle\gamma\rangle = \int_1^\infty {\rm d}\gamma\, \gamma n_{\rm th}(\gamma) = 3\Theta + \frac{K_1(1/\Theta)}{K_2(1/\Theta)}. \tag{2.76}$$

2.4.1.2 Nonthermal particles

As it was mentioned in §1.3.2, the detection of cosmic rays on Earth have shown that the accelerated particles which produce the observed spectra are described by a power-law distribution, rather than a thermal distribution (e.g. Bykov et al. 2012). We define a nonthermal power-law distribution in the following way:

$$n_{\rm nth}(\gamma) = n(\gamma_{\rm min})\left(\frac{\gamma}{\gamma_{\rm min}}\right)^{-q} H\left(\gamma;\gamma_{\rm min},\gamma_{\rm max}\right), \tag{2.77}$$

where $\gamma_{\rm min}$ and $\gamma_{\rm max}$ are the lower and upper cut-offs of the power-law interval, $n(\gamma_{\rm min})$ is the number density at the lower cut-off and q is the power-law index. $H(x;a,b)$ is the interval function defined as:

$$H(x;a,b) := \begin{cases} 1, & a \le x \le b \\ 0, & \text{elsewhere} \end{cases} . \tag{2.78}$$

We note that, while the thermal distribution can be described by only two parameters (T and the normalization constant), one needs four parameters to describe the nonthermal power-law distribution, namely, $\gamma_{\rm min}, \gamma_{\rm max}, n(\gamma_{\rm min})$ and q.

2.4.2 Injection of particles at a shock

It was shown by Bell (1978b) that in the vicinity of (nonrelativistic) shock fronts charged particles are accelerated downstream into a power-law distribution and estimated the rate of particles injected upstream crossing the shock (Bell 1978a). Later, Kirk & Schneider (1987) provided a solution for the case of relativistic shocks, making the first steps towards understanding this kind of shocks. Great advances have been made ever since on the understanding of these waves and the particles acceleration processes that may develop therein (e.g. Begelman & Kirk 1990; Bednarz & Ostrowski 1996, 1998). Nowadays, sophisticated numerical codes have proved useful tools for the understanding of relativistic shocks and particles acceleration (e.g. Achterberg et al. 2001; Sironi et al. 2013).

In the present section we will reproduce the formalism described in MA12 (p. 2637) and RMA17 (pp. 1170–1171) for a power-law and hybrid thermal-nonthermal distributions, respectively, expanding the intermediate steps.

2.4.2.1 Injection of a pure power-law distribution

Most IS models for blazars assume that the radiation is produced by a power-law energy distribution of nonthermal electrons accelerated behind the shock (Spada et al. 2001; Mimica et al. 2004; Böttcher & Dermer 2010). More specifically, from Eq. (2.77), the number density of nonthermal particles per unit time and unit Lorentz factor injected in the comoving frame is

$$\frac{\mathrm{d}n_{\mathrm{nth}}}{\mathrm{d}t'\,\mathrm{d}\gamma} = Q_0 \gamma^{-q} H(\gamma; \gamma_{\mathrm{min}}^{\mathrm{nth}}, \gamma_{\mathrm{max}}^{\mathrm{nth}}), \tag{2.79}$$

where Q_0 is the normalization constant in units of number density per unit of proper time ($\mathrm{cm}^{-3}\,\mathrm{s}^{-1}$).

As we inject electrons at a number rate described by Eq. (2.79), we also inject energy in the nonthermal population at a rate (MA12)

$$\frac{\mathrm{d}E'_{\mathrm{inj}}}{\mathrm{d}t'} = m_q c^2 V'_{\mathrm{acc}} Q_0 {\gamma_{\mathrm{min}}^{\mathrm{nth}}}^{q} \mathcal{P}\left(\frac{\gamma_{\mathrm{max}}^{\mathrm{nth}}}{\gamma_{\mathrm{min}}^{\mathrm{nth}}}, 1-q\right), \tag{2.80}$$

where the function $\mathcal{P}(a, s)$ is an integral over the power-law segment given by (3.1), whose careful numerical treatment will be described in detail in the following chapter. V'_{acc} is the comoving volume where the acceleration takes place, which for the case of cylindrical shells of cross-sectional radius R (see §2.3.1),

$$V'_{\mathrm{acc}} = \pi R^2 \Delta r'_{\mathrm{acc}}, \tag{2.81}$$

where $\Delta r'_{\mathrm{acc}}$ is given by (2.63).

The upper cut-off $\gamma_{\mathrm{max}}^{\mathrm{nth}}$ is given by (2.66), whereas the lower cut-off is obtained by, firstly, assuming that the number of accelerated particles is related to the number of particles crossing the shock front by

$$\frac{\mathrm{d}N'_{\mathrm{inj},i}}{\mathrm{d}t'} = \zeta_e \pi R^2 n_i \Gamma_i \beta_{\mathrm{S}} c = Q_0 {\gamma_{\mathrm{min}}^{\mathrm{nth}}}^{q+1} \mathcal{P}\left(\frac{\gamma_{\mathrm{max}}^{\mathrm{nth}}}{\gamma_{\mathrm{min}}^{\mathrm{nth}}}, -q\right) \tag{2.82}$$

where ζ_e is the fraction of charges accelerated into the power-law distribution. Secondly, solving Eq. (2.80) for Q_0,

$$Q_0 = {\gamma_{\mathrm{min}}^{\mathrm{nth}}}^{-q} \frac{\mathrm{d}E'_{\mathrm{inj},i}}{\mathrm{d}t'} \Bigg/ m_q c^2 V'_{\mathrm{acc}} \mathcal{P}\left(\frac{\gamma_{\mathrm{max}}^{\mathrm{nth}}}{\gamma_{\mathrm{min}}^{\mathrm{nth}}}, 1-q\right) \tag{2.83}$$

Finally, from Eqs. (2.64), (2.82) and (2.83), we get

$$\frac{\mathcal{P}\left(\frac{\gamma_{\rm max}^{\rm nth}}{\gamma_{\rm min}^{\rm nth}}, 1-q\right)}{\gamma_{\rm min}^{\rm nth}\mathcal{P}\left(\frac{\gamma_{\rm max}^{\rm nth}}{\gamma_{\rm min}^{\rm nth}}, -q\right)} = \frac{\epsilon_{\rm e} u'_{\rm S}}{\zeta_e \Gamma_i n_i m_q c^2}. \tag{2.84}$$

from which $\gamma_{\rm min}^{\rm nth}$ can be computed. Calculating $\gamma_{\rm min}^{\rm nth}$ from the last equation guarantees that $\gamma_{\rm min}^{\rm nth} \leq \gamma_{\rm max}^{\rm nth}$ [6].

2.4.2.2 Injection of a hybrid thermal-nonthermal distribution

The motivation for the study of a HD sprang from recent PIC simulations of weakly magnetized relativistic shocks (e.g., Sironi et al. 2013). In these simulations it has been found that the energy distribution of particles at the shock front follows a thermal distribution plus a high energy power-law tail. As it is mentioned in §2.4.1.1, relativistic thermal particles are described by (2.75) so that the number density of thermal particles per unit time and unit Lorentz factor reads

$$\frac{{\rm d}n_{\rm th}}{{\rm d}t'\,{\rm d}\gamma} = Q_{\rm th}\frac{\gamma^2\beta}{\Theta K_2(1/\Theta)}\exp\left(-\frac{\gamma}{\Theta}\right), \tag{2.85}$$

where $Q_{\rm th}$ is the thermal normalization factor in units of the number density per unit of proper time ($\rm cm^{-3}\,s^{-1}$).

An approximation to a HD has been proposed by Giannios et al. (2009). It consists of a thermal distribution below some threshold Lorentz factor and a power-law tail above it. The value of the threshold and the number of particles in each part are determined by specifying the proportion of nonthermal particles. Zdziarski et al. (1990) and Li et al. (1996) use a similar approach, joining the thermal and nonthermal distributions at the mean Lorentz factor of the Maxwell-Jüttner distribution, given by Eq. (2.76).

As mentioned in the previous section, in the standard IS model a fraction $\epsilon_{\rm e}$ of the energy dissipated at the shock accelerates the electrons into a pure power-law distribution. In this alternate procedure for the description of the injected particles behind a shock we avoid both finding a break Lorentz factor and estimating the value

[6] Despite the fact that a monoenergetic distribution is unlikely to occur, is not discarded in the present formalism.

of ϵ_e. As an alternative, we will consider first the following assumption: *all thermal energy dissipated at the shock* is used to accelerate both thermal and nonthermal particles (RMA17). Of all this energy, a fraction ζ_e is transferred to the nonthermal population while the rest $(1-\zeta_e)$ goes to the thermal one. In other words,

$$\zeta_e \frac{\mathrm{d}E'_{\mathrm{inj}}}{\mathrm{d}t'} = m_q c^2 V'_{\mathrm{acc}} Q_0 {\gamma^{\mathrm{nth}}_{\mathrm{min}}}^{q} \mathcal{P}\left(\frac{\gamma^{\mathrm{nth}}_{\mathrm{max}}}{\gamma^{\mathrm{nth}}_{\mathrm{min}}}, 1-q\right), \tag{2.86}$$

$$(1-\zeta_e) \frac{\mathrm{d}E'_{\mathrm{inj}}}{\mathrm{d}t'} = m_e c^2 V'_{\mathrm{acc}} Q_{\mathrm{th}} \langle\gamma\rangle. \tag{2.87}$$

Secondly, let us consider the energy spectrum of all particles. For that we add up Eqs. (2.79) and (2.85),

$$\frac{dn_{\mathrm{inj}}}{\mathrm{d}t'\mathrm{d}\gamma} = Q_0 \gamma^{-q} H(\gamma; \gamma^{\mathrm{nth}}_{\mathrm{min}}, \gamma^{\mathrm{nth}}_{\mathrm{max}}) + Q_{\mathrm{th}} \frac{\gamma^2 \beta}{\Theta K_2(1/\Theta)} \exp\left(\frac{-\gamma}{\Theta}\right). \tag{2.88}$$

Integrating Eq. (2.88) in Lorentz factor we obtain the number of (thermal and nonthermal) particles per unit time injected by the shock,

$$\frac{\mathrm{d}N'_{\mathrm{inj}}}{\mathrm{d}t'} = Q_{\mathrm{th}} + Q_0 {\gamma^{\mathrm{nth}}_{\mathrm{min}}}^{q+1} \mathcal{P}\left(\frac{\gamma^{\mathrm{nth}}_{\mathrm{max}}}{\gamma^{\mathrm{nth}}_{\mathrm{min}}}, -q\right). \tag{2.89}$$

On the other hand, we note that the number of injected particles per unit of proper time is given by an equation similar to the first equality of Eq. (2.82), but disregarding ζ_e since now we consider that all electrons are aceelerated and that ζ_e now denotes the fraction of accelerated particles that are nonthermal. Thus, we have

$$\frac{\mathrm{d}N'_{\mathrm{inj}}}{\mathrm{d}t'} = \pi R^2 n_i \Gamma_i \beta_{\mathrm{S}} c. \tag{2.90}$$

By assuming that the partition of the number of injected particles is the same as that of the injected energy we set the following relations for the normalization coefficients in Eq. (2.89)

$$Q_0 {\gamma^{\mathrm{nth}}_{\mathrm{min}}}^{q+1} \mathcal{P}\left(\frac{\gamma^{\mathrm{nth}}_{\mathrm{max}}}{\gamma^{\mathrm{nth}}_{\mathrm{min}}}, -q\right) = \zeta_e \frac{\mathrm{d}N'_{\mathrm{inj}}}{\mathrm{d}t'} \tag{2.91}$$

$$Q_{\mathrm{th}} = (1-\zeta_e) \frac{\mathrm{d}N'_{\mathrm{inj}}}{\mathrm{d}t'} \tag{2.92}$$

From Eqs. (2.91) and (2.92) we find that

$$Q_0 = \frac{\zeta_e Q_{th}}{(1-\zeta_e)\gamma_{min}^{nth\ q+1}\mathcal{P}\left(\frac{\gamma_{max}^{nth}}{\gamma_{min}^{nth}}, -q\right)}. \tag{2.93}$$

Finally, from Eqs. (2.86), (2.87) and (2.93) we arrive at the following expression:

$$\mathcal{P}\left(\frac{\gamma_{max}^{nth}}{\gamma_{min}^{nth}}, 1-q\right) = \langle\gamma\rangle\gamma_{min}^{nth}\mathcal{P}\left(\frac{\gamma_{max}^{nth}}{\gamma_{min}^{nth}}, -q\right), \tag{2.94}$$

from which we compute the lower cut-off of the nonthermal distribution γ_{min}^{nth} in the same manner as for a pure power-law plugging in the expression the average Lorentz factor $\langle\gamma\rangle$ is given by Eq. (2.76).

2.4.3 Particles evolution

In this chapter we expand on the treatment of the nonthermal particles described in Section 3.2.1 of Mimica (2004). Assuming no fluid adiabatic expansion or compression and no difusion (i.e., the particles are advected with the fluid) we can write the kinetic equation

$$\frac{\partial n(\gamma, t')}{\partial t'} + \frac{\partial}{\partial\gamma}\left[\dot{\gamma} n(\gamma, t')\right] = Q(\gamma, t'), \tag{2.95}$$

where $n(\gamma, t')$ is the number density of particles at comoving time t' with Lorentz factor γ, $\dot{\gamma}$ are the radiative energy losses of a particle with Lorentz factor γ, and Q is the source term i.e., the injection of particles with Lorentz factor γ at a time t'. Since we are considering only synchrotron and inverse-Compton losses, we can write the radiation loss term in the form (Dermer & Menon 2009)

$$\dot{\gamma} \equiv \frac{d\gamma}{dt'} = -\nu_0\gamma^2 \tag{2.96}$$

where $\nu_0 > 0$ depends on the magnetic energy density and (or) on the radiation field energy density. Solving Eq. (2.96) we get

$$\gamma(t') = \frac{\gamma(0)}{1+\nu_0\gamma(0)t'}, \tag{2.97}$$

where $\gamma(0)$ is the Lorentz factor of a particle at $t' = 0$. In Figure 2.8 we trace the time evolution of the Lorentz factor $\gamma(t')$ (Eq. (2.97)) for three different values of $\gamma(0)$.

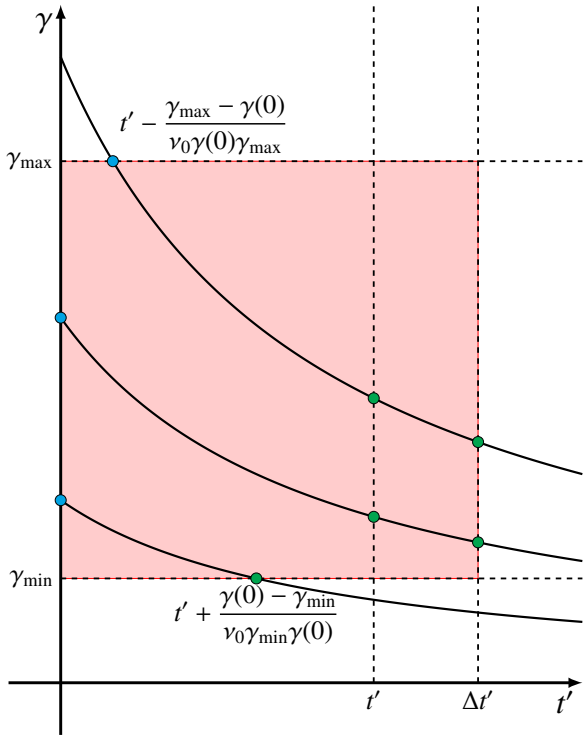

Figure 2.8: *Injection region and cooling trajectories in the $\gamma t'$–plane. In blue and green dots we highlight the values of $t'_{\min}$ and $t'_{\max}$, respectively.*

By solving (2.97) for $\gamma(0)$ we may backtrack the initial Lorentz factor of a particle whose Lorentz factor is $\gamma(t')$ after it cools during a time t'; i.e.,

$$\gamma(0) = \frac{\gamma(t')}{1 - \nu_0 \gamma(t') t'}. \tag{2.98}$$

Following Gratton (1972) we make the next transformations:

$$\tau(\gamma, t') := t' + \frac{1}{\nu_0 \gamma(t')}, \tag{2.99a}$$

$$\Psi(\gamma, t') := \nu_0 \gamma^2(t') n(\gamma, t'), \tag{2.99b}$$

$$J(\gamma, t') := \nu_0 \gamma^2(t') Q(\gamma, t'), \tag{2.99c}$$

where $\tau > 0$ is our new time variable. Substituting (2.99) in (2.95) we arrive at the following ordinary differential equation for Ψ:

$$\frac{d\Psi}{d\tau} = J. \tag{2.100}$$

whose general solution is:

$$\Psi = \int_{\tau_{\min}}^{\tau_{\max}} \mathrm{d}\tilde{\tau} J. \tag{2.101}$$

2.4.3.1 The case without source term

Let us consider first the case where $Q_0 \equiv Q(\gamma(0), t') = 0$. For this case we have the trivial solution for Eq. (2.100):

$$\Psi = \Psi_0, \tag{2.102}$$

where Ψ_0 is a constant determined by Eq. (2.99b) at $t' = 0$. Let us consider the case of an initial power-law distribution (§2.4.1.2, Eq. (2.77)), for which the solution reads (Mimica 2004)

$$\Psi_0 = n(\gamma_{\min})\gamma_{\min}^{q} \nu_0 \gamma^{2-q} H(\gamma; \gamma_{\min}, \gamma_{\max}). \tag{2.103}$$

Substituting the above result into (2.99b) and taking into account that the evolution of the Lorentz factor is given by Eqs. (2.97) and (2.98), the final solution for $n(\gamma, t')$ reads (Mimica 2004)

$$n(\gamma, t') = n(\gamma_{\min})\left(\frac{\gamma}{\gamma_{\min}}\right)^{-q} (1 - \nu_0 \gamma t')^{q-2} H\left(\gamma; \frac{\gamma_{\min}}{1 + \nu_0 \gamma_{\min} t'}, \frac{\gamma_{\max}}{1 + \nu_0 \gamma_{\max} t'}\right), \tag{2.104}$$

which is the so-called Kardashev solution (Kardashev 1962). This solution is constrained to the fact stated above that $\tau > 0$, or else $\gamma < 1/\nu_0 t'$, which for a distribution with finite Lorentz factor is always fulfilled.

Following the set-up of (Mimica 2004), in Figure 2.9 we show the evolution of a distribution of the particles according to (2.104). The initial setup of the distribution is $\gamma_{\min} = 10, \gamma_{\max} = 10^4$ and $q = 2.2$. We can appreciate that the particles pile up at low Lorentz factor, consistent with the cooling they are experiencing.

2.4.3.2 The case with a power-law source term

Let us consider now the case where the source term $Q(\gamma, t')$ follows a power-law in Lorentz factor, i.e., it is described by:

$$Q(\gamma, t') = Q(\gamma_{\min}, t')\left(\frac{\gamma}{\gamma_{\min}}\right)^{-q} H\left(\gamma; \gamma_{\min}, \gamma_{\max}\right), \tag{2.105}$$

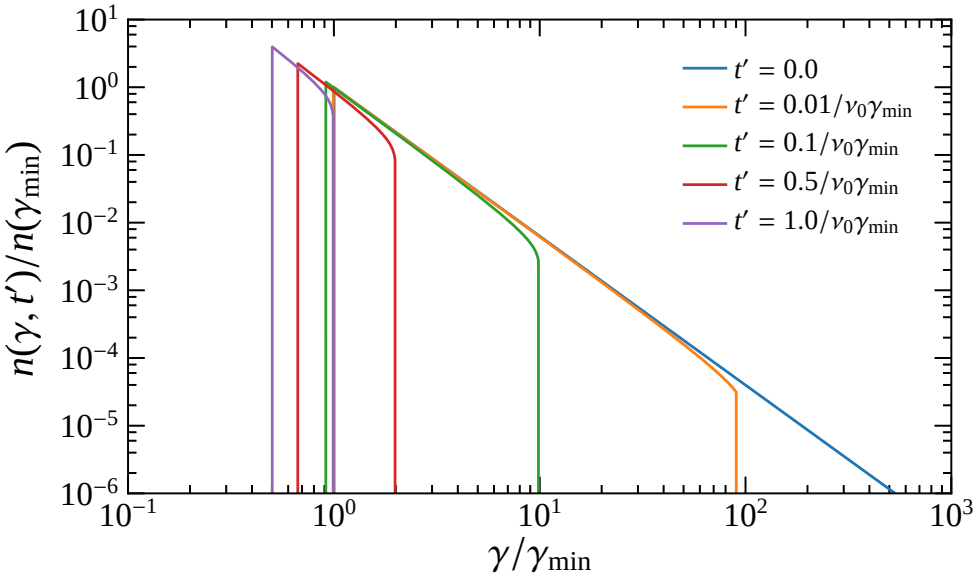

Figure 2.9: *Evolution of a power-law distribution with radiative energy losses and no source term. Initially* $\gamma_{\rm min} = 10, \gamma_{\rm max} = 10^4$*, and power-law index* $q = 2.2$ *(blue line). In orange, green, red, and purple we show the distribution at* $t' = 0.01/\nu_0\gamma_{\rm min}, 0.1/\nu_0\gamma_{\rm min}, 0.5/\nu_0\gamma_{\rm min}$ *and* $1/\nu_0\gamma_{\rm min}$*, respectively.*

and, following model 2 in Gratton (1972), let us assume that there are no relativistic particles present until $t' = 0$ (i.e., $n(\gamma, 0) = 0$) when the injection of particles (2.105) is turned on. Solving (2.99a) for $\gamma(t')$ we get

$$\gamma(t') = \frac{1}{\nu_0(\tau - t')} \tag{2.106}$$

Substituting Eqs. (2.105) and (2.106) in (2.99c) we arrive to the following result:

$$J = Q(\gamma_{\rm min}, t')\gamma_{\rm min}^q \nu_0^{q-1}(\tau - t')^{q-2} H\left(\frac{1}{\nu_0(\tau - t')}; \gamma_{\rm min}, \gamma_{\rm max}\right), \tag{2.107}$$

The solution (Eq. (2.101)) to the kinetic equation with the source term (2.107) reads

$$\Psi = Q(\gamma_{\rm min}, t') = Q(\gamma_{\rm min}, t')\gamma_{\rm min}^q \nu_0^{q-1} \int_{\varsigma_{\rm min}}^{\varsigma_{\rm max}} {\rm d}\varsigma\, \varsigma^{q-2}, \tag{2.108}$$

where $\varsigma \equiv \tau - t', \varsigma_{\rm min} \equiv \tau_{\rm min} - \bar{t}_{\rm min}$, $\varsigma_{\rm max} \equiv \tau_{\rm max} - \bar{t}_{\rm max}$, $\tau_{\rm min} \equiv \tau(\bar{t}_{\rm min})$ and $\tau_{\rm max} \equiv \tau(\bar{t}_{\rm max})$. The values $[\bar{t}_{\rm min}, \bar{t}_{\rm max}]$ define the time interval in which the injection of particles is active (see Eq. (2.113)). In order to find the proper value of $\varsigma_{\rm min}$

and $\varsigma_{\max}$ let us constrain first the injection of particles to happen during a finite period of time[7] $\Delta t'$. In other words, $Q(\gamma, t' > \Delta t') = 0$. Therefore the injection region, in the γ–t' plane, is (see the red area of Figure 2.8):

$$\gamma_{\min} \leq \gamma(t') \leq \gamma_{\max}, \tag{2.109a}$$

$$0 \leq t' \leq \Delta t'. \tag{2.109b}$$

Let us consider now a particle with Lorentz factor $\bar{\gamma}$ at a time $\bar{t}$ in the injection region. Making use of relations (2.97) and (2.98) we get that for such particle:

$$\bar{\gamma}(\bar{t}) = \frac{\gamma(t')}{1 - \nu_0 \gamma(t')\,(t' - \bar{t})}, \tag{2.110}$$

with $0 \leq \bar{t} \leq \min\{t', \Delta t'\}$.

Substituting (2.110) for the left-hand-side of (2.109a) we get that

$$\bar{t} \leq \frac{\gamma(t') - \gamma_{\min}}{\nu_0 \gamma(t') \gamma_{\min}} + t'. \tag{2.111}$$

In the same manner for the right-hand-side of (2.109a) we get that

$$\bar{t} \geq \frac{\gamma(t') - \gamma_{\max}}{\nu_0 \gamma(t') \gamma_{\max}} + t'. \tag{2.112}$$

From Eqs. (2.111) and (2.112) we can conclude that

$$\bar{t}_{\min} = \max\left\{0, t' - \frac{\gamma_{\max} - \gamma(t')}{\nu_0 \gamma(t') \gamma_{\max}}\right\}, \tag{2.113a}$$

$$\bar{t}_{\max} = \min\left\{t', \Delta t', t' + \frac{\gamma(t') - \gamma_{\min}}{\nu_0 \gamma(t') \gamma_{\min}}\right\}. \tag{2.113b}$$

In Figure 2.8 we depict (2.113a) and (2.113b) in blue and green dots, respectively. Substituting (2.113) into (2.110) we get

$$\bar{\gamma}_{\min} \equiv \bar{\gamma}(\bar{t}_{\min}) = \max\left\{\gamma(0), \gamma_{\max}\right\}, \tag{2.114a}$$

$$\bar{\gamma}_{\max} \equiv \bar{\gamma}(\bar{t}_{\max}) = \min\left\{\gamma(t'), \frac{\gamma(t')}{1 - \nu_0 \gamma(t')(t' - \Delta t')}, \gamma_{\min}\right\}. \tag{2.114b}$$

[7] We note that this assumption improves the treatment of the particle injection in Mimica (2004), where the injection was assumed to always be turned on.

At this point we have the means to calculate the integral boundaries in (2.108). From the above relations we have that

$$\varsigma_{\min} = \tau_{\min} - \bar{t}_{\min} = \max\left\{\frac{1}{\nu_0\gamma(0)}, \frac{1}{\nu_0\gamma_{\max}}\right\}, \tag{2.115a}$$

$$\varsigma_{\max} = \tau_{\max} - \bar{t}_{\max} = \min\left\{\frac{1}{\nu_0\gamma(t')}, \frac{1}{\nu_0\gamma(t')} - t' + \Delta t', \frac{1}{\nu_0\gamma_{\min}}\right\}. \tag{2.115b}$$

Accordingly, applying the change of variable $\hat{\varsigma} \equiv \varsigma/\varsigma_{\min}$ in Eq. (2.108), we get

$$\Psi(\tau) = Q(\gamma_{\min}, t')\gamma_{\min}^{q}(\nu_0\varsigma_{\min})^{q-1}\mathcal{P}\left(\frac{\varsigma_{\max}}{\varsigma_{\min}}, 2-q\right). \tag{2.116}$$

The numerical treatment will be described in the following chapter, §3.1.1.1.

Finally, the solution for the number of particles reads

$$n(\gamma, t') = Q(\gamma_{\min}, t')\gamma_{\min}^{q}\gamma^{-2}\nu_0^{-1}\gamma_{\text{high}}^{1-q}\mathcal{P}\left(\frac{\gamma_{\text{high}}}{\gamma_{\text{low}}}, 2-q\right) \tag{2.117}$$

where,

$$\gamma_{\text{low}} = \max\left\{\gamma(t'), \gamma_{\min}, \frac{\gamma(t')}{1-\nu_0\gamma(t')(t'-\Delta t')}\right\}, \tag{2.118a}$$

$$\gamma_{\text{high}} = \min\left\{\gamma(0), \gamma_{\max}\right\}. \tag{2.118b}$$

This formalism allows us to model the shock injection and synchrotron and IC cooling of particles in finite volume and during a finite time.

Chapter 3

The blazars code

In this chapter we will describe the improvements the author of this Ph.D. thesis has undertaken on the previous code (Mimica & Aloy 2012). Furthermore, we will describe in detail the new set of routines developed to compute the MBS emission from relativistic magnetized plasma.

3.1 The Internal-shocks code

The code developed in Mimica & Aloy (2012) is an adaptation of the code `SPEV` (see Mimica et al. 2009) to a cylindrical geometry. It was motivated by previous works where cylindrical shells were used to simulate ISs in blazars (Böttcher & Dermer 2010; Joshi & Böttcher 2011). In Figures 3.1–3.3 we sketch a general (and rather coarse) structure of the code. Blue nodes denote subroutines belonging to the version of the code used in Mimica & Aloy (2012); Rueda-Becerril et al. (2014b), while nodes in green refer to the new tools developed by the author of this PhD thesis.

The first stage is called `Precompute`. In this stage, given an input parameters file: (a) the Riemann problem is solved, (b) the EED (hybrid or power-law) is initialized as described in §§2.3 and 2.4, (c) the normalization coefficients of the EED at each shock front are calculated, (d) synchrotron/MBS emissivity is calculated for discrete time steps corresponding to a range of EED *ages* that are needed to correctly compute the observed emission (see Figure 3.2a and also 2.3.1.4), (e) time integration of synchrotron/MBS emissivity is performed for each time step (see Figure 3.2b), and

(f) emissivity and time integrals are saved into an `HDF5` file.

During the second stage (`Postcompute`) the synchrotron, EIC and SSC light curves are calculated (see Figure 3.3). This stage is highly parallelized using `MPI`[1].

In the rest of this section we will describe the new tools implemented to the Internal shocks code.

3.1.1 Numerical inverse-Compton radiation

In the present thesis we treat the IC radiation according to Mimica (2004, the in-depth development can be found therein). This technique has been applied to the IS model in previous works (e.g. Mimica & Aloy 2012; Rueda-Becerril et al. 2014b). In the present section we will describe new numerical tools that have been developed and applied to compute the IC radiation from a power-law distribution of electrons.

3.1.1.1 Power-law integrals

We need to rewrite the expression in Mimica (2004) used to calculate the emissivity of SSC and EIC scattering in order to compute these processes with the new MBS emissivity. Following Mimica (2004), we start by defining the following functions:

$$\mathcal{P}(a, s) := \int_1^a \mathrm{d}x\, x^{-s} \tag{3.1}$$

$$Q(a, s) := \int_1^a \mathrm{d}x\, x^{-s} \log(x) \tag{3.2}$$

$$Q_2(a, s) := \int_1^a \mathrm{d}x\, x^{-s} \log^2(x) \tag{3.3}$$

where $a > 1$.

[1] MPI (Message Passing Interface) is a standard used for the distributed-memory parallelism (i.e., parallel computation on a cluster of machines that do not share the same memory so that the calculation needs to be coordinated by sending messages between them). More information can be found at http://www.mpi-forum.org

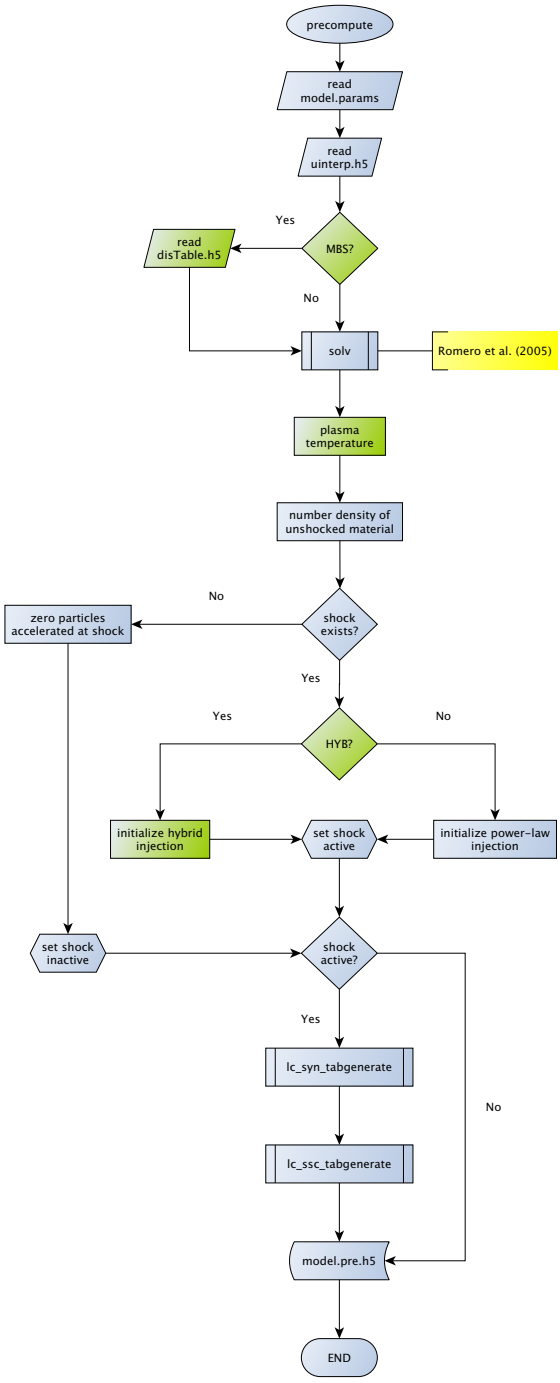

Figure 3.1: *Flow chart of the* `Precompute` *stage.*

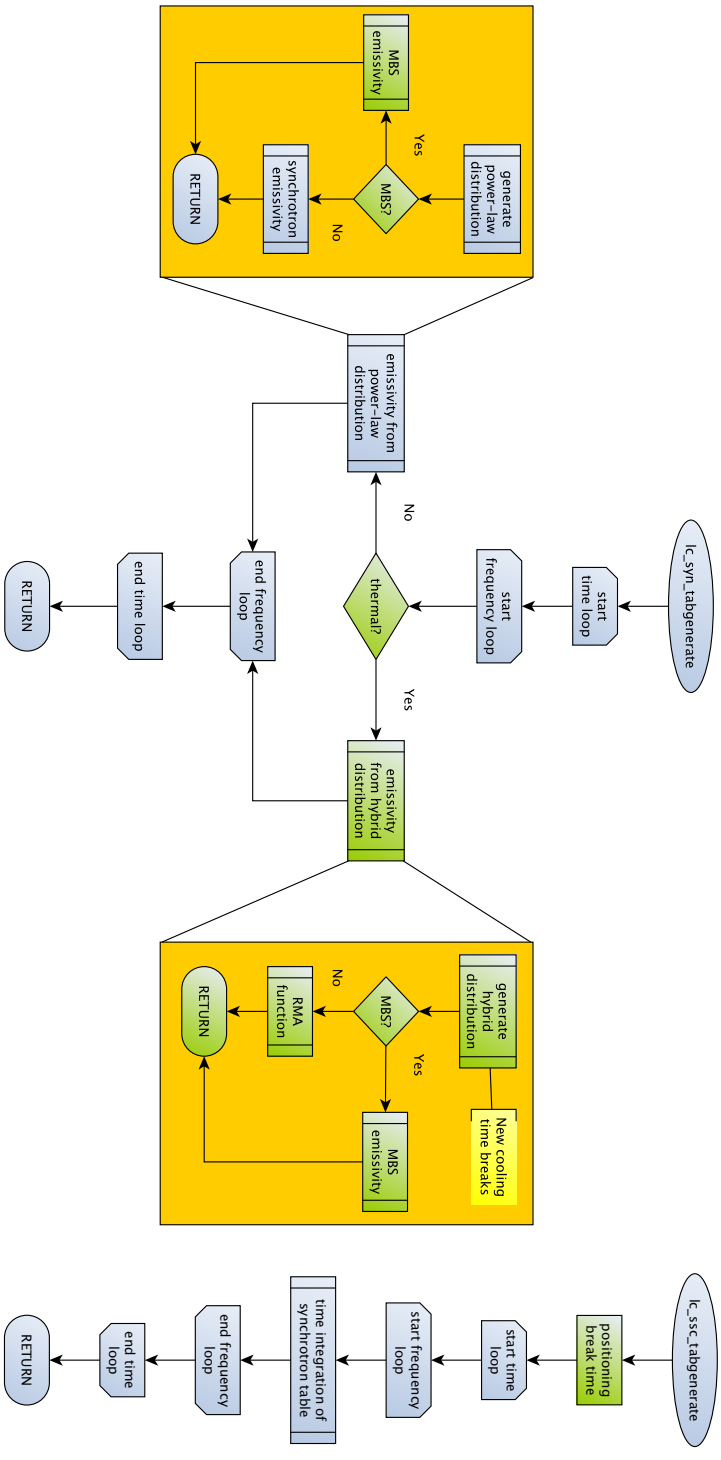

Figure 3.2: *Flow chart of the code for generating precomputed synchrotron and SSC tables.*

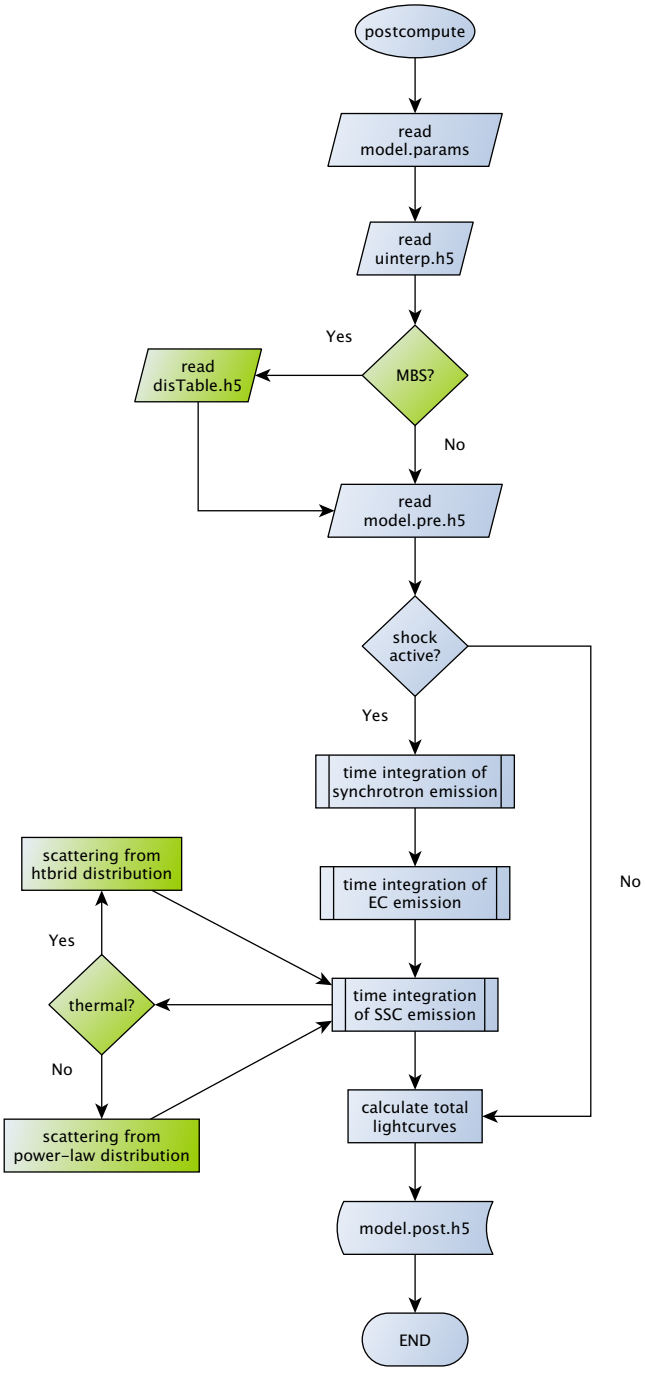

Figure 3.3: *Postcompute*.

These integrals take the values:

$$\mathcal{P}(a,s) := \begin{cases} \dfrac{1-a^{1-s}}{s-1}, & s \neq 1 \\ \log(a), & \text{otherwise} \end{cases}, \tag{3.4}$$

$$\mathcal{Q}(a,s) := \begin{cases} \dfrac{1-a^{1-s}\left[1+(s-1)\log(a)\right]}{(s-1)^2}, & s \neq 1 \\ \dfrac{\log^2(a)}{2}, & \text{otherwise} \end{cases}, \tag{3.5}$$

$$\mathcal{Q}_2(a,s) := \begin{cases} \dfrac{2-a^{1-s}}{(s-1)^3}\left[2+(s-1)\left\{2+(s-1)\log(a)\right\}\log(a)\right], & s \neq 1 \\ \dfrac{\log^3(a)}{3}, & \text{otherwise} \end{cases}. \tag{3.6}$$

However, numerically, the cases in which $s \approx 1$ are potentially problematic because of a division by a very small number. Thus, when $s \approx 1$ we make use of Taylor series expansion around $s = 1$ of the analytic results obtained for $s \neq 1$, i.e.,

$$\mathcal{P}(a,s) \approx \log(a) - \frac{1}{2}(s-1)\log^2(a) + O(s-1)^2, \tag{3.7}$$

$$\mathcal{Q}(a,s) \approx \frac{1}{2}\log^2(a) - \frac{1}{3}\log^3(a)(s-1) + O(s-1)^2, \tag{3.8}$$

$$\mathcal{Q}_2(a,s) \approx \frac{1}{3}\log^3(a) - \frac{1}{4}\log^4(a)(s-1) + O(s-1)^2. \tag{3.9}$$

We note that there is no need to treat a in a special way since we always expect $a > 1$. We introduce a threshold value ε_* and define the following functions aided by their Taylor expansions (3.7)–(3.9) and newly defined logarithmic functions (see Appendix A):

$$\mathcal{P}^*(a,s) := \begin{cases} \dfrac{1-a^{1-s}}{s-1}, & \dfrac{1}{6}(s-1)^2\mathtt{Log3}(a) > \varepsilon_* \\ \mathtt{Log1}(a) - \dfrac{1}{2}(s-1)\mathtt{Log2}(a), & \text{otherwise} \end{cases}, \tag{3.10}$$

$$\mathcal{Q}^*(a,s) := \begin{cases} \dfrac{1-a^{1-s}\left[1+(s-1)\mathtt{Log1}(a)\right]}{(s-1)^2}, & \dfrac{1}{8}(s-1)^2\mathtt{Log4}(a) > \varepsilon_* \\ \dfrac{1}{2}\mathtt{Log2}(a) - \dfrac{1}{3}(s-1)\mathtt{Log3}(a), & \text{otherwise} \end{cases}, \tag{3.11}$$

$$\mathcal{Q}_2^*(a,s) :=$$

$$\begin{cases} \dfrac{2-a^{1-s}}{(s-1)^3}\,[2+(s-1)\{2 \\ \qquad +\,(s-1)\mathtt{Log1}(a)\}\,\mathtt{Log1}(a)]\,, & \dfrac{1}{10}\mathtt{Log5}(a)(s-1)^2 > \varepsilon_* \,. \\ \dfrac{1}{3}\mathtt{Log3}(a) - \dfrac{1}{4}(s-1)\mathtt{Log4}(a), & \text{otherwise} \end{cases} \tag{3.12}$$

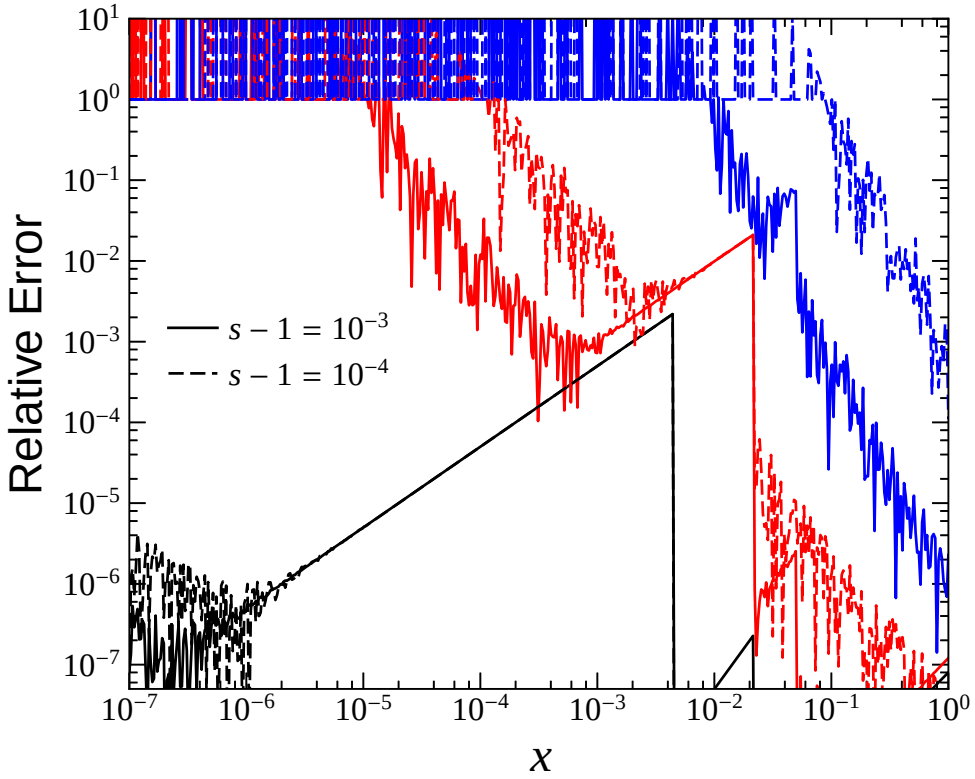

Figure 3.4: *Relative errors of $\mathcal{P}^*(x+1,s), Q^*(x+1,s)$ and $Q_2^*(x+1,s)$ for two $s-1 = 10^{-3}$ and 10^{-4} (solid and dashed lines respectively). We show the relative errors of functions* (3.10) *(black lines),* (3.11) *(red lines) and* (3.12) *(blue lines) with respect to the first branch of $\mathcal{P}$, Q and Q_2, respectively.*

In Figure 3.4 the relative error of $\mathcal{P}^*(x+1,s), Q^*(x+1,s)$ and $Q_2^*(x+1,s)$ are shown for two power-law indices: $s-1 = 10^{-3}$ and 10^{-4} (solid and dashed lines respectively). The relative errors are computed with respect to their first branch; i.e., with respect to $\mathcal{P}, Q$ and Q_2 for $s \neq 1$. Significant numerical noise appears as s gets close to 1 due to the fact that the $\mathcal{P}^*$, Q^* and Q_2^* are very sensible to the value of s.

The relative error of $\mathcal{P}^*$ and $\mathcal{Q}^*$ decreases for $x \gtrsim 0.06$. Besides, the behavior of $\mathcal{Q}_2$ (blue lines) for $x < 0.1$ is unreliable. We expect that in our simulations s will often take values very close to 1, therefore we need to resort to the starred functions.

Eqs. (2.90), (2.91), (2.96) and (2.97) from Mimica (2004) read

$$\mathcal{P}^{\mathrm{M04}}(a,b,\alpha) := \int_a^b \mathrm{d}x x^\alpha = \begin{cases} \dfrac{b^{\alpha+1}-a^{\alpha+1}}{\alpha+1}, & \alpha \neq -1 \\ \log\left(\frac{b}{a}\right), & \alpha = -1 \end{cases}, \tag{3.13}$$

$$\begin{aligned} \mathcal{Q}^{\mathrm{M04}}(a,b,\alpha) &:= \int_a^b \mathrm{d}x x^\alpha \log(x), \\ &= \begin{cases} \dfrac{b^{\alpha+1}\log(b) - a^{\alpha+1}\log(a) - \mathcal{P}^{\mathrm{M04}}(a,b,\alpha)}{\alpha+1}, & \alpha \neq -1 \\ \frac{1}{2}\log(ab)\mathcal{P}^{\mathrm{M04}}(a,b,\alpha), & \alpha = -1 \end{cases}, \end{aligned} \tag{3.14}$$

$$\begin{aligned} \mathcal{R}^{\mathrm{M04}}(a,b,c,d,\alpha,\lambda) &:= \int_c^d \mathrm{d}x x^\lambda \mathcal{P}^{\mathrm{M04}}(xa,xb,\alpha) \\ &= \mathcal{P}^{\mathrm{M04}}(a,b,\alpha)\mathcal{P}^{\mathrm{M04}}(c,d,\alpha+\lambda+1), \end{aligned} \tag{3.15}$$

$$\begin{aligned} \mathcal{S}^{\mathrm{M04}}(a,b,c,d,\alpha,\lambda) &:= \int_c^d \mathrm{d}x x^\lambda \mathcal{P}^{\mathrm{M04}}(xa,b,\alpha) \\ &= \begin{cases} \dfrac{b^{\alpha+1}\mathcal{P}^{\mathrm{M04}}(c,d,\lambda) - a^{\alpha+1}\mathcal{P}^{\mathrm{M04}}(c,d,\alpha+\lambda+1)}{\alpha+1}, & \alpha \neq -1 \\ \log\left(\frac{b}{a}\right)\mathcal{P}^{\mathrm{M04}}(c,d,\lambda) - \mathcal{Q}^{\mathrm{M04}}(c,d,\lambda), & \alpha = -1 \end{cases}. \end{aligned} \tag{3.16}$$

The above functions were rewritten in terms of $\mathcal{P}^*, \mathcal{Q}^*$ and $\mathcal{Q}_2^*$ as follows

$$\mathcal{P}^{\mathrm{M04}}(a,b,\alpha) = a^{\alpha+1}\mathcal{P}^*\left(\frac{b}{a}, -\alpha\right), \tag{3.17}$$

$$\mathcal{Q}^{\mathrm{M04}}(a,b,\alpha) = a^{\alpha+1}\left[\mathcal{Q}^*\left(\frac{b}{a}, -\alpha\right) + \log(a)\mathcal{P}^*\left(\frac{b}{a}, -\alpha\right)\right], \tag{3.18}$$

$$\mathcal{R}^{\mathrm{M04}}(a,b,c,d,\alpha,\lambda) = c^{\lambda+\alpha+2}a^{\alpha+1}\mathcal{P}^*\left(\frac{d}{c}, -\lambda-\alpha-1\right)\mathcal{Q}^*\left(\frac{b}{a}, -\alpha\right), \tag{3.19}$$

$$\mathcal{S}^{\mathrm{M04}}(a,b,c,d,\alpha,\lambda) = -c^{\lambda+1}b^{\alpha+1}\int_1^{d/c}\mathrm{d}x x^\lambda \int_1^{ax/b}\mathrm{d}y y^\alpha \tag{3.20}$$

where $0 < a < b$ and $0 < c < d$.

The case of (3.20) has not been reduced to the starred functions since it had to be treated piecewise owing to the fact that the upper limit of the innermost integral depends on the variable of integration of the outermost integral. Making use of Eq. (3.7) we establish a tolerance $\varepsilon_{\rm int}$

$$\mathcal{S}^{\rm M04}(a,b,c,d,\alpha,\lambda) = \begin{cases} \dfrac{c^{\lambda+1}}{\alpha+1}\left\{b^{\alpha+1}\mathcal{P}^*\left(\frac{d}{c},-\lambda\right) - (ac)^{\alpha+1} \right. \\ \quad \left. \times \mathcal{P}^*\left(\frac{d}{c},-(\alpha+\beta+1)\right)\right\}, & \frac{1}{6}(\alpha+1)^2\texttt{Log3}\left(\frac{b}{ad}\right) > \varepsilon_{\rm int} \\ c^{\alpha+\lambda+2}a^{\alpha+1}\left[\texttt{Log1}\left(\frac{b}{ac}\right)\mathcal{P}^*\left(\frac{d}{c},-\lambda\right)\right. & \\ \quad -\mathcal{Q}^*\left(\frac{d}{c},-\lambda\right) + \frac{1}{2}(\alpha+1)\left\{\texttt{Log2}\left(\frac{b}{ac}\right)\right. & \\ \quad \times\mathcal{P}^*\left(\frac{d}{c},-\lambda\right) - 2\texttt{Log1}\left(\frac{b}{ac}\right) & \\ \quad \left.\left.\times\mathcal{Q}^*\left(\frac{d}{c},-\lambda\right) + \mathcal{Q}_2^*\left(\frac{d}{c},-\lambda\right)\right\}\right], & \text{otherwise} \end{cases} . \tag{3.21}$$

In our simulations the tolerance was set to $\varepsilon_{\rm int} = 10^{-9}$.

3.1.1.2 Emissivity from Compton upscattering of monochromatic seed photons

Let us consider the following incoming intensity of the external radiation field in the CD frame is:

$$I'_{\nu'} = I'_{\nu'_{\rm in}}\,\delta(\nu' - \nu'_{\rm ext}), \tag{3.22}$$

in units of erg cm^{-2} s^{-1} sr^{-1} Hz^{-1}, where $I_{\nu'_{\rm in}}$ and $\nu'_{\rm ext}$ are the intensity and frequency of the incoming photons measured in the CD frame, and $\delta(x)$ is the Dirac delta-function. Setting our coordinate system such that in the laboratory frame (at rest with respect to the AGN) the direction of motion of the electron makes an angle $\theta_{\rm in} \equiv \arccos(\mu_{\rm in})$ with the incoming photon, and an angle $\theta_{\rm out} \equiv \arccos(\mu_{\rm out})$ with the scattered photon. The transformation of the intensity to the rest frame of the electrons, where physical quantities are denoted with a double prime, reads (Rybicki & Lightman 1979)

$$I''_{\nu''}(\mu''_{\rm in}) = I'_{\nu'}\left(\frac{\nu''}{\nu'}\right)^3, \tag{3.23}$$

where $\mu''_{\rm in} = \cos(\theta''_{\rm in})$, and $\theta''_{\rm in}$ is the angle corresponding to $\theta_{\rm in}$, but measured in the rest frame of the electrons. The dependence on the angle of the incoming photon

comes from the fact that in the rest frame of the electron the isotropy of the photon field is lost due to relativistic effects. Frequencies ν' and ν'' are related by the relativistic Doppler formula (e.g. Rybicki & Lightman 1979)

$$\nu' = \nu''\gamma(1 + \beta\mu''_{in}) \tag{3.24}$$

where γ and β are the Lorentz factor and speed of the electron in the CD frame. Inserting (3.23) and (3.24) into (3.22) we get the intensity of the radiation field as seen by the electron; i.e.,

$$I''_{\nu''} = \frac{I'_{\nu'_{\rm in}}}{\gamma^3(1 + \beta\mu''_{in})^3}\delta\left[\nu''\gamma\left(1 + \beta\mu''_{in}\right) - \nu'_{\rm ext}\right]. \tag{3.25}$$

For the sake of brevity the intermediate steps to arrive to the total emissivity are not included in the present thesis, although the procedure is well known and can be found in the literature (e.g. Blumenthal & Gould 1970; Rybicki & Lightman 1979; Dermer & Menon 2009). In previous works EIC seed photons, which surround the shock region, have been treated as monochromatic and isotropic in the AGN (i.e., laboratory) frame (e.g. Böttcher & Dermer 2010; Mimica & Aloy 2012).

The description of the radiation field in the context of the internal shocks model is best suited in the reference frame of the CD. As mentioned before, this frame coincides with the fluid comoving frame and, also, with the reference frame of the electrons. In the latter frame, we denote the frequency and energy density of the external radiation field as $\nu'_{\rm ext}$ and $u'_{\rm ext}$, respectively[2].

Let us consider our system constituted by electrons following a power-law distribution, given by (2.77), with power-law index q. For an isotropic radiation field, as seen in the comoving frame, $I'_{\nu'_{\rm in}} = cu'_{\rm ext}$, and assuming an isotropic cross section, the total scattered photons emissivity at frequency ν' is (Mimica 2004)

[2]The transformation from the AGN frame to the CD frame is as follows (e.g., Böttcher & Dermer 2010; Mimica & Aloy 2012):

$$\nu_{\rm ext} = \Gamma\nu'_{\rm ext}, \qquad u_{\rm ext} = \Gamma^2 u'_{\rm ext},$$

where the primed quantities are in the CD rest frame, and Γ corresponds to the Lorentz factor of the CD measured in the laboratory/AGN frame.

$$
\begin{aligned}
j'_{\nu'} = & c\sigma_{\rm T} u'_{\rm ext} {\nu'_{\rm ext}}^{-1} n(\gamma_{\rm min}) {\gamma^q_{\rm min}} w^{(1-q)/2} \\
& \times \begin{cases}
\mathcal{P}^{\rm M04}\left(\dfrac{w}{\gamma^2_{\rm max*}}, \dfrac{w}{\gamma^2_{\rm min}}, \dfrac{q-1}{2}\right) & \\
\quad -\mathcal{P}^{\rm M04}\left(\dfrac{w}{\gamma^2_{\rm max*}}, \dfrac{w}{\gamma^2_{\rm min}}, \dfrac{q+1}{2}\right), & \frac{1}{4} \leq w \leq \gamma^2_{\rm min} \\
\mathcal{P}^{\rm M04}\left(\dfrac{w}{\gamma^2_{\rm max*}}, 1, \dfrac{q-1}{2}\right) & \\
\quad -\mathcal{P}^{\rm M04}\left(\dfrac{w}{\gamma^2_{\rm max*}}, 1, \dfrac{q+1}{2}\right), & \gamma^2_{\rm min} < w \leq \gamma^2_{\rm max*} \\
0 & \text{otherwise}
\end{cases} ,
\end{aligned}
\tag{3.26}
$$

where $w \equiv \nu'/4\nu'_{\rm ext}$, and the Klein-Nishina cut-off (see Blumenthal & Gould 1970; Aloy & Mimica 2008) is taken into account by defining the *effective* upper cut-off

$$
\gamma_{\rm max*} := \min\left(\gamma_{\rm max}, \frac{m_{\rm e}c^2}{h\nu'_{\rm ext}}\right) . \tag{3.27}
$$

We note that Mimica (2004) did not consider the Klein-Nishina cut-off.

In Figure 3.5 we show in black lines the scattered emissivity from seed photons of a monochromatic external field with $\nu'_{\rm ext} = \nu'_1 = 10^{14}$ Hz (left axis). In analogy to Figure 2.7 of Mimica (2004), the EED considered were power-law distributions (see §2.4.1.2) with $\gamma_{\rm min} = 15, \gamma_{\rm max} = 3 \times 10^6$ and different power-law indices $q = 1.1$, 1.5, 2.25, 3.0 and 4.0[3]. The vertical blue lines in Figure 3.5 denote significant sharp turns in the spectrum. First of all, at around $4\gamma^2_{\rm min}\nu'_{\rm ext}$ (note that the monoenergetic photon field is set up with $\nu'_{\rm ext} = \nu'_1$), we observe the EIC photons upscattered by their interaction with the electrons of the smallest energy in the distribution (i.e., those with $\gamma = \gamma_{\rm min}$). In this particular case, the Klein-Nishina cut-off corresponds to the second of the factors of Eq. (3.27). Thus the spectrum drops quickly off at frequencies $\simeq 4(m_{\rm e}c^2/(h\nu'_{\rm ext}))^2\nu'_{\rm ext}$, if the EED is sufficiently flat (i.e., for $q = 1.1$ and $q = 1.5$; solid and dotted black lines in Figure 3.5). Steeper EED also attain the Klein-Nishina cut-off at the same location, though at a much smaller value of $j'_{\nu'}$ and, thus, it is not displayed in the range of the plot (see the dashed, dot-dashed and dot-do-dashed black lines in Figure 3.5).

[3]This value of $\gamma_{\rm max}$ corresponds to $a_{\rm acc}(B'_{\rm S}/1\,{\rm G}) \approx 160.449$ in Eq. (2.66).

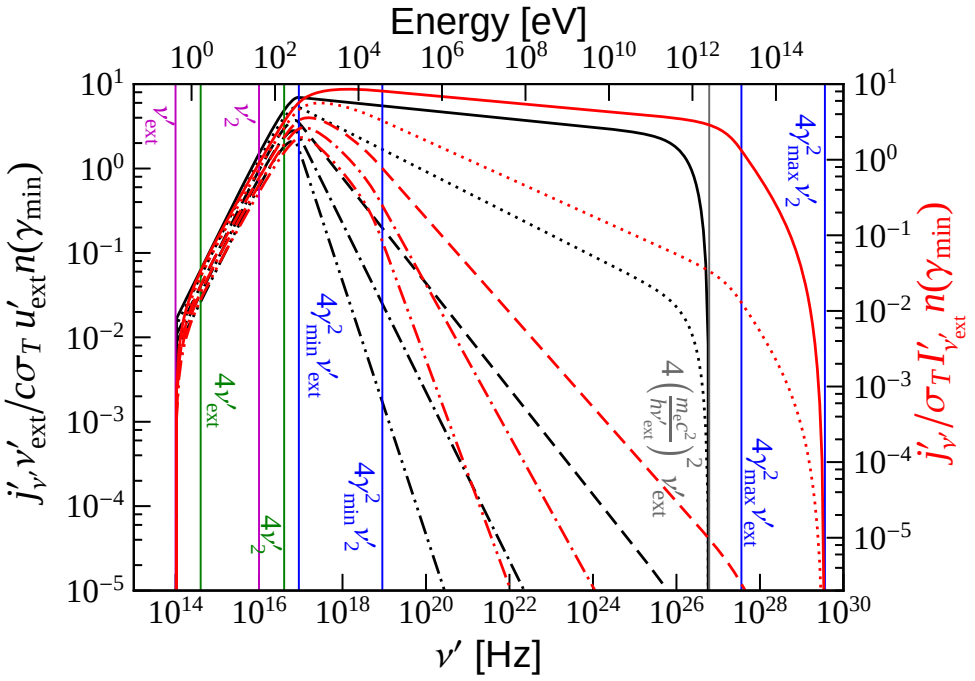

Figure 3.5: *Inverse-Compton emissivity from a δ-like and a power-law distribution of seed photons off a power-law distribution of electrons with $\gamma_{\rm min} = 15$, $\gamma_{\rm max} = 3 \times 10^6$ and index $q = 1.1$, 1.5, 2.25, 3.0 and 4.0 in solid, dotted, dashed, dot-dashed and dot-dot-dashed lines, respectively. Black lines (left axis) correspond to a δ-like spectrum (3.26) with $\nu'_{\rm ext} = 10^{14}$ Hz, whereas red lines (right axis) represent the emissivity due to an incoming power-law spectrum (3.28) with $l = 0.7$, $\nu'_1 = \nu'_{\rm ext}$ and $\nu'_2 = 10^{16}$ Hz (cf. Figure 2.7 Mimica 2004).*

3.1.1.3 Emissivity from Compton upscattering of a power-law distribution of seed photons

Let us assume now that the intensity of the incoming photons follows a power-law spectrum in the CD frame; i.e.,

$$I'_{\nu'} = I'_{\nu'_1}\left(\frac{\nu'}{\nu'_1}\right)^{-l} H(\nu'; \nu'_1, \nu'_2) \tag{3.28}$$

where ν'_1 and ν'_2 are the lower and upper limits of the spectrum, respectively, l the spectral index, and $H(x; a, b)$ is given by (2.78). Analogously to (3.26), the total emissivity of the scattered photons with a power-law spectrum off a power-law distri-

bution is (Mimica 2004)

$$
\begin{aligned}
j'_{\nu'} &= \sigma_{\mathrm{T}} n(\gamma_{\min}) \gamma_{\min}^{q} I'_{\nu'_1} (4\nu'_1)^{l} \nu'^{-l} \\
&\times \begin{cases}
G_1^{\mathrm{ISO}}\left(\gamma_{\max *}^{-2}, \gamma_{\min}^{-2}, w_2, w_1, \dfrac{q-1}{2}, \dfrac{2l-q-1}{2}\right), & \dfrac{1}{4} < \dfrac{\nu'}{4\nu'_1} < \gamma_{\min}^2 \\
G_1^{\mathrm{ISO}}\left(\gamma_{\max *}^{-2}, \gamma_{\min}^{-2}, w_2, \gamma_{\min}^2, \dfrac{q-1}{2}, \dfrac{2l-q-1}{2}\right) & \\
\quad + G_2^{\mathrm{ISO}}\left(\gamma_{\max *}^{-2}, 1, \gamma_{\min}^2, w_1, \dfrac{q+1}{2}, \dfrac{2l-q-1}{2}\right), & \dfrac{\nu'}{4\nu'_2} \le \gamma_{\min}^2 \le \dfrac{\nu'}{4\nu'_1} \\
G_2^{\mathrm{ISO}}\left(\gamma_{\max *}^{-2}, 1, w_2, w_1, \dfrac{q-1}{2}, \dfrac{2l-q-1}{2}\right), & \gamma_{\min}^2 < \dfrac{\nu'}{4\nu'_2} \le \gamma_{\max *}^2 \\
0 & \text{otherwise}
\end{cases}
\end{aligned}
\tag{3.29}
$$

where

$$
w_1 \equiv \min\left\{\frac{\nu'}{4\nu'_1}, \gamma_{\max *}^2\right\}, \tag{3.30a}
$$

$$
w_2 \equiv \max\left\{\frac{\nu'}{4\nu'_2}, \frac{1}{4}\right\}, \tag{3.30b}
$$

and

$$
G_1^{\mathrm{ISO}}(a,b,c,d,\alpha,\lambda) := \mathcal{R}^{\mathrm{M04}}(a,b,c,d,\alpha,\lambda) - \mathcal{R}^{\mathrm{M04}}(a,b,c,d,\alpha+1,\lambda), \tag{3.31}
$$

$$
G_2^{\mathrm{ISO}}(a,b,c,d,\alpha,\lambda) := \mathcal{S}^{\mathrm{M04}}(a,b,c,d,\alpha,\lambda) - \mathcal{S}^{\mathrm{M04}}(a,b,c,d,\alpha+1,\lambda). \tag{3.32}
$$

As above, the intermediate steps were excluded to avoid the repetition of equations from previous works in the present thesis. The goal here is to focus on the results.

Employing the starred functions ((3.10), (3.11) and (3.12)), we take the same parameters as in Figure 2.7 of Mimica (2004). In Figure 3.5 we show in red lines (right axis) the total scattered photons emissivity due to an incoming power-law spectrum photons field (3.28) with $l = 0.7$, $\nu'_1 = 10^6$ Hz and $\nu'_2 = 10^{10}$ Hz. Solid, dotted, dashed, dot-dashed and dot-dot-dashed lines correspond to power-law EEDs with index $q = 1.1$, 1.5, 2.25, 3.0 and 4.0, respectively.

The shape of the spectrum in this case shares some similarities to the case of an incoming monochromatic photon field (§3.1.1.2). For instance, the spectral peak happens above $4\gamma_{\min}^2 \nu'_{\mathrm{ext}}$, but it is broader than in the monochromatic case, with a relatively flat region extending up to $4\gamma_{\min}^2 \nu'_2$. However, the Klein-Nishina cut-off

corresponds to the first of the factors of Eq. (3.27)) in this case. The spectrum drops off more slowly at high-frequencies, with a shallower decay extending between $\simeq 4\gamma_{\rm max}^2\nu'_1$ and $\simeq 4\gamma_{\rm max}^2\nu'_2$, if the EED is sufficiently flat (i.e., for $q = 1.1$ and $q = 1.5$; solid and dotted red lines in Figure 3.5).

In a nutshell, the IC emissivity will be given by Eq. (3.26) if the incoming seed photons are monochromatic. If that is not the case, but rather the spectrum is continuous in a frequency range $[\nu'_{\rm min}, \nu'_{\rm max}]$, the intensity is approximated as a collection of piecewise power-law segments. More specifically, provided that the spectrum follows a power-law with spectral index l_i in the interval $[\nu'_i, \nu'_{i+1}]$, where $\nu'_{\rm min} \leq \nu'_i < \nu'_{i+1} \leq \nu'_{\rm max}$, the specific intensity at frequency ν' in that interval reads

$$I'_{\nu'} \approx I'_{\nu'_i}\left(\frac{\nu'}{\nu'_i}\right)^{-l_i} H(\nu'; \nu'_i, \nu'_{i+1}), \tag{3.33}$$

in which case we apply Eq. (3.29) to each piecewise power-law segment of the whole incoming photon spectrum. This procedure is computationally much more efficient than performing numerically the integrals required to compute the inverse Compton emissivity.

3.1.1.4 Computing the SSC seed photons in the shocked region

With all the above treatment we are in place to solve the radiative transfer Eq. (2.67) in the shocked region of our IS model (see §2.3) in order to evaluate the SSC emission of seed photons. We know *a priori* that the electrons in the shocked region will suffer a loss of energy as time passes (see §2.4.3), which implies that the emissivity depends on the position x and (observer) time $t_{\rm obs}$ at which it is measured. In other words, for a point in the jet axis the angle averaged intensity reads (Mimica & Aloy 2012)

$$I'_{\nu'}(t_{\rm obs}, x') = \frac{1}{2}\int_0^{\pi} {\rm d}\varphi' \int_0^{L(\varphi')} {\rm d}s'\, j'_{\nu'}\left(t'(t_{\rm obs}) - \frac{s}{c}, x' + s'\cos\varphi'\right), \tag{3.34}$$

where φ' is the polar angle in our current system of coordinates, $L(\varphi')$ is the length of the segment in the direction φ' from which the synchrotron/MBS emission has had time to arrive to point x' at a time $t'(t_{\rm obs})$. The values of x' and $t'(t_{\rm obs})$ are given by (2.70) and (2.68), respectively.

3.2 CHAMBA

The numerical evaluation of Eq. (2.15) is tremendously challenging both analytical and numerically since it requires performing the integral over an infinite sum of Bessel functions and their derivatives. As we have mentioned, several techniques have been used to compute such integral. In this section we focus on the implementation details of the code *Computational HArmonics for full MagnetoBremsstrahlung Applications* (CHAMBA) developed for an efficient computation of radiation coming from charged particles in a magnetic field (see §2.2) in the sub, trans and ultrarelativistic regimes.

3.2.1 Preamble

The treatment of MBS emissivity by transrelativistic electrons made by Petrosian (1981) relies on the following simplification:

$$\sum_s f(s) \simeq \int \mathrm{d}s f(s) \tag{3.35}$$

where $f(s)$ correspond to the addends in Eq. (2.15). Such approximation is valid in the regime where the harmonics are so close to each other that they are indistinguishable and the spectrum can be considered as a continuum. That is, an analytic expression was found for the cases where $\nu' \gg \nu_\mathrm{g}$ (see §2.2.5), with a typical relative error between 20 and 30% with respect to the exact result. Its success notwithstanding, it does not deal with the harmonics in the MBS emission that appear at low frequencies near ν_g, which is, in fact, the spectral range that is of interest for the present thesis.

Numerical methods and techniques that deal with the full cyclo-synchrotron emission have been improving. An extensive and concise numerical approach was first performed by Brainerd & Lamb (1987) who applied a Simpson-like method on a cubic fitted function to approximate the sum over harmonics:

$$\sum_{i=n-\Delta n}^{n+\Delta n} f_i \approx \left[\frac{(\Delta n-1)(2\Delta n-1)}{6\Delta n}+1\right](f_{n-\Delta n}+f_{n+\Delta n})+\left[\frac{(\Delta n-1)(4\Delta n+1)}{3\Delta n}+1\right]f_n \tag{3.36}$$

where f_i are the addends in Eq. (2.15). Moreover, this method was implemented to calculate the emissivity from thermal, nonthermal and hybrid distributions in GRBs

and applied to fit the photon flux obtained from observations, achieving accurate results.

Another strategy to tackle the difficulties that harmonics bring about has been by direct summation plus a δ-function broadening by means of a "kernel", which is a function that satisfies:

$$\lim_{\Delta x \to 0} f(x, x_0, \Delta x) = \delta(x - x_0). \tag{3.37}$$

This technique was used by Mahadevan et al. (1996) and later improved in Wolfe & Melia (2006).

Meanwhile, Pe'er & Waxman (2005) developed a code with split regimes. That is, while the frequency and Lorentz factor over which the calculations are performed fulfill that $\nu' < 200\nu_{\rm g}$ and $\gamma < 10$, respectively, the full expression for MBS (see §2.2.2) was computed. Otherwise, the classical synchrotron expression (e.g. Rybicki & Lightman 1979; Jackson 1999) is employed. A similar approached was made by Fleishman & Kuznetsov (2010), placing a frequency boundary below which the harmonic structure is recovered, and above which the analytic expressions found by Petrosian (1981) and Wild & Hill (1971) are used.

3.2.2 Kernel based treatment

In a first stage of the construction of the code, the MBS was treated following Mahadevan et al. (1996, hereafter MNY96). In their numerical code the Dirac δ-function in (2.15) is approximated with a kernel function; i.e., the power radiated for a single electron can be written as follows

$$P'_{\nu'}(\beta) = \frac{2\pi e^2 \nu_{\rm g}}{c} \int_0^1 {\rm d}\mu'_\alpha \int_{-1}^1 {\rm d}\mu' \frac{\mathcal{X}^2}{1 - \beta\mu'_\alpha\mu'} \sum_{m=1}^{\infty} S_m f_m(\mathcal{X}), \tag{3.38}$$

where

$$\mathcal{X} := \frac{\nu'}{\nu_{\rm g}} = \frac{\nu'}{\gamma\nu_{\rm B}}, \tag{3.39}$$

is the normalized frequency or *harmonic frequency*,

$$S_m := \frac{(\mu' - \beta\mu'_\alpha)^2}{1 - \mu'^2} J_m^2(z) + \beta^2 \left(1 - \mu'^2_\alpha\right) \left(\frac{{\rm d}J_m(z)}{{\rm d}z}\right)^2, \tag{3.40}$$

and $f_m(\mathcal{X})$ is the kernel function which satisfies that

$$\lim_{\mathcal{X} \to \mathcal{X}_m} f_m(\mathcal{X}) = \delta(\mathcal{X} - \mathcal{X}_m), \tag{3.41}$$

where

$$\mathcal{X}_m := \frac{m}{\gamma(1-\beta\mu'_\alpha\mu')}, \tag{3.42}$$

is the central frequency around which we will evaluate (3.38).

3.2.2.1 Comparison of different kernels

To approximate the Dirac δ-function MNY96 use the following kernel:

$$f_m^{\text{MNY96}}(\mathcal{X}) = \frac{15}{16\Delta\mathcal{X}}\left[1-\left(\frac{2}{\Delta\mathcal{X}^2}\right)(\mathcal{X}-\mathcal{X}_m)^2+\left(\frac{1}{\Delta\mathcal{X}^4}\right)(\mathcal{X}-\mathcal{X}_m)^4\right]. \tag{3.43}$$

where

$$\Delta\mathcal{X} \equiv \kappa\mathcal{X}_m, \tag{3.44}$$

and κ is a tunable constant (typically much smaller than 1). Despite the fact that (3.43) has compact support and satisfies condition (3.37), we found that this kernel function excludes some contributions to the power radiated due to its sharpness (see §3.2.2.3). This because f_m^{MNY96} is set to zero for $\mathcal{X} > \mathcal{X}_m + \Delta\mathcal{X}$ and $\mathcal{X} < \mathcal{X}_m - \Delta\mathcal{X}$. In order to enclose as much contribution as the numerical calculations can afford we implemented the approximation of the Dirac δ-function as a limit case of a Gaussian distribution

$$\delta(x-x_0) = \lim_{\Delta x\to 0}\frac{1}{\sqrt{\pi}\Delta x}\exp\left\{-\left(\frac{x-x_0}{\Delta x}\right)^2\right\}. \tag{3.45}$$

In Figure 3.6 we compare the Gaussian kernel

$$f_m^{\text{Gauss}}(\mathcal{X}) = \frac{1}{\sqrt{\pi}\Delta\mathcal{X}}\exp\left\{-\left(\frac{\mathcal{X}-\mathcal{X}_m}{\Delta\mathcal{X}}\right)^2\right\}, \tag{3.46}$$

with (3.43) for $\beta = 0.2$, 0.4 and 0.8 in black, red and blue lines, respectively. We can appreciate that at high frequencies the contribution to the power radiated is ignored when using (3.43).

3.2.2.2 Comparison using kernels computed with different tolerance

In order to avoid an infinite summation but consider as much radiated contribution as possible, we approximated the summation in Eq. (3.38) by introducing a tolerance factor, ε, defined as follows:

$$\varepsilon = 1 - \frac{\sum_{m=1}^{M} S_m}{\sum_{m=1}^{M+1} S_m}. \tag{3.47}$$

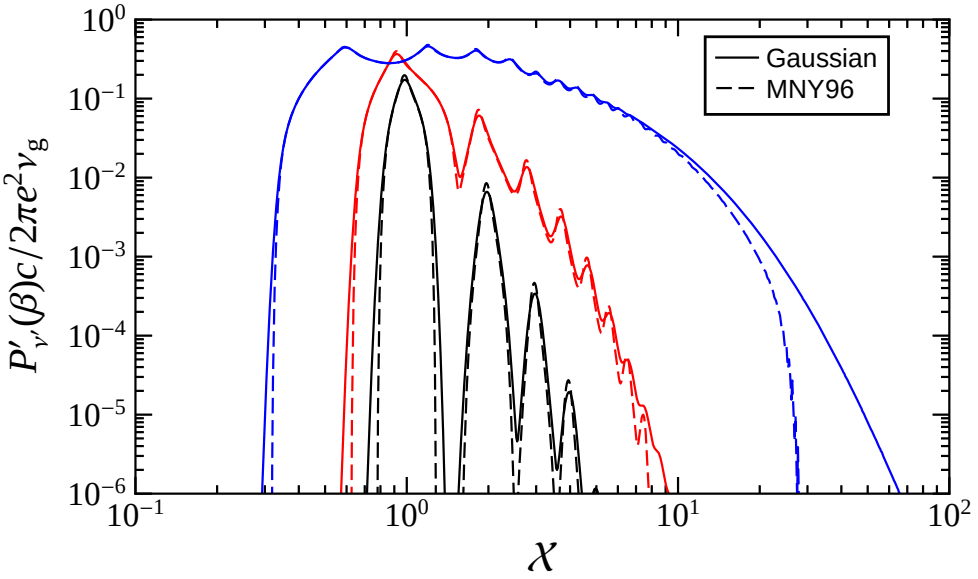

Figure 3.6: *Comparison of kernels. Numerical emissivities of one electron with* $\beta = 0.2$, 0.4 *and* 0.8, *shown in black, red and blue, respectively.*

In Figure 3.7 we present the behaviour of the harmonics for different tolerances for a constant kernel and using $\kappa = 0.05$. Black, red and blue lines are the power spectra for particles with speeds $\beta = 0.2$, 0.4 and 0.8, respectively. On the left panel are the calculations with a Gaussian distribution and on the right panel the calculations with the kernel defined in MNY96. On the left panel we can see that for slow electrons ($\beta = 0.2$ and 0.4), there are only small differences between the spectra, which means that a relatively large tolerance can be used in order to accumulate the most contribution of radiation. On the right panel we find that the kernel used in MNY96 needs a smaller tolerance in order to get the correct radiation contribution for higher frequencies. In a nutshell, the Gaussian kernel needs less terms in the sum than f_m^{MNY96}.

3.2.2.3 Comparison using kernels with different width

The width of the kernel is controlled by (3.44) and it is also responsible for how much contribution is added to the power radiated. In order to track how much of the contribution is lost we performed a test with different values of κ. In Figure 3.8, like

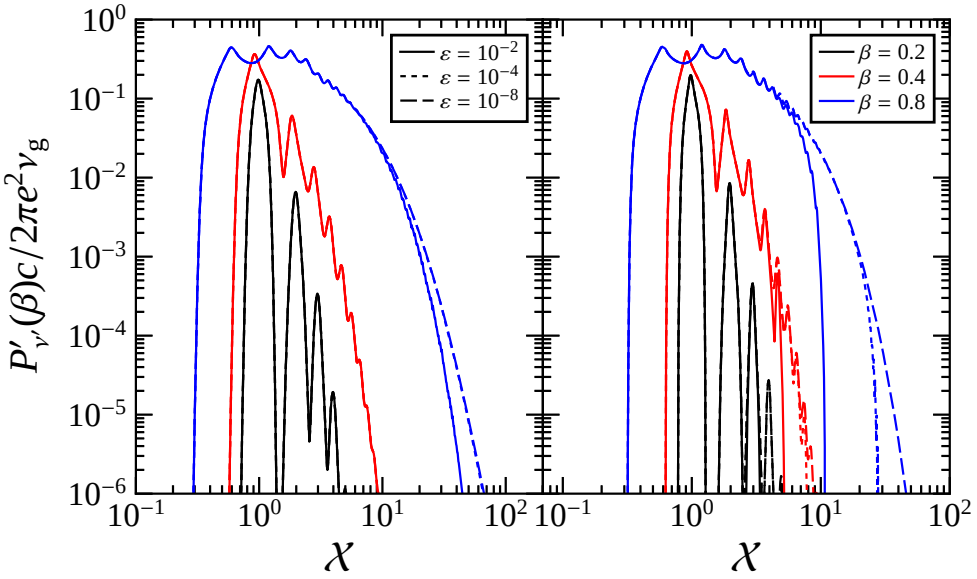

Figure 3.7: *Emissivity of one electron with $\beta = 0.2$ for varying tolerance (Eq. (3.47)). Left: numerical evaluation of the MBS emissivity using a Gaussian kernel. Right: same evaluation but for the kernel in Eq. (21) of MNY96.*

Figure 3.7, we make a comparison of the power radiated for single particles with $\beta = 0.2$, 0.4 and 0.8 for different values of κ. On the left panel we have the results using f_m^{Gauss}. We can see that a broad kernel (solid line) overestimates the power radiated at high frequencies but converges as the κ is reduced. On the right panel are the results using f_m^{MNY96}.

3.2.2.4 Integrals over angles

To compute the integrals over angles in (3.38) we first approximated both integrals using a power-law integration technique developed in Mimica (2004). However, given that the limits of the integral are -1 and 1 in the case of the integral over μ' (or between 0 and 1 in the case of the integral over μ'_α), we considered that a Gauss-Legendre quadrature with 120 nodes (evaluated numerically) would be more suitable for the integral over emission angles, while for the pitch angles a Romberg integration routine Press et al. (1992) was employed.

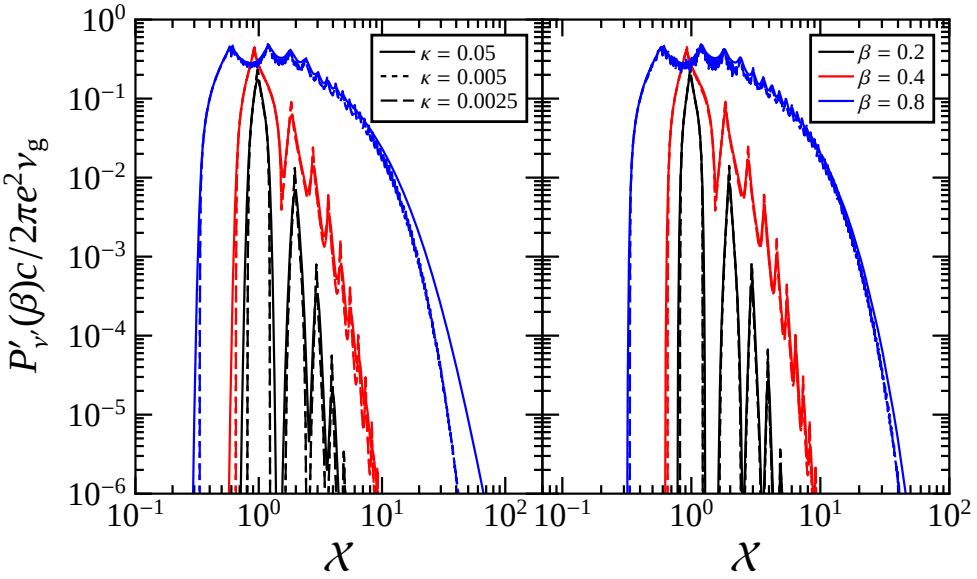

Figure 3.8: *Emissivity of one electron employing a varying kernel width, $\Delta\chi$. The left panel corresponds to the Gaussian kernel while the right panel to the kernel in Eq. (21) of MNY96. The emissivity in both panels is normalized to that of an electron with $\beta = 0.2$.*

3.2.2.5 Performance

To show the computational time that it takes to calculate the power radiated for a single velocity and a single frequency, in Figure 3.9 we display the performance of the code described above. The blue dots correspond to the wall clock time that it took the code to calculate the power radiated by a particle with $\beta = 0.8$ and $\chi = 0.1$, 0.5, 1, 5, 10, 50, 100, 500 and 10^3. We can see that for $\chi \simeq 100$ the elapsed time for a single frequency becomes ≈ 200 times larger than at $\chi \simeq 10^{-1}$, and for $\chi \simeq 1000$, the computational times grows to 4 orders of magnitude. The computational consequences are such that in practice it is unrealistic to take into account a large number of harmonic frequencies to reconstruct with accurately the MBS spectral radiated power for electrons with arbitrary Lorentz factor.

A way to tackle such handicap is the parallelization of the numerical code. The parallel version of the code is based on an `OpenMP`[4] implementation of the algorithm

[4]OpenMP (Open Multi-Processing) is a library for running parallel computations on a system with shared-memory, see http://openmp.org

for the γ and χ nested loops[5].

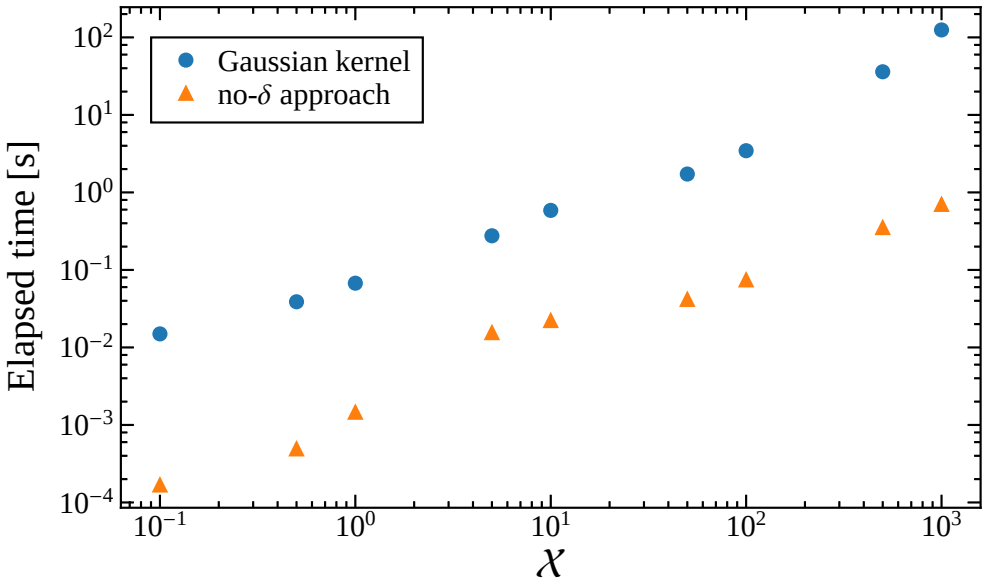

Figure 3.9: *Elapsed time for different frequencies calculating the MBS radiated power by an electron with $\gamma = 10$. Blue circles correspond to those calculations made using the kernels approach with a Gaussian function, $\kappa = 2.5 \times 10^{-3}$ and $\varepsilon = 10^{-8}$. The orange triangles correspond to the calculations made using the no-delta approach (see §3.2.3)*

3.2.2.6 Methodological conclusions

In this section we have described and assessed a methodology to tackle the problem of computing the MBS emission in the sub and mildly relativistic regimes. We have compared two different kernels and found out that a Gaussian kernel, with the proper width, is more efficient at the moment of accounting for most of the radiated power. Nonetheless, the fact that the summation has to be cut at some tolerance produces a noisy spectrum profile, which may cause severe numerical issues when attempting to calculate the spectral evolution from a dynamic distribution of particles. Not to mention that in the transrelativistic regime and at high frequencies the code was highly inefficient. So we ruled out this methodology to compute the harmonics contribu-

[5]The results displayed in Figures 3.6–3.8 were obtained using the parallelized version of the numerical code

tions to the MBS. Instead, we employ a different approach that is described in the next sections.

3.2.3 The no-δ approach

To get the efficiency and accuracy needed for a proper numerical code we decided to face this issue in the same spirit as previous works like Leung, Gammie, & Noble (2011, hereafter LGN11). Such procedure starts with the integration of Eq. (2.38) trivially over pitch angles, μ'_α, exploiting the presence of the δ-function (in LGN11 this integral was made over Lorentz factor γ). Our reason to not follow exactly their procedure was because in the time-dependent code by MA12 (see §3.1) the integral over Lorentz factors is performed dynamically and it is not affordable to calculate the harmonics at every time step.

Indeed, if we look at the δ-function in Eq. (2.15)

$$\delta(y_m) = \frac{1}{\nu_g}\delta\left(\frac{m}{\gamma} - \mathcal{X}(1-\beta\mu'\mu'_\alpha)\right), \tag{3.48}$$

and using the resonance condition (2.21), we have the following expression for μ'_α:

$$\mu'_\alpha = \frac{\gamma\mathcal{X} - m}{\gamma\mathcal{X}\beta\mu'}. \tag{3.49}$$

We can use the condition that $|\mu'_\alpha| < 1$, to set upper and lower boundaries for the summation in Eq. (2.15); i.e., we need to solve the system of inequalities

$$\frac{\gamma\mathcal{X} - m}{\gamma\mathcal{X}\beta\mu'} < 1 \quad \text{and} \quad \frac{\gamma\mathcal{X} - m}{\gamma\mathcal{X}\beta\mu'} > -1, \tag{3.50}$$

for m we arrive to the following expressions:

$$m > \gamma\mathcal{X}(1-\beta\mu'), \tag{3.51a}$$

$$m < \gamma\mathcal{X}(1+\beta\mu'). \tag{3.51b}$$

Since the values of m must be integer, from Eqs. (3.51a) and (3.51b) we define[6]

$$m_+ := \lfloor \gamma\mathcal{X}(1+\beta\mu') \rfloor, \tag{3.52a}$$

$$m_- := \lceil \gamma\mathcal{X}(1-\beta\mu') \rceil. \tag{3.52b}$$

[6]The upper and lower limits here found would have the same form if the integral of μ' had been performed instead of over μ'_α. This due to the symmetry between μ' and μ'_α in (2.21)

The case $\mu' = 0$ (emission perpendicular to the magnetic field) seems to be a pathological case in Eq. (3.49), although in the original expression of the radiated power (Eq. (2.15)) is not. Later in this section we will describe the numerical procedure followed to avoid it.

Finally, substituting (3.52) into (2.38) and integrating over μ'_α we obtain an expression without any δ function for the power radiated by a single charge:

$$P'_{\nu'}(\gamma) = \frac{8\pi^3 e^2 \nu_g \mathcal{X}^2}{c} \int_{-1}^{1} \mathrm{d}\mu' \frac{1}{\mathcal{X}\beta|\mu'|} \times \sum_{m=m_-}^{m_+} \left[\frac{(\mu' - \beta\mu'_\alpha)^2}{1-\mu'^2} J_m^2(z) + \beta^2(1-\mu'^2_\alpha)\left(\frac{\mathrm{d}J_m(z)}{\mathrm{d}z}\right)^2 \right]\Bigg|_{\mu'_\alpha = \frac{\gamma\mathcal{X}-m}{\gamma\mathcal{X}\beta\mu'}}, \tag{3.53}$$

where the factor before the summation symbol is $|\mathrm{d}y_m/\mathrm{d}\mu'_\alpha|^{-1}$, which comes from one of the properties of the δ-function.

Given the above result, let us now define the following functions:

$$\tilde{I}_1(\mathcal{X},\gamma) := \mathcal{X}^2 \int_{-1}^{1} \mathrm{d}\mu' \frac{1}{\mathcal{X}\beta|\mu'|} \times \sum_{m=m_-}^{m_+} \left[\frac{(\mu' - \beta\mu'_\alpha)^2}{1-\mu'^2} J_m^2(z) + \beta^2(1-\mu'^2_\alpha)\left(\frac{\mathrm{d}J_m(z)}{\mathrm{d}z}\right)^2 \right]\Bigg|_{\mu'_\alpha = \frac{\gamma\mathcal{X}-m}{\gamma\mathcal{X}\beta\mu'}}, \tag{3.54}$$

and

$$\tilde{I}_2(\mathcal{X},\gamma_\mathrm{a},\gamma_\mathrm{b}) := \int_{\gamma_\mathrm{a}}^{\gamma_\mathrm{b}} \mathrm{d}\gamma\, n(\gamma)\mathcal{X}^2 I_1(\mathcal{X},\gamma). \tag{3.55}$$

where γ_a and γ_b are generic input values corresponding to the upper and lower values of Lorentz factor interval in which the calculation of Eqs. (3.54) and (3.55) will be performed.

In terms of the integral quantities, if we discretize the Lorentz factor of the electron distribution in M bins, $\{\gamma_i\}_{i=1}^{M}$, the MBS emission coefficient for an isotropic distribution of electrons (2.36) reads

$$j'_{\nu'} = \frac{1}{(4\pi)^2} \sum_{i=1}^{M-1} \tilde{I}_2\left(\frac{\nu'}{\gamma\nu_\mathrm{B}}, \gamma_i, \gamma_{i+1}\right) \tag{3.56}$$

Analogously to the kernels approach, the integration over μ' in Eq. (3.54) is performed using a Gauss-Legendre quadrature (see §3.2.2.4) and assuming isotropic emission. At this stage the evaluation of the integrand at $\mu' = 0$ was avoided by

taking an even number of nodal points (specifically, 120 nodes). The numerical evaluation of the Bessel functions were performed using the tool `my_Bessel_J` developed in LGN11, which therein are shown to be faster than the intrinsic `FORTRAN` Bessel functions or even the `GSL` libraries.

In Figure 3.10 we show $\tilde{I}_1(\mathcal{X},\beta)$ in solid lines for $\beta = 0.2, 0.4$ and 0.8 in black, red and blue, respectively, in contrast with the Gaussian kernel calculations performed in §3.2.2 for the same cases (dashed lines). It is evident that both approaches provide qualitatively similar harmonic contributions, but in the case of the no-δ approach, they are free of uncertainties related to the choice of the kernel function or its parameterization. For that matter, in Figure 3.9 we can appreciate that the present approach (orange triangles) is more efficient by a factor 100 compared to the kernel based treatment. Not to mention that, as far as accuracy is concerned, the analytical boundaries obtained for the summation in (3.53) guarantee that all contributions to the radiated power are considered using finite sums.

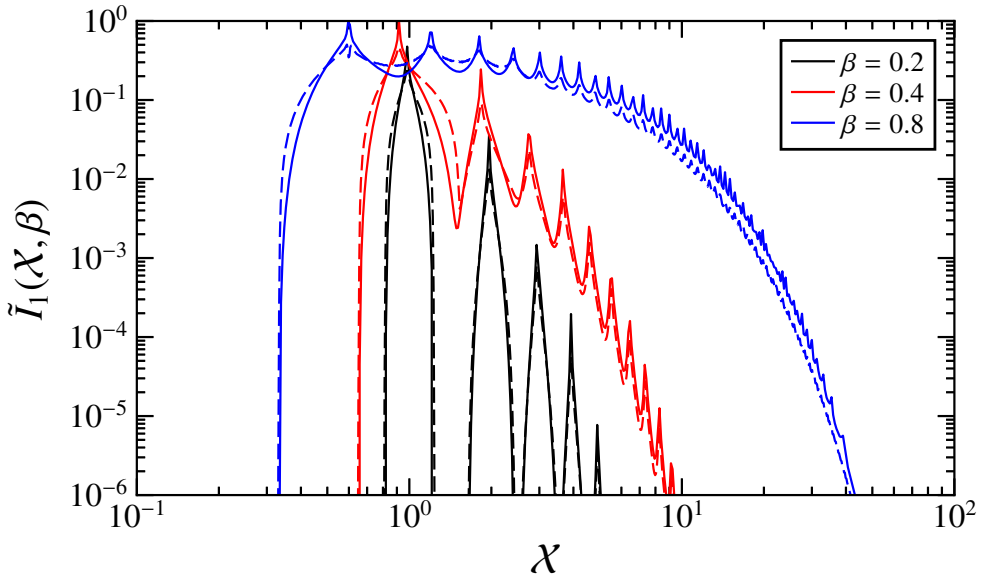

Figure 3.10: *Plot of $\tilde{I}_1(\mathcal{X},\gamma)$ for $\beta = 0.2, 0.4$ and 0.8 in black, red and blue solid lines, respectively. For comparison, dashed lines correspond to the results from the kernel based treatment with a Gaussian kernel (cf. 3.6).*

3.2.4 Building the single particle's radiated power table

The calculation of the function $I_1(\mathcal{X}, \gamma)$ becomes computationally expensive for large values of $\mathcal{X}$ and γ since the number of harmonics needed to be taken into account for the emitted power to be computed accurately enough increases dramatically. In the need of an efficient procedure to calculate the ultrarelativistic and high energy regime, a methodology based on approximate analytic functions was developed.

Moreover, in terms of computational time it is highly inefficient to calculate the emissivity at each time step of the spectral evolution of a system, not even for a synchrotron emitting shell collision, whose expression is analytical (see §2.2.4) and more straightforward to implement in a code. A way to sidestep this computational problem for the MBS emission is to build a table for (3.54) and another one for (3.55) as here will be described.

3.2.4.1 The *RMA* function

As we have seen in §2.2.4, the formula for the pitch-angle averaged synchrotron power of a single ultrarelativistic electron was derived by CS86. Afterwards an approximation was discovered by Schlickeiser & Lerche (2007, hereafter SL07). According to the latter the function (2.31) is approximated by

$$CS(X_c) \simeq SL(X_c) := \frac{X_c^{-\frac{2}{3}}}{0.869 + X_c^{\frac{1}{3}} \exp(X_c)}. \tag{3.57}$$

where, now in terms of $\mathcal{X}$, $X_c = 2\mathcal{X}/3\gamma^2$ (see Eq. (2.28)). Both (2.31) and (3.57) reproduce a continuous spectrum for arbitrary γ. In particular, these formulae do not take into account that for frequencies $\lesssim \nu_B$ the emission is null (see the abrupt decay of the MBS emissivity for small values of $\mathcal{X}$ in Figure 3.10). Nevertheless, (3.57) is analytic, a fact that makes it very convenient for a fast numerical implementation.

In order to determine the region in the $\mathcal{X}$–γ space where Eq. (3.57) holds with sufficient accuracy we must consider two restrictions. On the one hand, as numerical calculations of the cyclo-synchrotron radiated power were performed, it was soon found that the frequency of the first harmonic behaves as

$$\mathcal{X}_1(\gamma) = \frac{1}{\gamma}. \tag{3.58}$$

where $X_1(\gamma)$ denotes the normalized frequency of the first harmonic of an electron with Lorentz factor γ. On the other hand, the synchrotron limit (ultrarelativistic limit) happens for $\gamma \gg 1$.

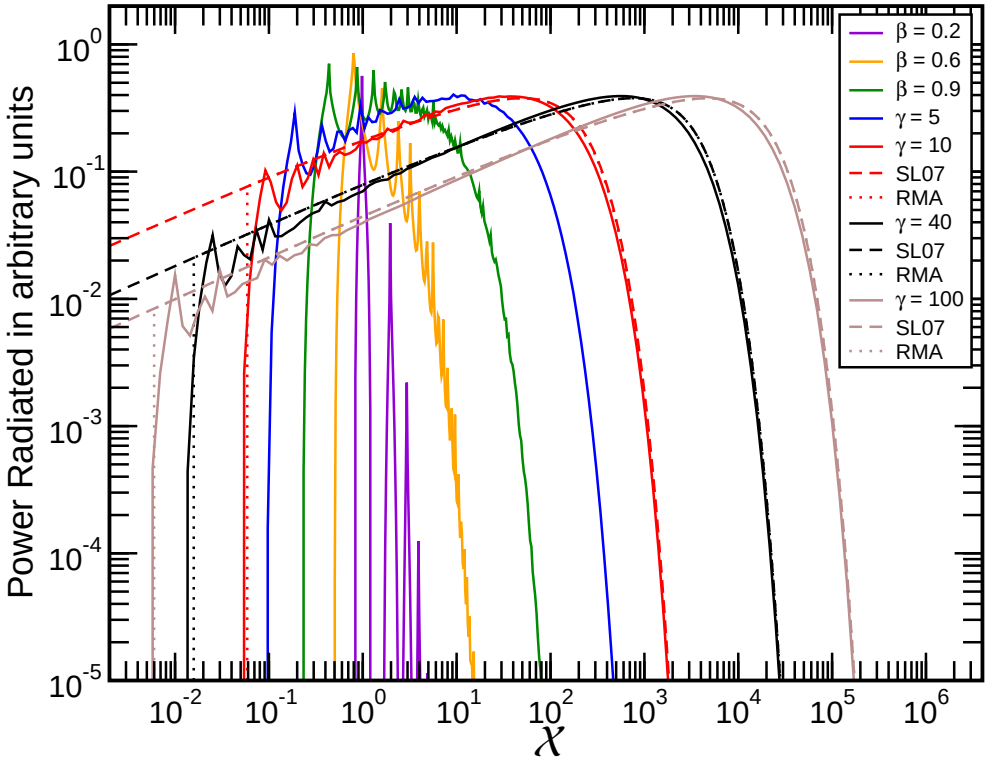

Figure 3.11: *Single electron radiated power as a function of normalized frequency computed for different speeds (cf. with Figure 2 of MNY96). See text for a detailed explanation. This figure is based on Figure 1 from RMA17*

The Figure 3.11 shows the power radiated by single electrons with different velocities or, equivalently, Lorentz factors (RMA17, p. 1172). In the non-relativistic limit (e.g., for $\beta = 0.2$; Figure 3.11 violet solid line) the spectrum is dominated by the first few harmonics (first terms in the sum of Eq. (2.38)), which results in a number of discrete peaks flanked by regions of almost no radiated power. The first harmonic ($m = 1$) peaks at $X \simeq 1$ (a consequence of the resonance condition, as mentioned above). As the electron velocity increases ($\beta = 0.6, 0.9$ and $\gamma = 5$; Figure 3.11 orange, green and blue solid lines, respectively) the gaps between the peaks of the emitted power are progressively filled. In addition, the spectrum broadens towards

ever smaller and larger values of $\mathcal{X}$, and an increasing number of harmonics shows up. At higher Lorentz factors it makes sense to compare the continuum synchrotron approximation for the electron emitting power with the MBS calculation. For that we display the cases with $\gamma = 10, 40$ and 100 in Figure 3.11 with lines colored in red, black and brown, respectively. The different line styles of the latter cases correspond to distinct approximations for the computation of the MBS power. Solid lines correspond to the numerical evaluation of Eq. (2.38) (the most accurate result). Dashed lines depict the computation of the synchrotron power as in SL07 (Eq. (3.61)). Dotted lines correspond to the emitted power calculated according to Eq. (3.63). The difference between the three approximations to compute the radiated power decreases as the Lorentz factor increases[7].

With these results in mind and for numerical convenience, we define $\gamma_{\rm up} \equiv 20$ as a threshold for when to use Eq. (3.57) since for $\gamma > \gamma_{\rm up}$ the evaluation of I_1 slows down dramatically given the fact that the number of terms needed to accurately compute it (Eq. (3.54)) rapidly increases. Furthermore, in order to reduce the overestimation of emission for $\mathcal{X} \lesssim \mathcal{X}_1$ we defined the function

$$RMA(X_{\rm c}, \gamma) := \begin{cases} X_{\rm c} CS(X_{\rm c}), & X_{\rm c} > \dfrac{2a_{\rm coff}}{3\gamma^2}\mathcal{X}_1(\gamma) \\ 0, & \text{otherwise} \end{cases}, \tag{3.59}$$

where $a_{\rm coff}$ is a numerical constant which sets the location of the cut-off and, as it will be shown later on, its value plays an important role when the emissivity is calculated. Let us, for the moment, take $a_{\rm coff} = 0.8$ (later it will be proven to be numerically an appropriate value), so that, using (3.58),

$$RMA(X_{\rm c}, \gamma) = \begin{cases} X_{\rm c} CS(X_{\rm c}), & X_{\rm c} > 0.53\gamma^{-3} \\ 0, & \text{otherwise} \end{cases}. \tag{3.60}$$

Moreover, according to SL07, the pitch-angle averaged synchrotron power of an electron having Lorentz factor γ can be written as

$$P'^{\rm SL07}_{\nu'}(\gamma) = 1.315 \times 10^{-28} \nu_{\rm g}\, X_{\rm c} CS(X_{\rm c}) \ \ {\rm erg\,s^{-1}\,cm^{-3}}. \tag{3.61}$$

Comparing the previous expression with (3.53) and taking into account Eq. (2.36) one obtains for sufficiently relativistic electrons

$$X_{\rm c} CS(X_{\rm c}) \approx \tilde{I}_1(\mathcal{X}, \gamma), \tag{3.62}$$

[7]This paragraph is taken from pp. 1172 and 1173 of RMA17

and employing the new *RMA* function (3.60) the resulting electron power becomes

$$P'^{\rm RMA}_{\nu'}(\gamma) = 1.315 \times 10^{-28} \nu_{\rm g}\, RMA(X_{\rm c}, \gamma)\ \ {\rm erg\,s^{-1}\,cm^{-3}}. \tag{3.63}$$

Looking back into Figure 3.11 we find that, indeed, for $\gamma > \gamma_{\rm up}$, both the exact calculation and the approximation given by $P'^{\rm RMA}_{\nu'}(\gamma)$ match rather well. Indeed, the difference becomes fairly small for $\mathcal{X} \gg 1$.

3.2.4.2 Minimum Lorentz factors for $\mathcal{X} < \mathcal{X}_1$

This subsection is taken from Appendix B1 of RMA17. In order to minimize the numerical problems caused by sharp drops in the power radiated at low Lorentz factors (keeping $\mathcal{X}$ constant, see Figure 3.12), a Lorentz factors cut-offs array $\{\hat{\gamma}_{\rm min}\}$ was designed. Such array is built prior to the calculation of the integral over Lorentz factors in (2.36).

In 3.2.5.3 we will show the cut-off criterion chosen to include as much power as possible while avoiding at the same time the zero emission frequencies below $\mathcal{X}_1(\gamma)$. We follow a similar procedure to construct the array $\{\hat{\gamma}_{\rm min}(\mathcal{X})\}$ in the range frequencies range $\mathcal{X} < \mathcal{X}_1$; i.e., $\hat{\gamma}_{\rm min}(\mathcal{X}) = a_{\rm coff}/\mathcal{X}$.

3.2.4.3 Minimum Lorentz factors for $\mathcal{X} \geq 100$

This subsection is taken from Appendix B2 of RMA17. In order to find $\hat{\gamma}_{\rm min}(\mathcal{X})$ in this part of the spectrum a two-step procedure is required:

1. For every $\mathcal{X}$ the bisection method was employed to find the value of γ at which $\tilde{I}_1$ is well below its maximum value.

2. A linear fit (in logarithmic space) was performed with the values of γ found in the previous step.

The fit obtained from the above procedure was:

$$\hat{\gamma}_{\rm min}(\mathcal{X}) = \exp\{0.491 \log(\mathcal{X}) - 2.212\} \approx 0.109 \mathcal{X}^{1/2}. \tag{3.64}$$

where $\mathcal{X} \geq 100$. We used this formula obtained from the fit to estimate the values of $\hat{\gamma}_{\rm min}(\mathcal{X})$ in this region.

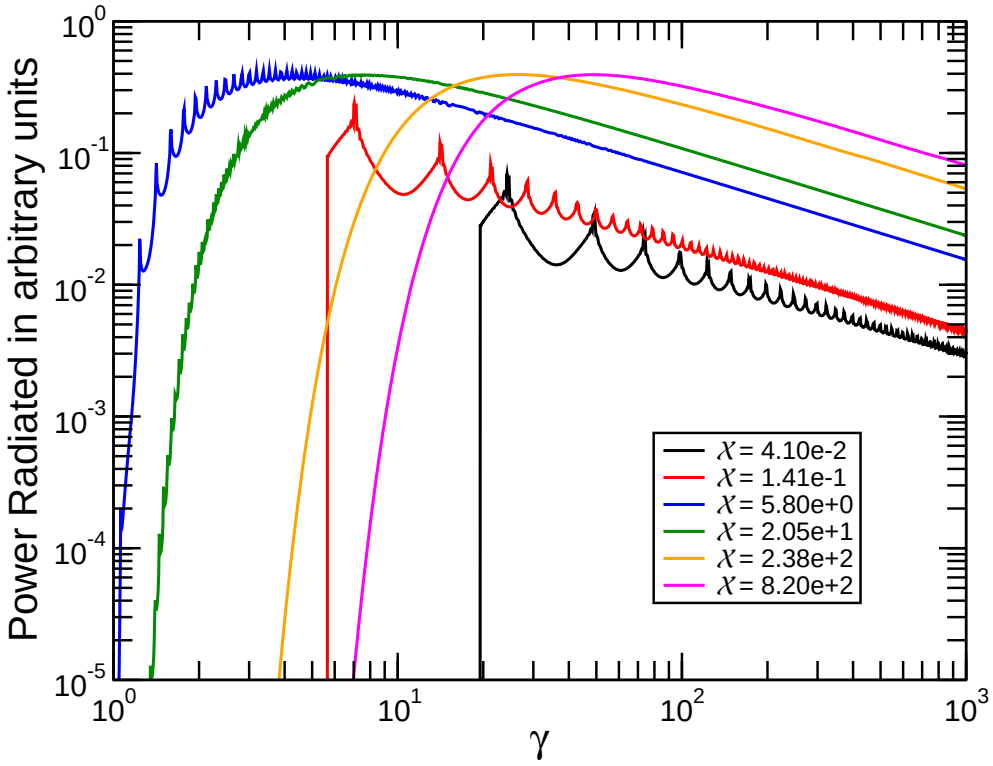

Figure 3.12: *Similar to Figure 3.11 but for a fixed $\mathcal{X}$. The black and red lines depict the radiated power for $\mathcal{X} < \mathcal{X}_1$. The break at low γ is set by hand considering the cut-off criteria described in Sec. 3.2.4.1. The blue and green lines correspond to $\mathcal{X}_1 \leq \mathcal{X} < 100$. The orange and magenta lines correspond to $\mathcal{X} \geq 100$. This figure is Fig. 1.13 from RMA17.*

3.2.4.4 Minimum Lorentz factors for $\mathcal{X}_1 \leq \mathcal{X} < 100$

This subsection is taken from Appendix B3 of RMA17. After several attempts our calculations showed that in the region where $1 \leq \mathcal{X} < 100$ there is practically no zero radiation region in the γ direction (see Figure 3.13). Since this region is above the first harmonic $\mathcal{X}_1$, neither the two criteria mentioned above can be used here since the profile of $\tilde{I}_1$ is too steep at $\gamma \sim 1$ (see Figure 3.12, solid green and blue lines). Applying a bisection method led to oscillating $\hat{\gamma}_{\rm min}(\mathcal{X})$, which in turn produces numerical problems when interpolating from the table. We therefore verified that a constant, close to 1 threshold produces good results in this region. Thus, we employ the input parameter $\gamma^{\rm th}_{\rm min}$ for this purpose. A typical value used is $\gamma^{\rm th}_{\rm min} \approx 1.005037815$ which corresponds to the Lorentz factor of a particle with $\beta = 0.1$. The exact value $\gamma = 1$

cannot be used as threshold because it corresponds to $\beta = 0$, which causes problems in e.g., the corresponding Lorentz factor, the resonance condition (Eq. (2.21)) and the subsequent equations.

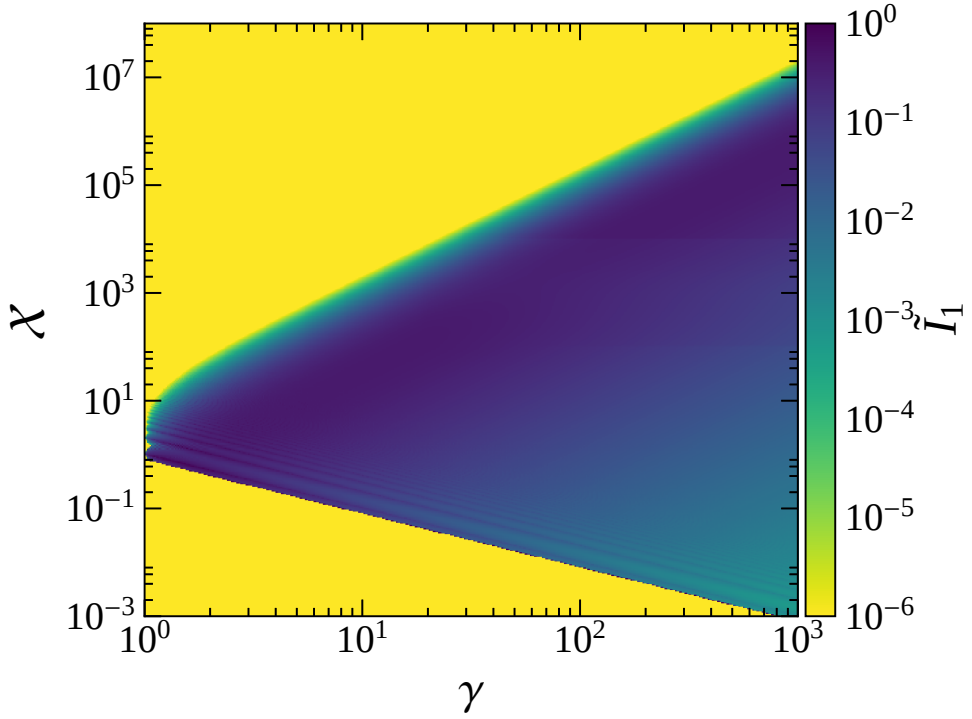

Figure 3.13: *$\mathcal{X}^2 I_1$ as a function of $\mathcal{X}$ and γ. The emission is zero in the light blue region. We also note that for arbitrary γ there is a sufficiently low $\mathcal{X}$ so that the emission is in the form of harmonics.*

3.2.4.5 Chebyshev interpolation

As we have mentioned before, it is computationally expensive to calculate $P'_{\nu'}(\gamma)$ at runtime. For this purpose, we built a high resolution table in the parameter space region $\mathcal{X} \in [\mathcal{X}_{\rm min}, \mathcal{X}_{\rm max}]$ and $\gamma \in [\gamma^{\rm th}_{\rm min}, \gamma^{\rm th}_{\rm max}]$[8]. We name this table `spTable`, which consists of $N_\mathcal{X} \times N_\gamma$ points in the $\mathcal{X} \times \gamma$ directions. The evaluation of I_1 is computed with different procedures depending on the range in which tabular points are

[8]We must point out that these values are part of the input parameters needed to construct `spTable`. Nonetheless, the nomenclature here used was picked in order to be consistent with the upper and lower values of the thermal component of the HD (see §2.4.2.2) used in Chapter 5 and avoid an overwhelming number of symbols.

calculated. For $\mathcal{X} \leq 100$ and $\gamma \leq \gamma_{\rm up}$ we directly use the numerical integration of Eq. (3.54) with the no-δ methodology (§3.2.3), while for $\mathcal{X} > 100$ and $\gamma > \gamma_{\rm up}$ we resort to the *RMA* function (Eq. (3.60)) The evaluation of $\mathcal{X}^2 I_1(\mathcal{X}, \gamma)$ in non tabular points is performed by interpolating among the nodes of the built up table. After experimenting with a number of possibilities, we find out that a Chebyshev interpolation in the direction of γ is extremely accurate and optimal for our purposes. In order to improve the computational efficiency, we store together with the tabular data, the N_γ coefficients needed for a Chebyshev interpolation of $\mathcal{X}^2 I_1(\mathcal{X}, \gamma)$ in the γ direction for each of the $\mathcal{X}_i \in [\mathcal{X}_{\rm min}, \mathcal{X}_{\rm max}], i = 1, \ldots, N_\mathcal{X}$, in the interval $[\hat{\gamma}_{{\rm min},i}/\gamma^{\rm th}_{\rm max}, 1]$ (i.e., we store also $N_\mathcal{X} \times N_\gamma$ Chebyshev coefficients in addition to the tabular data). The Chebyshev coefficients (3.65) (below) were computed according to the algorithm by Press et al. (1992, § 5.8), which is based on the following:

Theorem. *Let $f(x)$ be an arbitrary function in the interval $[-1, 1]$, and if N coefficients c_j, $j = 1, \ldots, N$, are defined by*

$$c_j = \frac{1}{2} \sum_{k=1}^{N} f(x_k) T_{j-1}(x_k), \tag{3.65}$$

where

$$T_n(x) = \cos(n \arccos(x)) \tag{3.66}$$

are the Chebychev polynomials of order n and

$$x_k = \cos\left(\frac{\pi \left(k - \frac{1}{2}\right)}{n} \right), \tag{3.67}$$

the position of the k-th zero (or nodes) of $T_n(x)$ in the interval $[-1, 1]$; then the approximation formula

$$f(x) \approx \left[\sum_{k=1}^{N} c_k T_{k-1}(x) \right] - \frac{1}{2} c_1 \tag{3.68}$$

is exact for x equal to all of the N zeros of $T_N(x)$.

3.2.4.6 Reconstruction of $\mathcal{X}^2 I_1(\mathcal{X}, \gamma)$ using the interpolation table

The usage of `spTable` is a two-step procedure: (a) Chebyshev interpolation (3.68) from the Chebyshev coefficients (3.65), and (b) a linear interpolation in the $\mathcal{X}$ direction using the values obtained in the first step.

Provided that $\gamma > \hat{\gamma}_{\rm min}$, the function $\tilde{I}_1$ is reconstructed for the desired γ and afterwards a linear interpolation is performed for the desired $\mathcal{X}$ using its closest neighbors (upper and lower) from `spTable`. The accuracy of the reconstruction routine can be seen in Figure 3.14. The size of `spTable` for this test was 1024×1024. The interpolation was done in 500×500 points in the same region of the $\mathcal{X}$–γ plane as the `spTable`. In the later set of points (which are not coincident with any of the tabulated points of $\tilde{I}_1$), we compute directly the value of $\tilde{I}_1$ and compared it with the interpolated values. As can be seen, the relative error in a majority of the points is $\lesssim 1\%$. We can also observe in Figure 3.14 that the largest relative errors concentrate close to the boundaries of the $\mathcal{X} - \gamma$ plane where the MBS emissivity is zero.

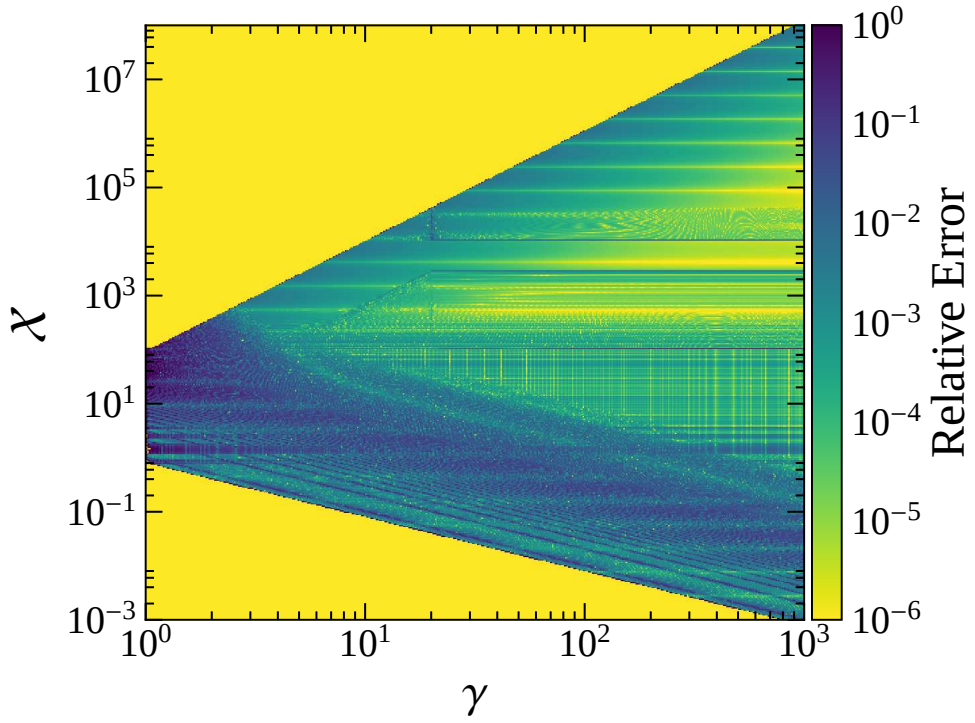

Figure 3.14: *Similar to Figure 3.13, but showing the relative error between the data obtained using numerical integration and the values interpolated from the table. The resolution of the plot is* 1024×1024 *points.*

3.2.4.7 The new *RMA* function

We attempted to continue along the lines similar to that of SL07 by fitting our numerical results with

$$\widetilde{CS}(X_{\rm c};\lambda_1,\lambda_2,\lambda_3) := \frac{X_{\rm c}^{-\lambda_1}}{\lambda_2 + X_{\rm c}^{\lambda_3}\exp(X_{\rm c})}. \tag{3.69}$$

Although the quality of the approximation of SL07 to CS86 is acceptable, we decided instead to follow Finke et al. (2008) so that an improvement to the *RMA* function (3.60) uses a piece-wise approach

$$RMA_{\rm fit}(X_{\rm c}) := \begin{cases} 1.80842\, X_{\rm c}^{\frac{1}{3}}, & X_{\rm c} < 0.00032 \\ \exp\{A_0 + A_1\texttt{Log1}(X_{\rm c}) + A_2\texttt{Log2}(X_{\rm c}) & \\ \quad + A_3\texttt{Log3}(X_{\rm c}) + A_4\texttt{Log4}(X_{\rm c}) + A_5\texttt{Log3}(X_{\rm c})\}, & 0.00032 \le X_{\rm c} \le 0.65 \\ \exp\{B_0 + B_1\texttt{Log1}(X_{\rm c}) + B_2\texttt{Log2}(X_{\rm c}) & \\ \quad + B_3\texttt{Log3}(X_{\rm c}) + B_4\texttt{Log4}(X_{\rm c}) + B_5\texttt{Log3}(X_{\rm c})\}, & 0.65 < X_{\rm c} \le 15.58 \\ \dfrac{\pi}{2}\left(1 - \dfrac{11}{18X_{\rm c}}\right)\exp(-X_{\rm c}) & X_{\rm c} > 15.58 \end{cases}, \tag{3.70}$$

where the Log functions are the logarithmic functions in Table A.1 and the coefficients $A_i, B_i, i = 1,\ldots,5$, are found coefficients of a polynomial fit (in the logarithmic space), whose values appear in Table 3.1.

i	A_i	B_i
0	−0.78716264	−0.82364552
1	−0.70509337	−0.83166861
2	−0.35531869	−0.52563035
3	−0.06503312	−0.22039315
4	−0.00609012	0.01669180
5	−0.00022765	−0.02865070

Table 3.1: *Coefficients of the polynomial fit for the new RMA function.*

In the upper panel of Figure 3.15 we show in thick solid black line the *CS* function (2.31) and in red solid line the approximation by SL07. Solid and dashed green

lines correspond to the asymptotic approximations of $CS(X_c)$ for $X_c \ll 1$ and $X_c \gg 1$, respectively (also given in the two branches of (2.31)). Solid and dashed orange lines correspond to the polynomial fits found by Finke et al. (2008). And finally, solid and dashed blue lines correspond to the polynomial fits found for the new *RMA* function as described above. In the lower panel we depict the relative error of each line of the upper panel with respect to the black line. While it is true that the analytical formula found by SL07 is a good approximation to CS, it should be emphasized that the relative error is between 10–20% in a wide range of the spectrum of X_c, and though it does decrease as the CS function approaches its asymptotic regimes, the overall value is not even close to 1%. On the contrary, we can appreciate that the polynomial fits are certainly below the error threshold of 1% in their respective range of X_c in which they are evaluated. Besides, the polynomial fit presented in this thesis was computed in a such a manner that the error at the joint points with the asymptotic approximations was $\lesssim 1\%$ without compromising the accuracy of the region of interest.

Taking all this into account, with the use of (3.70) the new *RMA* function reads

$$RMA(X_c, \gamma) = \begin{cases} X_c RMA_{\rm fit}(X_c), & X_c > 0.53\gamma^{-3} \\ 0, & \text{otherwise} \end{cases} . \tag{3.71}$$

In Figure 3.16 we show the same results as in Figure 3.13, but in this case Eq. (3.71) is used.

3.2.5 Numerical evaluation of the emissivity

In this section we describe how a second table is built by evaluating $\tilde{I}_1$ using the aforementioned `spTable`. This is an intermediate step that allows us to use this new table used to compute the emissivity (Eq. (2.36)) numerically.

3.2.5.1 The construction of the interpolation table

We first consider a discretization of the Lorentz factor of the electrons $\{\gamma_i\}_{i=1}^{M}$, where γ_1 and γ_M correspond to the minimum and maximum Lorentz factors of the given distribution.

After a detailled testing, we found that a direct numerical integration of Eq. (3.55) may lead to numerical noise in the final result due to the extremely large amplitude

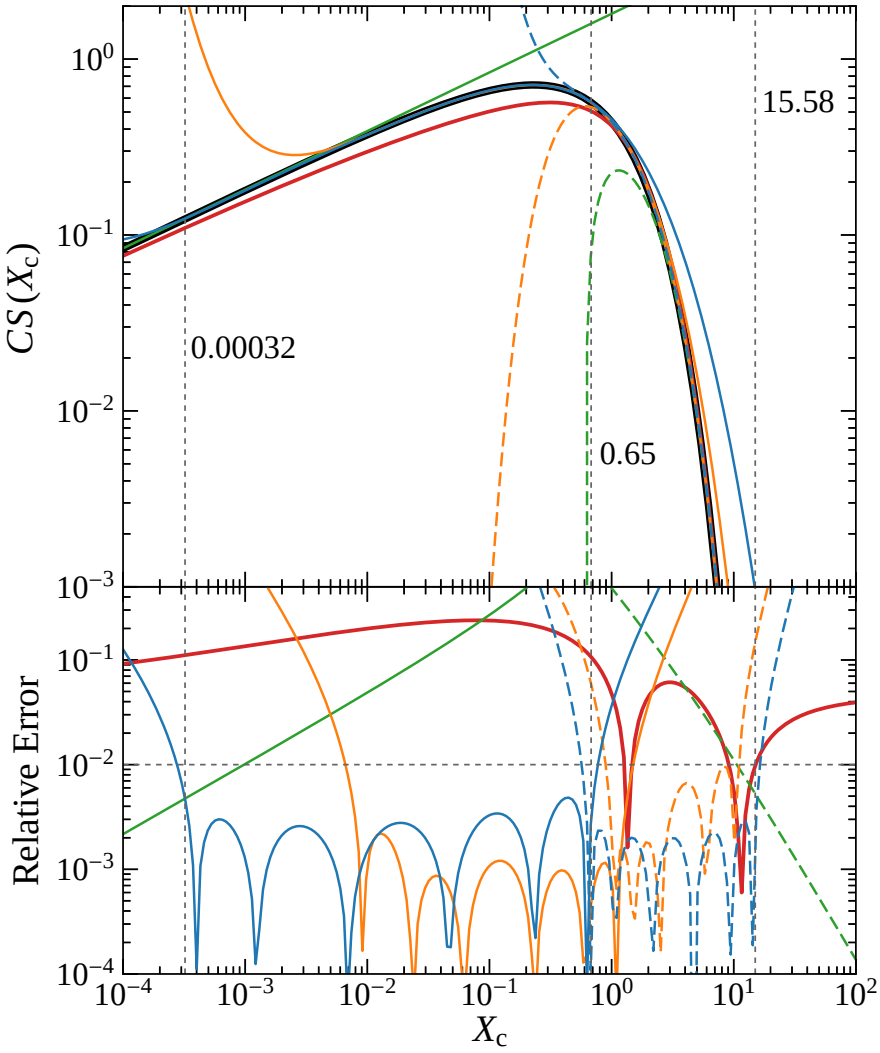

Figure 3.15: *Upper panel: different approximations to compute the CS function* (2.31) *(black solid line) and asymptotic approximations to it in the limits* $X_c \ll 1$ *and* $X_c \gg 1$. *Lower panel: relative error between the CS function and the different formulae employed to approximate it. See text for the explanation.*

oscillations of the integrand in the subrelativistic limit. Therefore, we reformulate the numerical evaluation of Eq. (3.55) assuming that the integrand in that equation can be approximated by a piecewise power-law distribution, so that in each power-law

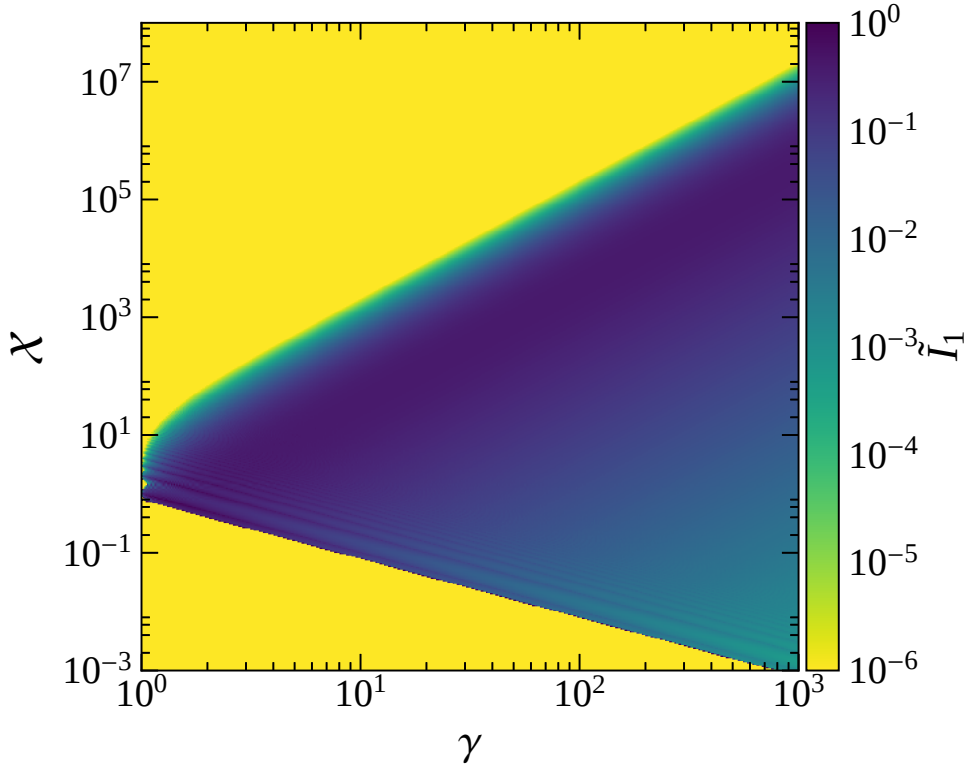

Figure 3.16: *Same as Figure 3.13, but showing $\tilde{I}_1$ computed using the new RMA function.*

segment we have

$$I_2\left(\mathcal{X}, q_i, \gamma_i, \gamma_{i+1}; \gamma_{\rm max}^{\rm th}\right) = \left(\gamma_{\rm max}^{\rm th}\right)^{1-q_i} \int_{\gamma_i/\gamma_{\rm max}^{\rm th}}^{\gamma_{i+1}/\gamma_{\rm max}^{\rm th}} {\rm d}\xi\, \xi^{-q_i} \tilde{I}_1\left(\mathcal{X}, \xi\gamma_{\rm max}^{\rm th}\right) \tag{3.72}$$

where q_i is the index of the power-law approximation to the EED within the interval $[\gamma_i, \gamma_{i+1}]$ and $\xi := \gamma/\gamma_{\rm max}^{\rm th}$. To compute $\tilde{I}_2$ (equation (3.55)), we define the function

$$I_3(\xi, \mathcal{X}, q) := \int_{\xi}^{1} {\rm d}\hat{\xi}\, \hat{\xi}^{-q} \tilde{I}_1(\mathcal{X}, \hat{\xi}\gamma_{\rm max}^{\rm th}). \tag{3.73}$$

Rewriting I_2 in terms of I_3 we get

$$I_2\left(\mathcal{X}, q_i, \gamma_i, \gamma_{i+1}; \gamma_{\rm max}^{\rm th}\right) = \left(\gamma_{\rm max}^{\rm th}\right)^{1-q_i} \left[I_3\left(\frac{\gamma_i}{\gamma_{\rm max}^{\rm th}}, \mathcal{X}, q_i\right) - I_3\left(\frac{\gamma_{i+1}}{\gamma_{\rm max}^{\rm th}}, \mathcal{X}, q_i\right)\right]. \tag{3.74}$$

The integral depends on the same three parameters variables as Eq. (3.73). We use the standard Romberg method (see §3.2.2.4) to compute its value for each triplet $(\xi, \mathcal{X}, q)$. In this way, a three dimensional array is built for I_3. As before, we apply the Chebyshev interpolation (see §3.2.4.5), in the ξ direction, in order to construct an interpolation table, where also the Chebychev coefficients (3.65) for I_2 (hereafter `disTable`) are stored to improve the numerical efficiency.

3.2.5.2 Computation of emissivity using an interpolation table

The total emissivity $j'_{\nu'}$ (Eq. (3.56)) is computed as the sum of the individual contributions of each of the power-law segments in which the original distribution has been discretized, but approximating the original function $\tilde{I}_2$ by I_2. The contribution from the segment i reads

$$j'_{\nu',i} = \frac{\pi e^2 \nu_b}{2c} n(\gamma_i) \gamma_i^{q_i} I_2 \left(\mathcal{X}, q_i, \gamma_i, \gamma_{i+1}; \gamma_{\max}^{\text{th}}\right). \tag{3.75}$$

As an example, in Figure 3.17 we present the emissivity from power-law distribution (2.77) of electrons with $\gamma_{\min} = 1.01$, $\gamma_{\max} = 100$ and various power-law indices ($q = 2.1, 2.5, 2.9, 3.3, 3.7$ and 4.1). For comparison, the dashed lines show the emissivity from power-law distributions of electrons with the same power-law indices but employing the standard formula for the synchrotron radiated power (CS86). With the numerical treatment and interpolation tables explained in the previous sections, we are able to reproduce the synchrotron regime and take into account the emissivity by subrelativistic, transrelativistic and ultrarelativistic electrons. We can also appreciate that the oscillations of the emissivity take place for frequencies $\lesssim 10^7$ Hz. Such oscillations are both numerical an real. The real oscillations can be found by realizing that they appear at the same frequency and with more or less the same magnitude for all power-law indices. For instance, at $\nu \sim 2 \times 10^6$, 3×10^6, 7×10^6 and 9×10^6 Hz we can see that the same oscillations arise. On the contrary, numerical oscillations can be recognized by the noise-like shape in the spectra; .e.g., at $\nu \sim 3 \times 10^6$, 4×10^6 and 7×10^6 Hz. For that matter, in our algorithm those peaks, or "noise", are modulated at runtime in order to diminish any possible contamination. These numerical issues can be caused by the narrowness and steepness characteristic of the emission lines-like cyclotron radiated power, which provokes numerical difficulties at the moment of integrating the spectra.

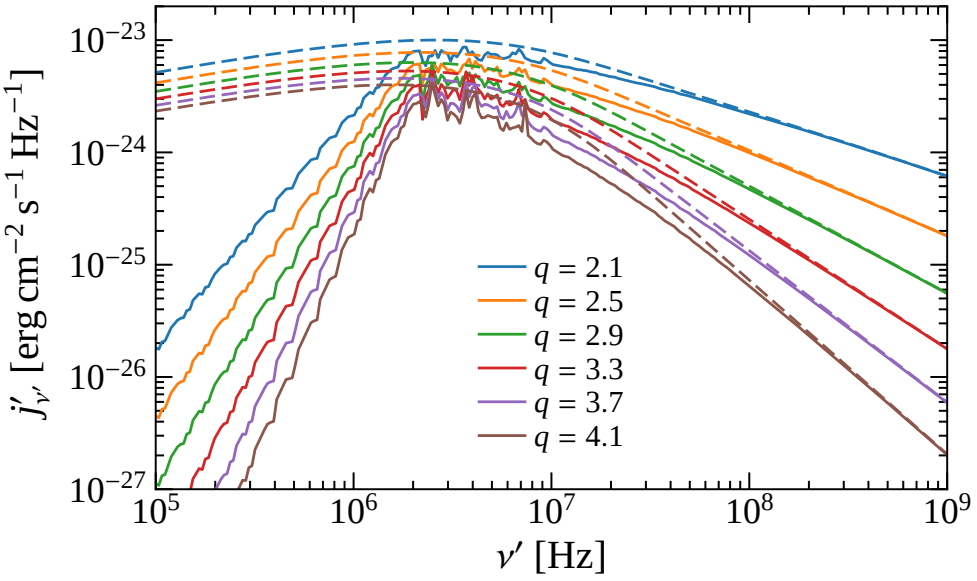

Figure 3.17: *Emissivity from a power-law distribution for different power-law indices. In blue, orange, green, red, purple and brown solid lines we present the emissivity from power-law distributions of electrons having q = 2.1, 2.5, 2.9, 3.3, 3.7 and 4.1, respectively (cf. Figure 7 in Wolfe & Melia 2006). Solid and dashed lines correspond to our computation of the MBS emissivity and to the synchrotron emissivity evaluated with the formula of CS86, respectively.*

The following paragraph belongs to the §4.2.2 of RMA17, p. 1172. The discretization of `disTable` in the $\mathcal{X}$–γ plane is not uniform. Many more points are explicitly computed in the regime corresponding to low electron energies and low emission frequencies than in the rest of the table. In this regime harmonics dominate the emissivity and accurate calculations demand a higher density of tabular points. In the ultrarelativistic regime the emission is also computed numerically. There, we use the table produced in MA12 (hereafter `uinterp`) that includes only the synchrotron process computed with relative errors smaller than 10^{-5}. Note that in the ultrarelativistic regime the errors made by not including the contribution of the MBS harmonics are negligible. We use both tables in order to cover a wider range of frequencies and Lorentz factors than would be possible if only `disTable` were to be used (due to prohibitively expensive calculation for high frequencies and Lorentz factors). In Figure 3.18 we sketch the different regions of the $\mathcal{X}$–ξ space spanned by our method to assemble a single (large) table. Whenever our calculations require the combina-

tion of $\mathcal{X}$ and ξ that falls in the blue region, we employ `disTable` to evaluate the emissivity, otherwise we use `uinterp`. In the particular case when $\gamma_i < \gamma^{\rm th}_{\rm max} < \gamma_{i+1}$, the emissivity is computed using both tables as follows:

$$j'_{\nu',i} = \frac{\pi e^2 \nu_{\rm g}}{2c} n(\gamma_i) \gamma_i^{q_i} \left(I_2^{\texttt{disTable}}(\mathcal{X}, q_i, \gamma_i, \gamma^{\rm th}_{\rm max}; \gamma^{\rm th}_{\rm max}) + I_2^{\texttt{uinterp}}(\mathcal{X}, q_i, \gamma^{\rm th}_{\rm max}, \gamma_{i+1}; \gamma^{\rm th}_{\rm max}) \right). \tag{3.76}$$

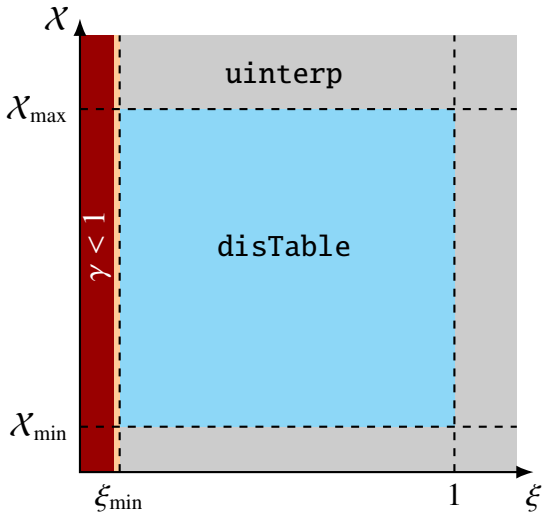

Figure 3.18: *Illustration of the different regions of the $\mathcal{X}$–ξ plane spanned by the distinct approximations employed to compute the values of emissivity according to Eq.* (3.75). *$\mathcal{X}_{\rm min}$ and $\mathcal{X}_{\rm max}$ are generic values for upper and lower limits of $\mathcal{X}$ for the table* `disTable` *and $\xi_{\rm min} \equiv \gamma^{\rm th}_{\rm min}/\gamma^{\rm th}_{\rm max}$. For a given q_i, a combination of ξ and $\mathcal{X}$ in the blue region means that* `disTable` *is employed. The red area corresponds to the physically forbidden regime where $\gamma < 1$ and, therefore, there is no MBS emission. The thin orange strap corresponds to the area of low speeds $1 \leq \gamma < \gamma_1$ excluded from the table.* The present figure and caption corresponds to Figure 2 and caption from RMA17.

3.2.5.3 Estimating the cut-off for the *RMA* function

In order to constrain the analytic function *RMA* (both (3.60) and (3.71)) so that it approximates the MBS spectrum, a proper value of $a_{\rm coff}$ must be set. The rest of this paragraph corresponds to an edited extract of Appendix A in RMA17, p. 1181. In Figure 3.19 we show the relative error of the emissivity using the $RMA(X_{\rm c}, \gamma)$ function (3.60) compared to the full MBS treatment. We assume a pure power-law

distribution of electrons with different power-law indices for two different values of the cut-off constant: $a_{\rm coff} = 0.8$ and $a_{\rm coff} = 1$. The magnetic field for this test was $B' = 10\,{\rm G}$ and the minimum and maximum Lorentz factors $\gamma^{\rm nth}_{\rm min} = 5, \gamma^{\rm nth}_{\rm max} = 500$, respectively. At low frequencies the errors are large because there the emission is dominated by harmonics and is thus not well represented by a continuous *RMA* function. Nevertheless, choosing an appropriate value for $a_{\rm coff}$ can decrease the errors in that region from $\sim 350\%$ ($a_{\rm coff} = 1$, right panel) to $\sim 25\%$ ($a_{\rm coff} = 0.8$, left panel). The relative error of the cases with power-law indices $q < 0$ are always below 1, and is somewhat lower for $a_{\rm coff} = 1$ than for $a_{\rm coff} = 0.8$. However, since we want the relative error to be the lowest for all power-law indices, we choose the cut-off constant $a_{\rm coff} = 0.8$. Further scanning of the values of $a_{\rm coff}$ showed that a decrement of this parameter rises the relative error at low frequencies.

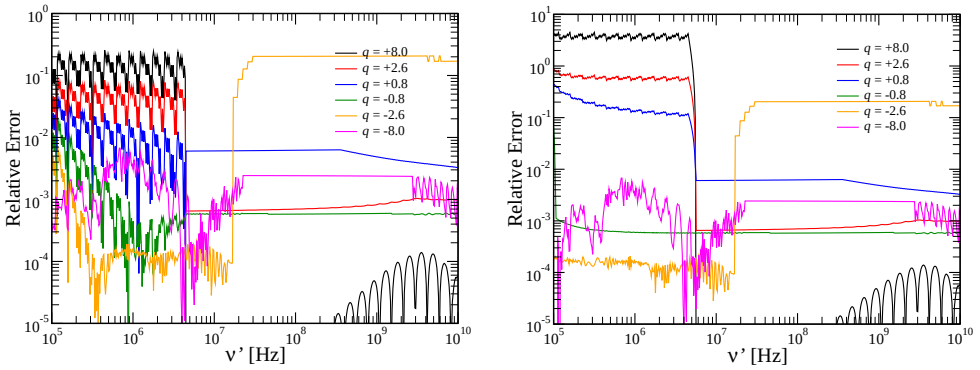

Figure 3.19: *The relative error between emissivity for a power-law distribution of electrons computed from the MBS interpolation tables and performing a numerical integration of the RMA function. Each of the different colours represent cases with different power-law indices, q, of the nonthermal EED. In the left and right panels we show the relative error considering $a_{\rm coff} = 0.8$ and $a_{\rm coff} = 1$ in Eq.* (3.59)*, respectively.* This figure and caption correspond to Figure A1 in RMA17.

3.2.6 The algorithm

The construction of the interpolation tables for a numerically efficient evaluation of the MBS emission is performed with an ancillary program, which is independent of `CHAMBA`. Constructing and assembling the interpolation tables is a rather involved process, as we have seen in the previous sections. Aiming to give a proper perspective of the work needed to arrive to the final product presented in this thesis, in Fig-

ure 3.20 we sketch the flowchart of these ancillary programs to construct `spTable` (Figure 3.20a) and `disTable` (Figure 3.20b).

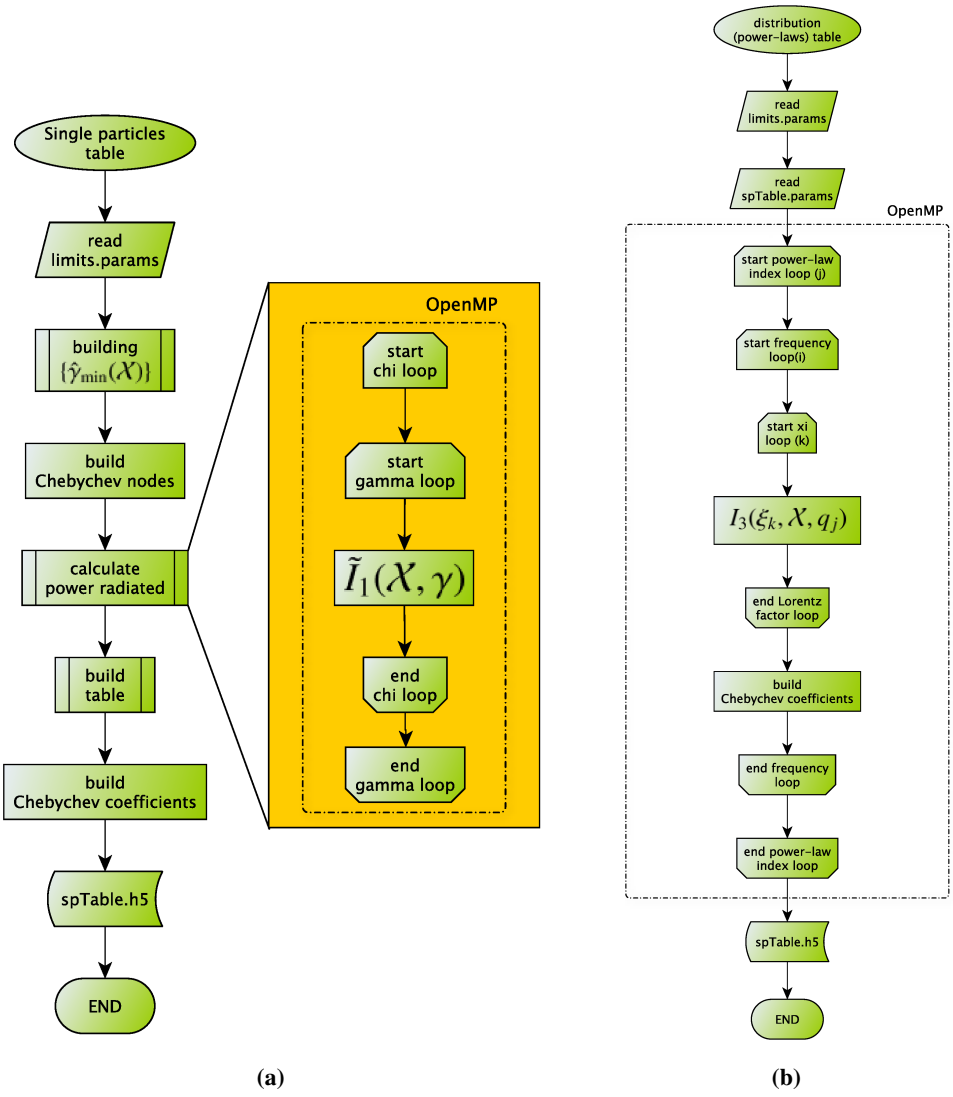

Figure 3.20: *Flowcharts of the algorithms followed to construct* `spTable` *(left) and* `disTable` *(right).*

We point out that constructing the interpolation tables is computationally expensive and, therefore, we have implemented its calculation in parallel (using `OpenMP`)

to reduce the time to build them.

3.2.6.1 Performance of the tables construction

To test the performance we tracked the wall clock time for different sizes of the tables. These tables were constructed in the users shared server `ARC1` of the Department of Astronomy and Astrophysics of the University of Valencia, subject to potential hyperthreding due to users sharing resources. In Table 3.2a are the construction times of `spTable`, while in Table 3.2b the construction times of `disTable`.

N_γ	N_χ	16 cores
64	64	8 209.467
64	128	13 665.200
128	64	15 032.170
128	128	21 930.001

(a) *`spTable` performance*

N_γ	N_χ	N_q	16 cores	32 cores
64	64	25	7.523	1.959
64	128	25	8.335	10.184
128	64	25	13.567	14.601
128	128	25	29.455	23.369
64	64	50	13.112	4.452
64	128	50	17.945	16.217
128	64	50	27.902	23.276
128	128	50	50.996	46.901

(b) *`disTable` performance.*

Table 3.2: *Wall clock computation time (in seconds) for different-sized `spTable` (left), using* 16 *computing cores, and `disTable` (right) tables using* 16 *or* 32 *computing cores.*

Chapter 4

The influence of the magnetic field on the spectral properties of blazars

In the present chapter we enclose an adapted version of the article RMA14, pp. 1857–1867.

4.1 Abstract

We explore the signature imprinted by dynamically relevant magnetic fields on the SED of blazars. It is assumed that the emission from these magnetohydrodynamic evolution we compute by numerically solving Riemann sources originates from the collision of cold plasma shells, whose problems. We compute the SEDs including the most relevant radiative processes and scan a broad parameter space that encompasses a significant fraction of the commonly accepted values of not directly measurable physical properties. We reproduce the standard double hump SED found in blazar observations for unmagnetized shells, but show that the prototype double hump structure of blazars can also be reproduced if the dynamical source of the radiation field is very ultrarelativistic both, in a kinematically sense (namely, if it has Lorentz factors $\gtrsim 50$) and regarding its magnetization (e.g., with flow magnetizations $\sigma \simeq 0.1$). A fair fraction of the *blazar sequence* could be explained as a consequence of shell magnetization: negligible magnetization in FSRQs, and moderate or large (and uniform) magnetization in BL Lac objects. The predicted photon spectral indices ($\Gamma_{\rm ph}$) in the

$\gamma-$ray band are above the observed values ($\Gamma_{\rm ph,obs} \lesssim 2.6$ for sources with redshifts $0.4 \leq z \leq 0.6$) if the magnetization of the sources is moderate ($\sigma \simeq 10^{-2}$).

4.2 Modeling dynamics and emission from internal shocks

In this section we summarize the method of MA12, which is used to model the dynamics of shell collisions and the resulting nonthermal emission (we follow Sections 2, 3 and 4 of MA12). We also discuss the three families of numerical models used in this work.

We assume that a fraction $\epsilon_{\rm e}$ of the dissipated kinetic energy is used to accelerate electrons in the vicinity of shock fronts. We keep $\epsilon_{\rm e}$ fixed in this work aiming to reduce the number of free parameters. We do not expect its possible variation to influence our results qualitatively (e.g., Böttcher & Dermer 2010, show in Figure 7 that a change in $\epsilon_{\rm e}$ does not change the Compton dominance A_C).

In order to compute synthetic time-dependent multi-wavelength spectra and light curves, we assume that the dominant emission processes resulting from the shocked plasma are synchrotron, EIC and SSC. The EIC component is the result of the upscattering of near infrared photons (likely emitted from a dusty torus around the central engine of the blazar or from the broad line region) by the nonthermal electrons existing in the jet. We further consider that the observer's line of sight makes an angle θ with the jet axis.

4.2.1 Models

The main difference between this work and MA12 is that we allow for shell Lorentz factors and the viewing angle θ to vary. Table 4.1 shows the spectrum of model parameters that we consider in the next sections. In order to group our models according to the initial shell magnetizations we denote by letters **W**, **M**, **S**, **S1** and **S2** the following families of models:

W: weakly magnetized, $\sigma_{\rm L} = 10^{-6}, \sigma_{\rm R} = 10^{-6}$,

M: moderately magnetized, $\sigma_{\rm L} = 10^{-2}, \sigma_{\rm R} = 10^{-2}$,

S: strongly magnetized, $\sigma_{\rm L} = 1, \sigma_{\rm R} = 10^{-1}$,

S1: strongly and equally magnetized, $\sigma_{\rm L} = 10^{-1}, \sigma_{\rm R} = 10^{-1}$, and

S2: strongly magnetized, $\sigma_{\rm L} = 10^{-1}, \sigma_{\rm R} = 1$.

The remaining three parameters, the Lorentz factor of the slower (right) shell, $\Gamma_{\rm R}$, the relative Lorentz factor,

$$\Delta g := 1 - \frac{\Gamma_{\rm R}}{\Gamma_{\rm L}}, \tag{4.1}$$

($\Gamma_{\rm L}$ being the Lorentz factor of the faster/left shell) and the viewing angle θ can take any of the values shown in Table 4.1. We have considered three families of strongly magnetized models (**S**, **S1** and **S2**), which differ in the distribution of the magnetization of the interacting shells. Our reference strongly magnetized model family is the **S**, since in MA12 we found that these models have the maximum dynamical efficiency. This set of models is supplemented with two additional families of models: **S1**, which accounts for shells having the same (high) magnetization, and **S2**, with parameters complementary of the **S**-family, and having the peculiarity that the colliding shells do not develop a forward shock (instead they form a forward rarefaction; see MA12) if $\Delta g \lesssim 1.5$, so that they only emit because of the presence of a reverse shock. For clarity, when we refer to a particular model we label it by appending values of each of these parameters to the model letter. For instance, **S**-**G**10-**D**1.0-**T**3 is the strongly magnetized model with $\Gamma_{\rm R} = 10$ (**G**10), $\Delta g = 1.0$ (**D**1.0) and $\theta = 3°$ (**T**3). If we refer to a subset of models with one or two parameters fixed we use an abbreviated notation, where we skip any reference to the varying parameters in the family name. As an example of this abbreviated notation, in order to refer to all weakly magnetized models with $\Gamma_{\rm R} = 10$ and $\theta = 5°$ we use **W**-**G**10-**T**5, while all moderately magnetized models with $\Delta g = 1.5$ are **M**-**D**1.5. We perform a systematic variation of parameters in order to find the dependence of the radiative signature on each of them separately, as well as their combinations by fixing, e.g. the Doppler factor $\mathcal{D}$ (Eq. (2.59)) of the shocked fluid. We perform such a parametric scan for a typical source located at redshift $z = 0.5$.

[2]The chosen value for q is representative for blazars according to observational (Ghisellini et al. 1998; Kardashev 1962) and theoretically deduced values (Böttcher & Dermer 2002). It also agrees with the ones used in numerical simulations of blazars made by (Mimica 2004) and (Zacharias & Schlickeiser 2010).

Parameter	value
$\Gamma_{\rm R}$	10, 12, 17, 20, 22, 25, 50, 100
Δg	0.5, 0.7, 1.0, 1.5, 2.0
$\sigma_{\rm L}$	10^{-6}, 10^{-2}, 10^{-1}, 1
$\sigma_{\rm R}$	10^{-6}, 10^{-2}, 10^{-1}, 1
$\epsilon_{\rm B}$	10^{-3}
$\epsilon_{\rm e}$	10^{-1}
$\zeta_{\rm e}$	10^{-2}
$\Delta_{\rm acc}$	10
$a_{\rm acc}$	10^{6}
R	3×10^{16} cm
Δr	6×10^{13} cm
q	2.6
$\mathcal{L}$	5×10^{48} erg s^{-1}
$u_{\rm ext}$	5×10^{-4} erg cm^{-3}
$\nu_{\rm ext}$	10^{14} Hz
z	0.5
θ	1, 3, 5, 8, 10°

Table 4.1: *Parameters of the models. $\Gamma_{\rm R}$ is the Lorentz factor of the slow shell, Δg, $\sigma_{\rm L}$ and $\sigma_{\rm R}$ are the fast and slow shell magnetizations, $\zeta_{\rm e}$ and q are the fraction of electrons accelerated into power-law Lorentz factor (or energy) distribution and its corresponding power-law index[1], $\Delta_{\rm acc}$ and $a_{\rm acc}$ are the parameters controlling the shock acceleration efficiency (see Section 3.2 of MA12 for details), L, R and Δr are the jet luminosity, jet radius and the initial width of the shells, $u_{\rm ext}$ and $\nu_{\rm ext}$ are the energy density and the frequency of the external radiation fiel in the reference frame of the AGN (see Section 4.2 of MA12 for details), z is the redshift of the source and θ is the viewing angle. Note that $\Gamma_{\rm R}$, Δg, $\sigma_{\rm L}$, $\sigma_{\rm R}$ and θ can take any of the values indicated.*

4.3 Results

Here we present the main results of the parameter study, grouping them according to the families defined in §4.2.1, so that the results for the weakly, moderately and strongly magnetized shell collisions are given in §§4.3.1, 4.3.2 and 4.3.3, respectively. To characterize the difference between models we resort to compute their light curves, average spectra, and their spectral slope $\Gamma_{\rm ph}$ and photon flux $F_{\rm ph}$ (assuming a relation $F_{\nu_{\rm obs}} \propto \nu^{-\Gamma_{\rm ph}+1}$; see § 4.5.1) in the band where the observed photon energy is above 200 MeV. In the rest of the text we will refer to this band as γ-ray band.

4.3.1 Weakly magnetized models

In Figure 4.1 we show the light curves at optical (R-band), X-ray (1–10 keV) and γ-ray (1 GeV) energies for two different values of the relative shell Lorentz factor, i.e., for two values of the parameter Δg while keeping the rest fixed. The duration of the light curve depends moderately on Δg, as can be seen from the difference in peak times for optical and γ-ray light curves. The time of the peak of the light curve in each band depends on the dominant emission process in that band: synchrotron and EIC dominate the R-band and the 1 GeV emission and peak soon after the shocks cross the shells. The SSC emission dominates the X-rays (dashed lines in Figure 4.1), and its peak is related to the physical length of the emission regions. The X-ray peak occurs later due to the fact that synchrotron photons from one shocked shell have to propagate across a substantial part of the shell volume before being scattered by the electrons in the other shell (see § 6.2 of MA12 for more details). The corresponding average flare spectra are shown in the left panel of Figure 4.2, where we also display (inset) $\Gamma_{\rm ph}$ as a function of the photon flux $F_{\rm ph}$ in the γ-ray band.

As can be seen from Figure 4.2, the parameter Δg has a very strong influence on both peak frequencies and peak fluxes (see also §5.8 of Böttcher & Dermer 2010). In particular, the synchrotron peak shifts steadily to ever higher frequencies (from $\simeq 10^{12}$ Hz for $\Delta g = 0.5$ to $\simeq 10^{15}$ Hz for $\Delta g = 2.0$), with a similar trend for the IC peak. $F_{\rm ph}$ has a maximum for $\Delta g = 0.7$, and then it decreases monotonically. The reason for this non monotonic behavior is that in the model with the smallest Δg, **W**-**G**10-**D**0.5-**T**5, the SSC and EIC components (black dot-dashed and dot-dot-dashed lines in the left panel of Figure 4.2, respectively) are of equal importance in the γ-ray band, but increasing Δg leads to the domination of the spectrum by SSC (e.g., orange dot-dashed and dot-dot-dashed lines in Figure 4.2 show the SSC and EIC components of **W**-**G**10-**D**2.0-**T**5, respectively). For the parameters and observational frequencies of blazars, the Klein-Nishina cutoff affects the EIC, but does not affect the SSC peak (see § 4.2 of MA12 or § 3.1 of Aloy & Mimica (2008)). Therefore, the SSC peak can increase with Δg, while the EIC peak cannot. In the model **W**-**G**10-**D**2.0-**T**5 the SSC peak enters the γ-ray band, thus causing the flattening of the spectrum. Finally, the appearance of a non-smooth IC hump in the spectrum happens when Δg is low (see the case of $\Delta g = 0.5$ in Figure 4.2). This result suggests that flares with a smooth IC spectrum in weakly magnetized blazars are likely produced by shells whose $\Delta g \gtrsim 0.5$

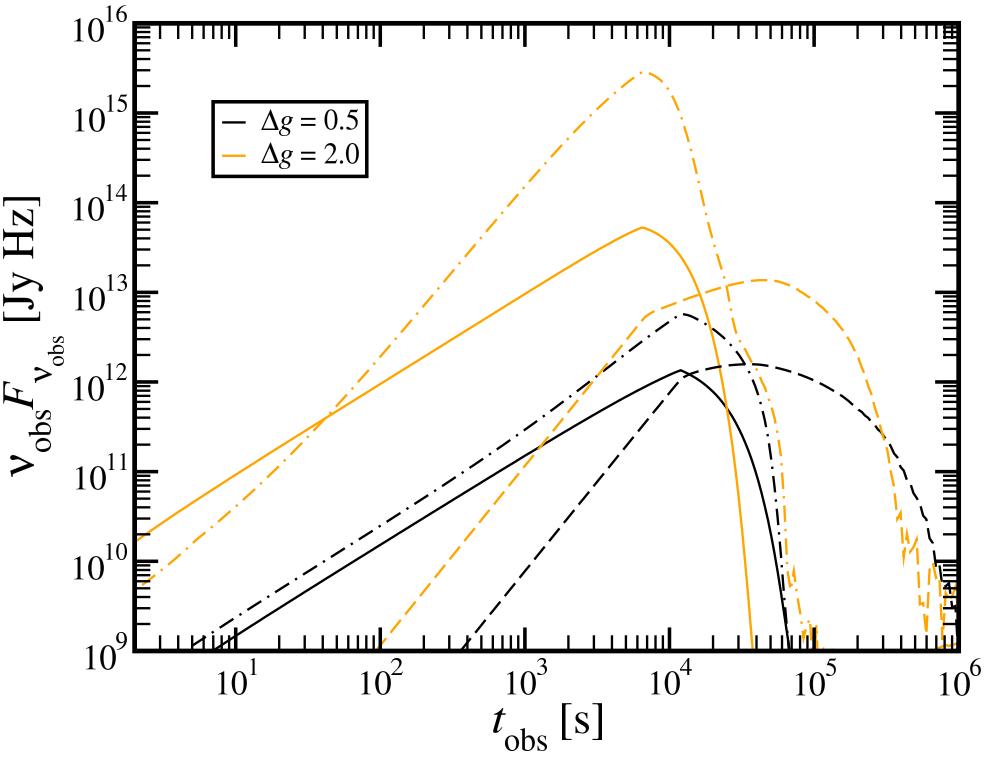

Figure 4.1: *Light curves for the weakly magnetized models **W**-**G**10-**D**0.5-**T**5 (black lines) and **W**-**G**10-**D**2.0-**T**5 (orange lines). The light curves in R-band, hard X-ray band (*1–10 keV*) and at* 1 GeV *are shown as full, dashed and dot-dashed lines, respectively. The time of the peaks of the R-band and* 1 GeV *light curves correspond to the moment the shocks cross the respective shells (first the RS, and then the FS). A steep decline after the peak is partly due to the assumed cylindrical geometry, since in a conical jet the high-latitude emission would smooth out the decline.*

(i.e., relative Lorentz factor is larger than $\simeq 1.1$).

Table 4.2 lists a number of physical parameters in the shocked regions of the models shown in the left panel of Figure 4.2. As can be seen, the increase in Δg has as a consequence a moderate increase in the compression ratio and the magnetic field in the shocked regions, as well as an increase in the number of injected electrons in the both shocks (FS and RS).

The nonthermal electrons in weakly magnetized models are in a slow-cooling regime, as inferred from the fact that $\gamma_c/\gamma_{\rm min} \gtrsim 1$. The typical magnetic field is of the order of 1 G and is of the same order of magnitude, though slightly larger in the

Δg	Γ	r_r	$\frac{B'_r}{\mathrm{G}}$	$\frac{Q_{r,11}}{\mathrm{cm^{-3}\,s^{-1}}}$	$\frac{\gamma_{\mathrm{min}r}}{10^2}$	$\frac{\gamma_{\mathrm{max}r}}{10^4}$	$\frac{t'_{crr}}{10^3\,\mathrm{s}}$	$\frac{\gamma_{cr}}{\gamma_{\mathrm{min}r}}$	r_f	$\frac{B'_f}{\mathrm{G}}$	$\frac{Q_{f,11}}{\mathrm{cm^{-3}\,s^{-1}}}$	$\frac{\gamma_{\mathrm{min}f}}{10^2}$	$\frac{\gamma_{\mathrm{max}f}}{10^4}$	$\frac{t'_{crf}}{10^3\,\mathrm{s}}$	$\frac{\gamma_{cf}}{\gamma_{\mathrm{min}f}}$
0.5	11.8	4.10	0.95	0.06	2.90	4.77	91.2	23.77	4.01	0.95	0.02	1.28	4.78	91.3	54.21
0.7	12.2	4.21	1.17	0.22	5.60	4.31	74.9	10.53	4.05	1.16	0.07	1.91	4.33	75.0	31.38
1.0	12.6	4.42	1.40	0.76	11.19	3.93	63.0	4.50	4.09	1.38	0.17	2.71	3.97	63.1	19.17
1.5	13.1	4.86	1.66	2.71	24.45	3.61	54.2	1.75	4.13	1.60	0.37	3.68	3.68	54.3	12.40
2.0	13.4	5.37	1.84	6.08	42.66	3.43	50.1	0.90	4.16	1.74	0.55	4.32	3.53	50.2	9.86

Table 4.2: *Physical parameters in the forward and reverse shocked regions for the family of models **W**-**G**10-**T**5, in which the Lorentz factor of the slower shell as well as the viewing angle are fixed to* $\Gamma_{\mathrm{R}} = 10$ *and* $\theta = 5°$*, respectively. Subscripts* r *and* f *denote the reverse and forward regions, respectively. The bulk Lorentz factor of both shocked regions is denoted by* Γ*. In each region* r*,* B'*,* Q*,* γ_{min} *and* γ_{max} *denote its compression ratio, comoving magnetic field, comoving number of electrons injected per unit volume and unit time, and lower and upper cutoffs of the injected electrons (see equation (11) of MA12). In the table we show* $Q_{r,11} = Q_r \times 10^{-11}$ *and* $Q_{f,11} = Q_f \times 10^{-11}$*.* $t'_{cr} := \Delta r'/(c|\beta'|)$ *is the shock crossing time, where* $\Delta r'$ *and* β' *are the shell width and the shock velocity in the frame moving with the contact discontinuity separating both shocks (section 2 of MA12 or §2.3.1.3).* $\gamma_c := \gamma_{\mathrm{max}}/(1 + \nu_0 \gamma_{\mathrm{max}} t'_{cr})$ *is the cooling Lorentz factor of an electron after a dynamical time scale (§2.4.3). In our case the dynamical time scale corresponds to the shock crossing time.* $\nu_0 = (4/3)c\sigma_{\mathrm{T}}(u'_{\mathrm{B}} + u'_{\mathrm{ext}})/(m_{\mathrm{e}}c^2)$ *is the cooling term and the primed quantities are measured in the comoving frame. When* $\gamma_c/\gamma_{\mathrm{min}} \gg (\ll) 1$ *the electrons are slow (fast) cooling.*

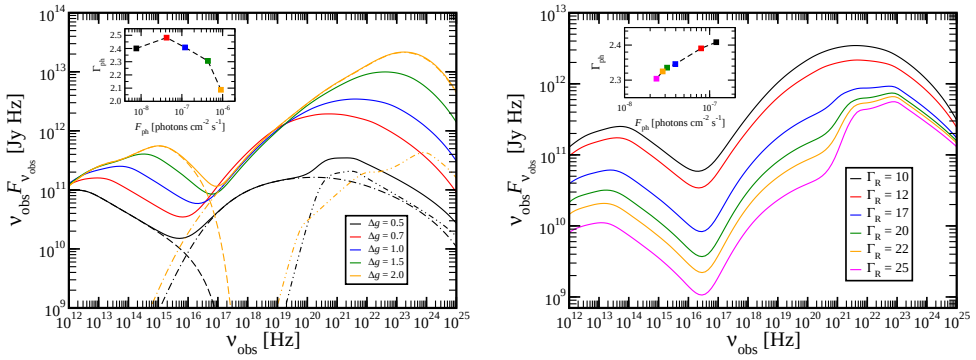

Figure 4.2: *Left panel: average spectra for weakly magnetized models* ***W-G10-T5*** *(i.e., with fixed* $\Gamma_R = 10$ *and* $\theta = 5$*). The spectrum of each model has been averaged over the time interval* $0 - 1000$ *ks. In addition, for the models* ***W-G10-D0.5-T5*** *and* ***W-G10-D2.0-T5*** *we show the synchrotron, SSC and EIC contributions (dashed, dot-dashed and dot-dot-dashed lines, respectively). The blue line shows the spectrum of the model* $(\sigma_L, \sigma_R) = (10^{-6}, 10^{-6})$ *of MA12. The inset shows the spectral slope* Γ_{ph} *as a function of the photon flux* F_{ph} *in the* γ*-ray band. We use the same band and the spectral slope definition as in Abdo et al. (2009). Right panel: same as left panel, but for the models* ***W-D1.0-T5****.*

reverse than in the forward shocked region. The difference becomes larger for higher Δg (see §4.3.3 for a more detailed discussion of this point).

Next we consider the case in which Γ_R is increased, and repeat the previous experiments, but fixing $\Delta g = 1$, i.e., we consider the series of models **W-D**1.0-**T**5 (right panel of Figure 4.2). We note that increasing the Lorentz factor of the slower shell yields a reduced flare luminosity. This behavior results because, for the fixed viewing angle ($\theta = 5°$) and Δg, increasing the Lorentz factor of the slower shell implies that both shells move faster, and the resulting shocked regions are Doppler dimmed (for an illustration of the case when both Γ_R and Δg are varied see Figure 6 of Joshi & Böttcher 2011). However, the most remarkable effect is that for values $\Gamma_R \gtrsim 17$, we note a qualitative change in the IC part of the spectrum. The EIC begins to dominate in γ-rays. Since, as discussed above, the peak of the EIC spectrum is shaped by the Klein-Nishina cut-off, for frequencies $\gtrsim 10^{23}$ Hz there is no dependence on Γ_R. However, since the synchrotron peak flux decreases with increasing Γ_R, this means that the IC-to-synchrotron ratio of peak fluxes increases with Γ_R. The weak dependence of the γ-ray spectrum on Γ_R can also be seen in the inset of the right panel of Figure 4.2, where the points for $\Gamma_R \gtrsim 17$ accumulate around $\Gamma_{ph} \lesssim 2.35$ and

$F_{\rm ph} \simeq 3 \times 10^{-8}\,{\rm cm}^{-2}\,{\rm s}^{-1}$.

4.3.2 Moderately magnetized models

The second family of models contains cases of intermediate magnetization $\sigma_{\rm L} = \sigma_{\rm R} = 10^{-2}$. The left panel of Figure 4.3 shows the effect of the variation of Δg on the average spectra for the models **M-G**10-**T**5. The blue line corresponds to the moderately magnetized model in MA12. It can be seen that for $\Delta g \gtrsim 1$, a flattening of the spectrum below the synchrotron peak starts to become noticeable. This effect becomes even more pronounced for the strongly magnetized models (see next section). Low values of Δg tend to reduce much more the IC spectral components than the synchrotron ones. This trend is also noticeable in weakly and strongly magnetized models. Thus, regardless of the magnetization, very small values of Δg may not be compatible with observations. In the γ-ray band, an increase in Δg causes an increase in $F_{\rm ph}$ and a variation in $\Gamma_{\rm ph}$ characterized by a maximum, where $\Gamma_{\rm ph} \simeq 2.9$, for $\Delta g = 1$.

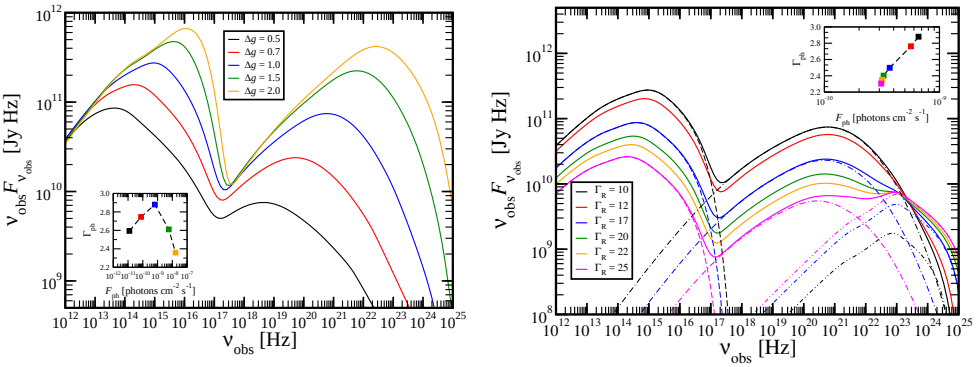

Figure 4.3: *Left panel: same as left panel of Figure 4.2, but for the moderately magnetized models* ***M-G****10-****T****5, i.e.,* $\sigma_{\rm L} = 10^{-2}$ *and* $\sigma_{\rm R} = 10^{-2}$*. Right panel: same as right panel of Figure 4.3, but for variable* $\Gamma_{\rm R}$ *while keeping fixed* $\Delta g = 1$ *and* $\theta = 5^o$ *(models* ***M-D****1.0-****T****5). For models* ***M-G****10-****D****1.0-****T****5 and* ***M-G****25-****D****1.0-****T****5 (i.e., models with* $\Gamma_{\rm R} = 10, 25$*) dashed, dot-dashed and dot-dot-dashed lines show the synchrotron, SSC and EIC contributions, respectively.*

Table 4.3 shows the microphysical parameters of the shocked regions in these models. As Δg grows, the magnetic field and the number of injected particles increase at the region swept by the forward shock, while the electrons transition from

a *moderate* or *intermediate*-cooling regime to fast-cooling one. A noticeable difference with respect to the weakly magnetized models is that now the comoving magnetic field in the region swept by the reverse shock decreases as Γ_L increases with increasing Δg (or, equivalently, Γ). This is a consequence of keeping the jet luminosity and the shell magnetization constant while increasing the Lorentz factor of the faster shell.

Let us consider now the spectral variations induced by a changing $\Gamma_{\rm R}$ and fixed Δg (right panel of Figure 4.3). In contrast to what has been seen in weakly magnetized models (§4.3.1; Figure 4.2), for $\Gamma_{\rm R} \gtrsim 20$, the two IC contributions are comparable (for smaller values of $\Gamma_{\rm R}$ the SSC component dominates the IC spectrum). For $\Gamma_{\rm R} = 10$ the maximum of the EIC emission is 100 times smaller than the corresponding SSC maximum, while for $\Gamma_{\rm R} = 25$ the EIC peak is higher than the SSC peak, and indeed it is expected to keep growing as the bulk Lorentz factor goes further into the ultrarelativistic regime. Similar to the right panel of Figure 4.2, the Klein-Nishina cut-off causes the coincidence of EIC spectra at $\simeq 10^{23}$ Hz. This effect is also seen in the $F_{\rm ph}$-$\Gamma_{\rm ph}$ plot, where for $\Gamma_{\rm R} \gtrsim 17$ the photon flux is approximately constant[3], with a slight decrease in $\Gamma_{\rm ph}$ as $\Gamma_{\rm R}$ grows.

Shell magnetization, Δg and $\Gamma_{\rm R}$ are related to the intrinsic properties of the emitting regions. It is also interesting to explore the effects on the SED of varying extrinsic properties of the models, such as the viewing angle θ, while keeping the intrinsic ones constant. Figure 4.4 shows the result of changing the jet orientation. With increasing θ both the synchrotron and IC maxima decrease. As it can be noticed looking at the brown lines, the maxima drop almost in a straight line with positive slope. To illustrate this fact, we show the spectrum normalized to the Doppler factor $\mathcal{D}^3$ in the left panel of Figure 4.5.[4] As can be seen, the synchrotron spectra coincide for all models (assuming the frequency is normalized by $\mathcal{D}$), while the IC spectral fluxes decrease with increasing θ. For comparison, in the right panel of Figure 4.5 we normalize the spectra by $\mathcal{D}^4$. In this case the IC spectra below the peak (cooling break) coincide, while the synchrotron part gets less luminous with decreasing angle. Thus, we find a remarkable agreement among the normalized spectra obtained from

[3]We point out that differences smaller than $\lesssim 0.1$ in $\Gamma_{\rm ph}$ are probably not distinguishable from an observational point of view.

[4]We note that the normalization in e.g. left panel of Figure 4.5 is equivalent to the $\mathcal{D}^{3+\alpha}$ of Dermer (1995) if we take into account that we do not only normalize the SED by the Doppler factor but also the frequencies.

Δg	Γ	r_r	$\frac{B'_r}{\mathrm{G}}$	$\frac{Q_{r,11}}{\mathrm{cm^{-3}\ s^{-1}}}$	$\frac{\gamma_{\mathrm{min}\,r}}{10^2}$	$\frac{\gamma_{\mathrm{max}\,r}}{10^4}$	$\frac{t'_{crr}}{10^3\ \mathrm{s}}$	$\frac{\gamma_{cr}}{\gamma_{\mathrm{min}\,r}}$	r_f	$\frac{B'_f}{\mathrm{G}}$	$\frac{Q_{f,11}}{\mathrm{cm^{-3}\ s^{-1}}}$	$\frac{\gamma_{\mathrm{min}\,f}}{10^2}$	$\frac{\gamma_{\mathrm{max}\,f}}{10^4}$	$\frac{t'_{crf}}{10^3\ \mathrm{s}}$	$\frac{\gamma_{cf}}{\gamma_{\mathrm{min}\,f}}$
0.5	11.7	3.17	19.07	1.20	2.88	1.07	79.3	0.09	2.55	23.09	0.32	0.91	0.97	77.8	0.20
0.7	12.1	3.55	18.88	4.05	6.03	1.07	68.2	0.05	2.80	25.35	0.93	1.47	0.92	66.9	0.12
1.0	12.5	3.97	17.94	13.14	13.15	1.10	59.1	0.03	3.02	27.36	2.32	2.24	0.89	58.1	0.08
1.5	13.0	4.55	16.44	48.22	32.57	1.15	51.9	0.02	3.22	29.09	5.14	3.23	0.86	51.1	0.06
2.0	13.3	5.12	15.41	155.20	64.93	1.19	48.4	0.01	3.31	29.98	7.75	3.90	0.85	47.7	0.05

Table 4.3: *Same as Table 4.2, but for models **M-G10-T5**.*

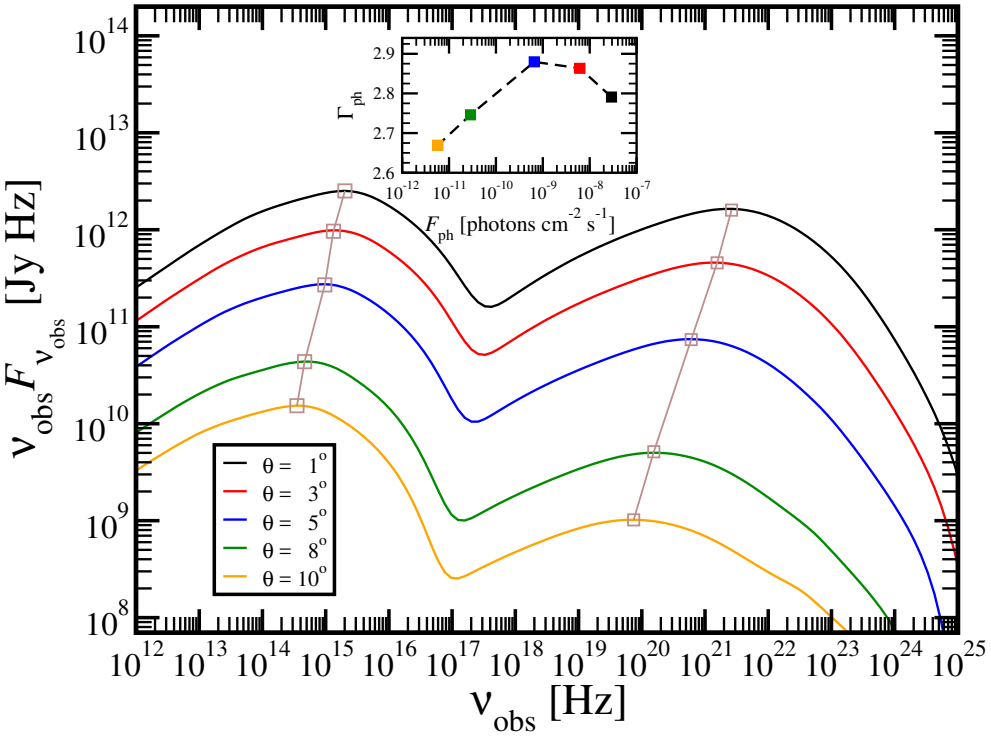

Figure 4.4: *Same as Figure 4.3, but for variable θ. $\Gamma_R = 10$ and $\Delta g = 1.0$ have been fixed, i.e., models **M**-**G**10-**D**1.0 are shown. For easier visualization the synchrotron and IC spectral maxima of different models have been marked by boxes and connected by brown lines.*

the same source but with different viewing angles, if we scale all the spectra by $\mathcal{D}^3$.

4.3.3 Strongly magnetized models

The third model family considers the strongly magnetized models where $\sigma_L = 1$ and $\sigma_R = 0.1$. The left panel of Figure 4.6 shows the dependence of the average spectra on Δg. Strongly magnetized models in moderately relativistic flows (i.e., having moderate values of Γ_R) dramatically suppress the IC spectral component. However, with increasing values of Δg the IC component broadens in frequency range and grows moderately. Another remarkable fact of strongly magnetized models is that for $\Delta g > 1.0$ the synchrotron spectrum ceases to be a parabolic, single-peaked curve and becomes a more complex curve where the contributions from the FS and the RS are separated, since the peak frequencies of the synchrotron radiation produced

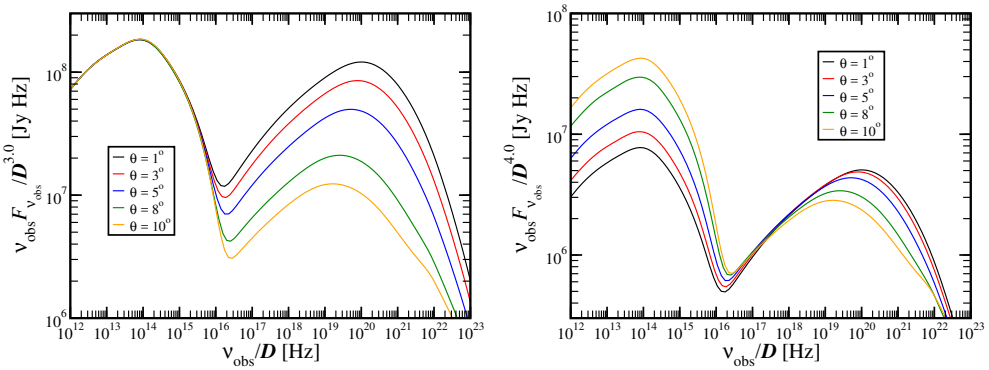

Figure 4.5: *Left panel: same as left panel of Figure 4.4, but dividing the frequencies by $\mathcal{D}$ and the SED by $\mathcal{D}^3$. Right panel: same as right panel of Figure 4.4, but normalizing the SED by $\mathcal{D}^4$.*

at the FS and at the RS differ by two or three orders of magnitude. The reason is the strong magnetic field in the emitting regions: magnetization in the shocked regions increases proportionally to their compression factors r_f and r_r, respectively (see Eq. (2.46) in §2.3.1.2), i.e. the shocked regions are even more magnetically dominated than the initial shells. In Table 4.4 we see that the electrons in the reverse shock of the strongly magnetized models are fast-cooling. In fact, for $\Delta g \gtrsim 1.5$ the injected electron spectrum is almost mono-energetic. In these models the lower cutoff $\gamma_{\min r}$ is about a factor of 30 larger than $\gamma_{\min f}$. Since the synchrotron maximum of the fast-cooling electrons is determined by the lower cutoff, the synchrotron spectrum of the RS peaks at a frequency which is $(\gamma_{\min f}/\gamma_{\min r})^2 \approx 10^3$ times higher than that of the FS. This can be seen in left panel of Figure 4.6, where dashed and dot-dashed lines show the respective spectra of the RS and FS of the model **S**-**G**10-**D**2.0-**T**5. The dominance of the EIC component for $\Gamma_{\rm R} \gtrsim 20$ and $\nu \gtrsim 10^{21}$ Hz appears to be a property tightly related to the increment of $\Gamma_{\rm R}$ (right panel of Figure 4.6). In this case, the EIC component "replicates" the synchrotron peak associated to the forward shock of the collision, modulated by the Klein-Nishina cut-off for large values of $\Gamma_{\rm R}$. Because of this effect, progressively larger values of $\Gamma_{\rm R}$ increase the Compton dominance, i.e. the trend is to recover the *standard* double-hump structure of the SED as $\Gamma_{\rm R}$ rises. We have tested that for $\Gamma_{\rm R} = 50$ and 100,the IC spectral component becomes almost monotonic and concave (Figure 4.7). For $\Gamma_{\rm R} \gtrsim 50$, the SED becomes akin to that of models with moderate or low shell magnetization, but the IC spectrum displays

Δg	Γ	r_r	$\frac{B'_r}{\mathrm{G}}$	$\frac{Q_{r,11}}{\mathrm{cm^{-3}\ s^{-1}}}$	$\frac{\gamma_{\mathrm{min}\,r}}{10^2}$	$\frac{\gamma_{\mathrm{max}\,r}}{10^4}$	$\frac{t'_{crr}}{10^3\mathrm{s}}$	$\frac{\gamma_{cr}}{\gamma_{\mathrm{min}\,r}}$	r_f	$\frac{B'_f}{\mathrm{G}}$	$\frac{Q_{f,11}}{\mathrm{cm^{-3}\ s^{-1}}}$	$\frac{\gamma_{\mathrm{min}\,f}}{10^2}$	$\frac{\gamma_{\mathrm{max}\,f}}{10^4}$	$\frac{t'_{crf}}{10^3\mathrm{s}}$	$\frac{\gamma_{cf}}{\gamma_{\mathrm{min}\,f}}$
0.5	12.7	1.26	53.51	0.11	0.66	0.64	34.6	0.12	1.89	51.57	3.30	1.91	0.65	37.5	0.04
0.7	12.8	1.46	54.72	1.03	2.29	0.63	34.1	0.03	1.93	52.68	4.20	2.14	0.64	36.7	0.04
1.0	13.0	1.75	55.84	7.33	7.25	0.62	33.6	0.01	1.98	53.90	5.45	2.41	0.63	35.8	0.03
1.5	13.2	2.22	56.63	68.00	26.38	0.62	32.9	0.003	2.02	55.22	7.14	2.73	0.63	34.8	0.03
2.0	13.3	2.67	56.82	112900.75	61.68	0.62	32.5	0.001	2.05	56.03	8.39	2.94	0.62	34.3	0.02

Table 4.4: *Same as Table 4.2, but for models **S**-**G**10-**T**5. Note that the $Q_{r,11}$ for $\Delta g = 2.0$ is much larger than $Q_{r,11}$ of the other models because $\gamma_{\mathrm{min}\,r}$ is very close to $\gamma_{\mathrm{max}\,r}$.*

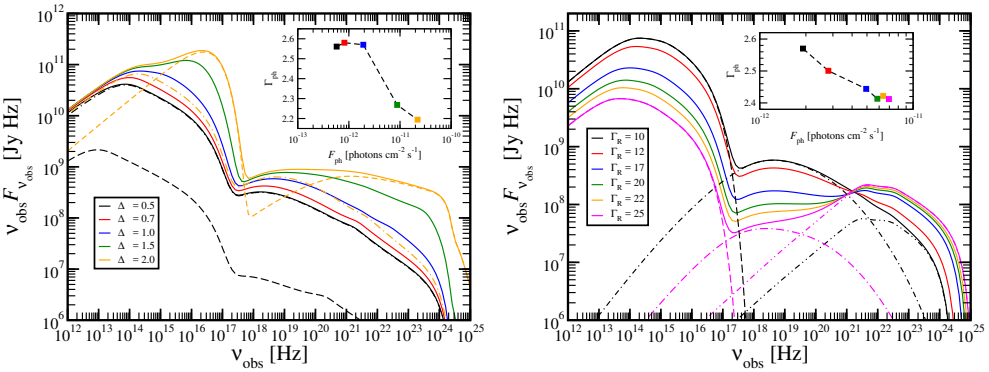

Figure 4.6: *Left panel: same as left panel of Figure 4.2, but for the strongly magnetized models* ***S*-*G*10-*T*5***, i.e.,* $\sigma_{\rm L} = 1$ *and* $\sigma_{\rm R} = 0.1$*. For the cases* $\Delta g = 0.5, 2.0$ *we show the reverse and forward shock contributions to their spectra in dashed and dot-dashed lines, respectively. While at small values of* Δg *the contribution of the RS dominates fully the spectrum, at larger values of* Δg *the FS contribution has increased relative to the RS one, and is an order of magnitude stronger than the former one in the case of the model with* $\Delta g = 0.5$*. This also explains a second (higher) peak in the synchrotron domain, as well as a flattening in the* γ*-ray band. Right panel: same as right panel of Figure 4.3, but for strongly magnetized models* ***S*-*D*1.0-*T*5***.

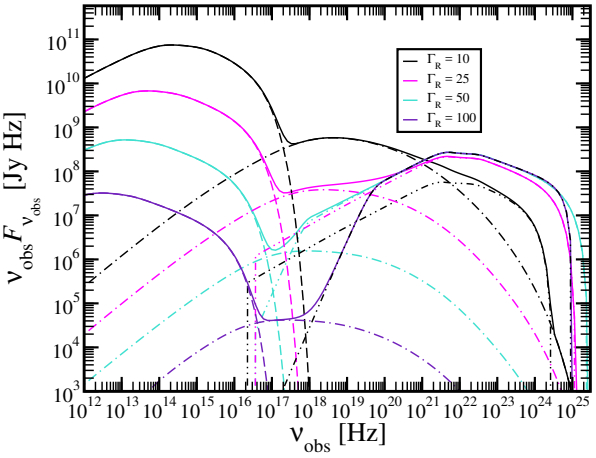

Figure 4.7: *Same as Figure 4.6, but for high* $\Gamma_{\rm R}$ *cases. For each model the synchrotron, SSC and EIC contributions are shown using dashed, dot-dashed and dot-dot-dashed lines, respectively.*

a plateau rather than a maximum. As the Lorentz factor increases ($\Gamma_{\rm R} \gtrsim 50$), our models form a flat spectrum in the soft X-ray band rather than a minimum between two concave regions. We note that the spectrum of the $\Gamma_{\rm R} = 100$ model displays very steep rising spectrum flanking the IC contribution because we have fixed a value of the microphysical parameter $a_{\rm acc} = 10^6$. Smaller values of such parameter tend to broaden significantly both the IC and the synchrotron peak (Böttcher & Dermer

2010, see e.g.,). Hence, we foresee that a suitable combination of microphysical and kinematical parameters would recover a more "standard" double-hump structure.

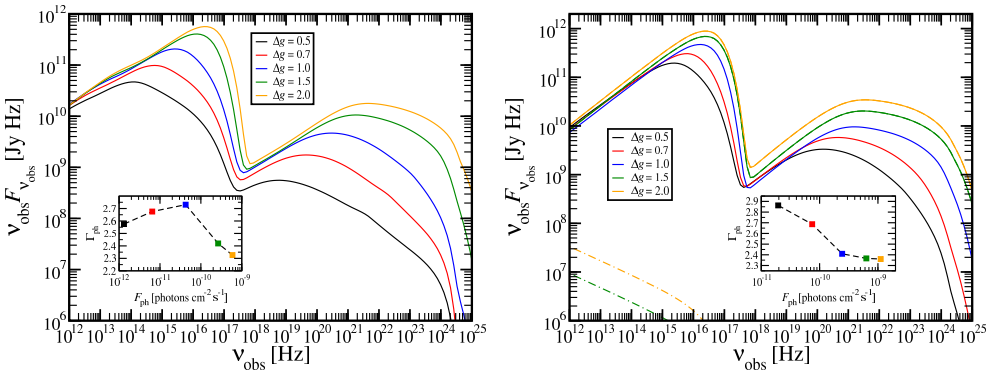

Figure 4.8: *Left: Same as the left panel of Figure 4.6 for the family **S1**-**G**10-**T**5. Right: Same as the left panel of Figure 4.6 for the family **S2**-**G**10-**T**5. In the **S2**-family, the forward shock is either non-existing (for $\Delta g \lesssim 1.5$) or extremely weak. We add in the figure the contribution to the spectrum of the forward shocks of the models with $\Delta g = 1.5, 2$. Note the difference in the stencil of the vertical axis with respect to the left panel.*

We also find that the SED of strongly magnetized models is very sensitive to relatively small variations of magnetization between colliding shells. To show such a variety of phenomenologies, we display in Figure 4.8 the SEDs of the families **S1**-**G**10-**T**5 (left panel) and **S2**-**G**10-**T**5, right panel, i.e., considering only the variations in the SED induced by a change in Δg. The three families of strongly magnetized models only have differences in magnetization within a factor 10. Clearly, when the faster shell is less magnetized than the slower one (the case of the **S2**-family), the models recover a more typical double-hump structure, closer to that found in actual observations. We note that for contribution to the SED of the forward shock in the **S2**-family is either non-existing, because these models do not form a FS or, if a FS forms, it is very weak (see dashed lines in the right panel of Figure 4.8).

For completeness, we consider how the SED changes when varying the viewing angle (Figure 4.9). In these models, increasing θ lowers the total emitted flux all over the spectral range under consideration. The Compton dominance for $\theta \lesssim 8°$ remains constant. To explain this behavior, we shall note that fixing both Γ_R and Δg, increasing θ is equivalent to decrease the Doppler factor $\mathcal{D}$. Theoretically, it is known that the beaming pattern of a relativistically moving blob of electrons that Thompson-scatters photons from an external isotropic radiation field changes as $\mathcal{D}^{4+\alpha}$ (α being

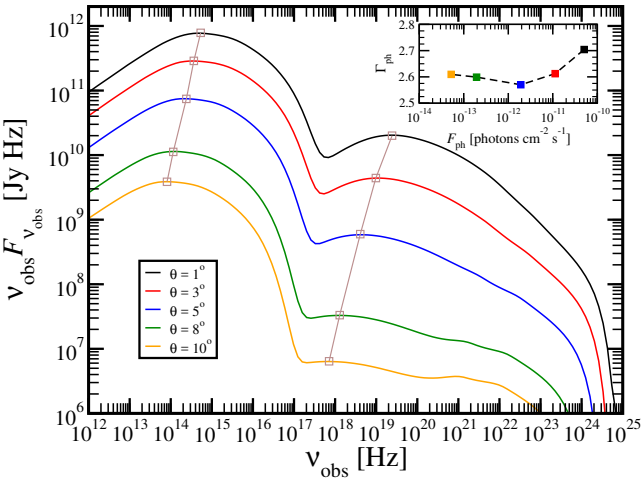

Figure 4.9: *Same as Figure 4.4, but for strongly magnetized models* ***S*-*G*10-*D*1.0***.*

the spectral index of the radiation), while the beaming pattern of radiation emitted isotropically in the blob frame (e.g., by synchrotron and SSC processes), changes as $\mathcal{D}^{3+\alpha}$ (Dermer 1995). Left and right panels in Figure 4.10 show the spectra from Figure 4.9 normalized to $\mathcal{D}^3$ and $\mathcal{D}^4$, respectively. Thus, we expect that the reduction of the Doppler factor results in a larger suppression of the IC part of the SED, only if it is dominated by the EIC contribution, as compared with the dimming of the synchrotron component. In the models at hand (**S**-**G**10-**D**1.0), the IC spectrum is dominated by the SSC component, and thus, reducing θ simply decreases the overall luminosity.

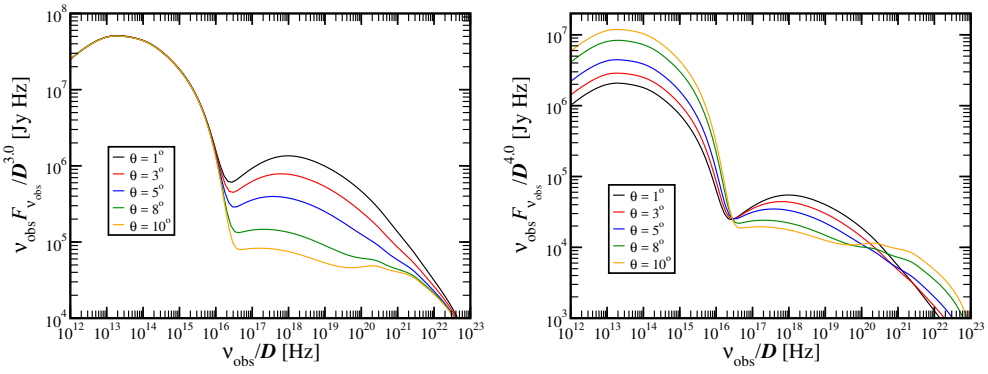

Figure 4.10: *Left panel: same as Figure 4.9, but normalizing the SED by $\mathcal{D}^3$. Right panel: same as Figure 4.4, but normalizing the SED by $\mathcal{D}^4$.*

4.4 Discussion and conclusions

We have extended the survey of parameters started in MA12 for the internal shocks scenario by computing the multi-wavelength, time-dependent emission for several model families chiefly characterized by the magnetization of the colliding shells. In this section we provide a discussion and a summary of our results.

4.4.1 Intrinsic parameters and emission

In what follows, we consider the effect that changes in intrinsic jet parameters (magnetization, Δg and $\Gamma_{\rm R}$) have on the observed emission.

4.4.1.1 Influence of the magnetic field

As was discussed in § 6.1 of MA12, the main signature of high magnetization is a drastic decrease of the SSC emission due to a much smaller number density of scattering electrons (Eq. (2.41)). As will be stated in §4.4.1.3, this decrease can be offset by increasing the bulk Lorentz factor (at a cost of decreasing the overall luminosity). However, extremely relativistic models (from a kinematical point of view), tend to form plateaus rather than clear maxima in the synchrotron and IC regimes, and display relatively small values of $\Gamma_{\rm ph}$. Indeed, the photon spectral index manifest itself as a good indicator of the flow magnetization. Values of $\Gamma_{\rm ph} \gtrsim 2.6$ result in models where the flow magnetization is $\sigma \simeq 10^{-2}$, while either strongly or weakly magnetized shell collisions yield $\Gamma_{\rm ph} \lesssim 2.5$. The observed degeneracy we have found in the case of strongly magnetized and very high Lorentz factor shells is a consequence of the fact that either raising the magnetization or the bulk Lorentz factor, the emitting plasma enters in the ultrarelativistic regime. Which of the two parameters determines most the final SED, depends on the precise magnitudes of σ and Γ.

Another way to correlate magnetization with observed properties can be found representing the Compton dominance A_C as a function of the ratio of IC-to-synchrotron peak frequencies $\nu_{\rm IC}^{\rm obs}/\nu_{\rm syn}^{\rm obs}$ (see §4.5.2). Models with intermediate or low magnetization occupate a range of A_C roughly compatible with observations, while the strongly magnetized models tend to have values of A_C hardly compatible with those

observed in actual sources, unless collisions in blazars happen at much larger Lorentz factors than currently inferred (see §4.4.3).

4.4.1.2 Influence of Δg

Δg is a parameter which indicates the magnitude of the velocity variations in the jet. From the average spectra shown in the left panels of Figures 4.2, 4.3 and 4.6 we see that the increase of Δg leads to the increase of the Compton dominance parameter (see also Figure 4.11), the effect being more important for either weakly or moderately magnetized models than for strongly magnetized ones (for which the Compton dominance is almost independent of Δg, or even A_C decreases for large values of that parameter). Furthermore, the total amount of emitted radiation also increases with increasing Δg, as is expected from the dynamic efficiency study (Mimica & Aloy 2010), and confirmed by the radiative efficiency study of MA12. Finally, for low values of Δg the EIC emission is either dominant or comparable to the SSC one, while SSC becomes dominant at higher Δg.

Looking at the physical parameters in the emitting regions (Tables 4.2–4.4), we see that the increase in Δg leads to the increase in the compression factor r_f and r_r of the FS and RS. The effect is strongest for the weakly magnetized models. This increase has as a consequence the increase in the number density of electrons injected at both, the FS and the RS. A similar argument can be made for the magnetic fields in the emitting regions, since the magnetic field undergoes the shock compression as well (see §2.3.1.2).

In the insets of left panels of Figures 4.2, 4.3 and 4.6 we see that in γ-rays the increase of Δg generally reflects in the increase of the photon flux and a decrease of the spectral slope $\Gamma_{\rm ph}$. Because of the sensitivity of the photon spectral index in the $\gamma-$ray band, we foresee that the change in $\Gamma_{\rm ph}$ can be a powerful observational proxy for the actual values of Δg and a distinctive feature of magnetized flows. Comparing equivalent weakly (Figure 4.2; left) and moderately magnetized models (Figure 4.3; left), we observe that the maximum $\Gamma_{\rm ph}$ as a function of Δg increases by $\sim 15\%$ due to the increase in magnetization, and the value of Δg for which the maximum $\Gamma_{\rm ph}$ occurs also grows, at the same time that $F_{\rm ph}$ decreases by a factor of 50.

We have also found that sufficiently large values of Δg tend to produce a double-peaked structure in the synchrotron dominated part of the SED. When the relative

difference of Lorentz factors grows above ~ 1.5, the contributions arising from the FS and the RS shocks peak at different times, the RS contribution lagging behind the FS contribution and being more intense, and occurring at larger frequencies than the latter. The reason for this phenomenology can be found looking at Table 4.4 and noting that γ_{min_r} becomes very large and comparable to γ_{max_r} for $\Delta g \gtrsim 1.5$. For these models $\gamma_{\mathrm{min}_r} \gg \gamma_{\mathrm{min}_f}$ and the frequency of the RS spectral peak is almost 10^3 times larger than the frequency of the FS spectral peak. The effect is the flattening of the synchrotron spectrum, or even an appearance of a second peak. This trend is even more clear when the magnetization of the shells is increased, so that the most obvious peak in the UV domain happens for strongly magnetized models (compare the left panels of Figures 4.2, 4.3 and 4.6). The observational consequences of the appearance of this peak are discussed below (§4.4.3).

4.4.1.3 Influence of Γ_{R}

Γ_{R} is the parameter which determines the bulk Lorentz factor of the jet flow, to a large extent. From Eq. (2.41) we see that the increase in Γ_{R} leads to a decrease of the number density in the shells, a trend which is seen in the right panels of Figures 4.2, 4.3 and 4.6, since it reduces the emitted flux. Another effect is the decrease in dominance of SSC over EIC as Γ_{R} increases. A related feature is the flattening of the γ-ray spectrum (see figure insets). A consequence of the increasing importance of the EIC is the shifting of the IC spectral maximum to higher frequencies, until the Klein-Nishina limit is reached. For moderately magnetized models (right panel of Figure 4.3) the IC maximum becomes independent of Γ_{R}.

The IC emission in the strongly magnetized models (right panel of Figure 4.6) is dominated by SSC for low values of Γ_{R}. However, as Γ_{R} is increased, the higher-frequency EIC component becomes ever more luminous. While none of the models in Figure 4.6 reproduces the prototype double-peaked structure of blazar spectra, the increase of the EIC component with Γ_{R} indicates that perhaps larger values of Γ_{R} might produce a blazar-like spectrum. We have shown in Figure 4.7 that the average spectra for strongly magnetized models where Γ_{R} is allowed to grow up to 100 display again a double-peaked spectrum, albeit with a much lower luminosity than the models with lower bulk Lorentz factors.

4.4.1.4 External radiation field

In this work we did not consider the sources of external radiation in such a detail as was recently done by e.g. Ghisellini & Tavecchio (2009). These authors show that, for a more realistic modeling of the external radiation field, the IC component might be dominating the emission even for a jet with $\sigma \simeq 0.1$. We note, however, that the difference between their and our approach is that we model the magnetohydrodynamics of the shell collision, while they concentrate on more accurately describing the external fields. In our model the magnetic field not only influences the cooling timescales of the emitting particles, but also the shock crossing timescales, making direct comparison difficult, especially for $\sigma \gtrsim 1$ where the dynamics changes substantially (see, e.g., MA12).

In our models, we take a monochromatic external radiation field with a frequency $\nu_{\rm ext}$ in the near infrared band, and with an energy density $u_{\rm ext}$ that tries to mimic, in a simple manner, the emission from a dusty torus or the emission from the broad line region. More complex modeling, such as that introduced by Giommi et al. (2012a) can be incorporated in our analysis, at the cost of increasing the number of parameters in our set up.

4.4.2 The effect of the observing angle

Increasing θ results in a Doppler deboosting of the collision region and a significant reduction of the observed flux. The decrease of the flux comes along with a moderate decrease of $\Gamma_{\rm ph}$ explained by the different scaling properties with the Doppler factor of the SSC and EIC contributions to the SED. From theoretical grounds, one expects that the synchrotron and SSC contributions to the SED scale as $\mathcal{D}^3$ for, while $\mathcal{D}^4$ is the correct scaling for the EIC spectral component. Such a theoretical inference is based on assuming a moving spherical blob of relativistic particles. In our case, instead a blob we have a pair of distinct cylindrical regions moving towards the observer. The practical consequence of such a morphological difference is that the synchrotron radiation is roughly emitted isotropically, and thus, it scales as $\mathcal{D}^3$ (left panels of Figures 4.5 and 4.10), but the IC contributions are no longer isotropic and thus do not scale either as $\mathcal{D}^3$ nor as $\mathcal{D}^4$. The effect is exacerbated when strong magnetizations are considered (compare the right panels of Figures 4.5 and 4.10).

4.4.3 Comparison with observations

It has been found in several blazar sources that their SEDs have more than two peaks. Particularly, in some cases a peak frequency of $\sim 10^{15}$ Hz (e.g., Lichti et al. 1995; Pian et al. 1999) is seen (a UV bump), which is assumed to come purely from the optically thick accretion disk (OTAD) and from the BLR. In recent works, thermal radiation from both OTAD and BLR are considered separately in order to classify blazars (Giommi et al. 2012a, 2013). In the present work, we have shown that a peak in the UV band can arise by means of nonthermal and purely internal jet dynamics. This "nonthermal" blue bump is due to the contribution to the SED of the *synchrotron* radiation from the reverse shock in a collision of shells with a sufficiently large relative Lorentz factor (see left panels of Figures 4.2, 4.3 and 4.6). We suggest that such a secondary peak in the UV domain is an alternative explanation for the thermal origin of the UV bump. In Giommi et al. (2012a), the prototype sources displayed in their Figure 1 all have synchrotron and IC components of comparable luminosity. In our case, the strength of the UV peak is larger for the models possessing the strongest magnetic fields. In such models, the IC part of the spectrum is strongly suppressed and, thus, they are not compatible with observations. However, moderate magnetization models display synchrotron and IC components of similar luminosity. In addition, an increase in the relative Lorentz factor of the interacting shells produces UV bumps which are more obvious and with peaks shifted to the far UV. According to Giommi et al. (2012a), the spectral slope at frequencies below the UV-bump ranges from $\alpha_{\rm r-BlueBump} \sim 0.4$ to ~ 0.95. We cannot directly compute such slope from our data, since we have limited ourselves to compute the SED above 10^{12} Hz. However, we find compatibility between our models and observations from comparison of the spectral slope at optical frequencies, where it is smaller than in the whole range $[5\,\mathrm{GHz}, \nu_{\rm BlueBump}]$. Extrapolating the data from our models, values $\Delta g \gtrsim 1.5$ combined with shell magnetizations $\sigma \simeq 10^{-3}$ could accommodate UV bumps with peak frequencies and luminosities in the range pointed out by current blazar observations.

It has to be noted that the intergalactic medium absorption at frequencies between $\sim 10^{15}$ and 3×10^{17} Hz is extremely strong, and is not incorporated into our models. Such an extrinsic suppression of the emitted radiation will impose a (redshift-dependent) upper limit to the position of the observed UV peak, below the intrinsic

reverse shock synchrotron peaks of our moderately and strongly magnetized models (see e.g., orange line in the left panel of Figure 4.6 which peaks at $\sim 10^{17}$ Hz). In other words, due to the absorption we expect the observed RS synchrotron peak of such a spectrum to appear at UV frequencies (instead of in X-rays), thus providing an alternative explanation for the UV bump.

The current observational picture shows that there are two types of blazar populations with notably different properties. Among other, type defining, properties that are different in BL Lacs and in FSRQ objects we find that their respective synchrotron peak frequencies $\nu_{\rm syn}^{\rm obs}$ are substantially different. BL Lacs have synchrotron peaks shifted to high frequencies, in some cases above 10^{18} Hz (e.g., Mkn 501). In contrast, FSRQs are strongly peaked at low energies (the mean synchrotron frequency peak is $\bar{\nu}_{\rm syn}^{\rm obs} \simeq 10^{13.1}$; Giommi et al. 2012a).

For the typically assumed or inferred values of the Lorentz factor in blazars (namely, $\Gamma < 30$), the locus of models with different magnetizations is different in the A_C vs $\nu_{\rm syn}^{\rm obs}$ graph (Figure 4.11). While weakly magnetized models display $A_C \gtrsim 3$, the most magnetized ones occupy a region $A_C \lesssim 0.1$. In between ($0.1 \lesssim A_C \lesssim 3$) we find the models with moderate magnetizations ($\sigma \simeq 10^{-2}$). Moreover, we can classify the weakly magnetized models as IC dominated with synchrotron peak in the IR band. According to observations (Finke 2013; Giommi et al. 2012b), this region is occupied by FSRQs, while the moderately magnetized cases fall into the area compatible with data from BL Lacs.

Strongly magnetized models are outside of the observational regime. However, the quite obvious separation of the locus of sources with different magnetizations is challenged when very large values of the slowest shell Lorentz factor ($\Gamma_{\rm R} \gtrsim 30$) are considered. The *path* followed by models of the family **S**-**D**1.0-**T**5 (red dash-dotted line in the lower part of Figure 4.11), heads towards the region of the graph filled by the weakly magnetized models as $\Gamma_{\rm R}$ is increased. This increase of A_C corresponds to the fact we have already pointed before: there is a degeneracy between increasing magnetization and increasing Lorentz factor (Figure 4.7). Higher values of $\Gamma_{\rm R}$ yield more luminous EIC components, making that strongly magnetized models recover the typical SED of blazars, tough with a much smaller flux than unmagnetized models.

Comparing our Figure 4.11 with Figure 5 of Finke (2013), we find that the Comp-

ton dominance is a good measurable parameter to correlate the magnetization of the shells with the observed spectra. Moderately magnetized models are located in the region where some BL Lacs are found, namely, with $0.1 \lesssim A_C \lesssim 1$ and 10^{14} Hz $\lesssim \nu_{\rm syn}^{\rm obs} \lesssim 10^{16}$ Hz. We also find that models with high and uniform magnetization ($\sigma_{\rm L} = \sigma_{\rm R} = 0.1$; **S1**-**G**10-**T**5 family), and large values of the relative Lorentz factor $\Delta g \gtrsim 1$ (dot-dot-dashed lines in Figure 4.11 and orange lines and symbols in Figure 4.12), may account for BL Lacs having peak synchrotron frequencies in excess of 10^{16} Hz and $A_C \lesssim 0.1$. There is, however, a region of the parameter space which is filled by X-ray peaked synchrotron blazars with $0.1 \lesssim A_C \lesssim 1$ that we cannot easily explain unless seemingly extreme values $\Delta g \gtrsim 2$ are considered. We point out that the most efficient way of shifting $\nu_{\rm syn}^{\rm obs}$ towards larger values is increasing Δg. Such a growth of $\nu_{\rm syn}^{\rm obs}$ comes with an increase in the Compton dominance, as is found observationally for FSRQ sources (Finke 2013). Comparatively, varying $\Gamma_{\rm R}$ drives moderate changes in $\nu_{\rm syn}^{\rm obs}$, unless extreme values $\Gamma_{\rm R} \gtrsim 50$ are considered. We must also take into account that the synchrotron peak frequency is determined by the high-Lorentz factor cut-off $\gamma_{\rm max}$. Most of our models display values $\gamma_{\rm max} \gtrsim 10^4$ in the emitting (shocked) regions. For comparison, in Finke (2013) $\gamma_{\rm max} = 10^6$ is fixed for all his models. The small values of $\gamma_{\rm max}$ in our shell collisions are due to the microphysical parameters we are using, in particular, our choice of the shock acceleration efficiency $a_{\rm acc}$, which was motivated by Böttcher & Dermer (2010). For the models and parameters picked up by Böttcher & Dermer (2010), they find that neither the peak synchrotron frequency, nor the peak flux were sensitively dependent on the choice of $a_{\rm acc}$ (if the power-law Lorentz factor index $q > 2$). However, $\gamma_{\rm max}$ shows the same dependence on $a_{\rm acc}$ than on the magnetic field strength: $\gamma_{\rm max} \simeq 4.6 \times 10^7 (a_{\rm acc} B[{\rm G}])^{-0.5}$. In practice, thus, we find a degeneracy in the dependence on both $a_{\rm acc}$ and B for our models.

Considering the location of the strongly magnetized models with $\sigma_{\rm L} = 1$, and $\sigma_{\rm R} = 0.1$ in the A_C vs $\nu_{\rm syn}^{\rm obs}$ graph (Figure 4.11), they appear as only marginally compatible with the observations of Finke (2013), where almost all sources have $A_C > 10^{-2}$. Since in such models is difficult to obtain $A_C > 10^{-2}$, unless the microphysical parameters of the emitting region are changed substantially (e.g., lowering $a_{\rm acc}$). This seems to indicate that strongly magnetized models with sensitively different magnetizations of the colliding shells (in our case there is a factor 10 difference

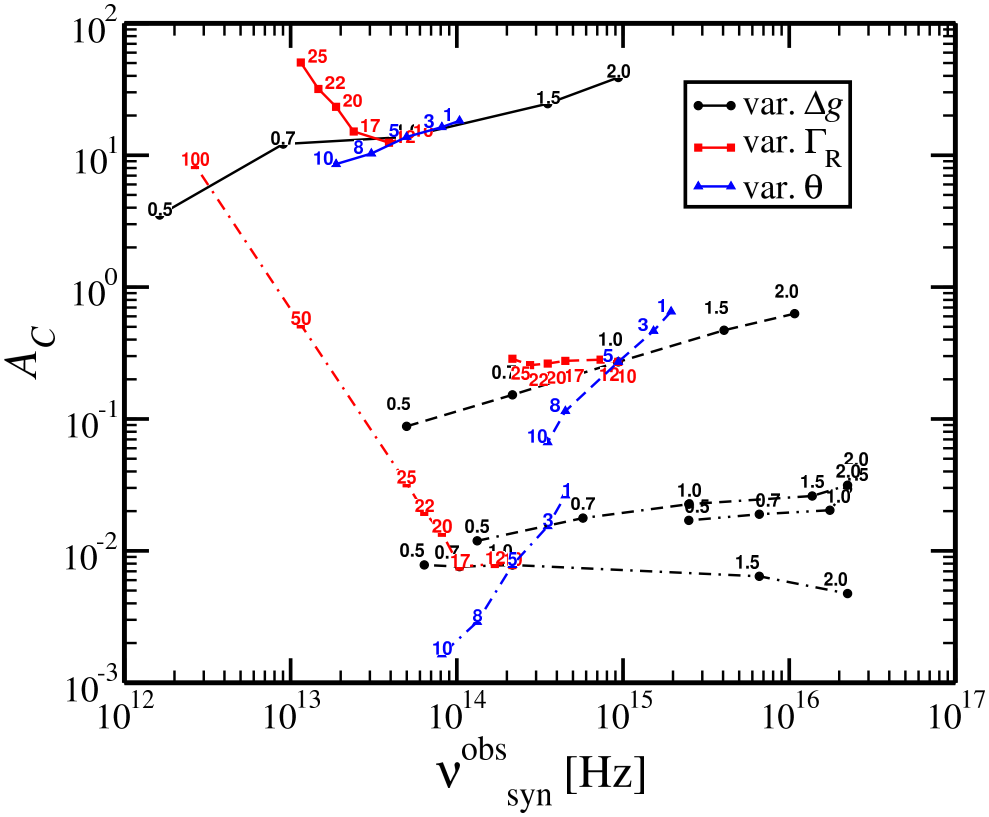

Figure 4.11: *Compton dominance A_C as a function of the synchrotron peak frequency $\nu^{\rm obs}_{\rm syn}$ for the three families of models corresponding to collisions of the three kinds of magnetized shells. We also display the Compton dominance for the families of strongly magnetized models **S1** and **S2**. The different lines are drawn to show the various trends when considering models where we vary a single parameter and keep the rest constant. The variation induced by the change in Δg, $\Gamma_{\rm R}$ and θ is shown with black, red and blue lines, respectively. The numbers denote the value of the varied parameter and the line type is associated to the magnetization, corresponding the solid, dashed and dot-dashed lines to weakly, moderately and strongly magnetized shells, respectively. Double-dotted-dashed and dotted-double-dashed lines correspond to the additional models of the families **S1**-**G**10-**T**5 and **S2**-**G**10-**T**5, respectively.*

between the magnetization of the faster and of the slower shell) are in the limit of compatibility with observations, and that even larger magnetizations are banned by data of actual sources. MA12 found that the combination $\sigma_{\rm L} = 1$, $\sigma_{\rm R} = 0.1$, brings the maximum dynamical efficiency in shell collisions ($\sim$ 13%), and that has been the reason to explore the properties of such models here. Models with large and uni-

form magnetization $\sigma_L = \sigma_R = 0.1$ display a dynamical efficiency $\sim 10\%$, quite close to the maximum one for a single shell collision, and clearly bracket better the observations in the A_C vs ν_{syn}^{obs} plane.

The family of **S2**-models with $\sigma_L = 0.1$, $\sigma_R = 1$ is complementary to the **S**-family, but in the former case, only a RS exists, since the FS turns into a forward rarefaction (MA12), if $\Delta g \lesssim 1.5$. These models possess a larger Compton dominance ($10^{-2} \lesssim A_C \lesssim 4{\times}10^{-2}$) than those of the **S**-family (Figure 4.11), and their locus in the F_{ph} vs Γ_{ph} plane (Figure 4.12; green line and symbols) is much more compatible with observations. Since the synchrotron emission of the **S2**-family is only determined by the RS, if $\Delta g \lesssim 1.5$, or dominated by the RS emission if $\Delta g \gtrsim 1.5$, the synchrotron peak tends to be at higher frequencies than in the **S** and **S1** families.

The value of Γ_{ph} has also been useful to differentiate observationally between BL Lacs and FSRQs. According to Abdo et al. (2010b) the photon index, provides a convenient mean to study the spectral hardness, which is the ratio between the *hard* sub-band and the *soft* sub-band (Abdo et al. 2009). In Figure 4.12 we compare the values of Γ_{ph} computed for our three families of models with actual observations of FSRQs and BL Lacs from the 2LAG catalog (Ackermann et al. 2011). We only represent values of such catalog corresponding to sources with redshifts $0.4 \leq z \leq 0.6$, since our models have been computed assuming $z = 0.5$. We note that the values of Γ_{ph} calculated from fits of the $\gamma-$ray spectra in our models with moderate magnetization (red colored in the figure) fall just above the observed maximum values attained in FSRQs ($\Gamma_{ph,obs}^{FSRQ} \lesssim 2.6$), if the Lorentz factor of the slower shell is $\Gamma_R \sim 10$. However, models with moderate magnetization and larger Lorentz factors $\Gamma_R \gtrsim 15$ display photon indices fully compatible with FSRQs and photon fluxes in the lower limit set by the technical threshold that prevents Fermi to detect sources with $F_{ph} \lesssim 2 \times 10^{-10}$ photons cm^{-2} s^{-1}. BL Lacs exhibit even flatter $\gamma-$ray spectra than FSRQs, with observed values of the photon index $\Gamma_{ph,obs}^{BLLac} \lesssim 2.4$. Values $\Gamma_{ph} \gtrsim 2$ are on reach of both strongly or weakly magnetized models. Nevertheless, the photon flux of strongly magnetized models falls below the current technical threshold. Being conservative, this under-prediction of the gamma-photon flux could be taken as a hint indicating that only models with small or negligible magnetization can reproduce properly the properties of FSRQs, LBLs, and perhaps IBL sources, while HBLs and BL Lacs have microphysical properties which differ from the ones parametrized in

this work. According to Abdo et al. (2009), the photon index is a quantity that could constrain the emission and acceleration processes that may be occurring within the jet that produce the flares at hand. Particularly, we have fixed a number of microphysical parameters (ϵ_B, ϵ_e, a_{acc}, etc.) to typically accepted values, but we shall not disregard that X-ray, synchrotron-peaked sources have different values of the aforementioned microphysical parameters. On the other hand, our values of Γ_{ph} are not fully precise, the reason being the approximated treatment of the Klein-Nishina cutoff. Being not so conservative, we may speculate that our current gamma ray detectors cannot observe sources with sufficiently small flux ($F_{ph} \lesssim 3 \times 10^{-11}$ photons cm^{-2} s^{-1}) to discard or confirm that strongly magnetized blazars may exist.

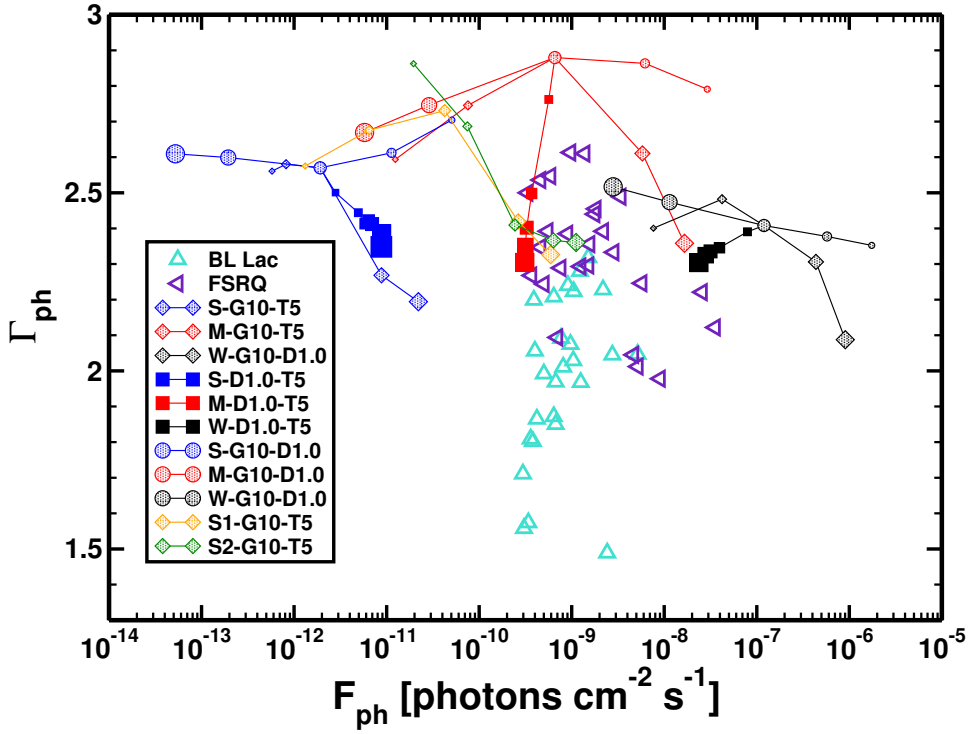

Figure 4.12: *Comparison between our numerical models and those sources (FRSQs and* BL Lacs*) whose redshift is* $0.4 \leq z \leq 0.6$ *in the 2LAG catalog (Ackermann et al. 2011). The size of the symbols associated to our models grows as the parameter which is varied does. For instance, in the case of models* ***M-G10-D1.0****, the smaller values of* θ *correspond to the smaller red circles in the plot.*

4.4.4 Conclusions and future work

In the standard model, the SEDs of FSRQs and BL Lacs can be fit by a double parabolic component with maxima corresponding to the synchrotron and to the IC peaks. We have shown that the SEDs of FSRQs and BL Lacs strongly depends on the magnetization of the emitting plasma. Our models predict a more complex phenomenology than is currently supported by the observational data. In a conservative approach this would imply that the observations restrict the probable magnetization of the colliding shells that take place in actual sources to, at most, moderate values (i.e., $\sigma \lesssim 10^{-1}$), and if the magnetization is large, with variations in magnetization between colliding shells which are smaller than a factor ~ 10. However, we have also demonstrated that if the shells Lorentz factor is sufficiently large (e.g., $\Gamma_{\rm R} \gtrsim 50$), magnetizations $\sigma \simeq 1$ (Figure 4.7) are also compatible with a doble hump. Therefore, we cannot completely discard the possibility that some sources are very ultrarelativistic both in a kinematically sense and regarding its magnetization.

We find that FSRQs have observational properties on reach of models with negligible or moderate magnetic fields. The scattering of the observed FSRQs in the A_C vs $\nu_{\rm syn}^{\rm obs}$ plane, can be explained by both variations of the intrinsic shell parameters (Δg and $\Gamma_{\rm R}$ most likely), and of the extrinsic ones (the orientation of the source). BL Lacs with moderate peak synchrotron frequencies $\nu_{\rm syn}^{\rm obs} \lesssim 10^{16}$ Hz and Compton dominance parameter $0.1 \gtrsim A_C \gtrsim 1$ display properties that can be reproduced with models with moderate and uniform magnetization ($\sigma_{\rm L} = \sigma_{\rm R} = 10^{-2}$). HBL sources can be partly accommodated within our model if the magnetization is relatively large and uniform ($\sigma_{\rm L} = \sigma_{\rm R} = 10^{-1}$) or if the magnetization of the faster colliding shell is a bit smaller than that of the slower one ($\sigma_{\rm L} = 10^{-1}, \sigma_{\rm R} = 1$). We therefore find that a fair fraction of the *blazar sequence* can be explained in terms of the intrinsically different magnetization of the colliding shells.

We observe that the change in the photon spectral index ($\Gamma_{\rm ph}$) in the $\gamma-$ray band can be a powerful observational proxy for the actual values of the magnetization and of the relative Lorentz factor of the colliding shells. Values $\Gamma_{\rm ph} \gtrsim 2.6$ result in models where the flow magnetization is $\sigma \sim 10^{-2}$, whereas strongly magnetized shell collisions ($\sigma > 0.1$) as well as weakly magnetized models may yield $\Gamma_{\rm ph} \lesssim 2.6$.

The EIC contribution to the SED has been included in a very simplified way in this work. We plan to improve on this item by considering more realistic background

field photons as in, e.g., Giommi et al. (2012a). We expect that including seed photons in a wider frequency range will modify the IC spectrum of strongly magnetized models or of models with low-to-moderate magnetization, but large bulk Lorentz factor. Finally, the microphysical parameters characterizing the emitting plasma have been fixed in this manuscript. In a follow up work, we will explore the sensitivity of the results (particularly in moderately to highly magnetized models) to variations of the most significant microphysical parameters (e.g., $a_{\rm acc}$, $\epsilon_{\rm B}$, $\epsilon_{\rm e}$, etc).

4.5 Appendices

The following subsctions enclose an editted version of the appendices in the article RMA14, pp. 1868–1869.

4.5.1 Photon index

The spectral index of a source measures the frequency dependence of its nonthermal radiation flux density. We assume that the photon flux $F_{\rm ph}$ in a certain frequency range can be approximated by

$$F_{\rm ph} \propto \nu_{\rm obs}^{-\Gamma_{\rm ph}}. \tag{4.2}$$

where $\Gamma_{\rm ph}$ is the spectral index. In other words, the spectral index gives a measure of the slope of the radiation flux in logarithmic scale, within a frequency range $[\nu_{\rm obs}, \nu_{\rm obs} + \Delta\nu_{\rm obs}]$. If we have the radiation flux at two sufficiently close frequencies, the spectral index is calculated in the following manner:

$$\Gamma_{\rm ph} = \log\left(\frac{F_{\nu_{\rm obs},1}}{F_{\nu_{\rm obs},2}}\right) \Big/ \log\left(\frac{\nu_{\rm obs,1}}{\nu_{\rm obs,2}}\right) \tag{4.3}$$

The value of $\Gamma_{\rm ph}$ has also been useful to differentiate observationally between BL Lacs and FSRQs. According to Abdo et al. (2010b) the photon index, provides a convenient mean to study the spectral hardness, which is the ratio between the *hard* sub-band and the *soft* sub-band (Abdo et al. 2009).

In the present section we describe a way to obtain the photon index in the γ-ray band from synthetic SEDs, specifically in the range 10^{-1}–1 GeV. First of all, we must take into account that

$$F_{\rm ph} = \frac{1}{h}\int_{\nu^{obs}_{\rm min}}^{\nu^{\rm obs}_{\rm max}} {\rm d}\nu_{\rm obs}\,\frac{\nu_{\rm obs} F_{\nu_{\rm obs}}}{\nu^2_{\rm obs}}, \tag{4.4}$$

with $F_{\rm ph}$ is in units of photons cm^{-2} s^{-1} and h is the Planck constant. Discretizing the frequency range and using the approximation $\nu_{\rm obs} F_{\nu_{\rm obs}} \nu_{\rm obs}^{-2} \propto \nu_{\rm obs}^{-s}$ at each sub-interval, we get that

$$F_{\rm ph} \approx \frac{\nu_{{\rm obs},i}^{s}}{h} f(\nu_{{\rm obs},i}) P\left(\frac{\nu_{{\rm obs},i+1}}{\nu_{{\rm obs},i}}, s\right), \tag{4.5}$$

where

$$f(\nu_{\rm obs}) := \frac{\nu_{\rm obs} F_{\nu_{\rm obs}}}{\nu_{\rm obs}^{2}}. \tag{4.6}$$

By using formula (4.3) and approximation (4.5) we can calculate the spectral index at each sub-interval. With a linear least-squares routine the final photon index $\Gamma_{\rm ph}$ is calculated.

4.5.2 Relation between A_C and $F_{\rm IC}/F_{\rm syn}$

Some parts of the following section contains extracts from Appendix B of RMA14, p. 1868. In a previous study made by Mimica & Aloy (2012) regarding the Compton to synchrotron fluences ratio $F_{\rm IC}/F_{\rm syn}$, where $F_{\rm IC}$ and $F_{\rm syn}$ are the fluences of the IC and synchrotron component, respectively. A trend was found by comparing it with the Compton to synchrotron peak frequencies ratio $\nu_{\rm IC}/\nu_{\rm syn}$. Both ratios are Doppler shift independent likewise A_C.

In Figure 4.13 (upper panel) we present a plot of the Compton dominance parameter as a function of the ratio of peak frequencies $\nu_{\rm IC}/\nu_{\rm syn}$, since these properties can be directly measured from observations. The models here considered correspond to the ones described in the next chapter. The lower Compton dominance happens for strongly magnetized models ($\sigma_{\rm L} = 1, \sigma_{\rm R} = 0.1$, dot-dashed lines in the figure), while the weakly magnetized shell collisions ($\sigma_{\rm L} = \sigma_{\rm R} = 10^{-6}$) display the larger A_C. According to A_C, there is a factor of more than ten in Compton dominance when considering shells with magnetizations $\sigma \sim 10^{-2}$, as compared with basically unmagnetized models. We also note that models with varying viewing angle θ are shifted along diagonal lines in the plot (blue lines in Figure 4.13). This is also the case for families of models in which we vary Γ_R above a threshold (magnetization dependent) such that the IC spectrum is dominated by the EIC contribution (red lines in Figure 4.13). If the IC spectrum is dominated by the SSC contribution, changing Γ_R yields a horizontal displacement in the plot. Models with varying Δg display a similar drift as those in which θ is changed in the case of the moderately magnetized shell

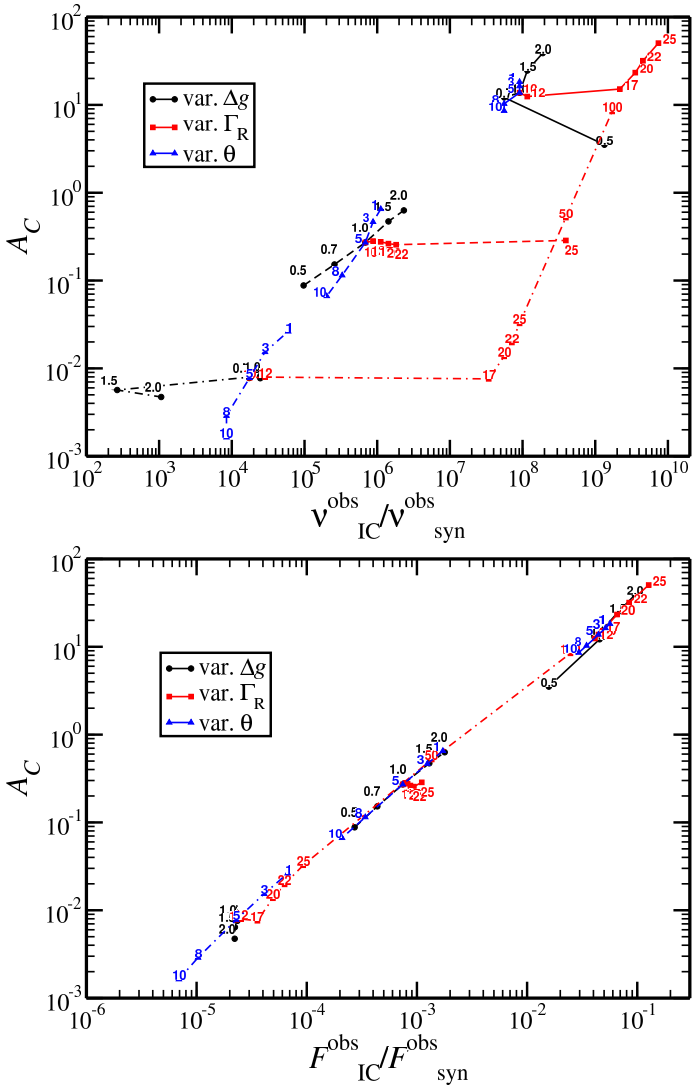

Figure 4.13: *Upper panel: Compton dominance, A_C, as a function of $\nu^{\rm obs}_{\rm IC}/\nu^{\rm obs}_{\rm syn}$. Lower panel: Same as the upper panel, but replacing $\nu^{\rm obs}_{\rm IC}/\nu^{\rm obs}_{\rm syn}$ by the ratio of peak fluxes $F^{\rm obs}_{\rm IC}/F^{\rm obs}_{\rm syn}$. The models and the lines in this figure correspond to the models studied in Chapter 4 (see Table B.3).*

collisions. The trend is not so well defined in case of weakly magnetized models, and for strongly magnetized models, the Compton dominance is rather insensitive to Δg, though lower values of Δg yield larger values of $\nu^{\rm obs}_{\rm IC}/\nu^{\rm obs}_{\rm syn}$.

As can be seen from Figure 4.13 (upper panel), there exists a very tight correla-

tion between $F_{\rm IC}^{\rm obs}/F_{\rm syn}^{\rm obs}$ and A_C, which means that either A_C or $F_{\rm IC}^{\rm obs}/F_{\rm syn}^{\rm obs}$ can be used interchangeably for the study of the global trends of the models MA12 and RMA14 (see Tables B.3 and B.4).

Chapter 5

On the influence of a Hybrid Thermal-Non thermal distribution in the Internal Shocks model for blazars

In the present chapter we enclose an adapted version of the article RMA17, pp. 1174–1179.

5.1 Abstract

Internal shocks occurring in blazars may accelerate both thermal and nonthermal electrons. In this work we examine the consequences that such a hybrid (thermal/non-thermal) EED has on the spectrum of blazars. Since the thermal component of the EED may extend to very low energies. We replace the standard synchrotron process by the more general MBS. Significant differences in the energy flux appear at low radio frequencies when considering MBS instead of the standard synchrotron emission. A drop in the spectrum appears in the all the radio band and a prominent valley between the infrared and soft X-rays bands when a hybrid EED is considered, instead of a power-law EED. In the γ-ray band an EED of mostly thermal particles displays significant differences with respect to the one dominated by nonthermal par-

ticles. A thermally-dominated EED produces a SSC peak extending only up to a few MeV, and the valley separating the MBS and the SSC peaks is much deeper than if the EED is dominated by nonthermal particles. The combination of these effects modifies the Compton dominance of a blazar, suggesting that the vertical scatter in the distribution of FSRQs and BL Lacs in the peak synchrotron frequency-Compton dominance parameter space could be attributed to different proportions of thermal/nonthermal particles in the EED of blazars. Finally, the temperature of the electrons in the shocked plasma is shown to be a degenerated quantity for different magnetizations of the ejected material.

5.2 Differences between MBS and standard synchrotron spectra

In this section we show the importance of the introduction of the new MBS method into our blazar model. We will first show the differences that arise from using different approximations for the emission process assuming the same HD with a dominant nonthermal component (§5.2.1) for each test. In the second test we compare the spectra produced by a nonthermally dominated HD with that of a pure power-law extending towards $\gamma_1 \simeq 1$ (§5.2.2) by computing both MBS and pure synchrotron emission.

For the evolution of the particles injected at shocks, we assume that the dominant processes are the synchrotron cooling and the IC scattering off the photons produced by the MBS processes (SSC[1]). We note that, in many cases, SSC cooling may be stronger than synchrotron cooling, as we shall see in §5.3. To compute synthetic time-dependent multiwavelength spectra and light curves, we include synchrotron and synchrotron self-Compton emission processes resulting from the shocked plasma. We further consider that the observer's line of sight makes an angle θ with the jet axis. A detailed description of how the integration of the radiative transfer equation along the line of sight is performed can be found in § 4 of MA12 as well as in §2.3.3.1.

[1]For simplicity we keep the abbreviation "SSC" to denote the process of scattering of the nonthermal emission produced by the local electrons off those same electrons, but it should be noted that in our model the seed photons for the inverse-Compton scattering are produced by the (more general) cyclo-synchrotron emission (§2.2).

To avoid repeated writing of the parameter values when referring to our models, we introduce a naming scheme in which the magnetization is denoted by the letters **S**, **M** and **W**, referring to the following families of models:

W: weakly magnetized, $\sigma_{\rm L} = 10^{-6}, \sigma_{\rm R} = 10^{-6}$,

M: moderately magnetized, $\sigma_{\rm L} = 10^{-2}, \sigma_{\rm R} = 10^{-2}$, and

S: strongly magnetized, $\sigma_{\rm L} = 10^{-1}, \sigma_{\rm R} = 10^{-1}$.

The remaining four parameters $\mathcal{L}$, $\Gamma_{\rm R}$, Δg and $\zeta_{\rm e}$ can take any of the values shown in Table 5.1. When we refer to a particular model we label it by appending values of each of these parameters to the model letter. For the parameter $\zeta_{\rm e}$ we use **Z**m2, **Z**m1 and **Z**09 to refer to the values $\zeta_{\rm e} = 10^{-2}, 10^{-1}$ and 0.9, respectively. Similarly, for the luminosity we write $\mathcal{L}$1, $\mathcal{L}$5, and $\mathcal{L}$50 to denote the values 10^{47}, 5×10^{47} and 5×10^{48} erg s^{-1}, respectively. In this notation, **W**-**G**10-**D**1.0-**Z**m1-$\mathcal{L}$5 corresponds to the weakly magnetized model with $\Gamma_{\rm R} = 10$ (**G**10), $\Delta g = 1.0$ (**D**1.0), $\zeta_{\rm e} = 0.1$ (**Z**m1) and $\mathcal{L} = 5 \times 10^{47}$ erg s^{-1} ($\mathcal{L}$5).

5.2.1 Spectral differences varying the emissivity for a fixed HD

In Figure 5.1 we display the instantaneous spectra of a weakly magnetized model containing a HD where 90% of the particles populate the nonthermal tail of the EED (model **W**-**G**10-**D**1.0-**Z**09-$\mathcal{L}$1) taken at 10, 10^2, 10^3, 10^4 and 10^5 seconds after the start of the shell collision. Solid, dotted and dashed lines show the emission computed using the full MBS method (§3.2) and the direct numerical integration of the analytic approximations $RMA(X_{\rm c}, \gamma)$ (equation 3.60)[2] and the numerical integration of the Crusius & Schlickeiser (1986) function employed in MA12 and RMA14 (referred hereafter as the standard synchrotron), respectively. The difference between the first two and the third is in the presence of a low-frequency cut-off which causes appreciable differences at early times. The purely synchrotron emission (dot-dashed lines) always produces an excess of emission with respect to the other two. This is explained by the fact that there is always a portion of the EED whose energy is too low for it to be emitting in the observed frequencies in a more realistic MBS

[2]We point out that after the publication of RMA17, we have developed an improved version of the $RMA(X_{\rm c}, \gamma)$ function, which we present in this thesis (§3.2.4.7).

model (see Figure 3.11). The approximate formula $RMA(X_c, \gamma)$ performs quite well and its spectra mostly overlap the MBS ones, except close to the first turnover in the spectrum (corresponding to the maximum of the emission from the lowest-energy electrons). Despite the presence of a cutoff in $RMA(X_c, \gamma)$, it still overestimates the low-frequency emission just below the first harmonic, which explains the observed slight mismatch.

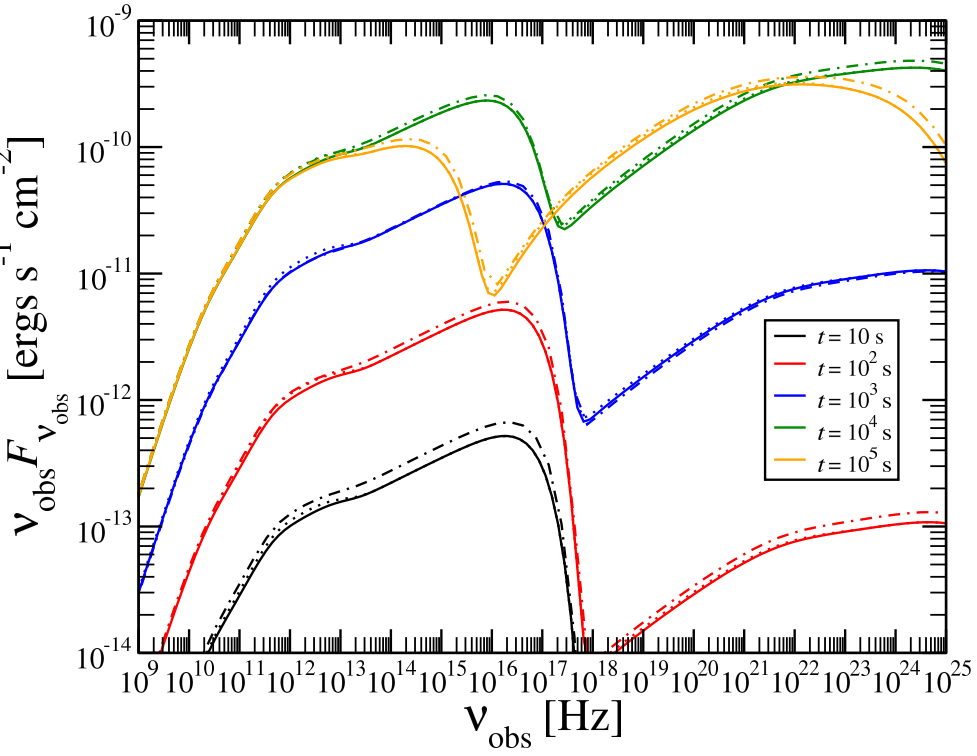

Figure 5.1: *Instantaneous spectra for a model including a HD in which 90% of the particles populate the nonthermal tail of the EED computed employing our new MBS numerical method (full lines), using the direct numerical integration of $RMA(X_c, \gamma)$ function (dotted lines, see Eq. (3.60)), and using the direct numerical integration of the Crusius & Schlickeiser (1986) function (dot-dashed lines). The dynamical model employed corresponds to a collision of weakly magnetized shells.*

5.2.2 Spectral differences between an HD and a pure power-law EED

In the previous section we have seen that the differences between the MBS emissivity and the pure synchrotron emissivity are relatively mild if we consider a hybrid, non-

thermally dominated EED. To a large extend this happens because a HD is flanked by a monotonically decaying tail at low electron energies (which indeed goes to zero as the electron Lorentz factor approaches 1, see inset of Figure 5.2). Here we are interested in outlining the spectral differences when the lower boundary of the EED is varied. For that we consider two different EEDs, namely, a nonthermally dominated HD (corresponding to model **W**-**G**10-**D**1.0-**Z**09-$\mathcal{L}$1) and a pure power-law EED extending to $\gamma_1 \simeq 1$. The rest of the parameters of our model, including the MBS emissivity are fixed. To set up the pure power-law EED we cannot follow exactly the same procedure as outlined in §2.4.2.2 because we must fix γ_1 instead of obtaining it numerically solving Eq. (2.84). Furthermore, we employ the same nonthermal normalization factor Q_0 for both the pure power-law EED and the HD.

In Figure 5.2 we show the spectral energy distribution corresponding to both the HD and pure power-law EED cases. It is evident that there are substantial differences at frequencies below the GHz range and in the infrared-to-X-rays band. On the other hand, the synchrotron tails above $\sim 10^{13}$ Hz are almost identical for both EED. Correspondingly, the cyclo-synchrotron photons there produced are inverse Compton upscattered forming nearly identical SSC tails above $\sim 10^{20}$ Hz.

5.2.3 Spectral differences between MBS and pure synchrotron for the same power-law distribution

In the previous section we pointed out how different the SEDs may result for different distributions. Let us now fix the same injected power-law EED starting from $\gamma_1 \approx 1$ and evaluate the emissivities corresponding to MBS and pure synchrotron processes. In both cases the SSC is also computed. In Figure 5.2 we included the averaged SED from a simulation with the same configuration as the pure power-law EED model mentioned above but the radiation treatment was numerical standard synchrotron (green lines). From 10^{10}–10^{22} Hz the MBS spectrum is quite similar to that of a pure synchrotron one, so that both emission models are observationally indistinguishable in the latter broad frequency range. On the other hand, if we look into the MHz band, we will find what we call the cyclotron break, which is the diminishing of the emissivity from each electron due to the cut-off that happens at frequencies below ν_g (Eq. (2.19)).

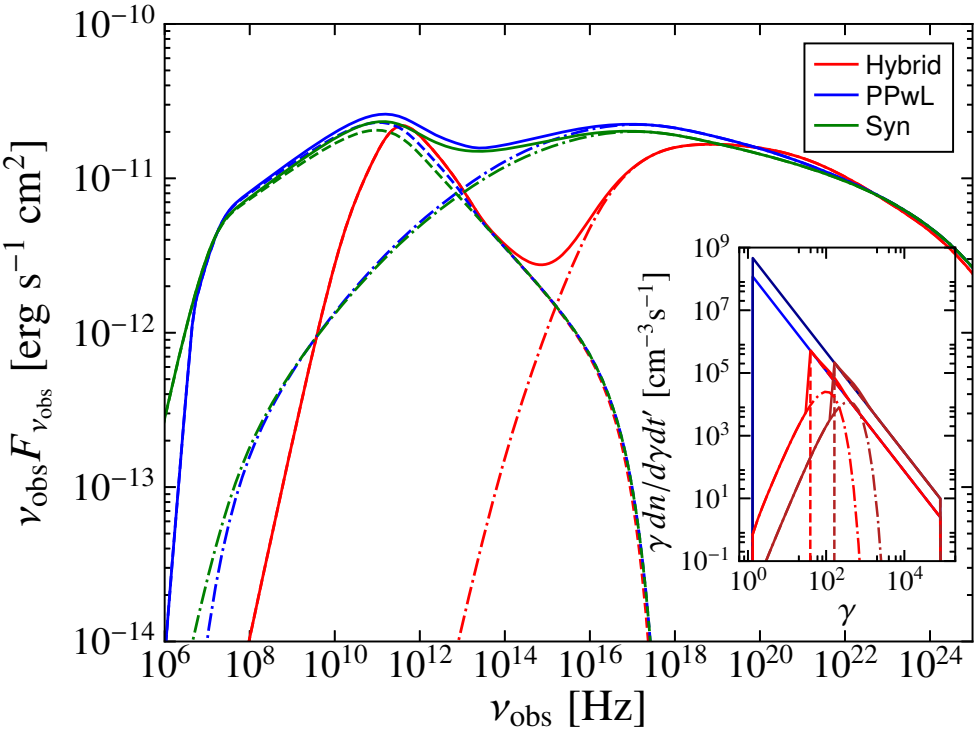

Figure 5.2: *Comparison between the same hybrid model as in Figure 5.1 and a pure power-law distribution with $\gamma_{\rm min}^{\rm nth} \simeq 1$. The red lines correspond to the former model while the green and blue lines correspond to simulations with the latter distributions using our MBS numerical method and numerical integration of Crusius & Schlickeiser (1986), respectively. Dashed and dot dashed lines show the synchrotron and SSC spectral contributions to each of the respective models. Inset: comoving frame evolution of the injected EEDs in each shock. Blue and dark blue colors correspond to the EED for a pure power-law distribution injected at the FS and at the RS, respectively. Red and dark red colors correspond to the HD distribution injected at the FS and at the RS, respectively.*

5.3 Parameter study

In order to assess the impact of the presence of a hybrid distribution composed by thermal and nonthermal electrons we have performed a parametric study varying a number of intrinsic properties of the shells. In the following subsections we examine the most important results of our parametric study. In the Table 5.1 we show the values of the parameters used in the present work. Some of them are fixed in the following and are shown with a single value in Table 5.1. Among such parameters,

we find the fraction of the internal energy density of the shocked shell converted into stochastic magnetic field energy density, ϵ_B, the size of the acceleration zone, Δ_{acc}, and the number of turns around magnetic field lines in the acceleration zone that electrons undergo before they cool down, a_{acc} (see MA12, or §2.3.2.1, §2.3.2 of this thesis for details). The cross-sectional radius and longitudinal size of the shells are given by the parameters R and Δr (see Figure 1.8), respectively.

One of the parameters kept constant in the previous studies is the total jet luminosity $\mathcal{L}$, which we now vary. We performed a number of test calculations to compute the lower and upper limits of $\mathcal{L}$ that produce a spectrum qualitatively similar to that of the source *Mrk 421* (Krawczynski & Treister 2013). In the Table 5.1 we show the range of variations of this and other parameters.

We perform our parametric scan for the typical redshift value of *Mrk 421*, namely, $z = 0.031$. The viewing angle is fixed to $\theta = 5°$ in all our models. The SEDs in this work were computed by averaging over a time interval of 10^7 s.

5.3.1 The presence of the nonthermal population

The influence of the parameter ζ_e on the blazar emission was examined in Böttcher & Dermer (2010), and is an essential model parameter in MA12 and RMA14 as well (though in the latter two papers it was not varied). In this section we explore its influence by studying three different fractions of nonthermal particles: $\zeta_e = 0.9, 0.1, 0.01$. In Figure 5.3 we show the averaged SEDs of the models with the aforementioned values of ζ_e for the weakly (left panel) and moderately (right panel) magnetized shells. In both panels we can appreciate that an EED dominated by nonthermal particles produces a broader SSC component. The SSC component of a thermally-dominated EED (**W**-**G**10-**D**1.0-**Z**09-$\mathcal{L}$5 and **M**-**G**10-**D**1.0-**Z**09-$\mathcal{L}$5) displays a steeper synchrotron-SSC valley, and the modelled blazar becomes γ-rays quiet. The synchrotron peak frequency ν_{syn}^{obs} is only very weakly dependent on ζ_e. According to their synchrotron peak frequency these models resemble LSP (Giommi et al. 2012a, 2013).

5.3.2 Magnetization

In Figure 5.4 we show the average spectra produced by the IS model with different combinations of the faster and slower shells magnetizations for a fixed EED with

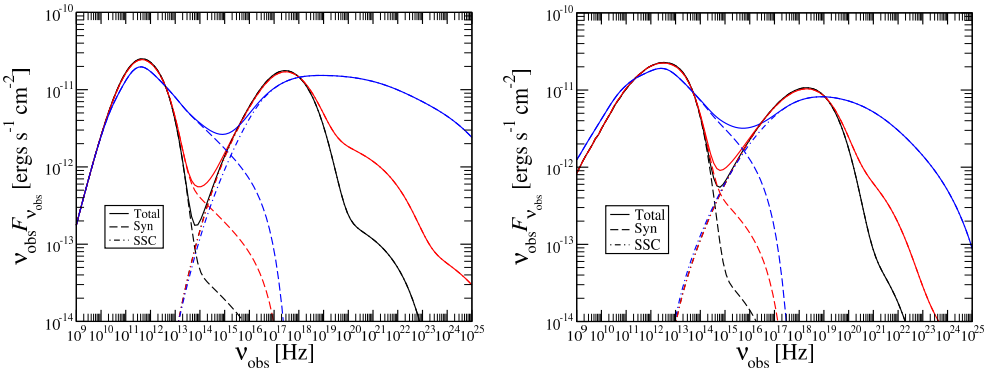

Figure 5.3: *Averaged spectra of the weakly (left panel) and moderately (right panel) magnetized models for $\zeta_e = 0.9, 0.1$ and 0.01 in blue, red and black lines respectively. Dashed lines show the synchrotron component while the dot-dashed lines show the SSC component.*

$\zeta_e = 0.9$. In black, red and blue we represent the models with faster shell magnetization $\sigma_L = 10^{-6}, 10^{-2}$ and 10^{-1}, respectively. The solid, dotted and dashed lines correspond to a slower shell magnetization $\sigma_R = 10^{-6}, 10^{-2}$ and 10^{-1} respectively. Consistent with the results in RMA14, the collision of strongly magnetized shells produces a SSC component dimmer than the synchrotron component. A double bump outline is reproduced by the model **M**-**G**10-**D**1.0-**Z**09-$\mathcal{L}$1 (dashed, red line) and all the models with $\sigma_L = 10^{-6}$. For most models ν_{syn} is situated at $\sim 10^{12}$ Hz. However, for the cases with $\sigma_L = 10^{-2}, 10^{-1}$ and $\sigma_R = 10^{-2}$, $\nu_{syn} \sim 10^{13}$ Hz. In both cases, these frequencies reside in the LSP regime. Remarkably, a change of 4 orders of magnitude in σ_R results in an increase of $\lesssim 2$ in the observed flux in models with an EED dominated by nonthermal electrons ($\zeta_e = 0.9$; Figure 5.4 left panel). In the case of models with a thermally-dominated EED ($\zeta_e = 0.1$; Figure 5.4 right panel), the change in flux under the same variation of the magnetization of the slower shell is a bit larger, but still by a factor $\lesssim 6$. In both cases the larger differences when changing σ_R happen in the decaying side of the spectrum occurring to the right of either the synchrotron or the SSC peaks. The variation of the magnetization of the faster shell yields, as expected (MA12; RMA14) larger spectral changes, especially in the SSC part of the spectrum.

[3]The chosen value for q is representative for blazars according to observational (Ghisellini et al. 1998) and theoretically deduced values (Kardashev 1962; Böttcher & Dermer 2002). It also agrees with the ones used in numerical simulations of blazars made by Mimica (2004) and Zacharias & Schlickeiser (2010).

Parameter	value
$\Gamma_{\rm R}$	2, 10, 20
Δg	1.0, 2.0, 3.0, 5.0
$\sigma_{\rm L}$	10^{-6}, 10^{-2}, 10^{-1}
$\sigma_{\rm R}$	10^{-6}, 10^{-2}, 10^{-1}
$\epsilon_{\rm B}$	10^{-3}
$\zeta_{\rm e}$	10^{-2}, 10^{-1}, 0.9
q	2.6
$\Delta_{\rm acc}$	10
$a_{\rm acc}$	10^{6}
$\mathcal{L}$	10^{47}, 5×10^{47}, 5×10^{48} erg s^{-1}
R	3×10^{16} cm
Δr	6×10^{13} cm
z	0.031
θ	5°

Table 5.1: *Model parameters.* $\Gamma_{\rm R}$ *is the Lorentz factor of the slow shell,* $\Delta g := \Gamma_{\rm L}/\Gamma_{\rm R} - 1$ *(*$\Gamma_{\rm L}$ *is the Lorentz factor of the fast shell),* $\sigma_{\rm L}$ *and* $\sigma_{\rm R}$ *are the fast and slow shell magnetizations,* $\epsilon_{\rm B}$ *is the fraction of the internal energy density at shocks that it is assumed to be converted into stochastic magnetic field energy density (Eq.* (2.48)*),* $\zeta_{\rm e}$ *and* q *are the fraction of electrons accelerated into power-law Lorentz factor (or energy) distribution and its corresponding power-law index*[3]*,* $\Delta_{\rm acc}$ *and* $a_{\rm acc}$ *are the parameters controlling the shock acceleration efficiency (see Section 3.2 of MA12 or §2.3.2.1, §2.3.2 -this thesis- for details),* $\mathcal{L}$*,* R *and* Δr *are the jet luminosity, jet radius and the initial width of the shells,* z *is the redshift of the source and* θ *is the viewing angle. Note that* $\Gamma_{\rm R}$*,* Δg*,* $\sigma_{\rm L}$*,* $\sigma_{\rm R}$ *and* $\zeta_{\rm e}$ *can take any of the values indicated.*

5.3.3 Relative Lorentz factor Δg

In Figure 5.5 we show the variation of the relative Lorentz factor, Δg, for $\zeta_{\rm e}$ = 0.1 and 0.9 (**W**-**G**10-**D**(1.0, . . ., 5.0)-**Z**m1-$\mathcal{L}$1 and **W**-**G**10-**D**(1.0, . . ., 5.0)-**Z**09-$\mathcal{L}$1). The dashed and dot-dashed lines depict the energy flux coming from the FS and RS, respectively. The model with Δg = 1.0 results from the collision with a fast shell having $\Gamma_{\rm L}$ = 20, whereas the case Δg = 5.0 assumes that the fast shell moves with $\Gamma_{\rm L}$ = 60 (i.e., slightly above the upper end of the Lorentz factor distribution for parsec-scale jets; Lister et al. 2016). Both panels show that the larger the Δg, the higher the SSC bump. The colliding shells with relative Lorentz factor Δg = 5.0 produced a spectrum with an SSC component one order of magnitude larger than its synchrotron component. On the other hand, the colliding shells with relative Lorentz

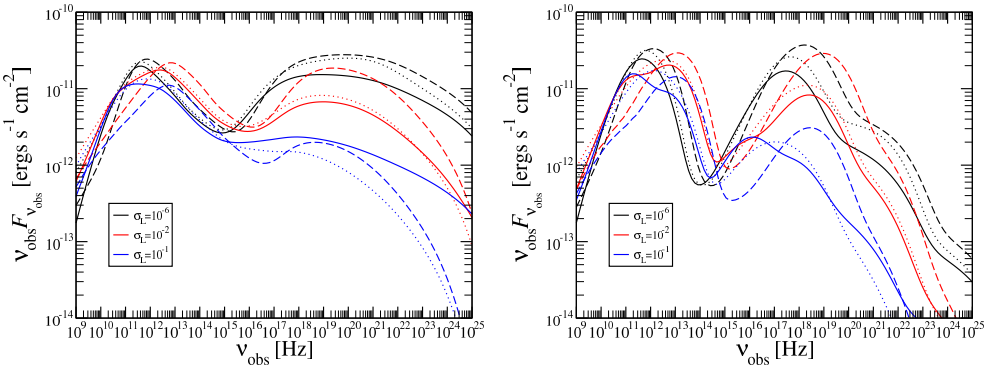

Figure 5.4: *Averaged spectra for different fast shell magnetization, σ_L, with nonthermal particles population fraction $\zeta_e = 0.9$ and 0.1 (left and right panels, respectively). The solid, dotted and dashed lines correspond to a magnetization of the slower shell $\sigma_R = 10^{-6}, 10^{-2}$ and 10^{-1}, respectively. As was shown in RMA14, the strongly magnetized fast shells do not display a prominent second bump at high frequencies. The synchrotron peak in all cases and in both panels, does not surpass $\sim 10^{13}$ Hz.*

factor $\Delta g = 1.0$ produced a SSC component less intense than the synchrotron component. Another important feature in these spectra is the emergence of a second bump in the synchrotron component at the near infrared (10^{14} Hz), which corresponds to emission coming from the reverse shock. The effect of changing ζ_e at high frequencies is that the larger the nonthermal population of electrons the broader the SSC component. Moreover, it can be seen that the FS cannot by itself reproduce the double bump structure of the SED for blazars, and that the emission coming from the RS dominates and clearly shapes the overall spectrum. More specifically, the emission due to the RS is γ-ray louder than that of the FS.

The inclusion of a thermal population in the EED combined with a variation of the relative shell Lorentz factor has a potentially measurable impact on the blazar spectra modelling. If narrower SSC peaks and a much steeper decay post-maximum are observed, that could identify the presence of a dominant thermal emission (Figure 5.5; right). The slope of the γ-to-TeV spectrum becomes steeper and more monotonically decaying as Δg increases for thermally-dominated EEDs.

5.3.4 Lorentz factor of the slower shell

In Figure 5.6 we depict the SEDs resulting from the collision of weakly magnetized shells with different Γ_R and ζ_e. The solid lines correspond to $\zeta_e = 0.9$ (models

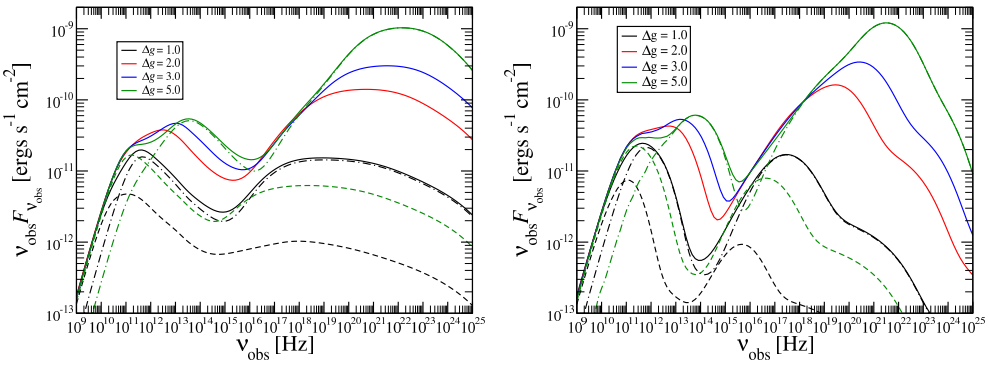

Figure 5.5: *Averaged spectra for different relative Lorentz factors and fractions of nonthermal particles. On the left panel we present the SED from a particle distribution with* $\zeta_e = 0.9$ *while on the right panel we show the SED for the same conditions, but with* $\zeta_e = 0.1$*. For the models with* $\Delta g = 1.0$ *(black lines) and* $\Delta g = 5.0$ *(green lines) the FS and the RS individual contributions are depicted in dashed and dot-dashed lines, respectively. The models depicted are* ***W*-*G*10-*D*(1.0, . . ., 5.0)-*Z*09-*L*1** *(left panel) and* ***W*-*G*10-*D*(1.0, . . ., 5.0)-*Z*m1-*L*1** *(right panel).*

W-**G**(2, 10, 20)-**D**1.0-**Z**09-$\mathcal{L}$1) while the dashed lines correspond to $\zeta_e = 0.1$ (modelsW-G(2, 10, 20)-D1.0-Zm1-$\mathcal{L}$1). The general trend is that the brightness of the source suffers an attenuation as Γ_R increases, regardless of ζ_e. From Eq. (2.41) we can see that an increase of the bulk Lorentz factor of a shell at constant luminosity implies a lower particle density number. Therefore, less particles are accelerated at the moment of the collision, which explains the overall flux decrease as Γ_R increases. Over almost the whole frequency range the brightness of models depends monotonically on Γ_R, brighter models corresponding to smaller values of Γ_R. However, the relative importance of the SSC component does not follow a monotonic dependence. At the lowest value of Γ_R the SSC component is brighter than the synchrotron component by one order of magnitude; with a steeper decay at high frequencies, though. This monotonic behavior is only broken in the vicinity of the synchrotron peak when the beaming cone half-opening angle ($\sim 1/\Gamma_R$) falls below the angle to the line of sight ($\theta = 5°$). This explains the larger synchrotron peak flux when $\Gamma_R = 10$ than when $\Gamma_R = 2$. In addition, models with $\Gamma_R = 20$ (**W**-**G**20-**D**1.0-**Z**(09,m1)-$\mathcal{L}$1) suffer a greater attenuation due to Doppler deboosting (see Rueda-Becerril et al. 2014b). In these models the half-opening angle of the beamed radiation is smaller than the observer viewing angle, therefore the apparent luminosity decreases.

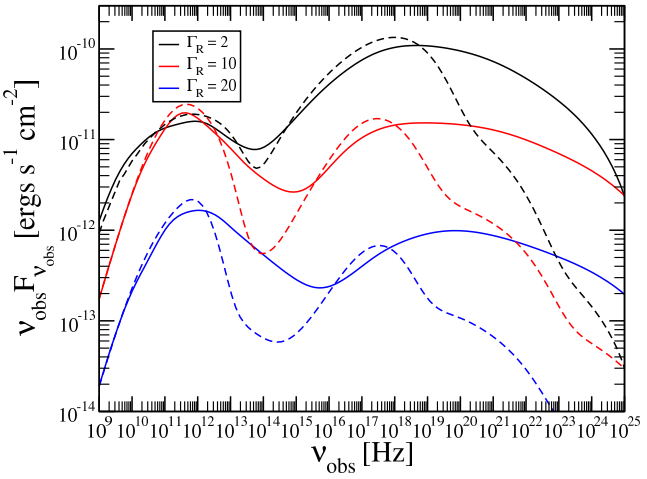

Figure 5.6: *Averaged spectra for weakly magnetized shells with varying slower shell bulk Lorentz factor, Γ_R, and two different nonthermal particles fractions: $\zeta_e = 0.9, 0.1$, solid and dashed lines respectively.*

5.3.5 Total luminosity

The number of particles accelerated by the internal shocks is an important quantity in our treatment of EEDs. The number of particles in each shell is dictated by Eq. (2.41). Such a direct influence of the luminosity on the number of particles motivates us to study the behaviour of the SEDs when this parameter is changed. In Figure 5.7 we show the SEDs produced by the IS model with different total jet luminosities and values of ζ_e (models **W**-**G**10-**D**1.0-**Z**(09, m1)-$\mathcal{L}$(1, 5, 50)). With solid and dashed lines we differentiate the HDs with $\zeta_e = 0.9, 0.1$, respectively, and in black, red and blue the luminosities $\mathcal{L} = 10^{47}, 5 \times 10^{47}, 5 \times 10^{48}$, respectively. The increase in flux of the thermally or nonthermally dominated cases is rather similar, and follows the expectations. An increase by 50 in the total luminosity $\mathcal{L}$ implies an overall increase of 100 in the particle density according to Eq. (2.41). Hence, the expected increase in flux in the synchrotron component is proportional to $n_i \sim 100$, while in the SSC component it is proportional to $n_i^2 \sim 10^4$.

5.4 Temperature vs. magnetization

The ratio between the thermal pressure and rest-mass density χ (which is proportional to the fluid temperature) is calculated by the exact Riemann solver for each shell collision. Assuming that the jet is composed of protons and electrons, the dimensionless temperature of the electrons in the plasma is $\Theta_e = \chi m_p / m_e$, where m_p is

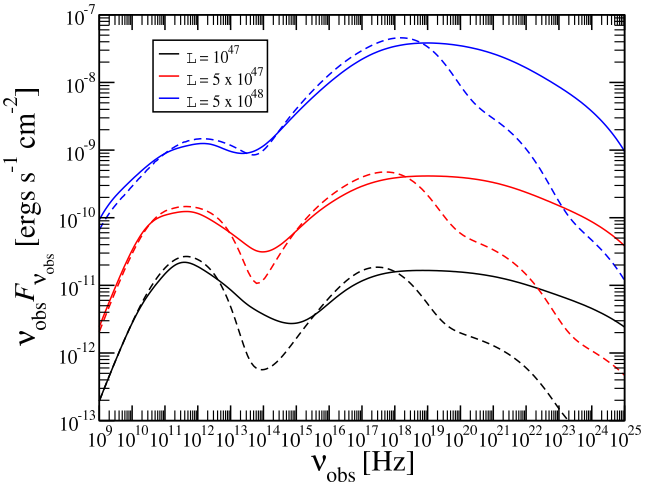

Figure 5.7: *Averaged spectra for different jet total luminosity. Solid and dashed lines display the models with* $\zeta_e = 0.9, 0.1$, *respectively. Different color lines correspond to different values of the jet luminosity (see legend).*

the proton mass. In order to systematically explore the dependence of the temperature on the properties of the shells we solved a large number of Riemann problems for different magnetizations and relative Lorentz factor. Here we present the behaviour of Θ_e in the ISs model in order to obtain insight into the temperature of the thermal component of the EED in the shocks. In Figure 5.8 we show the value of Θ_e as a function of the magnetizations σ_L and σ_R for both FS and RS (left and right panels, respectively).

The hottest region of the RS plane ($\sigma_L < 1$ and $\sigma_R > 0.1$) corresponds to the coldest region in the FS plane. Indeed, comparing both figures we observe that the RS is hotter than the FS wherever $\sigma_L \lesssim 0.2$ or $\sigma_R > 0.1$. As a result, in most of the moderately and weakly magnetized models, the radiation produced by the population of injected electrons that are thermally dominated could come from the RS. However, for $\sigma_R \lesssim 0.2$ and $\sigma_L \gtrsim 0.2$ the oposite true: the FS is hotter than the RS.

In Figure 5.9 we show the behavior of the electron temperature Θ_e in terms of the relative Lorentz factor Δg between the colliding shells for the FS and RS. In accordance with figures 5.8, the reverse shock is hotter than the forward shock. As the relative Lorentz factor Δg grows the temperature of the reverse shock tends to grow while the forward shock seems to be approaching asymptotically to a value, which depends slightly on the magnetization (the larger the magnetization the smaller the asymptotic temperature). Values $\Delta g > 5$ are inconsistent with the blazar scenario, for a fixed value $\Gamma_R = 10$, since they would imply that the faster shell was moving at

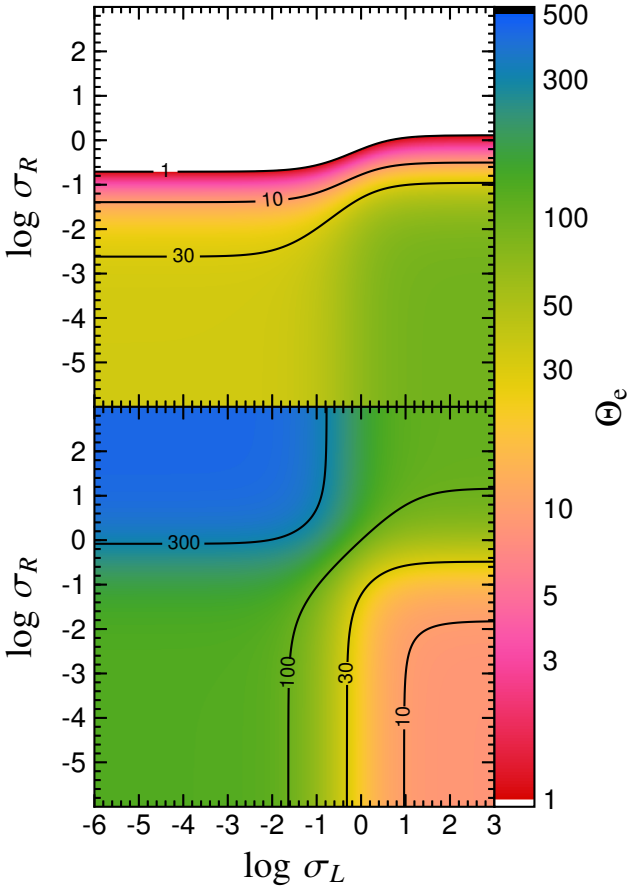

Figure 5.8: *Dependence of the electron temperature on shell magnetization. The top and bottom panels show the behaviour of Θ_e in the FS and RS, respectively. Contour lines of selected temperatures are overlaid in both panels.*

$\Gamma_L > 60$ (in excess of the maximum values of the Lorentz factor for the bulk motion inferred for blazars).

From figures 5.8 and 5.9 we can infer that Θ_e does not only depend on the velocity of the fluid but also on its magnetization. Therefore, we conclude that this degeneracy makes the determination of Θ_e a very difficult task.

5.5 Discussion and conclusions

In this work we introduce a hybrid thermal-nonthermal electron distribution into the internal shock model for blazars. To account for the fact that the thermal component of the HD extends to very low electron Lorentz factors, we also introduce a cyclo-synchrotron code that enables us to compute the nonthermal emission from electrons

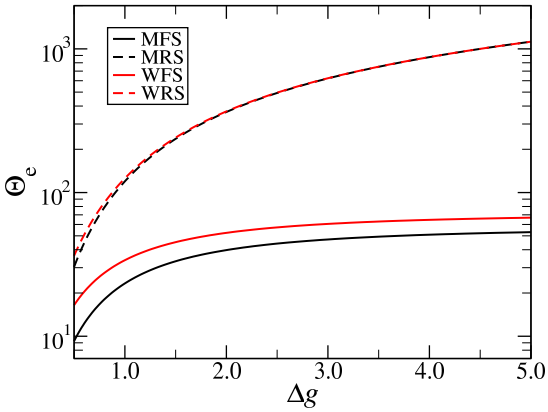

Figure 5.9: *Temperature as a function of the relative Lorentz factor. In this figure we show the temperature of both forward (full lines) and reverse (dashed lines) shocks for the weakly (red lines) and moderately (black lines) magnetized models. The value of the bulk Lorentz factor of the slower shell for both magnetization is* $\Gamma_R = 10$.

with arbitrary Lorentz factor. We show that our method for treating the temporal evolution of the HD and the calculation of MBS emission can be performed efficiently and with sufficient accuracy. The method is implemented as a generalization of the numerical code of MA12 (see Chapter 3).

To test the influence of the fraction of nonthermal particles ζ_e in the overall HD we apply the new method to the case of a blazar with $\mathcal{L} = 10^{47}\,\mathrm{erg\,s^{-1}}$ (Figure 5.3). Considering only MBS and SSC emission processes we see that increasing ζ_e (i.e., the distribution becoming more nonthermal) has as a consequence a shallower valley between the two spectral peaks, while the SSC emission extends to higher energies. In other words, a HD of mostly thermal particles emits only up to MeV (except when $\Delta g \sim 5$; see Figure 5.5). This would mean that the emission in the GeV range for the thermally-dominated HD cannot come from the SSC and would have to be produced by the EIC (not considered here). Furthermore, Figure 5.3 confirms that also for low ζ_e highly-magnetized blazar jets seem to be observationally excluded because their SSC peak is too dim.

Another effect of decreasing ζ_e is the shift of the SSC peak to lower frequencies and the narrowing of the high-frequency spectral bump, while at the same time the synchrotron peak and flux do not change appreciably. This means that (excluding possible effects from varying EIC) the Compton dominance (ratio of internal Compton and cyclosynchrotron luminosity) can be changed by varying ζ_e, while the peak MBS frequency remains constant. In other words, for all other parameters remaining constant, the variations in ζ_e may explain the vertical scatter in the distribution of FSRQs and BL Lacs in the peak synchrotron frequency-Compton dominance param-

eter space (see e.g., Figure 5 in Finke 2013). Changing ζ_e appears to not be able to change the blazar class.

Regarding the variations of the shell magnetization (§5.3.2), relative Lorentz factor (§5.3.3) and the bulk Lorentz factor (§5.3.4), the results are consistent with those of RMA14 (see Chapter 4). In this work we performed a more detailed study of the influence of the magnetization than in RMA14 since now we study 9 possible combinations of faster and slower shell magnetizations, instead of only three in RMA14. The truly novel result of this work is that the RMA14 trend generally holds for the thermally-dominated HD as well (right panel in Figure 5.4), with the difference that the collision of ($\sigma_L = 0.1, \sigma_R = 0.1$) shells produces a double-peaked spectrum for $\zeta_e = 0.1$, while its nonthermally dominated equivalent does not (blue dashed lines in Figure 5.4). Even so, the SSC component remains very dim for very magnetized shells.

Regarding Δg, the RS emission (dot-dashed lines in Figure 5.5) is crucial for reproducing the blazar spectrum. Therefore, in the case of $\zeta_e \ll 1$ the temperature of the RS is one of the most important parameters. Since this temperature increases with Δg (Figure 5.9), the effect of Δg on the MBS and the SSC peak frequencies and fluxes is qualitatively similar to that of the nonthermal electron distribution (Figure 5.5; see also RMA14). The changes induced by variations of Γ_R (Figure 5.6) are independent of the thermal/nonthermal EED content and agree with RMA14. The effects of the increase in total jet luminosity are visible both for $\zeta_e = 0.1$ and $\zeta_e = 0.9$. Varying the luminosity by a factor 50 increases the MBS flux by $\sim 10^2$ and the SSC flux by $\sim 10^4$. The relation between spectral components is very similar to the variations of Γ_R, i.e. the increase in $\mathcal{L}$ is similar to a decrease in Γ_R.

Overall, we show that the inclusion of the full cyclo-synchrotron treatment, motivated by the significant low-energy component of the HD, has a moderate effect on the blazar spectrum at optical-to-γ ray frequencies. However, at lower frequencies (e.g., below 1 GHz) where the self-absorption may play a role the differences between the synchrotron and the MBS will be more severe. We plan to include the effect of absorption in a future work as well as the effects by EIC emission.

Chapter 6

Conclusions and future work

In the present chapter we enclose the overall conclusions and the outlook of the present thesis We point out that more detailled conclusions have been spelled out at the end of each individual chapter. Here we recap the most salient features of this research.

6.1 Conclusions

To be able to perform consistent numerical simulations of astrophysical phenomena robust, easy to maintain and resource-saving computational tools are necessary. In order to be able to reproduce the observations of astrophysical objects on Earth, adequate numerical tools must be chosen and a well structured algorithm needs to be designed. For that purpose, one has to constantly keep up-to-date with state of the art of the theory, numerical techniques and observations. Otherwise, one runs the risk of misinterpreting the data and/or failing to correctly interpret them. In this thesis we have presented the methodology used to simulate the SED of blazars, following the shock-in-jet model.

Two complementary research projects have been presented here. They deal with the internal shock model for magnetized relativistic outflows, and are applied to blazars. The first one consisted of a parameter space scan that was performed using the IS code (MA12). The numerical results (e.g., synthetic SEDs) were compared with observational data (Chapter 4 and RMA14). This investigation stem from the

hypothesis that the radiation produced at the shocks propagating through the magnetized shells should contain a signature (in the observed SED) of the degree to which the shells are magnetized. We have found that, indeed, the magnetization plays an important role, leaving easily identifiable patterns in the SEDs and in the A_C–$\nu_{\rm syn}^{\rm obs}$ plane. In the latter, we identified the parameters whose variations account for the blazar sequence.

The second research project consisted of two sub-projects: the inclusion of thermal electrons to the population of injected ones at the shock front, and the proper treatment of MBS emission by nonrelativistic and transrelativistic electrons (Chapter 5 and RMA17). The idea for the former arose from previous studies of the thermal signatures in the light curves of GRBs (Giannios & Spitkovsky 2009), and from results out of PIC simulations (Sironi et al. 2013), which suggest that a large fraction of the energy dissipated in weakly magnetized shocks probably goes into a distribution of thermal electrons. This distribution extends from very low electron energies (i.e., Lorentz factors) to moderate electron energies, where it smoothly joins a power-law, high-energy tail. Including a full treatment of the MBS emission, was triggered by two basic facts. First of all, for consistency. Since the spectral radiated power of slow and mildly relativistic electrons develop a shape far from continuous (Mahadevan et al. 1996), contrary to what the synchrotron emission of ultrarelativistic electrons predicts (Rybicki & Lightman 1979; Jackson 1999). On the second place, because actual particle acceleration in shocks likely produces a broad electron distribution extending from very low electron Lorenz factors ($\gamma \gtrsim 1$) as we have commented. Furthermore, even if initially the accelerated electrons possess large Lorentz factors, they may eventually be cooled down by radiative or adiabatic loses. Hence, the lower energy end of the electron energy distribution may approach the limit $\gamma \sim 1$. In that limit, the standard (ultrarelativistic) synchrotron approximation breaks down and a complete MBS treatment becomes mandatory. We stress that, while the former effect could be ignored if the electron energy distribution is set up with a sufficiently large minimum Lorentz factor, the latter effect is almost unavoidably hit in evolutionary models. One only needs to wait long enough until the adiabatic expansion of the injected particles cools them down, or incorporate strong enough magnetic fields for that to happen. The simulations that include these two effects revealed that the presence of thermal (in addition to the nonthermal) electrons during the shock ac-

celeration moderately affects the spectrum at optical-to-γ ray frequencies, while $\nu_{\rm syn}^{\rm obs}$ suffers little variation. This means that the source location in the A_C–$\nu_{\rm syn}^{\rm obs}$ plane will suffer a vertical displacement; perhaps explaining a scatter of the FSRQ region and LSP region.

6.2 Future work

On the code-development side and regarding the new *RMA* function (3.71), the optimal value of the parameter $a_{\rm coff}$ must be estimated. To achieve this goal, we plan to calculate and compare systematically the accumulated relative error between the MBS emissivities using (3.71) and (3.56), for different values of $a_{\rm coff}$. We expect to obtain a value which can help us reducing the branching of (3.71). In other words, our intention is to find a fit which correctly takes into account the cut-off.

Regarding the IS model for blazars, further examination of the effects of the variations in magnetization and HDs including the full MBS emission on blazars SEDs are a clear goal, for which we intend to include the effects of absorption and EIC emission. Microphysical processes in this scenario are critical to understanding how are the particles being accelerated at relativistic shocks. The microphysical parameters $a_{\rm acc}$ and $\Delta_{\rm acc}$, which regulate the acceleration timescale and the size of acceleration region of the electrons, respectively, have already been studied and show novel effects in the light-curves of blazars. However, decisive studies are still pending and we expect these results to be part of some future publication soon. However, not only are the variations of parameters of the current version of the blazars code in the pipeline, but we are already working on the implementation of the SSC cooling (e.g. Chiaberge & Ghisellini 1999), as well as on the calculation the absorption coefficient (e.g. Ghisellini & Svensson 1991) out of MBS process for direct application to simulations of blazars.

In the astrophysical context, and regarding relativistic outflows in particular, the present thesis sets a landmark for the exploration of phenomena beyond blazars. For instance, the late-time flattening of light curves of GRBs afterglows, in the so called deep Newtonian phase (e.g. Huang & Cheng 2003; Sironi & Giannios 2013), is an ideal scenario in which the numerical tools showed in previous chapters could afford means to explore GRB remnants. This is because at this stage the accelerated elec-

trons at the shock front of the blast wave become transrelativistic (Sironi & Giannios 2013), and thus the effects of both MBS and HD may become relevant.

Likewise, further comparisons with observations must be performed to prove the model. However, since the emission region in our simulations is in sub-parsec scales, data from higher resolved observations from the high-energy emission region of blazars is needed in order to carry out proper comparisons of, e.g., the SEDs.

Appendix A

Numerical logarithmic functions

While performing the integrals in the SSC and EIC calculations we may encounter cases where the logarithmic function has an argument ∼1. In order to avoid numerical pathologies and the loss of precision that may be compiler- or library-dependent, the logarithmic functions were numerically extended on the basis of their Taylor series expansion around 1. In this way we can control their behaviour regardless of the way that a particular compiler or library treats the case of an argument being close to 1. In Table A.1 we describe the aforementioned functions, showing their respective expansion and tolerance functions (the second term of the series expansion). If the tolerance is below some threshold $\varepsilon_{\log}$ then we use the series expansion up to the first term, otherwise the intrinsic function of the programming language (i.e., `FORTRAN`, `C++` or `Python`) is called.

Name	Function	Series expansion	Tolerance function	$> \varepsilon_{\log}$	$\leq \varepsilon_{\log}$	$\varepsilon_{\log}$
`Log1`	$\log$	$(x-1) - \frac{1}{2}(x-1)^2 + O(x-1)^3$	$0.5(x-1)^2$	$\log(x)$	$x-1$	10^{-9}
`Log2`	$\log^2$	$(x-1)^2 - (x-1)^3 + O(x-1)^4$	$(x-1)^3$	$\log^2(x)$	$(x-1)^2$	10^{-9}
`Log3`	$\log^3$	$(x-1)^3 - \frac{3}{2}(x-1)^4 + O(x-1)^5$	$1.5(x-1)^4$	$\log^3(x)$	$(x-1)^3$	10^{-9}
`Log4`	$\log^4$	$(x-1)^4 - 2(x-1)^5 + O(x-1)^6$	$2.0(x-1)^5$	$\log^3(x)$	$(x-1)^4$	10^{-9}
`Log5`	$\log^5$	$(x-1)^5 - \frac{5}{2}(x-1)^6 + O(x-1)^7$	$2.5(x-1)^6$	$\log^5(x)$	$(x-1)^5$	10^{-9}

Table A.1: *Alternative logarithmic functions. In this table we outline the functions implemented in the code, and their corresponding analytic function. These functions were defined making use of a Taylor series expansion around 1 (third column). Here we also show the tolerance function (fourth column) for each function, which corresponds to the second term in the series expansion Fifth and sixth columns show which expressions is used if the tolerance function returns a value above of below the tolerance $\varepsilon_{\log}$. The last column shows the value of $\varepsilon_{\log}$ used for each function.*

Appendix B

Constants, units and models

The system of units used in this thesis was CGS.

Name	Symbol	Value (≈)	Units
Speed of light	c	$2.997\,92 \times 10^{10}$	$\mathrm{cm\,s^{-1}}$
Electron charge	e	$4.803\,20 \times 10^{-10}$	$\mathrm{cm^{3/2}g^{1/2}s^{-1}}$
Mass of electron	m_e	$9.109\,39 \times 10^{-28}$	g
Mass of proton	m_p	$1.672\,62 \times 10^{-24}$	g
Blotzmann constant	k_B	$1.380\,65 \times 10^{-16}$	$\mathrm{erg\,K^{-1}}$
Thomson crossection	σ_T	$6.652\,46 \times 10^{-28}$	$\mathrm{cm^2}$
Planck constant	h	$6.626\,08 \times 10^{-27}$	erg s

Table B.1: *Physical constants constants in the CGS system.*

Name	Symbol	Conversion factor	Units
Solar mass	$M_\odot$	$1.988\,55 \times 10^{33}$	g
Jansky	Jy	10^{-23}	$\mathrm{erg\,s^{-1}\,cm^{-2}\,Hz^{-1}}$
Light year	ly	$9.460\,73 \times 10^{17}$	cm
Parsec	pc	$3.085\,68 \times 10^{18}$	cm

Table B.2: *Astronomical constants and units in the CGS system.*

Name	σ_R	σ_L	Γ_R	Δg	θ	ζ_e	$\mathcal{L}$ (erg s^{-1})
S-**G**10-**D**1.0-**T**3	0.1	1.0	10	1.0	3°	1.0	5×10^{48}
W-**G**10-**T**5	10^{-6}	10^{-6}	10	0.5–2.0	5°	1.0	5×10^{48}
M-**D**1.5	10^{-2}	10^{-2}	10–25	1.5	1–10°	1.0	5×10^{48}
W-**G**10-**D**0.5-**T**5	10^{-6}	10^{-6}	10	0.5	5°	1.0	5×10^{48}
W-**G**10-**D**2.0-**T**2	10^{-6}	10^{-6}	10	2.0	5°	1.0	5×10^{48}
W-**D**1.0-**T**5	10^{-6}	10^{-6}	10–25	1.0	5°	1.0	5×10^{48}
M-**G**10-**T**5	10^{-2}	10^{-2}	10	0.5–2.0	5°	1.0	5×10^{48}
M-**D**1.0-**T**5	10^{-2}	10^{-2}	10–25	1.0	5°	1.0	5×10^{48}
M-**G**10-**D**1.0-**T**5	10^{-2}	10^{-2}	10	1.0	5°	1.0	5×10^{48}
M-**G**25-**D**1.0-**T**5	10^{-2}	10^{-2}	25	1.0	5°	1.0	5×10^{48}
M-**G**10-**D**0.5-**T**5	10^{-6}	10^{-6}	10	0.5	5°	1.0	5×10^{48}
M-**G**10-**D**1.0	10^{-2}	10^{-2}	10	1.0	1–10°	1.0	5×10^{48}
S-**G**10-**D**2.0-**T**5	0.1	1.0	10	2.0	5°	1.0	5×10^{48}
S-**G**10-**T**5	0.1	1.0	10	0.5–2.0	5°	1.0	5×10^{48}
S-**D**1.0-**T**5	0.1	1.0	10–25	1.0	5°	1.0	5×10^{48}
S1-**G**10-**T**5	0.1	0.1	10	1.0	5°	1.0	5×10^{48}
S2-**G**10-**T**5	1.0	0.1	10	0.5–2.0	5°	1.0	5×10^{48}
S-**G**10-**D**1.0	0.1	1.0	10	1.0	1–10°	1.0	5×10^{48}

Table B.3: *IS models (in order of appearance) studied in Chapter 4.*

Name	$\sigma_{\rm R}$	$\sigma_{\rm L}$	$\Gamma_{\rm R}$	Δg	θ	$\zeta_{\rm e}$	$\mathcal{L}$ (erg s^{-1})
W-**G**10-**D**1.0-**Z**m1-$\mathcal{L}$5	10^{-6}	10^{-6}	10	1.0	5°	0.1	5×10^{47}
W-**G**10-**D**1.0-**Z**09-$\mathcal{L}$1	10^{-6}	10^{-6}	10	1.0	5°	0.9	10^{47}
M-**G**10-**D**1.0-**Z**09-$\mathcal{L}$5	10^{-2}	10^{-2}	10	1.0	5°	0.9	5×10^{47}
M-**G**10-**D**1.0-**Z**09-$\mathcal{L}$1	10^{-2}	10^{-2}	10	1.0	5°	0.9	5×10^{47}
W-**G**10-**D**(1.0, ..., 5.0)-**Z**m1-$\mathcal{L}$1	10^{-6}	10^{-6}	10	1.0–5.0	5°	0.1	10^{47}
W-**G**10-**D**(1.0, ..., 5.0)-**Z**09-$\mathcal{L}$1	10^{-6}	10^{-6}	10	1.0–5.0	5°	0.9	10^{47}
W-**G**(2, 10, 20)-**D**1.0-**Z**09-$\mathcal{L}$1	10^{-6}	10^{-6}	2, 10, 20	1.0	5°	0.9	10^{47}
W-**G**20-**D**1.0-**Z**(09,m1)-$\mathcal{L}$1	10^{-6}	10^{-6}	20	1.0	5°	0.9, 0.1	10^{47}
W-**G**10-**D**1.0-**Z**(09, m1)-$\mathcal{L}$(1, 5, 50)	10^{-6}	10^{-6}	10	5°	1.0	0.9, 0.1	10^{47}, 5×10^{47}, 5×10^{48}

Table B.4: *IS models (in order of appearance) studied in Chapter 5.*

Appendix C

Acronyms and symbols

C.1 Acronyms

BL Lac	BL Lacertae object
EoS	equation of state
2LAC	*Fermi* LAT Second AGN Catalog
AD	accretion disc
AGN	active galactic nucleus
BAL QSO	broad absorption line quasar
BH	black hole
BLR	broad line region
CAMAP	*Computer Aided Modeling of Astrophysical Plasma*
CD	contact discontinuity
EED	electrons energy distribution
EHF	extremely high frequency band
EIC	external inverse-Compton
FS	forward shock
FSRQ	Flat Spectrum Radio Quasar
GRB	γ-ray burst

HBL	high-frequency-peaked BL Lac object
HD	hybrid distribution
HSP	high-synchrotron peaked
IBL	intermediate-frequency-peaked BL Lac object
IC	inverse-Compton
IS	internal shock
ISP	intermediate-synchrotron peaked
LBL	low-frequency-peaked BL Lac object
LSP	low-synchrotron peaked
MBS	magnetobremsstrahlung
MHD	magnetohydrodynamics
NLR	narrow line region
NLRG	narrow line radio galaxy
OTAD	optically thick accretion disk
PIC	particle-in-cell
QSO	quasi-stellar object
RMHD	relativistic magnetohydrodynamics
RS	reverse shock
SED	spectral energy distribution
SMBH	super massive black hole
SSC	synchrotron self-Compton
TD	dusty torus
TDE	tidal disruption event

C.2 Symbols

a_{acc}	Acceleration efficiency parameter
A_C	Compton dominance
a_{coff}	cut-off parameter of the *RMA* function
Δ_{acc}	Width of acceleration zone parameter
Δg	Relative Lorentz factor
ϵ_{B}	Fraction of the internal energy density of the plasma transformed into magnetic field

ϵ_e	Fraction of the shock power transferred to the charged particles
F_{ph}	Photons flux
Γ	Bulk Lorentz factor
γ	Electron Lorentz factor
γ_c	Cooling Lorentz factor
$\{\hat{\gamma}_{min}\}$	Lorentz factors cutoffs array
Γ_{ph}	Photon spectral index
$\mathcal{L}_{IC}$	Luminosity of the IC component of the SED
$\mathcal{L}_{syn}$	Luminosity of the synchrotron component of the SED
ν_0	Particles cooling term
ν_B	Gyrofrequency
$\bar{\nu}_c$	Critical frequency
ν_c	Critical frequency for pitch angle $\pi/2$
ν_g	Cyclotron frequency
ν_{IC}^{obs}	Peak frequency of the SED IC component
ν_{syn}^{obs}	Peak frequency of the SED synchrotron component
r	Compression factor
r_g	Larmor radius
RMA	RMA function
σ	Magnetization
t_{cr}	Shock crossing time
u_B	Magnetic energy density
u_{ext}	External photon field energy density
$\mathcal{X}$	Harmonic frequency
X_c	ν/ν_c
$\bar{X}_c$	$\nu/\bar{\nu}_c$
z	Redshift

Tratamiento numérico de procesos radiativos en choques internos de flujos relativistas magnetizados

Los blázares son un tipo de núcleo activo de galaxia (AGN, por sus siglas en ingés) que se encuentran entre los objetos astrofísicos más energéticos y violentos, a la par de los brotes de rayos γ (GRB por sus siglas en inglés). Los procesos físicos y, en particular, el escenario del chorro relativista en el que se genera la radiación ultraenergética detectada por observatorios terrestres y en órbita, han conseguido atraer la atención e interés de los astrónomos y astrofísicos desde su descubrimiento. En la presente tesis investigamos el modelo de choques internos (IS) cuya hipótesis consta del choque de dos capas de plasma con geometría cilíndrica, formando dos ondas de choque que atraviesan las antedichas capas acelerando electrones a su paso: tanto térmicos como no térmicos. Dichos electrones interaccionan con el campo magnético presente en el chorro produciendo, de acuerdo con las observaciones, emisión magnetobremsstrahlung (MBS). En este modelo consideramos también que el chorro se encuentra envuelto en un ambiente de fotones monocromático, que equivaldría a la región de banda ancha (BLR) de un AGN. Ambos tipos de fotones, los del medio externo y los producidos in situ, eventualmente interaccionan con los electrones acelerados mediante la dispersión Compton inversa (IC).

El objetivo básico de la presente tesis ha sido la búsqueda de algún indicio que

pudiera revelar las huellas dejadas tanto por la magnetización de las capas como por la distribución energética de los electrones (EED) inyectados en el frente de choque, en la distribución espectral de energía (SED). Nuestro enfoque ha sido numérico, lo cual significa que se desarrollaron herramientas numéricas sofisticadas que hemos usado sistemáticamente para simular el modelo de IS y reproducir las SEDs espectralmente amplias de los blazares. Datos observacionales fueron empleados para corroborar dichas simulaciones y delimitar el espacio de parametros para, de esta forma, conseguir que nuestras SEDs sintéticas estuviesen en concordancia con las observaciones.

Mostramos a partir de simulaciones que, si examinamos la dominancia Compton, A_C, y el índice espectral de fotones, $\Gamma_{\rm ph}$, en la banda de rayos γ, una parte considerable de la *sequencia de los blázares* podría ser explicada por la magnetización de las capas; siendo las menos magnetizadas las que se encuentran en la región de los radiocuásares de espectro plano (FSRQs), mientras que las capas medianamente magnetizadas caen en la región de los objetos *BL Lacertae* (BL Lac). Por otra parte, al incluir electrones térmicos en la población inyectada, y agregar una herramienta numérica que nos permite reproducir la emisión MBS de electrones poco energéticos, encontramos que el valle que separa las componentes sincrotrón e IC, se hace más "profundo" cuando las distribuciones inyectadas en el frente de choque son dominadas por electrones térmicos. Para estos casos descubrimos que el pico sincrotrón varía ligeramente entre modelos (entre 10^{11}–10^{13} Hz), al contrario de una componente IC sensible a la variación de parámetros. Este efecto induce una disperción vertical en el plano dominancia Compton-pico sincrotrón, sugiriendo que quizá la proporción de electrones térmicos sobre los no térmicos está relacionada con la posición de los blázares en ese plano.

Prefacio

En el Capítulo 2 profundizamos en los conceptos físicos sobre los que reside la emisión MBS y el modelo de IS para blazars. Empezamos describiendo la dinámica y electrodinámica de una partícula cargada inmersa en un campo magnético homogéneo. Continuamos con la descripción de la dinámica de de la colisión de dos capas de plasma, como parte del modelo de IS, basándonos en el trabajo de Mimica & Aloy (2012). La última parte de dicho capítulo consiste en la descripción de los

diferentes tipos de distribuciones de partículas, cómo modelamos la inyección en un frente de onda de choque y la evolución de partículas que se encuentran en una región que ha sido afectada por una onda de choque, considerando tanto el caso en el que no existe un término de enfriamiento en la ecuación de evolución como el caso en el que sí se considera dicho término en un intervalo de tiempo finito.

En el Capítulo 3 se engloba la descripción de las técnicas numéricas y métodos desarrollados y usados durante mi estancia en el grupo de investigación *Computer Aided Modeling of Astrophysical Plasma* (CAMAP) con el Prof. Miguel A. Aloy y el Dr. Petar Mimica. La primera parte de dicho capítulo está centrada en el código para IS desarrollado por Mimica & Aloy (2012), el cual es la piedra angular de la presente tesis. En la segunda parte describo detalladamente el código `CHAMBA`: una nueva herramienta computacional cuya intención es la de reproducir la emisividad MBS producida por una partícula cargada y por una distribución de partículas con perfil arbitrario. Nuestras publicaciones (Rueda-Becerril et al. 2014b, 2017) corresponden a resultados obtenidos del uso sistemático estas herramientas.

El Capítulo 4 está basado en la investigación hecha en el grupo CAMAP con el Prof. Miguel A. Aloy y el Dr. Petar Mimica, como continuación del trabajo previamente publicado por los miembros de este grupo (Mimica & Aloy 2012). Nuestro trabajo fue sujeto a revisión por pares y publicado en 2014: J. M. Rueda-Becerril, P. Mimica, & M. A. Aloy. The influence of the magnetic field on the spectral properties of blazars. *Monthly Notices of the Royal Astronomical Society*, **438**:1856–1869, Feb. 2014b. doi: 10.1093/mnras/stt2335. RMA14. Éste consistió en ampliar la exploración del espacio de parámetros del código para ISs desarrollado por el Dr. Petar Mimica y el Prof. Miguel A. Aloy para simular el modelo de IS para blazars, incluyendo el cómputo del índice espectral de fotones a partir de nuestras simulaciones (descrito en §4.5.1). Los datos observacionales que se muestran en dicho trabajo fueron obtenidos de la base de datos correspondiente al segundo catálogo de núcleos activos de galaxias del instrumento LAT a bordo del satélite *Fermi* (*Fermi* LAT Second AGN Catalog (2LAC), por sus siglas en inglés)[1]. Todas las simulaciones para este trabajo fueron realizadas en el superordenador `Tirant` de la Universidad de Valencia.

El Capítulo 5 está basado en la investigación hecha en el grupo CAMAP con

[1] `https://heasarc.gsfc.nasa.gov/W3Browse/all/fermilac.html`

el Prof. Miguel A. Aloy y el Dr. Petar. Nuestro trabajo se sometió a revisión por pares y resultó en un artículo publicado en 2017: J. M. Rueda-Becerril, P. Mimica, & M. A. Aloy. On the influence of a hybrid thermal–non-thermal distribution in the internal shocks model for blazars. *Monthly Notices of the Royal Astronomical Society*, **468**:1169–1182, June 2017. doi: 10.1093/mnras/stx476. RMA17. Los resultados ahí descritos son derivados de simulaciones hechas usando el código de IS (Mimica & Aloy 2012) para distribuciones híbridas de partículas (térmicas y no térmicas). Además de la implementación de la nueva herramienta numérica `CHAMBA` (§3.2)

La astrofísica ha sido para mi como salir a la aventura por la naturaleza. En ningún momento supe con qué me iba a topar en el camino pero cada paso me ha traído alegría y nuevos aprendizajes. Saber un poco de los fenómenos que ocurren allá arriba ha sido como respirar el aire fresco de los bosques, cuya brisa purifica los pulmones y te llena de paz, o como una lluvia torrencial que te empapa de ese vital líquido pero que es tanto que tienes que correr en busca de refugio. El proceso de proponer el desarrollo de una nueva herramienta numérica como `CHAMBA` me ha ayudado a tener una idea de lo que hay fuera. El proceso de escritura de dicho código, por otro lado, ha sido como subir a una montaña: nunca sabes si conseguirás llegar a la cima o si la naturaleza terminará enviando una tormenta que te obligará a replegar. Nuestro ascenso empezó en el campamento base *electrones ultra energéticos*. Allí planeamos nuestra ruta, siempre al pendiente de cualquier previsión de tempestad. Durante nuestros días en el campamento base tuvimos que respondernos a cuestiones fundamentales como si realmente vale la pena ir más allá de las cumbres transrelativistas, a las que muchos exploradores han subido y bajado con gran destreza por décadas, o quedarnos en las faldas del monte MBS. Con un impulso blazarístico decidimos abandonar la tranquilidad del campamento base adentrarnos en el corazón de la montaña. En el camino tuvimos que atravesar barrancos de grava (numérica) inestable, escalar y rapelar despeñaderos y riscos impresionantes. Ergios y ergios de paredes verticales. Hubo momentos, incluso, en los que no había un solo agarre a la vista, rezando por que la cuerda aguantara. Para fortuna de nuestra expedición lo hizo, y conseguimos llegar a la cima ciclotrón.

Objetivos

En un intento por entender las observaciones de blazares, se han propuesto muchos modelos e hipótesis a lo largo de los años que han abierto un abanico de ideas sobre la física involucrada en los procesos de altas energías que en ellos ocurren. Aún así, no hay suficiente evidencia observacional que nos indique el grado de importancia de cada proceso físico que interviene en la producción de la emisión ultraenergética observada (p. ej., es bien sabido que los campos magnéticos juegan un papel importante en los flujos relativistas, pero no conocemos la magnetización del chorro ni sabemos con certeza si los campos magnéticos juegan un papel importante en los procesos de disipación los chorros). Hay modelos que se han propuesto para clasificar y unificar los AGNs (y blazars en particular). Sin embargo, no sabemos con certeza si estos modelos describen la verdadera naturaleza de los AGNs.

Vivimos en una época en la que los observatorios existentes y venideros, tanto terrestres como espaciales, observan el universo en muchas bandas espectrales, de modo que se espera que en los próximos años nueva información salga a la luz (valga la redundancia electromagnética) de todo tipo de objetos astrofísicos; con los blázares entre ellos. Sin embargo, la imposibilidad de replicar en el laboratorio las condiciones necesarias para observar y medir los procesos que producen, p. ej., las fulguraciones en blazares ha favorecido el desarrollo constante de códigos numéricos sofisticados que ejecutan simulaciones de estos procesos. Dichas simulaciones nos ayudan a tener una intuición física de los fenómenos astrofísicos; ya sea por comparación con los datos observacionales existentes, o por la predicción de las propiedades de futuros eventos. Los códigos de última generación para blázares incorporan tanta macro y microfísica como las capacidades computacionales lo permitan. Típicamente, existe un equilibrio entre ambas. Es decir, uno necesita decidir cuánto esfuerzo se dedica a las escalas macroscópicas (p. ej., procesos MHD) y cuánto a las microscópicas (p. ej., la aceleración en una onda de choque). En nuestro trabajo constantemente tratamos de mejorar nuestro modelado a ambos rangos de las escalas dinámicas en blázares.

El modelo de IS para blázares ha logrado modelar datos observacionales (e.g. Böttcher & Dermer 2010). Uno de nuestros principales objetivos de la presente tesis es el de ampliar el estudio del espacio de parámetros, iniciados por MA12, para el modelo de IS mediante el cálculo de la emisión, dependiente del tiempo y para

múltiples longitudes de onda, de varias familias de modelos; principalmente caracterizados por la magnetización de las capas. Partiendo de trabajos previos (Böttcher & Dermer 2010; Mimica 2004; Mimica & Aloy 2012; Mahadevan et al. 1996; Leung et al. 2011), pretendemos profundizar en la exploración del modelo de IS con el plan de identificar en las SEDs y curvas de luz, las huellas dejadas por la magnetización de las capas (macro escalas) y por las distintas propiedades de las partículas inyectados en el frente de onda de choque (micro escalas). Tomamos en cuenta la existencia de partículas subrelativistas y transrelativistas en la población de partículas inyectadas, por lo que englobamos los procesos de emisión ciclotrón, sincrotrón y ciclo-sincrotrón.

Metodología

En la presente tesis se estudian los mecanismos de emisión en blazars, una subclase de AGN en la que un chorro relativista se propaga en dirección cercana a la línea de visión de un observador en la Tierra (Urry & Padovani 1995). Una componente importante de la radiación observada en blazars es producida por la emisión no térmica de dicho chorro. Su espectro muestra dos crestas muy anchas. La primera está situada entre radiofrecuencias y rayos X, mientras que la segunda aparece entre los rayos X y los γ (p. ej. Fossati et al. 1998). Dependiendo de las frecuencias de máxima luminosidad y la intensidad de las líneas de emisión, los blazars pueden subdividirse en objetos BL Lac y FSRQ (Giommi et al. 2012a). Existe un consenso general de que el pico que aparece a bajas frecuencias se debe a la emisión sincrotrón de electrones relativistas que giran en un campo magnético. En cuanto que al pico a altas frecuencias, actualmente hay dos modelos en disputa: (a) el modelo leptónico que propone que la la emisión a altas energías es producida por los electrones relativistas que dispersan mediante el proceso IC tanto a los fotones fríos del medio externo (Compton inverso externo; EIC) y a los fotones tipo sincrotrón producidos in situ en el chorro (auto–Compton de sincrotrón; SSC), y (b) el modelo hadrónico que plantea la existencia de protones relativistas en el chorro que, en presencia de campos magnéticos muy intensos, son capaces de producir radiación ultraenergética a través tanto del proceso sincrotrón directamente, como de cascadas electromagnéticas (véase Böttcher 2010, para una discusión detallada de ambos modelos). En la presente tesis limitamos nuestro estudio al modelo leptónico.

En este trabajo, nos concentramos exclusivamente en la contribución del chorro relativista. El escenario de IS (p. ej. Rees & Mészáros 1994; Spada et al. 2001; Mimica et al. 2004) ha sido exitoso en explicar muchas de las características sobre la variabilidad en blázares. Como hipótesis central se encuentra la idea de que la presencia de movimientos relativos en el chorro relativista eventualmente producirá choques de capas densas de plasma frío. En el transcurso de la colisión de dichas capas, el plasma sufre los efectos del choque y parte de la energía cinética del chorro es disipada en el relativamente débil IS, lo que explicaría las fulguraciones observadas en las curvas de luz de estos eventos. En las dos últimas décadas este escenario ha sido explorado a fondo utilizando modelos analíticos y simplificados (Kobayashi et al. 1997; Daigne & Mochkovitch 1998; Bošnjak et al. 2009; Daigne et al. 2011) así como también por medio de simulaciones de hidrodinámica numérica (Kino et al. 2004; Mimica et al. 2004, 2007).

Esta tesis continúa a lo largo de las líneas esbozadas en trabajos anteriores (Mimica & Aloy 2012, MA12 de aquí en adelante), y extiende los trabajos publicados en el periodo de doctorado (Rueda-Becerril et al. 2014b, 2017, RMA14 y RMA17 de aquí en adelante, respectivamente). MA12 extiende el trabajo sobre la disipación (eficiencia dinámica) de los ISs magnetizados (Mimica & Aloy 2010), incluyendo procesos radiativos de una manera similar a los modelos detallados recientes para el cálculo de la emisión de los ISs (Böttcher & Dermer 2010; Joshi & Böttcher 2011; Chen et al. 2011). En MA12 se asume que la luminosidad del flujo es constante, pero se varía el grado de magnetización de las capas para investigar las consecuencias de dicha variación en los espectros y curvas de luz observadas. Encuentran que la eficiencia radiativa de una sola colisión de capas es máxima cuando una de ellas está altamente magnetizada y la otra posee un campo magnético débil o casi nulo. De igual menera, los autores proponen una manera de distinguir observacionalmente entre colisiones de capas escasa y altamente magnetizadas por medio de la comparación entre las frecuencias máximas y fluencias de las componentes sinctrotrón y IC.

Una de las limitaciones del estudio mostrado por MA12 es que sólo se varía la magnetización de las capas (aunque cuberiendo una gama relativamente amplia del potencial espacio de parámetros), dejando el resto de parámetros sin cambios. En este trabajo se presentan los resultados de un estudio paramétrico más sistemático en el que se consideran tres combinaciones de magnetizaciones de las capas que

Mimica & Aloy (2012) consideraron de interés, pero variando tanto los parámetros cinemáticos (el factor de Lorentz del fluido y la velocidad relativa de las capas) como los parámetros extrínsecos (p. ej., el ángulo de visión θ del chorro), mientras que los parámetros microfísicos se fijan a valores típicos.

La radiación emitida por blazes resulta de la disipación del flujo cinético y del flujo tipo Poynting. En la presente tesis consideramos el modelo de IS, en el cual la disipación antes mencionada es producida por la colisión de capas densas de plasma frío dentro del chorro relativista (p. ej. Rees & Mészáros 1994; Spada et al. 2001; Mimica et al. 2004). Cada colisión de dichas capas puede producir ISs que aceleran a los electrones que son, a fin de cuentas, los responsables de la emisión observada.

Nos centramos también en estudiar la influencia de las propiedades de la EED en la emisión observada. Giannios & Spitkovsky (2009) propusieron una EED; es decir Maxwelliana más no térmica (denominada en lo subsiguiente como "distribución híbrida", o simplemente HD) como una explicación de algunas de las características de la emisión temprana y de la posluminiscencia en GRBs. Para llevar a cabo dicho objetivo, introducimos una HD en nuestro código numérico y estudiamos cómo afecta a las curvas de luz y espectros de emición en blázares.

No obstante, dado que la componente térmica en una HD la energía de los electrones se extiende hasta regímenes subrelativistas, necesitamos replantear el mecanismo de emisión (sincrotrón) empleado hasta ahora. La radiación de partículas cargadas que atraviesan un campo magnético se conoce como MBS. Dependiendo de la velocidad βc de las partículas, esta radiación se clasifica en ciclotrón si $\beta \sim 1$, y sincrotrón si $\beta \sim 1$. Ambos regímenes han sido estudiados ampliamente y se han desarrollado expresiones analíticas precisas para cada uno (p. ej. Ginzburg & Syrovatskii 1965; Pacholczyk 1970; Rybicki & Lightman 1979). Sin embargo, la radiación ciclo-sincrotrón, es decir, el régimen transrelativista, no cuenta con una descripción analítica sencilla. Cumpliendo con uno de los objetivos de la presente tesis, en efecto, implementamos un modelo de emisión MBS en nuestro código, para poder tratar con precisión la emisión en todos los rangos de energía de la EED.

Para la evolución de las partículas inyectadas en los choques, suponemos que los procesos dominantes son el enfriamiento sincrotrón y la dispersión IC de los fotones producidos por el prooceso EIC. Para calcular los espectros y curvas de luz sintéticas, dependientes del tiempo y para múltiples frequencias, incluimos los pro-

cesos de emisión sincrotrón y IC resultantes del plasma que ha sufrido el choque. Consideramos además que la línea de visión del observador respecto al eje del chorro forma un ángulo θ. Una descripción detallada de cómo se realiza la integración de la ecuación de transferencia radiativa a lo largo de la línea de visión se puede encontrar en la sección §2.3.

Conclusiones

Para poder realizar simulaciones numéricas consistentes de fenómenos astrofísicos, se necesitan herramientas computacionales robustas fáciles de mantener y que sean eficientes en el uso de los recursos computacionales disponibles. Para poder reproducir las observaciones de los objetos astrofísicos en la Tierra, se deben elegir las herramientas numéricas adecuadas y diseñar un algoritmo bien estructurado. Para ello, hay que mantenerse al día con los postulados teóricos, técnicas numéricas y observaciones más recientes. De lo contrario, se corre el riesgo de malinterpretar los datos. En esta tesis hemos presentado la metodología utilizada para simular los SEDs de blázares, siguiendo el modelo de IS.

Aquí se han presentado dos proyectos de investigación complementarios. Ambos tratan el modelo de ISs para los flujos relativistas magnetizados y se aplica a los blázares. El primero consistió en la exploración del espacio de parámetros haciendo uso del código para ISs (MA12). Los resultados numéricos (p. ej., SEDs sintéticas) se compararon con datos observacionales (Capítulo 4 y RMA14). Esta investigación partió de la hipótesis que la radiación producida en los choques que se propagan a través de las capas magnetizadas debe contener la firma (en las SEDs observadas) del grado de magnetización de dichas capas. Hemos encontrado que, de hecho, la magnetización juega un papel importante y que, en efecto, deja patrones fácilmente identificables en las SEDs y en el plano A_C–$\nu_{\rm syn}^{\rm obs}$. En este último, hemos identificado los parámetros cuyas variaciones explican la secuencia de los blázares.

El segundo proyecto de investigación consistió en dos subproyectos: la inclusión de electrones térmicos en la población de los inyectados en el frente de choque y el tratamiento adecuado de la emisión MBS por electrones no relativistas y transrelativistas (Capítulo 5 y Rueda-Becerril et al. 2017). La idea para el primero surgió de estudios previos sobre la trazas térmicas en las curvas de luz de BRGs (Giannios & Spitkovsky 2009), y de resultados obtenidos con simulaciones de partículas

en céldas (PIC) (Sironi et al. 2013) que sugieren que una gran fracción de la energía disipada en choques escasamente magnetizados probablemente termina en electrones térmicos. En cuanto a un tratamiento completo de la emisión MBS, la motivación para esto provino del hecho de que la potencia radiada espectral de electrones lentos y ligeramente relativistas desarrollan patrones prácticamente discontinuos (Mahadevan et al. 1996), al contrario de lo que la emisión sincrotrón de electrones ultrarelativistas predice (Rybicki & Lightman 1979; Jackson 1999). Las simulaciones que incluyeron ambos efectos revelaron que la presencia de electrones térmicos (además de los no térmicos) durante la aceleración en el choque afecta razonablemente el espectro a frecuencias entre el óptico y los rayos γ, mientras que las $\nu_{\rm syn}^{\rm obs}$ sufre muy poca variación. Esto significa que la localización de la fuente en el plano A_C–$\nu_{\rm syn}^{\rm obs}$ sufrirá un desplazamiento vertical; tal vez dando explicación la dispersión de las fuentes en la región de los FSRQs.

En el modelo estándar, las SEDs de FSRQs y BL Lacs pueden ser ajustados por dos componentes parabólicas con máximos correspondientes a los picos sincrotrón e IC. Demostramos que las SEDs de FSRQs y BL Lacs dependen íntimamente de la magnetización del plasma emisor. Nuestros modelos predicen una fenomenología aún más compleja que los que actualmente están respaldados por los datos observacionales. Con un enfoque conservador, esto implicaría que las observaciones restringen la posible magnetización en el choque de capas que tiene lugar en las fuentes reales a, a lo sumo, valores moderados ($\sigma \lesssim 10^{-1}$). Aunque también hemos demostrado que si el valor del factor de Lorentz del fluido de las capas es lo suficientemente alto (p. ej. $\Gamma_{\rm R}$ y Δg), magnetizationes $\sigma \simeq 1$ también son compatibles con la doble joroba en los espectros. Por tanto, no podemos descartar del todo la posibilidad de que algunas fuentes sean muy ultrarelativistas tanto en el sentido cinemático como en el de su magnetización.

Encontramos que FSRQs tienen propiedades observacionales al alcance de modelos con campos magnéticos despreciables o moderados. La dispersión de los FSRQs observados en el plano A_C–$\nu_{\rm syn}^{\rm obs}$ puede explicarse por ambas variaciones de los parámetros intrínsecos de los grumos (Δg y $\Gamma_{\rm R}$ muy probable), y de los extrínsecos (la orientación de la fuente respecto al observador en la Tierra). Por su parte, BL Lacs con frecuencias sincrotrón máximas $\nu_{\rm syn}^{\rm obs} \lesssim 10^{16}$ Hz y parámetro de dominancia Compton $0.1 \gtrsim A_C \gtrsim 1$ despliega propiedades que se pueden reproducir con

modelos de moderada y uniforme magnetización ($\sigma_L = \sigma_R = 10^{-2}$). Por lo tanto, encontramos que una buena fracción de la secuencia de los blázares puede ser explicada en términos de diferentes magnetizaciones intrínsecas de las capas colisionantes.

En la presente tesis, introducimos una distribución de electrones térmica y no térmica (híbrida) en el modelo ISs para blázaress. Para explicar el hecho de que la componente térmica de la HD se extiende a valores bajos del factor de Lorentz de los electrones, también hemos desarrollado un código ciclo-sincrotrón que nos permite calcular la emisión no térmica de electrones con un factor de Lorentz arbitrario. Se muestra que nuestro método para el tratamiento de la evolución temporal de la HD y el cálculo de la emisión MBS se puede realizar de manera eficiente y con suficiente precisión. El método se implementa como una generalización del código numérico de MA12.

Trabajo futuro

Respecto al desarrollo de nuestro código `CHAMBA` y la nueva función *RMA* (véase la Eq. (3.71)), el valor óptimo del parámetro $a_{\rm coff}$ debe ser estimado. Para lograr este objetivo, planeamos calcular y comparar sistemáticamente el error relativo acumulado entre las emisividades MBS usando (3.71) y (3.56), para diferentes valores de $a_{\rm coff}$. Esperamos obtener un valor que nos ayude a reducir las ramificaciones en (3.71). En otras palabras, nuestra intención es encontrar un ajuste que apropiadamente tenga en cuenta el corte.

Con respecto al modelo de IS para blázares, tenemos como objetivo claro realizar exploraciones adicionales de los efectos en las SEDs de blázares debido a las variaciones en la magnetización y HDs, incluyendo la emisión MBS completa, para lo cual pretendemos incluir efectos como la absorción y emisión EIC. Los procesos microfísicos en este escenario son críticos para entender cómo se aceleran las partículas en los frentes de ondas de choque relativistas. Los parámetros microfísicos $a_{\rm acc}$ y $\Delta_{\rm acc}$ que regulan la escala de tiempo de aceleración y el tamaño de la región de aceleración de los electrones, respectivamente, ya han empezado a ser estudiados y hemos encontrado nuevos efectos en las curvas de luz de blazars. Sin embargo, queda pendiente un estudio definitivo y esperamos que estos resultados sean parte de alguna publicación futura. Por otra parte, no sólo está en curso las variación de parámetros de la versión actual del código para blázaress, sino que ya estamos trabajando en

la implementación del enfriamiento SSC (p. ej. Chiaberge & Ghisellini 1999), así como también el cálculo del coeficiente de absorción (Ghisellini & Svensson 1991) del proceso MBS para su aplicación directa a las simulaciones de blázars.

En el contexto astrofísico, y en relación con los flujos relativistas en particular, la presente tesis establece un punto de arranque para la exploración de fenómenos más allá de blázars. Por ejemplo, el aplanamiento tardío de las curvas de luz de las posluminiscencias de GRBs, en la llamada etapa newtoniana profunda (p. ej. Huang & Cheng 2003; Sironi & Giannios 2013), es un escenario ideal en el que las herramientas numéricas desarrolladas en la presente tesis podrían proporcionar un medio para explorar los remanentes de GRBs. Y en efecto lo es porque en esta etapa los electrones acelerados en el frente de choque de la onda expansiva se vuelven transrelativistas (Sironi & Giannios 2013), y por lo tanto los efectos tanto de la emisión MBS como de las HDs pueden ser relevantes.

Hace falta igualmente realizar más comparaciones de las simulaciones con observaciones para probar este modelo. Sin embargo, dado que la escala de la región de la que se compila la emisión en nuestras simulaciones es sub-parsec, hacen falta observaciones de las regiones de los blázares que emiten a altas energías tengan una mayor resolución para poder hacer una comparación adecuada de, p. ej., sus respectivas SEDs.

Bibliography

A. A. Abdo, M. Ackermann, M. Ajello, et al. Bright Active Galactic Nuclei Source List from the First Three Months of the Fermi Large Area Telescope All-Sky Survey. *The Astrophysical Journal*, **700**: 597–622, July 2009. doi: 10.1088/0004-637X/700/1/597.

A. A. Abdo, M. Ackermann, I. Agudo, et al. The Spectral Energy Distribution of Fermi Bright Blazars. *The Astrophysical Journal*, **716**:30–70, June 2010a. doi: 10.1088/0004-637X/716/1/30.

A. A. Abdo, M. Ackermann, W. B. Ajello, M. Atwood, et al. Spectral Properties of Bright Fermi-Detected Blazars in the Gamma-Ray Band. *The Astrophysical Journal*, **710**:1271–1285, Feb. 2010b. doi: 10.1088/0004-637X/710/2/1271.

M. Abramowitz & I. A. Stegun, editors. *Handbook of Mathematical Functions with Formulas, Graphs, and Mathematical Tables*. Dover, New York, 1972.

A. Achterberg, Y. A. Gallant, J. G. Kirk, & A. W. Guthmann. Particle acceleration by ultrarelativistic shocks: theory and simulations. *Monthly Notices of the Royal Astronomical Society*, **328**:393–408, Dec. 2001. doi: 10.1046/j.1365-8711.2001.04851.x.

M. Ackermann, M. Ajello, A. Allafort, et al. The Second Catalog of Active Galactic Nuclei Detected by the Fermi Large Area Telescope. *The Astrophysical Journal*, 743:171, Dec. 2011. doi: 10.1088/0004-637X/743/2/171.

I. Agudo, S. G. Jorstad, A. P. Marscher, et al. Location of γ-ray Flare Emission in the Jet of the BL Lacertae Object OJ287 More than 14 pc from the Central Engine. *The Astrophysical Journal Letters*, 726:L13, Jan. 2011. doi: 10.1088/2041-8205/726/1/L13.

M. Ajello, L. Costamante, R. M. Sambruna, et al. The Evolution of Swift/BAT Blazars and the Origin of the MeV Background. *The Astrophysical Journal*, **699**:603–625, July 2009. doi: 10.1088/0004-637X/699/1/603.

M. Ajello, D. M. Alexander, J. Greiner, et al. The 60 Month All-sky Burst Alert Telescope Survey of Active Galactic Nucleus and the Anisotropy of nearby AGNs. *The Astrophysical Journal*, 749:21, Apr. 2012. doi: 10.1088/0004-637X/749/1/21.

H. Alfvén & N. Herlofson. Cosmic Radiation and Radio Stars. *Physical Review*, **78**:616–616, June 1950. doi: 10.1103/PhysRev.78.616.

M. A. Aloy & P. Mimica. Observational Effects of Anomalous Boundary Layers in Relativistic Jets. *The Astrophysical Journal*, 681:84-95, July 2008. doi: 10.1086/588605.

W. Baade & R. Minkowski. On the Identification of Radio Sources. *The Astrophysical Journal*, **119**: 215, Jan. 1954. doi: 10.1086/145813.

M. G. Baring. Particle Acceleration in Turbulent Magnetohydrodynamic Shocks. In M. Böttcher, D. E. Harris, & H. Krawczynski, editors, *Relativistic Jets from Active Galactic Nuclei*, pages 245–295. Wiley-VCH Verlag GmbH & Co. KGaA, Weinheim, Germany, Jan. 2012. ISBN 978-3-527-41037-8. doi: 10.1002/9783527641741.ch9.

J. Bednarz & M. Ostrowski. The acceleration time-scale for first-order Fermi acceleration in relativistic shock waves. *Monthly Notices of the Royal Astronomical Society*, **283**:447–456, Nov. 1996. doi: 10.1093/mnras/283.2.447.

J. Bednarz & M. Ostrowski. Energy Spectra of Cosmic Rays Accelerated at Ultrarelativistic Shock Waves. *Physical Review Letters*, **80**:3911–3914, May 1998. doi: 10.1103/PhysRevLett.80.3911.

M. C. Begelman & J. G. Kirk. Shock-drift particle acceleration in superluminal shocks - A model for hot spots in extragalactic radio sources. *The Astrophysical Journal*, **353**:66–80, Apr. 1990. doi: 10.1086/168590.

M. C. Begelman, B. Rudak, & M. Sikora. Consequences of relativistic proton injection in active galactic nuclei. *The Astrophysical Journal*, **362**:38–51, Oct. 1990. doi: 10.1086/169241.

G. Bekefi. *Radiation processes in plasmas*. Wiley series in plasma physics. Wiley, 1966.

A. R. Bell. The acceleration of cosmic rays in shock fronts. II. *Monthly Notices of the Royal Astronomical Society*, **182**:443–455, Feb. 1978a. doi: 10.1093/mnras/182.3.443.

A. R. Bell. The acceleration of cosmic rays in shock fronts. I. *Monthly Notices of the Royal Astronomical Society*, **182**:147–156, Jan. 1978b. doi: 10.1093/mnras/182.2.147.

G. V. Bicknell & S. J. Wagner. The Evolution of Shocks in Blazar Jets. *Publications of the Astronomical Society of Australia*, **19**:129–137, 2002. doi: 10.1071/AS02009.

R. D. Blandford & A. Königl. Relativistic jets as compact radio sources. *The Astrophysical Journal*, **232**:34–48, Aug. 1979. doi: 10.1086/157262.

R. D. Blandford & M. J. Rees. A 'twin-exhaust' model for double radio sources. *Monthly Notices of the Royal Astronomical Society*, **169**:395–415, Dec. 1974. doi: 10.1093/mnras/169.3.395.

S. D. Bloom & A. P. Marscher. An Analysis of the Synchrotron Self-Compton Model for the Multi–Wave Band Spectra of Blazars. *The Astrophysical Journal*, **461**:657, Apr. 1996. doi: 10.1086/177092.

G. R. Blumenthal & R. J. Gould. Bremsstrahlung, Synchrotron Radiation, and Compton Scattering of High-Energy Electrons Traversing Dilute Gases. *Reviews of Modern Physics*, **42**:237–270, Apr 1970. doi: 10.1103/RevModPhys.42.237.

T. Boch & P. Fernique. Aladin Lite: Embed your Sky in the Browser. In N. Manset & P. Forshay, editors, *Astronomical Data Analysis Software and Systems XXIII*, volume 485 of *Astronomical Society of the Pacific Conference Series*, page 277, May 2014.

F. Bonnarel, P. Fernique, O. Bienaymé, et al. The ALADIN interactive sky atlas. A reference tool for identification of astronomical sources. *Astronomy & Astrophysics Supplement Series*, **143**:33–40, Apr. 2000. doi: 10.1051/aas:2000331.

M. Böttcher. Models for the Spectral Energy Distributions and Variability of Blazars. In T. Sovalainen, E. Ros, R. W. Porcas, & J. A. Zensus, editors, *Fermi meets Jansky - AGN in Radio and Gamma-Rays*, page 41, Bonn, 2010.

M. Böttcher & C. D. Dermer. An Evolutionary Scenario for Blazar Unification. *The Astrophysical Journal*, **564**:86–91, Jan. 2002. doi: 10.1086/324134.

M. Böttcher & C. D. Dermer. Timing Signatures of the Internal-Shock Model for Blazars. *The Astrophysical Journal*, **711**:445–460, Mar. 2010. doi: 10.1088/0004-637X/711/1/445.

Ž. Bošnjak, F. Daigne, & G. Dubus. Prompt high-energy emission from gamma-ray bursts in the internal shock model. *Astronomy & Astrophysics*, **498**:677–703, May 2009. doi: 10.1051/0004-6361/200811375.

J. J. Brainerd & D. Q. Lamb. Synchrotron emission and gamma-ray bursts. *The Astrophysical Journal*, **313**:231–262, Feb. 1987. doi: 10.1086/164965.

G. R. Burbidge. On Synchrotron Radiation from Messier 87. *The Astrophysical Journal*, **124**:416, Sept. 1956. doi: 10.1086/146237.

G. R. Burbidge. The theoretical explanation of radio emission (Introductory Lecture). In R. N. Bracewell, editor, *URSI Symp. 1: Paris Symposium on Radio Astronomy*, volume 9 of *IAU Symposium*, page 541, 1959.

A. Bykov, N. Gehrels, H. Krawczynski, et al. Particle Acceleration in Relativistic Outflows. *Space Science Reviews*, **173**:309–339, Nov. 2012. doi: 10.1007/s11214-012-9896-y.

S. Chandrasekhar. *An introduction to the study of stellar structure*. Dover books on advanced mathematics. Dover, New York, NY, 1st ed. edition, 1939.

X. Chen, G. Fossati, E. P. Liang, & M. Böttcher. Time-dependent simulations of multiwavelength variability of the blazar Mrk 421 with a Monte Carlo multizone code. *Monthly Notices of the Royal Astronomical Society*, **416**:2368–2387, Sept. 2011. doi: 10.1111/j.1365-2966.2011.19215.x.

M. Chiaberge & G. Ghisellini. Rapid variability in the synchrotron self-Compton model for blazars. *Monthly Notices of the Royal Astronomical Society*, **306**:551–560, July 1999. doi: 10.1046/j.1365-8711.1999.02538.x.

A. Crusius & R. Schlickeiser. Synchrotron radiation in random magnetic fields. *Astronomy & Astrophysics*, **164**:L16–L18, Aug. 1986. CS86.

F. Daigne & R. Mochkovitch. Gamma-ray bursts from internal shocks in a relativistic wind: temporal and spectral properties. *Monthly Notices of the Royal Astronomical Society*, **296**:275–286, May 1998. doi: 10.1046/j.1365-8711.1998.01305.x.

F. Daigne, Ž. Bošnjak, & G. Dubus. Reconciling observed gamma-ray burst prompt spectra with synchrotron radiation? *Astronomy & Astrophysics*, 526:A110, Feb. 2011. doi: 10.1051/0004-6361/201015457.

G. de Berredo-Peixoto, I. L. Shapiro, & F. Sobreira. Simple Cosmological Model with Relativistic Gas. *Modern Physics Letters A*, **20**:2723–2734, 2005. doi: 10.1142/S0217732305018104.

D. S. De Young & W. I. Axford. Inertial Confinement of Extended Radio Sources. *Nature*, **216**:129–131, Oct. 1967. doi: 10.1038/216129a0.

C. D. Dermer. On the Beaming Statistics of Gamma-Ray Sources. *The Astrophysical Journal Letters*, **446**:L63, June 1995. doi: 10.1086/187931.

C. D. Dermer. Curvature Effects in Gamma-Ray Burst Colliding Shells. *The Astrophysical Journal*, **614**:284–292, Oct. 2004. doi: 10.1086/426532.

C. D. Dermer & B. Giebels. Active galactic nuclei at gamma-ray energies. *Comptes Rendus Physique*, **17**:594–616, June 2016. doi: 10.1016/j.crhy.2016.04.004.

C. D. Dermer & G. Menon. *High Energy Radiation from Black Holes. Gamma Rays, Cosmic Rays, and*

Neutrinos. Princeton Series in Astrophysics. Princeton University Press, Princeton, 2009.

C. D. Dermer & R. Schlickeiser. Model for the High-Energy Emission from Blazars. *The Astrophysical Journal*, **416**:458, Oct. 1993. doi: 10.1086/173251.

F. R. Elder, A. M. Gurewitsch, R. V. Langmuir, & H. C. Pollock. Radiation from Electrons in a Synchrotron. *Physical Review*, **71**:829–830, June 1947. doi: 10.1103/PhysRev.71.829.5.

Y. Z. Fan, D. M. Wei, & B. Zhang. γ-ray burst internal shocks with magnetization. *Monthly Notices of the Royal Astronomical Society*, **354**:1031–1039, Nov. 2004. doi: 10.1111/j.1365-2966.2004.08263.x.

B. L. Fanaroff & J. M. Riley. The morphology of extragalactic radio sources of high and low luminosity. *Monthly Notices of the Royal Astronomical Society*, **167**:31P–36P, May 1974. doi: 10.1093/mnras/167.1.31P.

E. Fermi. Galactic Magnetic Fields and the Origin of Cosmic Radiation. *The Astrophysical Journal*, **119**:1, Jan. 1954. doi: 10.1086/145789.

J. D. Finke. Compton Dominance and the Blazar Sequence. *The Astrophysical Journal*, 763:134, Feb. 2013. doi: 10.1088/0004-637X/763/2/134.

J. D. Finke, C. D. Dermer, & M. Böttcher. Synchrotron Self-Compton Analysis of TeV X-Ray-Selected BL Lacertae Objects. *The Astrophysical Journal*, 686:181-194, Oct. 2008. doi: 10.1086/590900.

G. D. Fleishman & A. A. Kuznetsov. Fast Gyrosynchrotron Codes. *The Astrophysical Journal*, 721:1127-1141, Oct. 2010. doi: 10.1088/0004-637X/721/2/1127.

G. Fossati, L. Maraschi, A. Celotti, A. Comastri, & G. Ghisellini. A unifying view of the spectral energy distributions of blazars. *Monthly Notices of the Royal Astronomical Society*, **299**:433–448, Sept. 1998. doi: 10.1046/j.1365-8711.1998.01828.x.

C. M. Fromm, E. Ros, M. Perucho, et al. Catching the radio flare in CTA 102. II. VLBI kinematic analysis. *Astronomy & Astrophysics*, 551:A32, Mar. 2013. doi: 10.1051/0004-6361/201219913.

M. Georganopoulos, J. G. Kirk, & A. Mastichiadis. Size-Luminosity-Scaling and Inverse Compton Seed Photons in Blazars. In P. Padovani & C. M. Urry, editors, *Blazar Demographics and Physics*, volume 227 of *Astronomical Society of the Pacific Conference Series*, page 116, 2001.

G. Ghisellini & P. Madau. On the origin of the gamma-ray emission in blazars. *Monthly Notices of the Royal Astronomical Society*, **280**:67–76, May 1996. doi: 10.1093/mnras/280.1.67.

G. Ghisellini & R. Svensson. The synchrotron and cyclo-synchrotron absorption cross-section. *Monthly Notices of the Royal Astronomical Society*, **252**:313–318, Oct. 1991. doi: 10.1093/mnras/252.3.313.

G. Ghisellini & F. Tavecchio. Canonical high-power blazars. *Monthly Notices of the Royal Astronomical Society*, **397**:985–1002, Aug. 2009. doi: 10.1111/j.1365-2966.2009.15007.x.

G. Ghisellini, P. W. Guilbert, & R. Svensson. The synchrotron boiler. *The Astrophysical Journal Letters*, **334**:L5–L8, Nov. 1988. doi: 10.1086/185300.

G. Ghisellini, A. Celotti, G. Fossati, L. Maraschi, & A. Comastri. A theoretical unifying scheme for gamma-ray bright blazars. *Monthly Notices of the Royal Astronomical Society*, **301**:451–468, Dec. 1998. doi: 10.1046/j.1365-8711.1998.02032.x.

G. Ghisellini, F. Tavecchio, & M. Chiaberge. Structured jets in TeV BL Lac objects and radiogalaxies. Implications for the observed properties. *Astronomy & Astrophysics*, **432**:401–410, Mar. 2005. doi: 10.1051/0004-6361:20041404.

D. Giannios & A. Spitkovsky. Signatures of a Maxwellian component in shock-accelerated electrons in GRBs. *Monthly Notices of the Royal Astronomical Society*, **400**:330–336, Nov. 2009. doi: 10.

1111/j.1365-2966.2009.15454.x.

D. Giannios, D. A. Uzdensky, & M. C. Begelman. Fast TeV variability in blazars: jets in a jet. *Monthly Notices of the Royal Astronomical Society*, **395**:L29–L33, May 2009. doi: 10.1111/j.1745-3933.2009.00635.x.

V. L. Ginzburg. 1951, Cosmic Rays as the Source of Galactic Radio Emission. In W. T. Sullivan, III, editor, *Classics in Radio Astronomy*, page 93. Springer Netherlands, Dordrecht, 1982.

V. L. Ginzburg & S. I. Syrovatskii. Cosmic Rays in Metagalactic Space. *Soviet Astronomy*, **7**:357, Dec. 1963. Translated from Astronomicheskii Zhurnal, Vol. 40, No. 3, pp. 466-476, March-April, 1963.

V. L. Ginzburg & S. I. Syrovatskii. Cosmic Magnetobremsstrahlung (synchrotron Radiation). *Annual Review of Astronomy & Astrophysics*, **3**:297, 1965. doi: 10.1146/annurev.aa.03.090165.001501.

V. L. Ginzburg, G. G. Getmantsev, & M. I. Fradkin. On the Electrons in the Composition of Primary Cosmic Rays. In *Trudy Tret'yego Soveshchaniya po Voprosam Kosmogonii (Proceedings of the Third Conference on Problems of Cosmogony)*, pages 149–190, Moscow, 1954.

P. Giommi, P. Padovani, G. Polenta, et al. A simplified view of blazars: clearing the fog around long-standing selection effects. *Monthly Notices of the Royal Astronomical Society*, **420**:2899–2911, Mar. 2012a. doi: 10.1111/j.1365-2966.2011.20044.x.

P. Giommi, G. Polenta, A. Lähteenmäki, et al. Simultaneous Planck, Swift, and Fermi observations of X-ray and γ-ray selected blazars. *Astronomy & Astrophysics*, 541:A160, May 2012b. doi: 10.1051/0004-6361/201117825.

P. Giommi, P. Padovani, & G. Polenta. A simplified view of blazars: the γ-ray case. *Monthly Notices of the Royal Astronomical Society*, **431**:1914–1922, May 2013. doi: 10.1093/mnras/stt305.

L. Gratton. Source Models with Electron Diffusion. *Astrophysics & Space Science*, **16**:81–100, Apr. 1972. doi: 10.1007/BF00643094.

J. L. Greenstein & M. Schmidt. The Quasi-Stellar Radio Sources 3C 48 and 3C 273. *The Astrophysical Journal*, **140**:1, July 1964. doi: 10.1086/147889.

A. Gruzinov & E. Waxman. Gamma-Ray Burst Afterglow: Polarization and Analytic Light Curves. *The Astrophysical Journal*, **511**:852–861, Feb. 1999. doi: 10.1086/306720.

C. B. Hededal, T. Haugbølle, J. T. Frederiksen, & Å. Nordlund. Non-Fermi Power-Law Acceleration in Astrophysical Plasma Shocks. *The Astrophysical Journal Letters*, **617**:L107–L110, Dec. 2004. doi: 10.1086/427387.

G. Henri & G. Pelletier. Relativistic electron-positron beam formation in the framework of the two-flow model for active galactic nuclei. *The Astrophysical Journal Letters*, **383**:L7–L10, Dec. 1991. doi: 10.1086/186228.

J. L. Hirshfield, D. E. Baldwin, & S. C. Brown. Cyclotron Radiation from a Hot Plasma. *Physics of Fluids*, **4**(2):198–203, Feb. 1961.

C. Hoffmeister. 354 neue Veränderliche. *Astronomische Nachrichten*, **236**:233, Sept. 1929. doi: 10.1002/asna.19292361502.

F. Hoyle, G. R. Burbidge, & W. L. W. Sargent. On the Nature of the Quasi-stellar Sources. *Nature*, **209**:751–753, Feb. 1966. doi: 10.1038/209751a0.

Y. F. Huang & K. S. Cheng. Gamma-ray bursts: optical afterglows in the deep Newtonian phase. *Monthly Notices of the Royal Astronomical Society*, **341**:263–269, May 2003. doi: 10.1046/j.1365-8711.2003.06430.x.

B. Husemann, T. Urrutia, G. R. Tremblay, et al. The Close AGN Reference Survey (CARS). What is

causing Mrk 1018's return to the shadows after 30 years? *Astronomy & Astrophysics*, 593:L9, Sept. 2016. doi: 10.1051/0004-6361/201629245.

J. D. Jackson. *Classical Electrodynamics*. Wiley, 3rd edition, 1999.

M. Janiak, M. Sikora, & R. Moderski. Magnetization of jets in luminous blazars. *Monthly Notices of the Royal Astronomical Society*, **449**:431–439, May 2015. doi: 10.1093/mnras/stv200.

K. G. Jansky. Directional Studies of Atmospherics at High Frequencies. *Proceedings of the Institute of Radio Engineers*, **20**(12):1920–1932, Dec. 1932. doi: 10.1109/JRPROC.1932.227477.

K. G. Jansky. A Note on the Source of Interstellar Interference. *Proceedings of the Institute of Radio Engineers*, **23**(10):1158–1163, Oct. 1935. doi: 10.1109/JRPROC.1935.227275.

R. C. Jennison & M. K. Das Gupta. Fine Structure of the Extra-terrestrial Radio Source Cygnus I. *Nature*, **172**:996–997, Nov. 1953. doi: 10.1038/172996a0.

T. W. Jones, S. L. O'dell, & W. A. Stein. Physics of Compact Nonthermal Sources. I. Theory of Radiation Processes. *The Astrophysical Journal*, **188**:353–368, Mar. 1974. doi: 10.1086/152724.

S. G. Jorstad & A. P. Marscher. The Highly Relativistic Kiloparsec-Scale Jet of the Gamma-Ray Quasar 0827+243. *The Astrophysical Journal*, **614**:615–625, Oct. 2004. doi: 10.1086/423800.

S. G. Jorstad, A. P. Marscher, M. L. Lister, et al. Polarimetric Observations of 15 Active Galactic Nuclei at High Frequencies: Jet Kinematics from Bimonthly Monitoring with the Very Long Baseline Array. *Astronomical Journal*, **130**:1418–1465, Oct. 2005. doi: 10.1086/444593.

M. Joshi & M. Böttcher. Time-dependent Radiation Transfer in the Internal Shock Model Scenario for Blazar Jets. *The Astrophysical Journal*, 727:21, Jan. 2011. doi: 10.1088/0004-637X/727/1/21.

F. Jüttner. Das Maxwellsche Gesetz der Geschwindigkeitsverteilung in der Relativtheorie. *Annalen der Physik*, **339**(5):856–882, 1911.

N. S. Kardashev. Nonstationarity of Spectra of Young Sources of Nonthermal Radio Emission. *Soviet Astronomy*, **6**:317, Dec. 1962. Translated from Astronomicheskii Zhurnal, Vol. 39, No. 3, pp. 393-409, May-June, 1962.

J. Kataoka, J. R. Mattox, J. Quinn, et al. High-Energy Emission from the TEV Blazar Markarian 501 during Multiwavelength Observations in 1996. *The Astrophysical Journal*, **514**:138–147, Mar. 1999. doi: 10.1086/306918.

K. O. Kiepenheuer. Cosmic Rays as the Source of General Galactic Radio Emission. *Physical Review*, **79**:738–739, Aug. 1950. doi: 10.1103/PhysRev.79.738.

M. Kino, A. Mizuta, & S. Yamada. Hydrodynamic Effects in Internal Shock of Relativistic Outflows. *The Astrophysical Journal*, **611**:1021–1032, Aug. 2004. doi: 10.1086/422305.

J. G. Kirk & P. Schneider. On the acceleration of charged particles at relativistic shock fronts. *The Astrophysical Journal*, **315**:425–433, Apr. 1987. doi: 10.1086/165147.

K.-L. Klein. Microwave radiation from a dense magneto-active plasma. *Astronomy & Astrophysics*, **183**:341–350, Sept. 1987.

S. Kobayashi, T. Piran, & R. Sari. Can Internal Shocks Produce the Variability in Gamma-Ray Bursts? *The Astrophysical Journal*, **490**:92, Nov. 1997. doi: 10.1086/512791.

S. Komissarov. Central Engines: Acceleration, Collimation and Confinement of Jets. In M. Boettcher, D. E. Harris, & H. Krawczynski, editors, *Relativistic Jets from Active Galactic Nuclei, by M. Boettcher, D.E. Harris, and H. Krawczynski, 425 pages. Berlin: Wiley, 2012, p. 81-114*, pages 81–114. Wiley-VCH Verlag GmbH & Co. KGaA, Jan. 2012. doi: 10.1002/9783527641741.ch4.

H. Krawczynski & E. Treister. Active galactic nuclei — the physics of individual sources and the

cosmic history of formation and evolution. *Frontiers of Physics*, **8**:609–629, Dec. 2013. doi: 10.1007/s11467-013-0310-3.

P. Kumar & B. Zhang. The physics of gamma-ray bursts & relativistic jets. *Physics Reports*, **561**:1–109, Feb. 2015. doi: 10.1016/j.physrep.2014.09.008.

P. K. Leung, C. F. Gammie, & S. C. Noble. Numerical Calculation of Magnetobremsstrahlung Emission and Absorption Coefficients. *The Astrophysical Journal*, 737:21, Aug. 2011. doi: 10.1088/0004-637X/737/1/21. LGN11.

H. Li, M. Kusunose, & E. P. Liang. Gamma Rays from Galactic Black Hole Candidates with Stochastic Particle Acceleration. *The Astrophysical Journal Letters*, **460**:L29, Mar. 1996. doi: 10.1086/309960.

G. G. Lichti, T. Balonek, T. J.-L. Courvoisier, et al. Simultaneous and quasi-simultaneous observations of the continuum emission of the quasar 3C 273 from radio to γ-ray energies. *Astronomy & Astrophysics*, **298**:711, June 1995.

M. L. Lister, M. F. Aller, H. D. Aller, et al. MOJAVE: XIII. Parsec-scale AGN Jet Kinematics Analysis Based on 19 years of VLBA Observations at 15 GHz. *Astronomical Journal*, 152:12, July 2016. doi: 10.3847/0004-6256/152/1/12.

M. S. Longair. *High Energy Astrophysics*. Cambridge University Press, Cambridge, 3rd edition, 2011.

D. Lynden-Bell. Galactic Nuclei as Collapsed Old Quasars. *Nature*, **223**:690–694, Aug. 1969. doi: 10.1038/223690a0.

R. Mahadevan, R. Narayan, & I. Yi. Harmony in Electrons: Cyclotron and Synchrotron Emission by Thermal Electrons in a Magnetic Field. *The Astrophysical Journal*, **465**:327, July 1996. doi: 10.1086/177422. MNY96.

K. Mannheim. The proton blazar. *Astronomy & Astrophysics*, **269**:67–76, Mar. 1993.

A. Marcowith & J. Malzac. Cyclotron-synchrotron: Harmonic fitting functions in the non-relativistic and trans-relativistic regimes. *Astronomy & Astrophysics*, **409**:9–19, Oct. 2003. doi: 10.1051/0004-6361:20031060.

A. P. Marscher. Turbulent, Extreme Multi-zone Model for Simulating Flux and Polarization Variability in Blazars. *The Astrophysical Journal*, 780:87, Jan. 2014. doi: 10.1088/0004-637X/780/1/87.

A. P. Marscher & W. K. Gear. Models for high-frequency radio outbursts in extragalactic sources, with application to the early 1983 millimeter-to-infrared flare of 3C 273. *The Astrophysical Journal*, **298**:114–127, Nov. 1985. doi: 10.1086/163592.

A. P. Marscher, S. G. Jorstad, F. D. D'Arcangelo, et al. The inner jet of an active galactic nucleus as revealed by a radio-to-γ-ray outburst. *Nature*, **452**:966–969, Apr. 2008. doi: 10.1038/nature06895.

A. P. Marscher, S. G. Jorstad, V. M. Larionov, et al. Probing the Inner Jet of the Quasar PKS 1510-089 with Multi-Waveband Monitoring During Strong Gamma-Ray Activity. *The Astrophysical Journal Letters*, **710**:L126–L131, Feb. 2010. doi: 10.1088/2041-8205/710/2/L126.

T. A. Matthews & A. R. Sandage. Optical Identification of 3C 48, 3C 196, and 3C 286 with Stellar Objects. *The Astrophysical Journal*, **138**:30, July 1963. doi: 10.1086/147615.

M. V. Medvedev & A. Loeb. Generation of Magnetic Fields in the Relativistic Shock of Gamma-Ray Burst Sources. *The Astrophysical Journal*, **526**:697–706, Dec. 1999. doi: 10.1086/308038.

D. B. Melrose & R. C. McPhedran. *Electromagnetic Processes in Dispersive Media*. Cambridge University Press, Cambridge, Sept. 1991.

A. Mignone, T. Plewa, & G. Bodo. The Piecewise Parabolic Method for Multidimensional Relativistic Fluid Dynamics. *The Astrophysical Journal Supplement Series*, **160**:199–219, Sept. 2005. doi:

10.1086/430905.

P. Mimica. *Numerical Simulations of Blazar Jets and their Non-thermal Radiation*. PhD thesis, Ludwig-Maximilians-Universität München, Munich, November 2004. URL `http://edoc.ub.uni-muenchen.de/2879/`.

P. Mimica & M. A. Aloy. On the dynamic efficiency of internal shocks in magnetized relativistic outflows. *Monthly Notices of the Royal Astronomical Society*, **401**:525–532, Jan. 2010. doi: 10.1111/j.1365-2966.2009.15669.x.

P. Mimica & M. A. Aloy. Radiative signature of magnetic fields in internal shocks. *Monthly Notices of the Royal Astronomical Society*, **421**:2635–2647, Apr. 2012. doi: 10.1111/j.1365-2966.2012.20495.x. MA12.

P. Mimica, M. A. Aloy, E. Müller, & W. Brinkmann. Synthetic X-ray light curves of BL Lacs from relativistic hydrodynamic simulations. *Astronomy & Astrophysics*, **418**:947–958, May 2004. doi: 10.1051/0004-6361:20034261.

P. Mimica, M. A. Aloy, E. Müller, & W. Brinkmann. Which physical parameters can be inferred from the emission variability of relativistic jets? *Astronomy & Astrophysics*, **441**:103–115, Oct. 2005. doi: 10.1051/0004-6361:20053218.

P. Mimica, M. A. Aloy, & E. Müller. Internal shocks in relativistic outflows: collisions of magnetized shells. *Astronomy & Astrophysics*, **466**:93–106, Apr. 2007. doi: 10.1051/0004-6361:20066811.

P. Mimica, M. A. Aloy, I. Agudo, et al. Spectral Evolution of Superluminal Components in Parsec-Scale Jets. *The Astrophysical Journal*, **696**:1142–1163, May 2009. doi: 10.1088/0004-637X/696/2/1142.

P. Mimica, M. A. Aloy, J. M. Rueda-Becerril, S. Tabik, & C. Aloy. Numerical simulations of dynamics and emission from relativistic astrophysical jets. In *Journal of Physics Conference Series*, volume 454 of *Journal of Physics Conference Series*, page 012001, Aug. 2013. doi: 10.1088/1742-6596/454/1/012001.

A. Mücke, R. J. Protheroe, R. Engel, J. P. Rachen, & T. Stanev. BL Lac objects in the synchrotron proton blazar model. *Astroparticle Physics*, **18**:593–613, Mar. 2003. doi: 10.1016/S0927-6505(02)00185-8.

K.-I. Nishikawa, P. Hardee, G. Richardson, et al. Particle Acceleration in Relativistic Jets Due to Weibel Instability. *The Astrophysical Journal*, **595**:555–563, Sept. 2003. doi: 10.1086/377260.

K.-I. Nishikawa, P. Hardee, G. Richardson, et al. Particle Acceleration and Magnetic Field Generation in Electron-Positron Relativistic Shocks. *The Astrophysical Journal*, **622**:927–937, Apr. 2005. doi: 10.1086/428394.

J. B. Oke & J. E. Gunn. The Distance of BL Lacertae. *The Astrophysical Journal Letters*, **189**:L5, Apr. 1974. doi: 10.1086/181450.

L. Oster. Cyclotron Radiation from Relativistic Particles with an Arbitrary Velocity Distribution. *Physical Review*, **121**:961–967, Feb. 1961. doi: 10.1103/PhysRev.121.961.

F. Özel, D. Psaltis, & R. Narayan. Hybrid Thermal-Nonthermal Synchrotron Emission from Hot Accretion Flows. *The Astrophysical Journal*, **541**:234–249, Sept. 2000. doi: 10.1086/309396.

A. G. Pacholczyk. *Radio astrophysics. Nonthermal processes in galactic and extragalactic sources*. Series of Books in Astronomy and Astrophysics. Freeman, San Francisco, 1970.

A. Pandya, Z. Zhang, M. Chandra, & C. F. Gammie. Polarized Synchrotron Emissivities and Absorptivities for Relativistic Thermal, Power-law, and Kappa Distribution Functions. *The Astrophysical Journal*, 822:34, May 2016. doi: 10.3847/0004-637X/822/1/34.

A. Pe'er & P. Casella. A Model for Emission from Jets in X-Ray Binaries: Consequences of

a Single Acceleration Episode. *The Astrophysical Journal*, **699**:1919–1937, July 2009. doi: 10.1088/0004-637X/699/2/1919.

A. Pe'er & E. Waxman. Time-dependent Numerical Model for the Emission of Radiation from Relativistic Plasma. *The Astrophysical Journal*, **628**:857–866, Aug. 2005. doi: 10.1086/431139.

V. Petrosian. Synchrotron emissivity from mildly relativistic particles. *The Astrophysical Journal*, **251**: 727–738, Dec. 1981. doi: 10.1086/159517.

E. Pian, C. M. Urry, L. Maraschi, et al. Ultraviolet and Multiwavelength Variability of the Blazar 3C 279: Evidence for Thermal Emission. *The Astrophysical Journal*, **521**:112–120, Aug. 1999. doi: 10.1086/307548.

O. Porth, C. Fendt, Z. Meliani, & B. Vaidya. Synchrotron Radiation of Self-collimating Relativistic Magnetohydrodynamic Jets. *The Astrophysical Journal*, 737:42, Aug. 2011. doi: 10.1088/0004-637X/737/1/42.

W. H. Press, S. A. Teukolsky, W. T. Vetterling, & B. P. Flannery. *Numerical Recipes in Fortran 77. The art of scientific computing*, volume 1. Cambridge University Press, 2nd edition, 1992.

M. J. Rees. The M87 jet - Internal shocks in a plasma beam. *Monthly Notices of the Royal Astronomical Society*, **184**:61P–65P, Sept. 1978. doi: 10.1093/mnras/184.1.61P.

M. J. Rees & P. Mészáros. Unsteady outflow models for cosmological gamma-ray bursts. *The Astrophysical Journal Letters*, **430**:L93–L96, Aug. 1994. doi: 10.1086/187446.

P. A. Robinson & D. B. Melrose. Gyromagnetic emission and absorption - Approximate formulas of wide validity. *Australian Journal of Physics*, **37**:675–704, 1984. doi: 10.1071/PH840675.

R. Romero, J. M. Martí, J. A. Pons, J. M. Ibáñez, & J. A. Miralles. The exact solution of the Riemann problem in relativistic magnetohydrodynamics with tangential magnetic fields. *Journal of Fluid Mechanics*, **544**:323–338, Dec. 2005. doi: 10.1017/S0022112005006701.

J. Rueda-Becerril, P. Mimica, & M. A. Aloy. Numerical simulations of the internal shock model in magnetized relativistic jets of blazars. In *Proceedings of Swift: 10 Years of Discovery (SWIFT 10), held 2-5 December 2014 at La Sapienza University, Rome, Italy.*, page 159, 2014a.

J. M. Rueda-Becerril, P. Mimica, M. A. Aloy, & C. Aloy. Numerical study of broadband spectra caused by internal shocks in magnetized relativistic jets of blazars. In *European Physical Journal Web of Conferences*, volume 61 of *European Physical Journal Web of Conferences*, page 02007, Dec. 2013. doi: 10.1051/epjconf/20136102007.

J. M. Rueda-Becerril, P. Mimica, & M. A. Aloy. The influence of the magnetic field on the spectral properties of blazars. *Monthly Notices of the Royal Astronomical Society*, **438**:1856–1869, Feb. 2014b. doi: 10.1093/mnras/stt2335. RMA14.

J. M. Rueda-Becerril, P. Mimica, & M. A. Aloy. On the influence of a hybrid thermal–non-thermal distribution in the internal shocks model for blazars. *Monthly Notices of the Royal Astronomical Society*, **468**:1169–1182, June 2017. doi: 10.1093/mnras/stx476. RMA17.

G. B. Rybicki & A. P. Lightman. *Radiative processes in astrophysics*. Wiley-Interscience, New York, 1979. RL79.

S. Saito, Ł. Stawarz, Y. T. Tanaka, et al. Time-dependent Modeling of Gamma-Ray Flares in Blazar PKS1510–089. *The Astrophysical Journal*, 809:171, Aug. 2015. doi: 10.1088/0004-637X/809/2/171.

R. M. Sambruna, L. Maraschi, & C. M. Urry. On the Spectral Energy Distributions of Blazars. *The Astrophysical Journal*, **463**:444, June 1996. doi: 10.1086/177260.

R. Santana, R. Barniol Duran, & P. Kumar. Magnetic Fields in Relativistic Collisionless Shocks. *The*

Astrophysical Journal, 785:29, Apr. 2014. doi: 10.1088/0004-637X/785/1/29.

R. Schlickeiser & I. Lerche. Nonlinear radiative cooling of relativistic particles under equipartition conditions. I. Instantaneous monoenergetic injection. *Astronomy & Astrophysics*, **476**:1–8, Dec. 2007. doi: 10.1051/0004-6361:20078088. SL07.

M. Schmidt. 3C 273 : A Star-Like Object with Large Red-Shift. *Nature*, **197**:1040, Mar. 1963. doi: 10.1038/1971040a0.

M. Schmidt & T. A. Matthews. Redshift of the Quasi-Stellar Radio Sources 3c 47 and 3c 147. *The Astrophysical Journal*, **139**:781, Feb. 1964. doi: 10.1086/147815.

J. L. Schmitt. BL Lac identified as a Radio Source. *Nature*, **218**:663, May 1968. doi: 10.1038/218663a0.

J. Schwinger. On the classical radiation of accelerated electrons. *Physical Review*, **75**:1912–1925, Jun 1949. doi: 10.1103/PhysRev.75.1912.

C. K. Seyfert. Nuclear Emission in Spiral Nebulae. *The Astrophysical Journal*, **97**:28, Jan. 1943. doi: 10.1086/144488.

G. A. Shields. A Brief History of Active Galactic Nuclei. *Publications of the Astronomical Society of the Pacific*, **111**:661–678, June 1999. doi: 10.1086/316378.

M. Sikora, M. C. Begelman, & M. J. Rees. Comptonization of diffuse ambient radiation by a relativistic jet: The source of gamma rays from blazars? *The Astrophysical Journal*, **421**:153–162, Jan. 1994. doi: 10.1086/173633.

M. Sikora, Ł. Stawarz, R. Moderski, K. Nalewajko, & G. M. Madejski. Constraining Emission Models of Luminous Blazar Sources. *The Astrophysical Journal*, **704**:38–50, Oct. 2009. doi: 10.1088/0004-637X/704/1/38.

L. Sironi & D. Giannios. A Late-time Flattening of Light Curves in Gamma-Ray Burst Afterglows. *The Astrophysical Journal*, 778:107, Dec. 2013. doi: 10.1088/0004-637X/778/2/107.

L. Sironi & A. Spitkovsky. Particle Acceleration in Relativistic Magnetized Collisionless Pair Shocks: Dependence of Shock Acceleration on Magnetic Obliquity. *The Astrophysical Journal*, **698**:1523–1549, June 2009. doi: 10.1088/0004-637X/698/2/1523.

L. Sironi, A. Spitkovsky, & J. Arons. The Maximum Energy of Accelerated Particles in Relativistic Collisionless Shocks. *The Astrophysical Journal*, 771:54, July 2013. doi: 10.1088/0004-637X/771/1/54.

M. Spada, G. Ghisellini, D. Lazzati, & A. Celotti. Internal shocks in the jets of radio-loud quasars. *Monthly Notices of the Royal Astronomical Society*, **325**:1559–1570, Aug. 2001. doi: 10.1046/j.1365-8711.2001.04557.x.

A. Spitkovsky. Particle Acceleration in Relativistic Collisionless Shocks: Fermi Process at Last? *The Astrophysical Journal Letters*, 682:L5, July 2008. doi: 10.1086/590248.

C. Tadhunter. An introduction to active galactic nuclei: Classification and unification. *New Astronomy Review*, **52**:227–239, Aug. 2008. doi: 10.1016/j.newar.2008.06.004.

C. M. Urry & P. Padovani. Unified Schemes for Radio-Loud Active Galactic Nuclei. *Publications of the Astronomical Society of the Pacific*, **107**:803, Sept. 1995. doi: 10.1086/133630.

C. M. Urry, R. Scarpa, M. O'Dowd, et al. The Hubble Space Telescope Survey of BL Lacertae Objects. II. Host Galaxies. *The Astrophysical Journal*, **532**:816–829, Apr. 2000. doi: 10.1086/308616.

G. Wardziński & A. A. Zdziarski. Thermal synchrotron radiation and its Comptonization in compact X-ray sources. *Monthly Notices of the Royal Astronomical Society*, **314**:183–198, May 2000. doi:

10.1046/j.1365-8711.2000.03297.x.

E. S. Weibel. Spontaneously growing transverse waves in a plasma due to an anisotropic velocity distribution. *Phys. Rev. Lett.*, **2**:83–84, Feb 1959. doi: 10.1103/PhysRevLett.2.83.

J. P. Wild & E. R. Hill. Approximation of the general formulae for gyro and synchrotron radiation in a vacuum and isotropic plasma. *Australian Journal of Physics*, **24**:43, Feb. 1971. doi: 10.1071/PH710043.

B. Wolfe & F. Melia. Transrelativistic Synchrotron Emissivity, Cross Section, and Polarization. *The Astrophysical Journal*, **637**:313–321, Jan. 2006. doi: 10.1086/497890.

M. Zacharias & R. Schlickeiser. Blazar synchrotron emission of instantaneously power-law injected electrons under linear synchrotron, non-linear SSC, and combined synchrotron-SSC cooling. *Astronomy & Astrophysics*, 524:A31, Dec. 2010. doi: 10.1051/0004-6361/201015284.

A. A. Zdziarski, P. S. Coppi, & D. Q. Lamb. Physical processes in photon-starved nonthermal pair plasmas. *The Astrophysical Journal*, **357**:149–160, July 1990. doi: 10.1086/168901.

Publications

The following peer-reviewed publications and proceedings reports have been published during the duration of the doctoral period:

- J. M. Rueda-Becerril, P. Mimica, & M. A. Aloy. On the influence of a hybrid thermal–non-thermal distribution in the internal shocks model for blazars. *Monthly Notices of the Royal Astronomical Society*, **468**:1169–1182, June 2017. doi: 10.1093/mnras/stx476. RMA17

- J. Rueda-Becerril, P. Mimica, & M. A. Aloy. Numerical simulations of the internal shock model in magnetized relativistic jets of blazars. In *Proceedings of Swift: 10 Years of Discovery (SWIFT 10), held 2-5 December 2014 at La Sapienza University, Rome, Italy.*, page 159, 2014a

- J. M. Rueda-Becerril, P. Mimica, & M. A. Aloy. The influence of the magnetic field on the spectral properties of blazars. *Monthly Notices of the Royal Astronomical Society*, **438**:1856–1869, Feb. 2014b. doi: 10.1093/mnras/stt2335. RMA14

- J. M. Rueda-Becerril, P. Mimica, M. A. Aloy, & C. Aloy. Numerical study of broadband spectra caused by internal shocks in magnetized relativistic jets of blazars. In *European Physical Journal Web of Conferences*, volume 61 of *European Physical Journal Web of Conferences*, page 02007, Dec. 2013. doi: 10.1051/epjconf/20136102007

- P. Mimica, M. A. Aloy, J. M. Rueda-Becerril, S. Tabik, & C. Aloy. Numerical simulations of dynamics and emission from relativistic astrophysical jets. In *Journal of Physics Conference Series*, volume 454 of *Journal of Physics Conference Series*, page 012001, Aug. 2013. doi: 10.1088/1742-6596/454/1/012001